EPRI-NP-756

Analytical Model for Bottom Reflooding Heat Transfer in Light Water Reactors (The UCFLOOD Code)

NP-756
Research Project 248-1

Key Phase Report, August 1978

Prepared by

UNIVERSITY OF CALIFORNIA
Department of Nuclear Engineering
Berkeley, California 94720

Authors
L. Arrieta
G. Yadigaroglu

Prepared for

Electric Power Research Institute
3412 Hillview Avenue
Palo Alto, California 94304

EPRI Project Manager
K. H. Sun
Nuclear Power Division

LEGAL NOTICE

This report was prepared by the University of California, Berkeley (UCB), as an account of work sponsored by the Electric Power Research Institute, Inc. (EPRI). Neither EPRI, members of EPRI, UCB, nor any person acting on behalf of either: (a) makes any warranty or representation, express or implied, with respect to the accuracy, completeness, or usefulness of the information contained in this report, or that the use of any information, apparatus, method, or process disclosed in this report may not infringe privately owned rights; or (b) assumes any liabilities with respect to the use of, or for damages resulting from the use of, any information, apparatus, method, or process disclosed in this report.

EPRI PERSPECTIVE

PROJECT DESCRIPTION

Reflooding is one of the important Emergency Core Cooling mechanisms for Light Water Reactors during the hypothetical Loss-of-Coolant Accident (LOCA). Extensive large-scale experiments have been conducted worldwide in recent years to investigate the heat transfer effectiveness of reflooding under simulated LOCA conditions. Simultaneously, continuing efforts have been made, both experimentally and theoretically, to enhance the fundamental understanding of the thermal-hydraulic phenomena occurring during the reflooding process. The EPRI RP248-1 project, which has been underway since 1974 at the University of California, Berkeley campus, is a part of this continuing effort.

The research project consists of state-of-the-art evaluation of the technology in the LOCA reflood area, and experimental and analytical studies of the reflooding phenomena. Principal investigators are R. Greif, R. Seban, and G. Yadigaroglu.

PROJECT OBJECTIVES

The objective of the project is to develop analytical models capable of predicting the thermal-hydraulic performance under reflooding conditions. Data from a laboratory-scale single-tube experimental facility are obtained to provide phenomenological understanding and to assist model development. This project is integrated with EPRI's program in facilitating comprehensive and realistic evaluations of reflood concerns. In particular, it is parallel to the large-scale bundle experiment project RP959-1, FLECHT-SEASET (Full Length Emergency Core Heat Transfer - Separate Effect and System Effect Tests), which is jointly sponsored by EPRI, NRC, and Westinghouse Electric Corporation.

Accomplishments to date are documented in the following reports:

(1) "Heat Transfer During the Reflooding Phase of the LOCA - State of the Art," EPRI 248-1, September, 1975.

(2) "UC-B Reflood Experimental Plan," EPRI NP-457, April, 1977.

(3) "Rewetting and Liquid Entrainment During Reflooding - State of the Art," EPRI NP-435, May, 1977.

(4) "Rewetting Model Using a Generalized Boiling Curve," EPRI NP-571, October, 1977.

(5) "UC-B Reflood Program: Experimental Data Report," EPRI-743, April, 1978.

CONCLUSIONS AND RECOMMENDATIONS

This report documents the detailed analysis and coding of a mechanistic reflooding model called UCFLOOD for the prediction of thermal-hydraulic performance in a single-flow channel and its associated fuel rod (or a tubular test section with internal flow). The current version of UCFLOOD code has a general framework that incorporates the current technology. The code subroutines for the individual phenomenological models can be modified and updated as more advanced or upgraded models become available. It is my suggestion that UCFLOOD can be used as a guide to assist in the development of realistic reflooding models for potential future nuclear reactor licensing applications.

K. H. Sun, Project Manager
Nuclear Power Division

ABSTRACT

The UCFLOOD code is based on mechanistic models developed to analyze bottom reflooding of a single flow channel and its associated fuel rod, or a tubular test section with internal flow.

From the hydrodynamic point of view the flow channel is divided into a single-phase liquid region, a continuous-liquid two-phase region, and a dispersed-liquid region. The void fraction is obtained from drift flux models. The onset of liquid entrainment is determined using a criterion based on the instability of the liquid core in the inverted-annular flow regime.

For heat transfer calculations, the channel is divided into regions of single-phase-liquid heat transfer, nucleate boiling and forced-convection vaporization, inverted-annular film boiling, and dispersed-flow film boiling. The heat transfer coefficients are functions of the local flow conditions. The wall temperature history is calculated by solving the time-dependent radial conduction equation. Quench front propagation is treated separately from the overall heat transfer calculations by models including the effects of axial conduction.

Good agreement of calculated and experimental results has been obtained. A code user's manual is appended.

ACKNOWLEDGMENTS

The authors wish to acknowledge helpful discussions with Professors V. E. Schrock, R. Greif, and R. Seban, and with Dr. E. Elias. They are thankful to Dr. K. H. Sun, EPRI project manager, for his careful review of the manuscript and suggestions for improvements.

The assistance of M. K.-P. Yu in providing reduced UC-Berkeley experimental data is greatly appreciated.

L. Arrieta received financial assistance during his graduate studies at Berkeley from the Brazilian Comissão Nacional de Energia Nuclear. G. Yadigaroglu worked on various aspects of the research presented here while he was on sabbatical leave during the 1976-1977 academic year at the Centre d'Etudes Nucléaires of Grenoble, in France.

The authors wish to thank Mrs. Joy Kono for her excellent typing of the manuscript.

CONTENTS

ILLUSTRATIONS

SUMMARY

The UCFLOOD code is based on a mechanistic, best-estimate, "local-conditions" model of a fuel rod and its associated flow channel undergoing bottom reflooding. The code can also be used to predict reflooding of internally cooled tubular test sections. The report contains a detailed description of the UCFLOOD model and predictions of reflooding data obtained with tubular test sections at Berkeley.

The initial state of the rod or tube wall, the system pressure, and the variations in time of the reflooding rate, of the inlet coolant temperature, and of the power generation are inputs to UCFLOOD. The local flow conditions are first determined all along the channel, and then heat transfer is calculated according to these local conditions.

For hydrodynamic calculations, the channel is divided in three major control volumes according to the prevailing flow regimes, namely a single-phase, a continuous-liquid-phase (bubbly, slug, annular, or inverted-annular flow), and a dispersed-liquid region. Conservation of mass and energy is considered in a fully transient form in the single-phase region using a Lagrangian flow description, while in the continuous-liquid-phase and dispersed-liquid regions these equations are solved in their quasi-steady-state form, including, however, appropriate corrections for the variation of the mass flux along the channel. Profile-fit methods are used to estimate the liquid subcooling in the subcooled-boiling region and the vapor superheat in the dispersed-flow region. The void fraction distribution is obtained from drift-flux models.

The onset of liquid entrainment is determined from a critical Weber number based on the relative velocity between the phases and the radial dimension of the liquid core in the inverted-annular flow regime. The initial droplet size following break-up of the liquid core is also determined from a Weber number, now based on droplet diameter.

For heat transfer calculations, the channel is similarly divided into a number of regions, including regions of single-phase heat transfer to the liquid, nucleate

boiling and forced-convection vaporization, inverted-annular and transition-flow film boiling. Heat transfer coefficients in these regions are obtained from correlations available in the literature, except for the coefficient in the inverted-annular-flow region that was extracted from experimental data. The wall temperature history is calculated by solving the time-dependent radial conduction equation at a number of axial locations.

The very important problem of quench front propagation is treated separately from the overall thermo-hydraulic calculations by modeling the narrow quench front region, including the effects of axial conduction. Two methods are available for estimating quench front velocity: The two-dimensional heat conduction equation can be solved locally using a moving-grid technique or, alternatively (for tubular test sections), a semi-empirical approach based on an analytical two-dimensional conduction solution and an empirical correlation of the heat transfer coefficient can be used. The overall thermo-hydraulic calculations provide the boundary conditions and the local conditions needed to obtain the heat transfer coefficients for the quench-front-region model. The semi-empirical method for estimating quench front velocity gave good agreement with the UC-Berkeley experimental data.

Use of tubular test section data for model verification (instead of rod bundle data) offers a number of advantages including the absence of bundle and housing effects, and greater sensitivity of the wall temperatures to the choice of the heat transfer coefficients due to reduced heater heat capacity.

Prediction of a limited number of UC-Berkeley experimental reflooding runs by the UCFLOOD code has shown very good agreement with measured wall temperature histories at a number of axial locations. Additional model verification is obtained by comparing predicted and measured quench front propagation. Good agreement was typical of the comparisons made. Finally, predictions of liquid and total carry-over rates out of the test section were very good, confirming the validity of the hydrodynamic models used in the code.

The report contains a detailed code description and a user's manual.

NOMENCLATURE

Most commonly used general nomenclature is given here. Additional symbols and subscripts are defined and used locally in the text and the appendices.

SYMBOLS - LATIN ALPHABET

A_c	flow area
c, c_p	specific heat
C_D	droplet drag coefficient
C_o	drift-flux model distribution parameter, Eq. 2-21
D_H	hydraulic diameter of flow channel
E	liquid entrainment fraction, Eq. 2-37
g	acceleration of gravity
G	mass flux
h	enthalpy or heat transfer coefficient
j	volumetric flux
k	thermal conductivity
n	droplet number density
N	droplet number flux
p	pressure
P_H	heated perimeter of the flow channel
q'	heat generation or transfer rate per unit length
q"	heat flux
q'''	volumetric heat source
r	radial coordinate
t	time
T	temperature

u	phase velocity
U	velocity of control volume boundary
v, V	fluid velocity
v	specific volume
x	flow quality
z, Z	axial coordinate
Z	location of control volume boundary

SYMBOLS - GREEK ALPHABET

α	void fraction
Γ_g	vapor generation rate per unit volume
δ	droplet diameter
ε	emissivity
θ	non-dimensional temperature
μ	viscosity
ρ	density
σ	surface tension
σ_R	Boltzman's constant
τ	fuel rod time constant, Eq. 3-11

NON-DIMENSIONAL NUMBERS

Bi	Biot number
Nu	Nusselt number
Pe	Peclet number
Pr	Prandtl number
Re	Reynolds number
We	Weber number

SUBSCRIPTS

a	conditions behind the quench front

b	conditions ahead of the quench front
b	bulk fluid
B	upstream boundary of quench front region
c	convective or coolant
cq	coolant condition at the quench front
d	droplet
D, D'	downstream limits of quench front region
eq	thermodynamic equilibrium
f	saturated liquid
fg	vaporization
fℓ	film-temperature conditions
g	saturated vapor
g	gap or heat generation in quench front region
gj	drift between gas and mixture
in	channel inlet
ℓ	subcooled liquid
ℓ	loss in quench front region
out	channel outlet
q	quench front
r, R	radiative heat transfer
s	reference coolant temperature
sat	saturation conditions
turn	turnaround temperature
T	downstream boundary of quench front region
U, U'	upstream limits of quench front region
v	superheated vapor
w	wall
δ	droplet
o	conditions at upstream limit of dispersed-flow region

1	average property in single-phase region (control volume 1)
2	average property in control volume 2 or at downstream limit of control volume 2

SUPERSCRIPTS

-	conditions just upstream of some boundary
+	conditions just downstream of some boundary
+	non-dimensional

ABBREVIATIONS (USED ALSO AS SUBSCRIPTS)

CHF	critical heat flux
DFFB	dispersed-flow film-boiling
DNB	departure from nucleate boiling
DO	dryout
IAFB	inverted-annular film-boiling
IB	incipience of boiling
LEV	continuous-liquid (swollen) level
NB	nucleate boiling
NVG	net vapor generation
OC	onset of liquid carryover
OE	onset of liquid entrainment
QF	quench front
SAT	slug-to-annular transition
TE	total liquid entrainment
TP	two-phase

Chapter 1

INTRODUCTION

A process of fundamental interest and licensing importance for Light Water Reactors (LWR) is the re-establishment of effective cooling of the core following a hypothetical Loss of Coolant Accident (LOCA).

During the initial phase of the LOCA the fuel cladding temperature increases due to stored heat in the fuel pellets and the fission-product decay-heat generation. To prevent the cladding temperature from rising to an unacceptable level, it is necessary to inject sufficient coolant and re-establish adequate heat removal. This task is performed by the Emergency Core Cooling Systems (ECCS).

This report describes the analytical model and the computer code UCFLOOD assembled to predict the thermal transient of a single fuel pin, from the time at which coolant reaches the bottom of the bundle until the fuel element is completely quenched. This period is referred to as the Reflooding Phase of the LOCA. The variation in time of the coolant inlet flow rate and temperature and of the pressure in the core are inputs to this model.

1.1 THE REFLOODING PHASE [1]

As the liquid level reaches the bottom of the bundle and starts to rise around the rods, complex heat transfer processes take place. From top to bottom, the rods experience free and forced-convection cooling by steam, dispersed-flow film boiling, nucleate boiling and finally free or forced convection to the liquid. Figure 1.1 shows schematically the flow patterns likely to be found some time after the beginning of reflooding. This entire configuration slowly moves up, until the top of the rods is completely quenched.

The reflooding flow rate is controlled by the balance between the driving head forcing the water into the core (the height of water in the downcomer above the equivalent water level in the core), and the back pressure in the upper plenum created by the steam-water mixture flowing from the core exit to the break (steam binding).

When the liquid first approaches the rods, the rod temperature is above the surface rewetting temperature and a sputtering spray of water droplets is produced. Liquid droplets are also produced by breaking up of waves created on the liquid-vapor interfaces and by bubbles piercing the liquid interface. Steam generated by boiling in the lower part of the bundle swells the liquid level and eventually reaches a

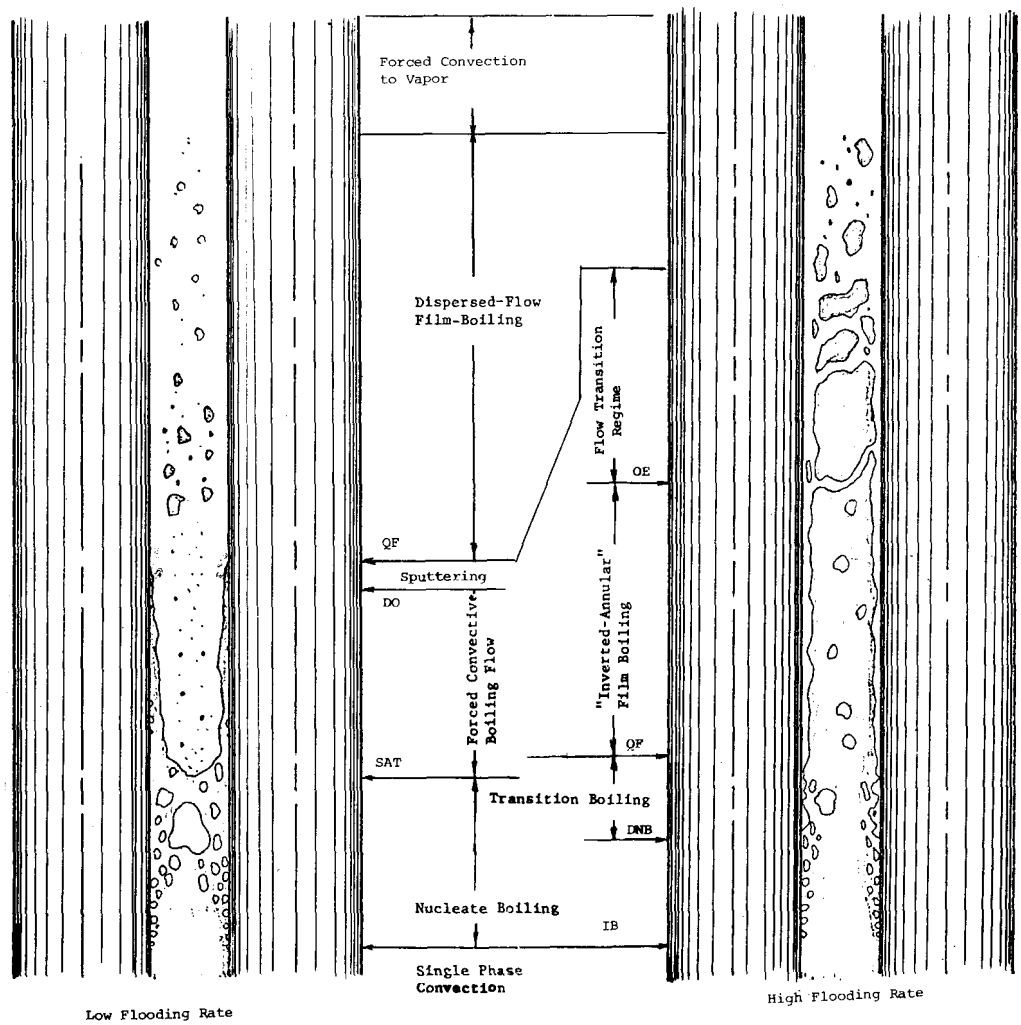

Figure 1-1. Heat transfer and two-phase flow regimes observed during reflooding.

IB - incipience of boiling
SAT - slug-to-annular transition
DNB - departure from nucleate boiling
DO - dryout
QF - quench front
OE - onset of entrainment

velocity at which entrainment and carryover of liquid droplets becomes possible. These droplets cool the rods higher up and continue upward until they are completely evaporated, or leave the bundle, or fall back into the liquid. The rods eventually cool below a rewetting temperature and quench.

The propagation of the quench front is accompanied by a large increase of the heat transfer coefficient and generally progresses on the rods from bottom to top, even though simultaneous quenching in more than one location has been observed. The quench front moves at relatively constant velocity, and it might be well below the liquid level in the lower part of the bundle. It should be kept in mind that large departures from thermal equilibrium and from homogeneous two-phase flow exist during the entire reflooding period.

1.2 METHOD OF ANALYSIS

The primary goal of the reflooding heat transfer analysis is to produce cladding temperature histories. In the overall LOCA analysis one must first consider the entire primary system and calculate the flow and pressure conditions at the boundaries of the core ("loop" calculations). This information can then be used to calculate the flow conditions along the fuel bundles, from which the distribution of heat transfer coefficients can be obtained. The local heat transfer coefficients provide the boundary condition for the solution of the transient conduction equation in the rod that yields the temperature history of the fuel and cladding (the last two steps are referred to as the "hot channel" calculations. Since heat transfer from the rods influences the core exit conditions, there is a coupling between core heat transfer and primary system hydrodynamics and iteration or simultaneous solution might be required.

A major effort to produce large-bundle reflooding heat transfer information was carried out in the United States under the PWR-FLECHT program [2-5]. The results of these experiments were used to correlate heat transfer coefficients along the core as a function of core inlet conditions, system pressure level, rod power, and peak cladding temperature at the beginning of reflooding.

Several numerical fits of the measured heat transfer coefficients as function of axial position, time, and system parameters have been proposed. These fits have been incorporated in the computer codes used for licensing purposes in the United States.

This report presents a simple analytical model for predicting reflooding heat

transfer based on calculated local flow conditions and "best-estimate" heat transfer correlations. Since the model is only concerned with the core (hot channel calculation) the flow conditions at the boundaries of the core must be specified.

Figure 1.2, shows a typical cladding temperature history at mid-plane, measured during the PWR-FLECHT experiments. At time zero the cooolant starts rising around the heated portion of the rods. Vapor generated in the lower part of the core and entrained liquid improve the heat transfer coefficient at higher elevations; however, the midplane temperature is still rising due to decay heat generation.

As the heat transfer coefficient is improved, mostly due to increases in the vapor flow rate and liquid entrainment, the local clad temperature excursion is arrested, and at the "turnaround" time, t_{turn}, the clad temperature starts dropping, Fig. 1-2. The maximum increase in the clad temperature, T_{rise}, is the most important information for licensing calculations. It should be noted that since the temperature excursion is arrested by a film-boiling heat transfer regime, the importance of accurate prediction of flow conditions downstream of the quench front becomes obvious.

Finally the rod surface temperature drops below a rewetting temperature and the cladding is quickly quenched down to roughly the cooolant temperature.

From the local cladding temperature history and the rod heat capacity, the local surface heat flux may be calculated. The calculation is very simple if a lumped-parameter conduction model is used. The local heat flux as a function of wall temperature obtained by this procedure is sketched in Fig. 1.2. The lumped-parameter assumption is not good during quenching when steep temperature gradients may develop. However, this calculation gives a rough idea of the variation of the heat flux. The shape of the curve in Fig. 1.2, strongly suggests that a "boiling curve" can be followed to define mechanisms of heat transfer near the quench front under reflooding conditions. This approach was tested in the present work, as described in Section 3.4.

Figures 1.3, show the various flow regimes and regions of heat transfer defined and used in the model. Some of these regions may not exist during some time, and some may not appear at all, under certain reflooding conditions, during the entire reflooding period.

The main features of the present calculational model are presented below and will be discussed in detail later.

- o the model considers a flow channel of constant cross section and and its associated fuel pin (or heated wall in case of simulation

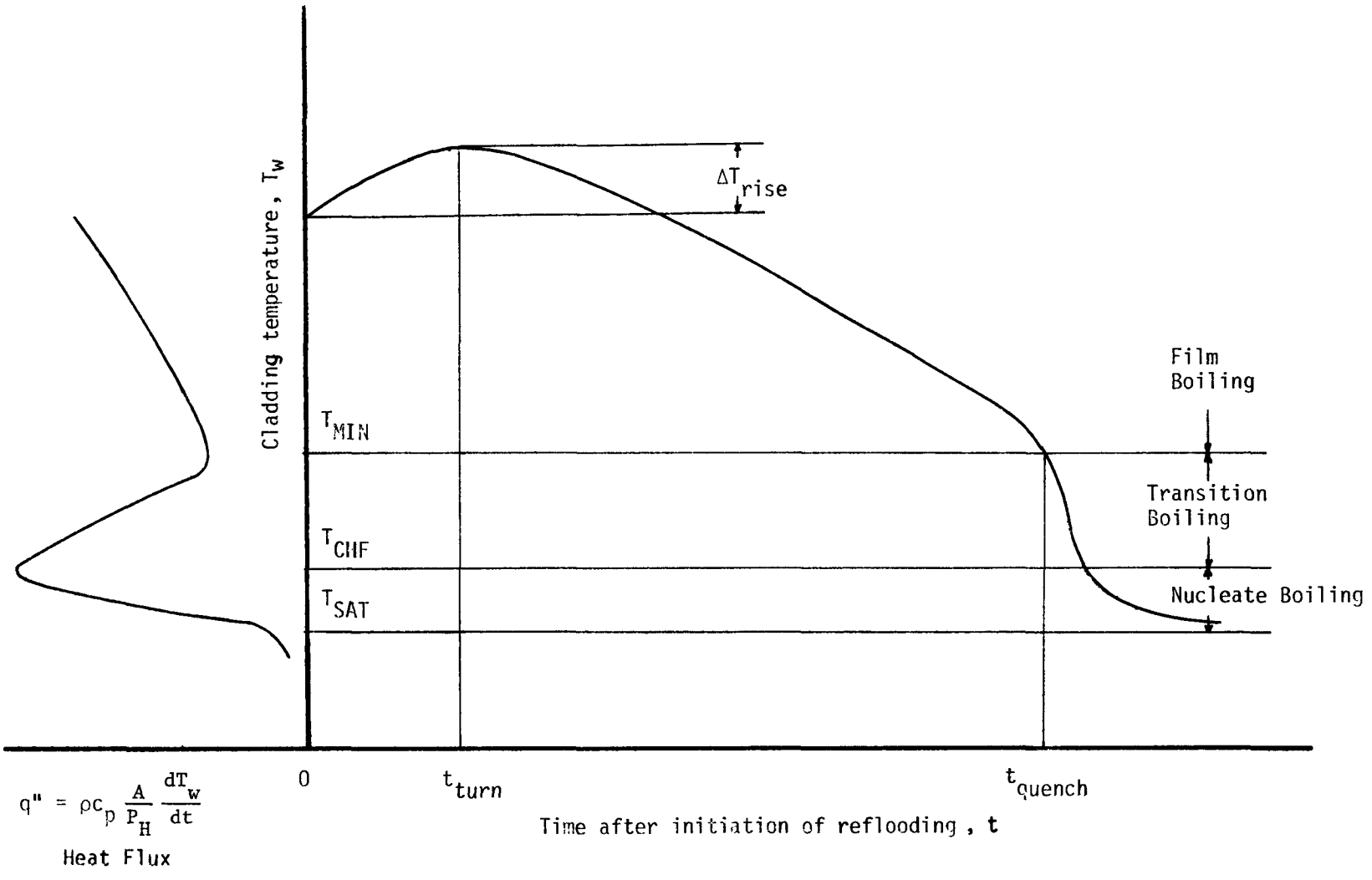

Figure 1-2. Variation of the cladding temperature during reflooding.

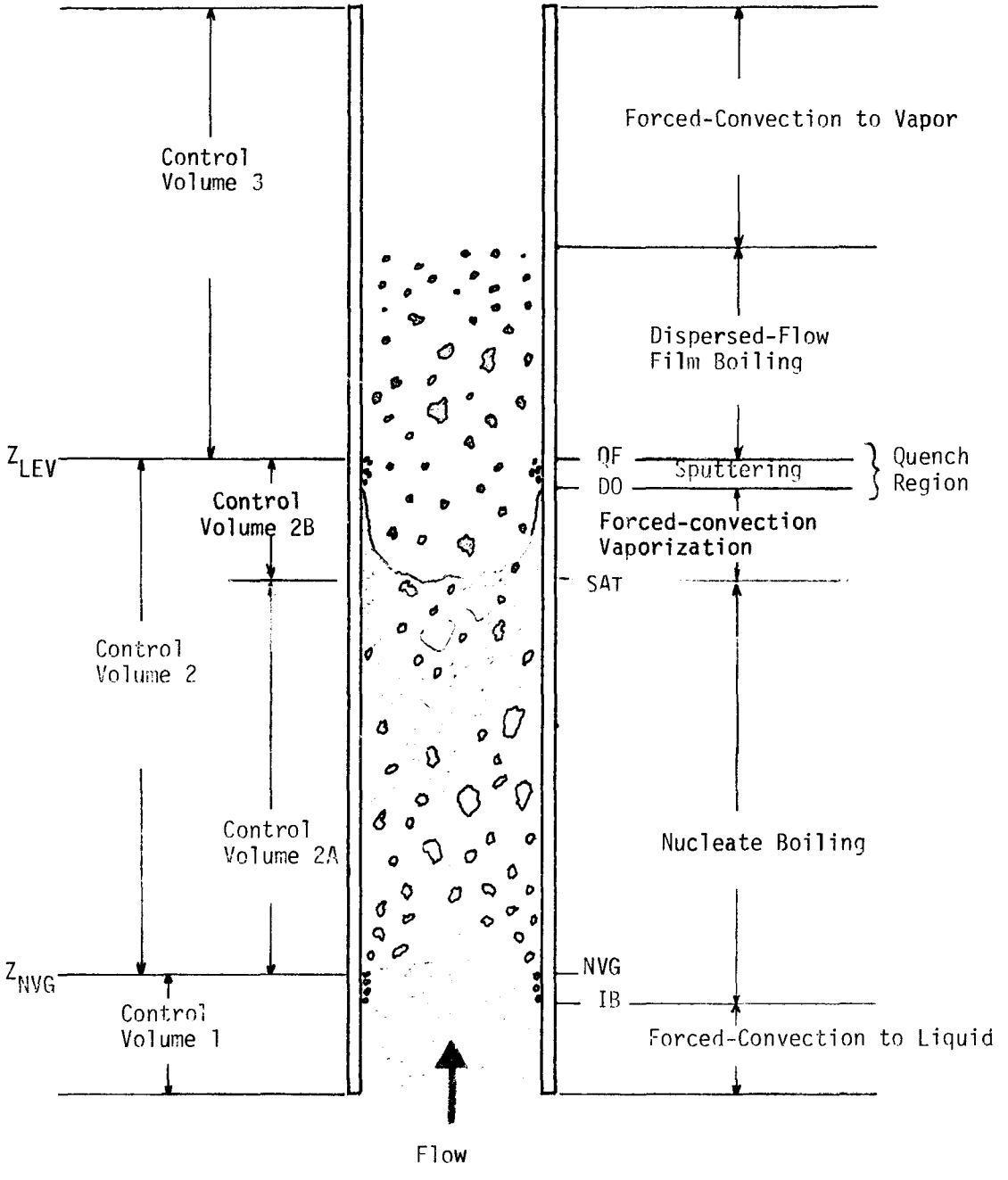

Figure 1-3A. Flow and heat transfer regions; low flooding rate cases (case A).

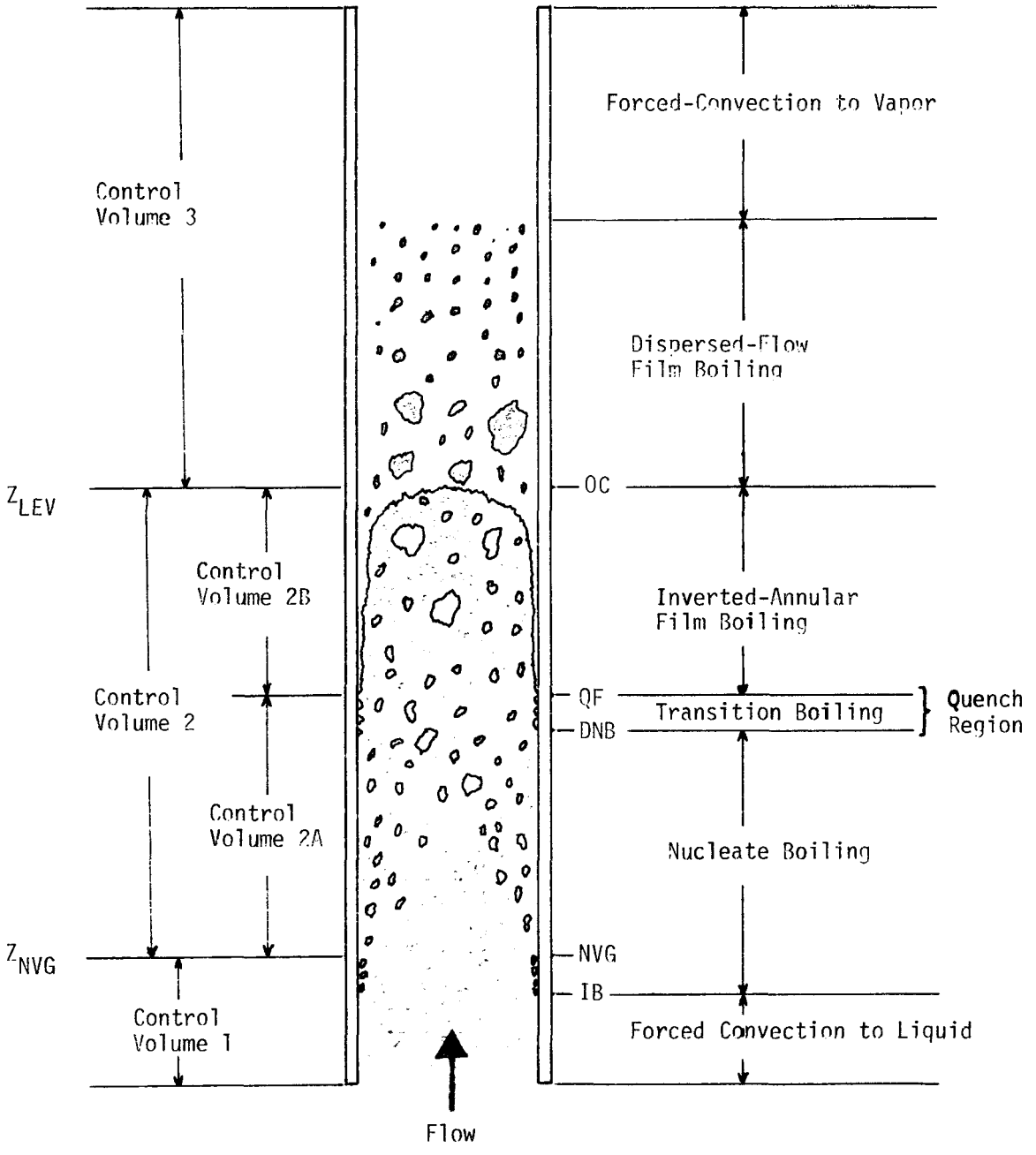

Figure 1-3B. Flow and heat transfer regions; high flooding rate cases (case B)

experiments).

- the conservation equations are used in their one-dimensional form.
- the required boundary and initial conditions are: reflooding rate and inlet subcooling as a function of time, system pressure, intial fuel-pin temperature field, and heat generation rate distribution in the rod as a function of time and axial coordinate.
- the momentum equation is decoupled from the mass and energy conservation equations by assuming a constant pressure level along the channel.
- the flow channel is divided from the hydrodynamic point of view in three main control volumes; each control volume may contain one or more heat transfer regions.
- the conservation equations are solved in a transient or quasi-steady-state form, according to the regions.
- non-homogeneous two-hase flow is accounted for by the use of drift flux model.
- the radial transient heat conduction equation is solved in the fuel rods for a number of axial nodes to calculate local temperature transients, except in the quench region where a special procedure is used.
- a selection logic based on local wall temperature, location with respect to quench front, and flow conditions (mixture level) is used to determine the appropriate heat transfer coefficients.
- heat transfer in the quench region, including the effects of axial concution, is treated by a special quench-region model discussed in Chapter 3.

The computer code UCFLOOD, including the above features was used to predict temperature histories of a number reflood simulation tests.

Only slow varations of the boundary conditions applied at the inlet of the channel and of the pressure level are considered in this development. Indeed it seems premature to embark into a fully dynamic description of the various two-phase flow and heat transfer phenomena taking place in a channel undergoing reflooding, in spite of the fact that strong flow and temperature oscillations have actually been observed during reflooding tests [4]. This is due to the fact that presently all our understanding of the various reflooding heat transfer and two-phase flow phenomena comes from steady-state or quasi-steady-state experiments and analyses, and very little is known about the effect of transients on these processes. Thus it is felt that with the present "steady-state" understanding of the various reflooding phenomena such as quench-front propagation and liquid carryover, efforts to produce fully dynamic heat transfer codes are premature. Indeed phenomena such as

liquid carryover must probably be viewed under a completely new light under transient conditions. Carryover of liquid higher up the channel during flow oscillations might enhance heat transfer well beyond the rate expected from equivalent, average, quasi-steady-state conditions.

Reflooding experiments conducted under oscillatory conditions have shown that the flow oscillations tend to enhance heat transfer [4]. Thus an analysis of the reflood phenomena that does not consider explicitly the effect of the oscillations would tend to overestimate the cladding temperature. It is also possible to analyze in this fashion the large amount of experimental data that have been obtained under constant forced-flow-rate conditions.

The succession of flow and heat transfer regimes shown in Fig. 1-3 and the points that mark the boundaries of the various regions move along the channel. However, the distribution of flow parameters such as void fraction inside each region remains largely constant. For example, the boundaries of control volume 2 coincide with points of approximately constant quality. This observation leads to the use of Lagrangian flow descriptions. Furthermore, it will not be necessary to describe in great detail the time-dependent variation of flow parameters within each control volume; the variation of parameters such as quality and void fraction will be assumed instead, on the basis of available data and theoretical models. This will facilitate the integration of the conservation equations along the channel. Examples of this approach can be found in the treatment of the subcooled-boiling and of the dispersed-flow regions.

In the absence of flow oscillations and other rapid transients, the behavior of the channel, viewed in a Lagrangian frame of reference moving along with the region boundaries, is not far from being steady state. This observation will be used to simplify the thermal-hydraulic calculations whenever possible. Thus the conservation equations will be integrated along the channel in their quasi-steady-state form whenever possible to increase computation efficiency. This is especially important when one considers the very long time scale of the reflooding transients.

Chapter 2

THEORY AND CALCULATIONAL PROCEDURE

The flow channel is divided in three main control volumes as shown in Fig. 1.3. Inside each control volume a detailed calculation of local flow conditions is performed.

In the single-phase liquid region, control volume 1, the flow conditions are calculated using a Lagrangian frame of reference. This control volume extends from the channel inlet to the instantaneous position of the net vapor generation (NVG) point. The Saha and Zuber [6] criterion for net vapor generation is adopted to define the NVG boundary.

Control volume 2 is defined as the two-phase region where the liquid phase is predominantly continuous. For case A of Fig. 1.3 it extends up to the dryout (DO) point, while for Case B, it is the swollen liquid level that determines the downstream boundary of this control volume.

Control volume 2 is divided into two sub-volumes in order to account correctly for the variation of the void fraction along the channel. The dividing point for the low-flooding-rate cases (case A) is the slug-to-annular (SAT) flow transition. For the high-flooding-rate cases the quench front determines the upstream boundary of the inverted-annual flow region, as shown in Fig. 1.3. The presence of different regimes in the two sub-volumes is accounted for by using different appropriate drift-flux model parameters in each region, as discussed later in Section 2.2.1.

For heat transfer calculations, the low-flooding-rate case can be obtained as a particular case of the high-flooding-rate condition simply by eliminating the inverted-annular film-boiling region. This is valid since, as it will be seen later, nucleate-boiling and forced-convection-vaporization heat transfer can be described by a unique correlation.

A swollen liquid level may exist in the channel for Case-B conditions. This level is defined as the location of a sharp discontinuity in the axial void fraction profile. Only vapor and entrained liquid droplets are assumed to cross this level.

Criteria for the onset of liquid entrainment and carryover (OE and OC) are develop-

ed and used to define the position of the swollen liquid level for flow Case B. For Case A, the swollen-liquid level is set at the location of the quench front, which is very close to the dryout point.

Control volume 3 contains the dispersed-droplet-flow region where the vapor phase is continuous, and extends from the swollen liquid level up to the channel exit. The drift flux model used to describe the hydrodynamics in this region makes use of the drift velocity of the droplets with respect to the mixture, rather than using the drift velocity of the bubbles. Heat exchanges between the superheated vapor and the droplets are considered using a new model based on a suggestion by Saha [7].

In the two-phase regions, control volumes 2 and 3, the local flow conditions are calculated by solving the conservation equations in their quasi-steady-state form. A detailed assessment of the validity of this procedure is given in Appendix A.

The cladding temperature history is calculated either by solving the transient heat conduction equations in the fuel rod, or a by a lumped-parameter technique in the case of thin-wall test sections. Appendix B describes the two-step numerical scheme used to solve the transient heat condition equation, and the lumped-parameter solution. In the quench-front region a special procedure, to be presented in Chapter 3, is used to calculate the cladding temperature history and the quench front velocity.

2.1 SINGLE-PHASE LIQUID REGION

This region, defined as control volume 1 in Fig. 1.3, extends from the channel inlet up to the point where net vapor generation (NVG) is calculated to occur.

2.1.1 Hydrodynamics of Single-Phase Region

A Lagrangian description of the flow is adopted, since it provides a natural way for following the NVG boundary. By assuming a constant pressure level, and that the liquid density is constant and equal to the arithmetic average of the inlet and saturation values,* the equations governing the flow become:

Mass Continuity,

$$\frac{\partial u_\ell}{\partial z} = 0 \qquad (2\text{-}1)$$

*In the worst case, i.e., for an inlet temperature of 100^o F (38^o C) and a system pressure of 60 psia (4 bar-a) the error is only 4%.

and conservation of energy,

$$\rho_l \frac{\partial h_\ell}{\partial t} + \rho_l u_\ell \frac{\partial h_\ell}{\partial z} = \frac{q'' P_H}{A_c} \tag{2-2}$$

where

ρ_l - average density of the liquid in single-phase region
$h_\ell(z,t)$ - liquid enthalpy
$u_\ell(z,t)$ - liquid velocity
$q''(z,t)$ - wall heat flux
P_H - heated perimeter
A_c - flow-channel cross sectional area

Eq. 2-1 shows that the liquid velocity along this control volume is a function of time only, i.e.,

$$u_\ell(z,t) = u_{\ell,in}(t) \tag{2-3}$$

where $u_{\ell,in}(t)$ is the prescribed inlet velocity (reflooding rate).

By defining a substantial derivative (changes in time seen by an observer moving with the liquid), Eq. 2-2 can be written as

$$\frac{Dh_\ell}{Dt} = \frac{\partial h_\ell}{\partial t} + u_{\ell,in} \frac{\partial h_\ell}{\partial z} = \frac{q'' P_H}{P_l A_c} \tag{2-4}$$

Position and time are then related by

$$\frac{dz}{dt} = u_{\ell,in}(t) \tag{2-5}$$

Eq. 2-5 defines the trajectories of the various liquid elements. Eqs. 2-4 and 2-5 represent the Lagrangian description of the flow. Integration of Eq. 2-5 gives the future positions, and Eq. 2-4 the corresponding enthalpies of a fluid element that was at $z = 0$ at time $t = t_o$.

It should be noted that this procedure avoids the solution of the partial differential Eq. 2-2, at the expense of having to keep track of the various fluid elements inside the control volume.

The wall heat flux required to solve Eq. 2-4 can be obtained by using a heat transfer coefficient and the cladding surface temperature calculated using the transient heat conduction equation.

Sometime after the initiation of reflooding, the point of NVG would have moved up the channel. In the absence of prescribed inlet flow and temperature changes and rapid variations of the heat generation rate, the wall temperatures in the single-phase region will stabilize, this region will behave in a steady-state fashion and the wall heat flux will correspond to the imposed heat generation rate. This situation occurs during a large number of constant forced-flooding-rate experiments.

Since the continuous integration of Eqs. 2-4 and 2-5 is time consuming, when the situation described above happens, a "fictitious channel inlet" is defined a few axial nodes below the NVG point. The flow conditions at this point do not change in time and are calculated by a simple steady-state energy balance in the fluid from the entrance up to the fictitious channel inlet, based on the imposed heat generation rate. The energy equation above the fictitious channel inlet continues to be solved by the Lagrangian scheme described above. Significant computer time savings are achieved in this manner.

2.1.2 Heat Transfer

The mechanism of heat transfer in the single-phase liquid region is convection to the liquid, and the heat transfer coefficient is primarily a function of the liquid Reynolds number,*

$$Re_\ell = \frac{\rho_l u_\ell D_H}{\mu_\ell} \qquad (2\text{-}6)$$

where D_H is the hydraulic diameter, defined as $D_H = 4\ A_c/P_H$.

For Re larger than 2000, i.e., for turbulent flow,** the Dittus-Boelter correlation [8] is a proper choice for calculating the heat transfer coefficient

$$h_c = 0.023\ \frac{k_\ell}{D_H}\ Re_\ell^{0.8}\ Pr_\ell^{0.4} \qquad (2\text{-}7$$

* The validity of heat transfer coefficient correlations obtained at steady state under transient conditions is not questioned here since the value of the heat transfer coefficient is not a critical parameter in this region.

** For D_H = 0.5 in. and water at 150° F, Re= 2000 corresponds to $u_\ell \simeq$ 2.6 in/s (66 mm/s).

If the Reynolds number is low, free convection might be a competing mechanism. Collier [8] gives an empirical correlation that accounts for the variation of the physical properties across the flow channel and for the influence of free convection:

$$h_c = 0.17 \frac{k_\ell}{D_H} Re_\ell^{0.33} Pr_\ell^{0.43} \left|\frac{Pr_\ell}{Pr_w}\right|^{-0.25} \left|\frac{D_H^3 \rho_f^2 g\beta\Delta T}{\mu_\ell^2}\right|^{0.1}, \quad Re < 2000 \qquad (2\text{-}8)$$

where

- k - thermal conductivity
- μ - dynamic viscosity
- c_p - specific heat
- $Pr = \mu c_p/k$ - Prandtl number
- β - coefficient of thermal expansion
- ΔT - difference between the wall and liquid temperatures
- g - acceleration of gravity

the indicies ℓ and w refer to properties evaluated at the bulk liquid and wall temperatures, respectively.

The local wall heat flux is then calculated from

$$q'' = h_c(T_w - T_\ell) \qquad (2\text{-}9)$$

As the liquid moves up, it loses subcooling, and a point is reached where local boiling starts. A criterion developed by Bergles and Rohsenow [9] is adopted to calculate the wall superheat at the incipience of boiling,

$$(T_w - T_{sat})_{IB} = \left(\frac{q''}{15.6p^{1.156}}\right)^{\frac{p^{0.0234}}{2.3}} \qquad (2\text{-}10)$$

where

- p - system pressure (psia)
- T_{sat} - saturation temperature (^oF)

The heat flux is calculated by Eq. 2-9 together with Eqs. 2-7 or 2-8.

Downstream of the point of incipience of boiling the wall heat flux is evaluated by,

$$q'' = h_c(T_w - T_\ell) + h_{NB}(T_w - T_{sat}) \qquad (2\text{-}11)$$

where h_{NB} is a boiling heat transfer coefficient to be introduced in Section 2.2.2.1.

2.1.3 Net Vapor Generation Boundary

As the wall superheat increases and the bulk subcooling decreases, a point will be reached where the evaporation rate, due to nucleation at the wall overcomes the condensation rate of the vapor. This is known as the point of net vapor generation (NVG) and a criterion derived by Saha and Zuber [6] is adopted to locate this point. For a Peclet number, Pe = Re.Pr, less than 70,000, which is always the case under reflooding conditions, the phenomenon is thermally controlled, i.e., independent of flow rate, and the following NVG criterion is recommended [6],

$$Nu = \frac{q'' D_H}{k_\ell (T_{sat} - T_\ell)} = 455 \qquad (2\text{-}12)$$

where q" is given by Eq. 2-11. Note that there are no experimental data supporting the validity of this criterion under reflooding conditions. This method should therefore be considered as tentative and should be reexamined if actual data on NVG obtained under reflooding conditions become available.

The wall voidage and the flow quality below the NVG point are neglected. This assumption is supported by the fact that experimental measurements of void fraction below the NVG point were found to be extremely low.

Eq. 2-12 defines the upper boundary of control volume 1, Z_{NVG} (Fig. 1-3). In the presence of highly subcooled liquid the location of the NVG point might be estimated to be downstream of the quench front. In this case the NVG point is set at the quench front.

2.2 TWO-PHASE FLOW REGIONS BELOW THE SWOLLEN LIQUID LEVEL

This section describes the hydrodynamics and heat transfer regions, embodied in control volume 2, namely, the nucleate-boiling, forced-convection-vaporization, and inverted-annular film-boiling regions, when present. Heat transfer in the quench region is treated separately in Chapter 3.

The two-phase-flow conservation equations are solved in a quasi-steady-state form, which is equivalent to assuming that the flow conditions accommodate immediately to

the time-dependent boundary conditions, namely the inlet reflooding rate, subcooling at the NVG point, and the axial wall heat flux distribution. This assumption is proven in Appendix A to be quite acceptable as long as the reflooding rate varies in a moderate fashion. A further refinement of this assumption is given in Section 2.2.4.

Zuber and Findlay's [10] drift flux model is used to account for the non-homogeneous nature of the two-phase flow. A profile-fit method for the liquid enthalpy [11, 12] is used to account for the absence of thermodynamic equilibrium in the subcooled boiling region.

A procedure based on liquid entrainment and carryover criteria, presented in Section 2.2.5, is used to predict the onset of liquid carryover and the swollen mixture level.

2.2.1 Two-Phase Flow Hydrodynamics

Assuming that any vapor in this region is at saturation, a uniform pressure level, and that the liquid density is constant and equal to the saturation density, the governing equations become:

Continuity of the Vapor

$$\frac{\partial \alpha}{\partial t} + \frac{\partial j_g}{\partial z} = \frac{\Gamma_g}{\rho_g} \tag{2-13}$$

Continuity of the Liquid

$$\frac{\partial (1 - \alpha)}{\partial t} + \frac{\partial j_\ell}{\partial z} = - \frac{\Gamma_g}{\rho_f} \tag{2-14}$$

Mixture Energy Equation

$$(1-\alpha)\rho_f \frac{\partial h_\ell}{\partial t} + \alpha \rho_g \frac{\partial h_g}{\partial t} + \rho_f j_\ell \frac{\partial h_\ell}{\partial z} + \rho_g j_g \frac{\partial h_g}{\partial z} = \frac{q'' P_H}{A_c} - (h_g - h_\ell)\Gamma_g \tag{2-15}$$

where

ρ_f - density of saturated liquid
α - void fraction
j_ℓ - liquid volumetric flux
j_g - vapor volumetric flux
Γ_g - vapor generation rate per unit volume
h_g - enthalpy of saturated vapor

The subscript ℓ denotes actual liquid conditions, while f denotes saturated liquid conditions. All the quantities in this subsection refer to cross-sectional averages.

By definition

$$j_\ell = (1 - \alpha)u_\ell$$

$$j_g = \alpha u_g$$

where u_ℓ and u_g are the liquid and vapor velocities, respectively.

The mass flux is given by

$$G = G_\ell + G_g = \rho_f j_\ell + \rho_g j_g$$

and the flow quality by

$$x = \frac{G_g}{G_g + G_\ell} = \frac{\rho_g j_g}{\rho_g j_g + \rho_f j_\ell} \tag{2-16}$$

As it was mentioned before, a quasi-steady-state is assumed, so that the time derivatives in the conservation equations are dropped. This results in the use of a unique, constant value of the mass flux all along the length of control volume 2, instead of calculating the mass flux variations in this control volume. Since, at low pressures, the void fraction and the mixture velocity increase very rapidly in the vicinity of the NVG point and remain thereafter relatively constant, it follows that the mass flux distribution also changes rapidly right after the NVG point and remains relatively constant thereafter. Thus it appears that a calculated value of the mass flux at the exit of control volume 2 is a better approximation than the value of the mass flux at the inlet of this volume. This value is estimated in Section 2.2.4 and used throughout control volume 2.

Since it was assumed that in control volume 2, all the vapor is in a saturated state, thermal non-equilibirum exists only due to possible liquid subcooling. Thus at steady state

$$\Gamma_g = \frac{dG_g}{dz} = G\frac{dx}{dz} \tag{2.17}$$

$$\frac{dh}{dz} = \frac{q'' P_H}{G A_c} \tag{2-18}$$

where h is the bulk enthalpy. The flow quality of the non-equilibrium two-phase mixture can be shown to be

$$x = \frac{h - h_\ell}{h_g - h_\ell} \tag{2-19}$$

In the present model, Eq. 2-18 is integrated every time step, with a boundary condition $h = h_{NVG}$ at $z = Z_{NVG}$, to obtain the bulk-enthalpy axial distribution inside control volume 2.

2.2.1.1 Profile Fit for the Liquid Enthalpy

Under thermodynamic equilibrium conditions, the solution of the energy equation provides directly the flow quality distribution along the channel. However, if the bulk of the flow is subcooled, a fraction of the wall heat flux goes to net vapor formation while the remainder is used up in raising the enthalpy of the subcooled liquid.

Two different approaches have been used to tackle this problem, namely mechanistic models and profile-fit models. The mechanistic models attempt to describe the problem by including all the physical phenomena involved; a good review of these models can be found in reference [13]. The profile-fit models [11, 12] do not attempt to specify the mechanisms of subcooled boiling, but instead assume a profile for the liquid enthalpy or flow quality between the NVG point and the point where themodynamic equilibrium is achieved.

The second approach is adopted in the present work, mainly because it is simpler and provides results of an acceptable accuracy in this region.

According to Zuber et al. [11]

$$h_f - h_\ell = (h_f - h_{NVG}) \exp[-(h - h_{NVG})/(h_f - h_{NVG})] \tag{2-20}$$

The choice of the function is made by simply requiring it to satisfy the proper boundary conditions, i.e.,

$$h_\ell = h_{NVG} \quad \text{at} \quad z = Z_{NVG}$$

$$h_\ell \to h_f \quad \text{for} \quad h >> h_f$$

$$\frac{dh_\ell}{dz} = \frac{dh}{dz} \quad \text{at} \quad z = Z_{NVG}$$

Solution of Eq. 2-18 together with Eqs. 2-19 and 2-20 determines the flow quality $x(z)$ along the channel.

2.2.1.2 Zuber-and-Findlay Drift Flux Model [10]

The drift velocity of the gas is defined at any point of the channel cross section by the local relationship

$$v_{gj} = u_g - j$$

where

$$j = j_\ell + j_g = (1 - \alpha)u_\ell + \alpha u_g$$

Since the velocities as well as the void fraction vary radially across the channel cross section, the equation is averaged after multiplication by α, i.e.,

$$< \alpha\, v_{gj} > = < \alpha\, u_g > - < \alpha j >$$

or

$$< j_g > = < \alpha j > + < \alpha\, v_{gj} >$$

where the symbol $<>$ denotes averaging over the cross sectional area.

By defining a distribution parameter C_o

$$C_o \equiv \frac{<\alpha j>}{<\alpha>\ <j>} \tag{2-21}$$

and a mean weighted drift velocity V_{gj}

$$V_{gj} = \frac{<\alpha\, v_{gj}>}{<\alpha>} \tag{2.22}$$

the cross-sectional-average void fraction is obtained as

$$\langle\alpha\rangle = \frac{\langle j_g \rangle}{C_o \langle j \rangle + V_{gj}}$$

By making use of the flow quality defined by Eq. 2-16,

$$\alpha = \frac{x}{C_o\left[x + \frac{\rho_g}{\rho_f}(1 - x)\right] + \frac{\rho_g V_{gj}}{G}} \tag{2-23}$$

where we have resumed the use of cross-sectional-average values shown without angle brakets to alleviate the notations.

Two quantities remain to be specified before the void fraction can be calculated by Eq. 2-23, namely C_o and V_{gj}. The value of these parameters will depend on the two-phase flow regime, as discussed below.

Bubbly and Churn Flow

A functional form for the variation of C_o with pressure and flow quality has been deduced by Dix [13],

$$C_o = \beta\left[1 + (1/\beta - 1)^b\right] \tag{2-24}$$

where

$$b = (\rho_g/\rho_f)^{0.1}$$

and

$$\beta = \frac{x}{\left[x + \frac{\rho_g}{\rho_f}(1 - x)\right]} = \frac{j_g}{j}$$, is the flowing concentration.

The exponent 0.1, was obtained to best fit Dix's data, however, Eq 2-24 in any case satisfies the required limit conditions, i.e.,

$$C_o \rightarrow 0 \quad \text{as} \quad x \rightarrow 0$$

$$C_o \rightarrow 1 \quad \text{as} \quad x \rightarrow 1$$

and should give best results, the alternative being to assume a constant value for C_o.

For the mean weighted drift velocity, the following expression is recommended [10]

$$V_{gj} = 1.53 \left[\frac{\sigma g (\rho_f - \rho_g)}{\rho_f^2}\right]^{\frac{1}{4}} (1 - \alpha)^{3/2} \tag{2-25}$$

which has the convenient feature of not being dependent on bubble size, and is valid for bubbles with diameters of the order 1-20 mm. The $(1 - \alpha)^{3/2}$ term accounts for the fact that the bubbles are not rising in an infinite liquid medium, but in the presence of other bubbles.

Annular Flow

For the case of low reflooding rate, low inlet subcooling, and high power input, an annular flow regime may develop below the quench front as shown in Fig. 1.3A. This flow regime usually arises as a result of breaking down of the liquid bridges between vapor slugs in slug flow.

Usually a criterion for the slug-to-annular transition is defined in terms of a critical vapor volumetric flux. One such criterion, presented by Wallis [22], is adopted in the present work, namely

$$j_g^* \geq 0.9$$

where

$$j_g^* = j_g \rho_g^{\frac{1}{2}} [g D_H (\rho_f - \rho_g)]^{-1/2}$$

Expressions for the Zuber-Findlay drift-flux model parameters C_o and V_{gj} in annular flow can be obtained by considering an idealized annular flow where all the liquid flows in a film of thickness δ on the wall and all the gas is in the central core, as shown in Fig. 2-1.

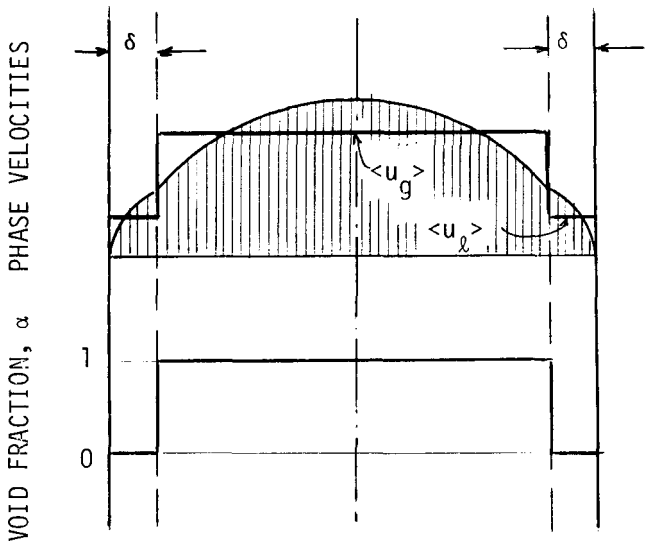

Figure 2-1. Idealized Annular Flow.

The average liquid and gas velocities are denoted by $\langle u_f \rangle$ and $\langle u_g \rangle$. Starting from the definitions of C_o and V_{gj}, Eqs. 2-21 and 2-22, we can calculate

$$C_o = \frac{\langle u_g \rangle}{\langle \alpha \rangle (\langle u_g \rangle + \langle u_f \rangle)} \tag{2-25a}$$

and

$$V_{gj} = 0$$

Starting from the definitions of the local values of v_{gj} and j, we can show that

$$\langle U_g \rangle - \langle j \rangle = V'_{gj} = (C_o - 1) \langle j \rangle + V_{gj}$$

Ishii [14] developed an expression for V'_{gj} which can be used to define the value of C_o to be used in our equations, namely:

$$C_o = 1 + \frac{1}{\langle j \rangle} \left[\frac{\rho_f}{\rho_g} \frac{\alpha^{\frac{1}{2}}}{1 + 75(1 - \alpha)} \frac{f_w}{0.005} \langle j_f \rangle^2 + \frac{(\rho_f - \rho_g)}{\rho_g} \frac{\alpha^{\frac{1}{2}} (1 - \alpha)^3}{1 + 75(1 - \alpha)} \frac{gD_H}{0.015} \right]^{\frac{1}{2}} \tag{2-25b}$$

with

$$f_w = \frac{16}{Re_f} \quad \text{for} \quad Re_f \leq 3200$$

$$0.005 \quad \text{for} \quad Re_f > 3200$$

where

$$Re_f = \frac{j_f \rho_f D_H}{\mu_f}$$

Inverted-Annular Flow

No model for the hydrodynamics of two-phase flow in the inverted-annular flow region exists. In fact such a model should consider both two-phase flow and heat transfer in this region.

In the present state of development of the model, C_o and V_{gj} in the inverted-annular flow region are considered as adjustable parameters and are specified as input to the UCFLOOD code.

2.2.2 Heat Transfer

2.2.2.1 Boiling Heat Transfer below the Quench Front. Following the incipience of boiling, two rather different boiling mechanisms may take place, namely nucleate boiling and forced-convection vaporization. Nucleate boiling is characterized by bubble nucleation on the wall, depends primarily on the wall superheat, and is quite independent of flow rate. It is the dominant heat transfer mechanism found in two-phase flow regimes with low and medium values of the void fraction. For high void fractions the flow regime is likely to be annular; the core vapor velocity can be high and the turbulence at the vapor-liquid interface strong, so that the heat transfer maechanism changes its character. Heat is then transferred by conduction and convection through the liquid film and vapor is generated at the interface. This mechanism of boiling heat transfer is characterized by being flow-rate dependent and it is referred to as forced-convection vaporization.

Chen [15] developed a correlation by assuming that both mechanisms discussed above occur to some degree and that the contributions made by the two mechanisms are additive. Chen's correlation is adopted here because of its very good agreement with

a wide variety of experimental data, and because it can adequately cover heat transfer below the quench front without discontinuities in the value of the heat transfer coefficient.

Chen represented the convective component by a Dittus-Boelter type equation modified by a factor F to account for the two-phase nature of the flow.

$$h_c = 0.023 \left[\frac{G(1-x)D_H}{\mu_f}\right]^{0.8} \left[\frac{\mu c_p}{k}\right]_f^{0.4} \frac{k_f}{D_H} F \tag{2-26}$$

where

$$F = \left[\frac{Re_{TP}}{G\,(1 - x)D_H/\mu_f}\right]^{0.8} = \left[\frac{Re_{TP}}{Re_\ell}\right]^{0.8} \tag{2-27}$$

The factor F was correlated as a function of the Martinelli parameter X_{tt} and is shown in Fig. 2-2.

For the nucleate-boiling component, Chen used the Forster and Zuber analysis for pool boiling. A modification was introduced, however, to account for the fact that the mean superheat of the fluid in which the bubble grows is lower than the wall superheat ΔT_{SAT}. A suppression factor S was introduced to account for this effect, and S was correlated as a function of the two-phase Reynolds number, Re_{TP}, as shown in Fig. 2-3.

$$h_{NB} = 0.0012 \left[\frac{k_f^{0.79} c_{pf}^{0.45} \rho_f^{0.49}}{\sigma_f^{0.5} \mu_f^{0.29} h_{fg}^{0.24} \rho_g^{0.24}}\right] \Delta T_{sat}^{0.24} \Delta p_{sat}^{0.75} S \tag{2-28}$$

where

σ - surface tension
h_{fg} - latent heat of vaporization
ΔT_{sat} - wall superheat, $T_w - T_{sat}$
ΔP_{sat} - increment in pressure corresponding to the wall superheat.

Collier [8] suggested that Chen's correlation is applicable for subcooled boiling, provided F is made equal to one. Then the heat flux in the boiling region is given by

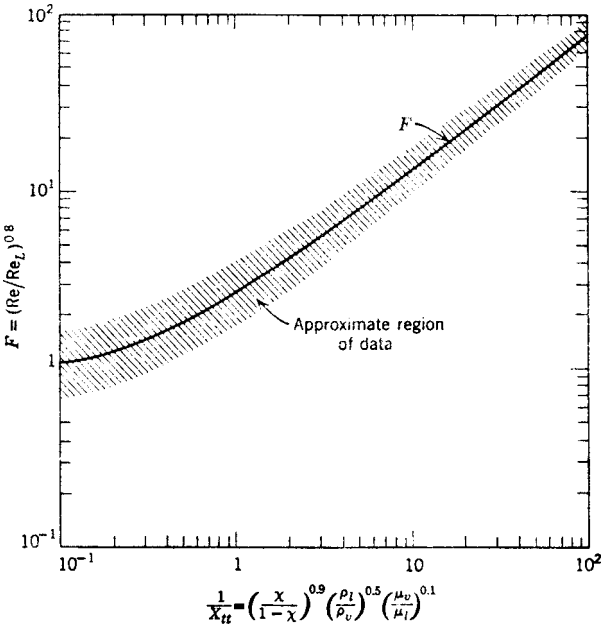

Figure 2-2. F factor used in Chen correlation.

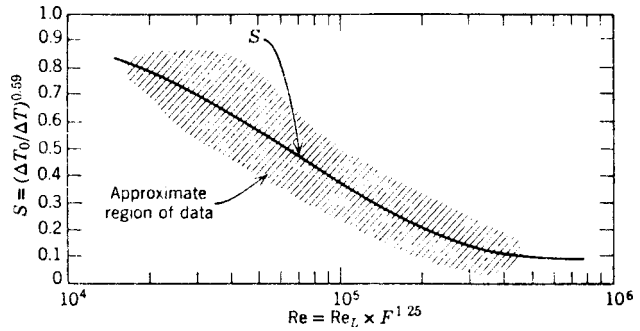

Figure 2-3. S factor used in Chen correlation.

$$q'' = h_c(T_w - T_\ell) + h_{NB}(T_w - T_{sat}) \tag{2-29}$$

2.2.2.2 Inverted-Annular Film Boiling above the Quench Front. The term "inverted-annular" film boiling is normally used to define a post-dryout heat transfer mechanism where a vapor layer separates a continuous liquid core from the heater surface.

At dryout the continuous liquid core, which may contain some entrained bubbles, becomes separated from the wall by a low-viscosity vapor layer. Once the vapor blanket has been formed the heat will be transferred from the wall to the vapor and subsequently from the vapor to the liquid core. Some heat will also be transferred directly from the wall to the liquid core by radiation. Heat transfer across the wavy vapor-core interface will take place by forced convection evaporation. The low-viscosity, low-density vapor flow will experience a higher acceleration than the dense core flow, thus producing an increased velocity differential across the interface which may lead to an unstable interface.

Bromley [16] first established a relationship for the heat transfer coefficient for laminar film boiling from a horizontal tube by direct analogy with identical relationships derived for film-wise condensation. Bailey [17] in his experiments noticed the presence of waves on the vapor-liquid interface and varicosities of vapor occurring at regular intervals along the surface. He concluded that this instability (Taylor instability), causes the laminar boundary layer to restart over each wavelength inhibiting transition to turbulent film. The film instability also eliminates the continuing decrease in heat transfer coefficient associated with a growing laminar film.

Recently, Andersen et al [18] did a comprehensive study of the problem and their resulting correlation that incorporates the effects discussed above, thereafter referred to as the modified Bromley correlation, was initially adopted in the present work.

$$h_{IAFB} = h_{FB} + h_R \tag{2-30}$$

$$h_{FB} = 0.62 \left[\frac{k_v^3 \rho_v (\rho_f - \rho_v) h'_{fg} g}{\mu_v (T_w - T_{sat})} \frac{1}{2\pi} \sqrt{\frac{g(\rho_f - \rho_v)}{\sigma}} \right]^{0.25} \tag{2-31}$$

$$h_R = \varepsilon_w \sigma_R \frac{(T_w^4 - T_{sat}^4)}{(T_w - T_{sat})} \tag{2-32}$$

where

$$h'_{fg} = h_{fg}\left[1 + 0.68\,\frac{c_{pv}(T_w - T_{sat})}{h_{fg}}\right] \tag{2.33}$$

h_R - takes into account radiation between the wall and the liquid core. h'_{fg} accounts for the vapor superheat in the film.

ε_w - wall emissivity

σ_R - Boltzman constant, 1.713×10^{-9} Btu/hr-ft^2 $^oR^4$

All the vapor properties are to be evaluated at the vapor film temperature, $(T_w + T_{sat})/2$.

The boiling part of Bromley's correlations as modified by Anderson et al gives near-atmospheric-pressure heat transfer coefficient values in the vicinity of 30 Btu/hr-ft^2 ^oF (170 W/m^2 ^oC) while experimental values obtained from single-tube reflooding experiments at the University of California-Berkeley (UC-B) [19] and other experimental data show that the heat transfer coefficient is a strong function of the instantaneous distance from the quench front. Attempts to correlate this dependence on distance from the quench front by using the dependence on length of the original Bromley correlation failed [48], since this dependence is too weak ($z^{-1/4}$) to account for the observed experimental effect.

The UC-B experimental reflood data [19] show an exponential variation of the heat transfer coefficient with distance from the quench front for distances of the order of one foot above the quench front. This led to the search for an empirical correlation of the form

$$h = h_q e^{-a\Delta z_q}$$

where

$$\Delta z_q = z - z_q$$

is the distance from the quench front and a and h_q are coefficients, possibly functions of local flow conditions at the location of the quench front. An analysis of a large number of data obtained from the UC-B reflooding experiments [19] by Yu [20] has shown that a and h_q can be correlated in terms of the equilibrium quality

downstream of the quench front, x_q^+, the velocity of the quench front U_q, and the inlet velocity U_{in} (i.e. the mass flux). The two coefficients were found to be otherwise not directly dependent of wall temperature. The correlations for a and h_q proposed by Yu and programmed tentatively into the UCFLOOD code are:

$$h_q = \left[\frac{1.5}{U_{in}} + (U_{in} - U_q)^{0.9}\right]\left[A + B(x_q^+ - \frac{0.1}{U_{in}})\right] \left(\frac{Btu}{hr\text{-}ft^2\ ^oF}\right) \qquad (2\text{-}33a)$$

$$a = A' + B'x_q^- \quad (ft^{-1})$$

The equilibrium quality just upstream of the quench front, x_q^-, is obtained from a heat balance on the fluid up to the actual location of the quench front. The equilibrium quality just downstream of the quench front, x_q^+ is obtained by adding to x_q^- the quality increment due to heat release from the wall during passage of the quench front,

$$\Delta x_q = \frac{\dot{Q}_s}{h_{fg} G A_c}$$

$$x_q^+ = x_q^- + \Delta x_q$$

where $\dot{Q}_s$ is the rate of heat transfer to the coolant in the quench front region, defined later by Eq. 3-6 of Section 3.3.1.

The values of the coefficients A, B, A' and B' are given in the tables below:

Values of A and B

$x_q^+ - 0.1/U_{in}$	A	B
> 0	4.379	31.605
< 0	4.483	-176.587

Values of A' and B'

$\bar{x}_q < 0$	$A' = 2.11 - 0.519U_{in} + 0.045U_{in}^2$ $B' = 12.86 - 3.10U_{in}$
$\bar{x}_q > 0$	$A' = 1.47 - 0.361U_{in} + 0.033U_{in}^2$ $B' = 1.29 - 1.02U_{in} - 0.122U_{in}^2$

In all these equations the velocities, U_{in} and U_q, must be inserted in in/s.

2.2.3 Criteria for the Onset of Liquid Entrainment and Carryover

In order to properly estimate post-dryout heat transfer as well as the total carryover fraction* it is necessary to predict the point where liquid carryover starts.

Note that the prediction of this carryover point is important only for the Case-B flow conditions of Fig. 1-3. Indeed liquid carryover predictions in the annular-flow regime are not required for heat transfer calculations. For Case-A conditions, i.e. in the presence of annular flow, liquid entrainment and carryover may start well below the quench front; at the film dryout point all the liquid is assumed to be entrained in droplet form and carried over by the vapor.

The various "entrainment" mechanisms are responsible for the separation of liquid drops from either the liquid core or from the liquid film on the wall. When the steam velocity exceeds a certain value these entrained droplets can be "carried over." Thus a necessary condition for liquid carryover is the presence of entrained liquid in the vapor flow.

From the point of view of heat transfer in the dispersed-flow region, the important phenomenon is liquid carryover and not just local liquid entrainment. For instance, the existence of a few droplets bouncing up and down from a liquid-vapor interface is not relevant to the cooling of the channel at higher elevations.

The various entrainment mechanisms and proposed methods for prediction of the onset of entrainment are discussed briefly in reference [21]. Wallis [22] summarizes

*The total carryover fraction is defined as the ratio of the total flow rate at the core exit to the total flow rate at the core inlet.

the available experimental data on entrainment; unfortunately, a general synthesis of these results is yet to be achieved. Furthermore, little information is available on entrainment in the inverted-annular flow regime.

To properly estimate the liquid carryover fraction, the following questions must be answered:

1) What are the flow conditions necessary for the onset of liquid entrainment? This question is generally answered by considering the stability of the liquid-vapor interface. Usually, a critical vapor velocity is used to predict entrainment data.

2) Once this critical vapor velocity is exceeded, what is the entrainment fraction and what is the average size of the entrained droplets?

3) Are the drag forces acting on these entrained droplets larger than the gravity forces? Only if the answer to this last question is yes, liquid carryover will indeed take place.

Additional experimental and theoretical work remains to be done in order to answer the above questions in a detailed manner. Before presenting the methods proposed for dealing with entrainment and carryover questions, a brief review of the state of the art will be made.

Westinghouse workers [23] using FLECHT results, developed a carryover correlation. The carryover fraction is a function of quench front position, flooding rate, maximum linear heat generation rate, pressure, and inlet subcooling. However, the actual dependence on these parameters is not published. While such correlations have great practical interest, they shed very little light on the local phenomenon of liquid entrainment.

Plummer [24] developed a criterion for the onset of liquid carryover, by assuming that at that point all the liquid is transformed in droplets of critical size, and that there is a balance between the gravity and drag forces acting on these droplets. Prescribing a critical Weber number for the droplets, and using the droplet equation of motion, the initial droplet size and the minimum velocity differential between the vapor and the liquid can be calculated. This criterion, implicitly assumes that if flow conditions for carryover do exist, then necessarily conditions for the onset of liquid entrainment have already been exceeded. Our major criticism of this model is that the droplet Weber number considers the stability to shattering of the droplets instead of dealing with the instability of the interface.

Sun and Duffey [58] used a simple mass balance over the test section to calculate the carryover fraction. They obtained an estimate of the variation of the average void fraction in the test section by assuming that the channel contained only liquid up to the location of the quench front and only vapor above the quench front. Their simple method predicted FLECHT and UC-B [19] carryover data fairly well. There is no need, however, to introduce simplifying assumptions when the calculations are performed by a computer code capable of calculating in a detailed manner the state of the fluid in the channel.

In the present work, a criterion for the onset of liquid entrainment, together with a suggestion for an entrainment-fraction correlation are adopted. It is also assumed that if liquid droplets have been formed, carryover will be possible, i.e., it is assumed that liquid entrainment implies also liquid carryover. The carryover fraction is obtained naturally from mass balances along the channel.

The onset of entrainment (OE) criterion is obtained by prescribing a Weber number, based on the diameter of the liquid core, at which entrainment starts. For the inverted-annular flow regime the diameter of the liquid core can be approximated by the diameter of an equivalent circular flow area,

$$D_E = \sqrt{\frac{4}{\pi}} A_c$$

Thus

$$We_{OE} = \frac{\rho_g (u_g - u_\ell)^2 D_E}{\sigma} \tag{2-34}$$

Therefore, by specifying We_{OE} the relative velocity between the steam and the liquid at which the onset of entrainment takes place can be calculated from Eq. 2-34 as

$$\Delta u_{OE} = (u_g - u_\ell)_{OE} = \left[\frac{\sigma We_{OE}}{\rho_g D_E}\right]^{1/2} \tag{2-35}$$

Similarly, by specifying a Weber number at which the core becomes so unstable that all the liquid present is entrained (total entrainment, TE) the velocity differential at this point can be calculated from

$$\Delta u_{TE} = (u_g - u_\ell)_{TE} = \left[\frac{\sigma We_{TE}}{\rho_g D_E}\right]^{1/2} \tag{2-36}$$

Therefore, an entrainment fraction can be defined as a function of the velocity difference, i.e.

$$E = \frac{G_\ell^{ent}}{G_\ell} = E(\Delta u) \tag{2-37}$$

where G_ℓ is the liquid mass flux and G_ℓ^{ent} is the liquid mass flux being entrained. The actual functional dependence of E on Δu, and possibly on other flow parameters, will have to come from future experiments. A linear dependence, as shown in Fig. 2-4, seems to be a reasonable assumption

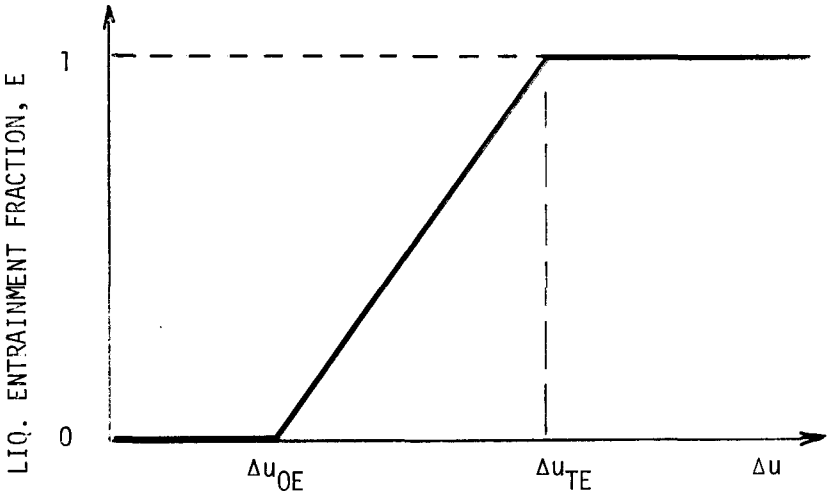

Figure 2-4. Variation of the Entrainment Fraction

Thus we have:

$$\begin{aligned} E &= 0 && \text{for } \Delta u < \Delta u_{OE} \\ &= 1 - \frac{\Delta u_{TE} - \Delta u}{\Delta u_{TE} - \Delta u_{OE}} && \text{for } \Delta u_{OE} \leqslant \Delta u \leqslant \Delta u_{TE} \\ &= 1 && \text{for } \Delta u > \Delta u_{TE} \end{aligned} \tag{2-38}$$

The swollen liquid level is defined as the elevation in the channel above which only entrained liquid (carryover) and vapor exist. The swollen liquid level can also be defined as the position in the channel where a discontinuity in the void fraction exists and consequently a change in the flow regime takes place. The entrainment fraction at the swollen liquid level, function of the velocity differential Δu, determines how much liquid will be carried over. If Δu is below Δu_{OE} liquid carryover will not occur and only vapor will cross the swollen liquid level. As Δu at the swollen liquid level increases, the liquid carryover also increases. Finally for Δu equal to Δu_{TE} all the liquid is carried over above the swollen liquid level. At this point the discontinuity in the liquid mass flux vanishes, although a near-discontinuity in the void fraction and a change in the flow regime may remain.

Since at steady state the mass flux along the channel is uniform, it follows that at steady state conditions at the swollen liquid level must correspond to E=1 and Δu must be equal to Δu_{TE} at the location of the level.

Jensen [25] studied the stability of the interface in inverted-annular flow. His analysis shows that the Weber number based on the radial channel dimension is a critical parameter. His parametric studies result in the following dependence of his Weber number, We* (based on liquid density instead of gas density and channel radial dimension D), on the non-dimensional wavelength of the instability that results in a maximum growth rate

$$\frac{D}{\lambda_{max}} = 0.107 \frac{\rho_v}{\rho_\ell} We^*$$

Assuming, in agreement with experimental observations [25,26], that D/λ_{max} is of the order of unity,

$$We_{OE} = \frac{\rho_v}{\rho_\ell} We^* = \frac{1}{0.107} \cdot \frac{\rho_v}{\rho_\ell} \cdot \frac{\rho_\ell}{\rho_v} \approx 10$$

The predictions of UC-B data [19] presented in Chapter 4 were obtained using $We_{OE} = We_{TE} = 10$, i.e. the correlation was used as a step function: no liquid entrainment occurred below We_{OE}, while all the liquid was entrained above We_{OE}. The good agreement of the limited number of predictions with the measured liquid entrainment rates gives tentatively confidence in the method presented here.

2.2.4 Variation of the Mass Flux Along the Channel

The boundaries of control volume 2 are defined downstream by the swollen liquid level and upstream by the NVG boundary. At the swollen liquid level there may be a discontinuity in mass flux, and consequently in void fraction and phase velocities

Figure 2-5 shows schematically the variation of the mass flux G with elevation at a given time. The continuity equation determines the distribution of G along the channel as a function of time, i,e,

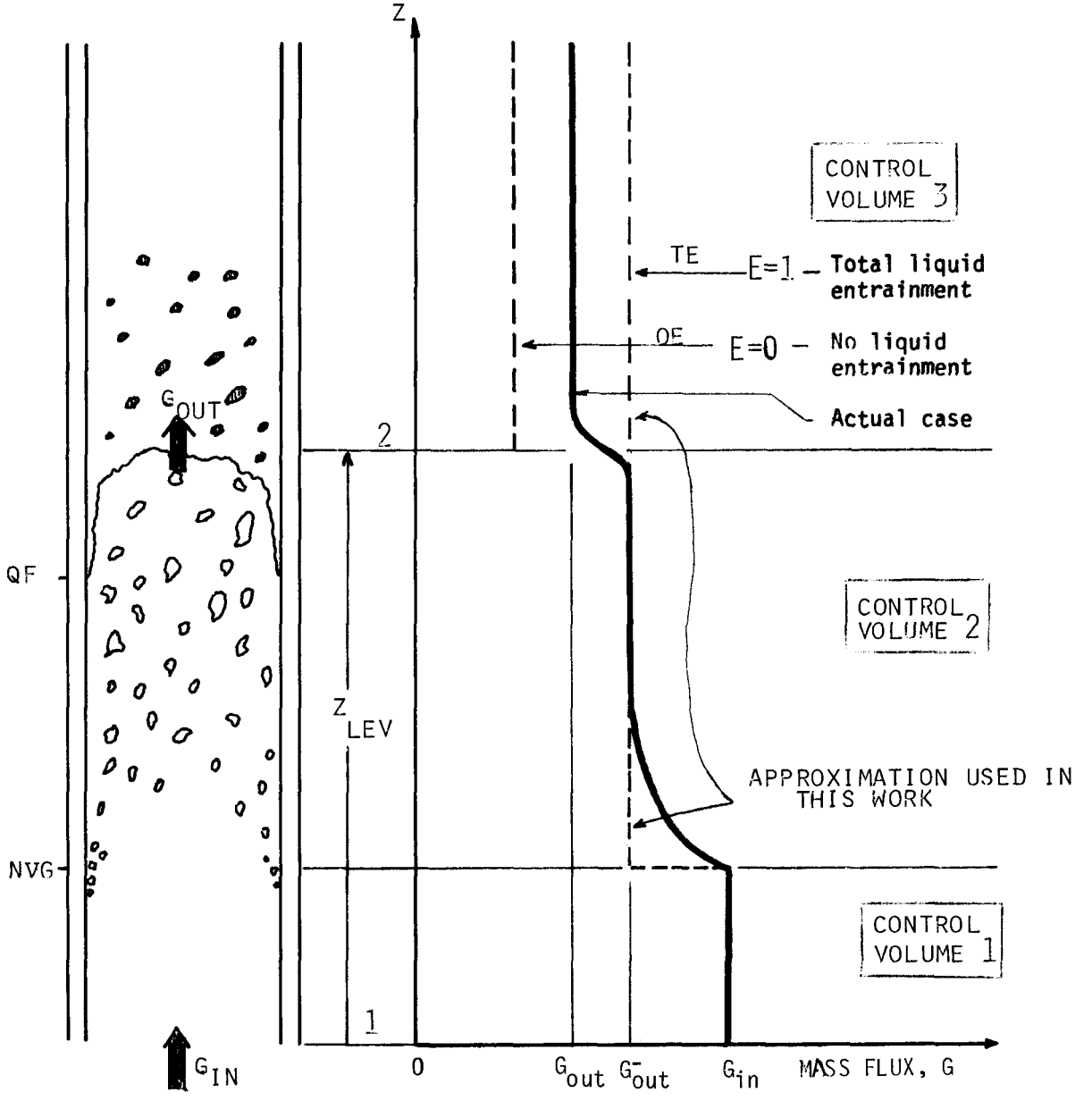

Figure 2-5. Mass flux variation along the channel.

$$\frac{\partial G}{\partial z} = - \frac{\partial \rho}{\partial t} \tag{2-39}$$

In control volume 1 (C.V.1) it has been assumed that the liquid density is constant, therefore

$$G = G_{in} \qquad \text{for} \quad z \leqslant Z_{NVG}$$

In control volume 2 (C.V.2), however, the bulk density ρ is function of time and position, so integrating Eq. 2-39 up to Z^-_{LEV}, just below the boundary, yields

$$\int_0^{Z^-_{LEV}} \frac{\partial G}{\partial z}\, dz = G^-_{out} - G_{in} = - \int_0^{Z^-_{LEV}} \frac{\partial \rho}{\partial t}\, dz \tag{2-40}$$

where the superscript - is used to identify quantities just below Z_{LEV}. We explicit the last integral as

$$\int_0^{Z^-_{LEV}} \frac{\partial \rho}{\partial t}\, dz = \frac{d}{dt} \int_0^{Z^-_{LEV}} \rho dz - \bar{\rho}_z \frac{dZ_{LEV}}{dt}$$

We further write

$$\frac{d}{dt} \int_0^{Z^-_{LEV}} \rho dz = \frac{d}{dt} \int_0^{Z_{NVG}} \rho_1 dz + \frac{d}{dt} \int_{Z_{NVG}}^{Z^-_{LEV}} \rho dz$$

where ρ_1 is the average single-phase density which does not change much. Therefore, Eq. 2-40 yields

$$G^-_{out} = G_{in} - \rho_1 \frac{dZ_{NVG}}{dt} + \rho^-_2 \frac{dZ_{LEV}}{dt} - \frac{d}{dt} \int_{Z_{NVG}}^{Z^-_{LEV}} \rho dz \tag{2-41}$$

Equation 2-41 gives the mass flux just below the swollen liquid level if the level velocity dZ_{LEV}/dt is known. The last term of Eq. 2-41 is the rate of change of

the mass contents of C.V.2 per unit of cross-sectional area and can be approximated numerically by a backward difference.

After the inception of liquid carryover, Z_{NVG} and Z_{LEV} mark points of approximately constant quality and void fraction. Therefore, the average of the density in control volume 2 should not change much; it is mostly the length of this volume that changes. We can in this case approximate the integral by

$$\frac{d}{dt}\int_{Z_{NVG}}^{Z_{LEV}^-} \rho dz = \bar{\rho}_{CV2}\left[\frac{dZ_{LEV}}{dt} - \frac{dZ_{NVG}}{dt}\right]$$

and Eq. 2-41 becomes

$$G_{out}^- = G_{in} - (\rho_1 - \bar{\rho}_{CV2})\frac{dZ_{NVG}}{dt} - (\bar{\rho}_{CV2} - \rho_2^-)\frac{dZ_{LEV}}{dt} \qquad (2\text{-}41a)$$

This alternative form of Eq. 2-41 shows that the mass flux at the exit of C.V.2 changes as the boundaries of this control volume move. For positive boundary velocities, mass is stored below these two levels and $G_{out}^- < G_{in}$.

The mass flux inside C.V.2 actually varies from G_{in} at the upstream boundary to G_{out}^- at the downstream boundary. This variation can be determined only by the solution of the time-dependent differential mass and energy conservation equations. Since the time-dependent solution was deliberately avoided, a first-order estimate of the average mass flux inside C.V.2 will be obtained by taking advantage of our physical understanding of the situation: At low pressure the void fraction increases very fast as the flow quality goes from zero to a few percent. Therefore the density gradient inside this control volume is very large near the upstream boundary and very small everywhere else. Inspection of the continuity equation shows that the mass flux will also vary mostly near the upstream boundary, as shown in Fig. 2-5. Therefore G_{out}^-, as calculated from Eqs. 2-41 or 2-41a is a better estimate than G_{in} for calculating flow conditions in C.V.2.

The mass flux just above the swollen liquid level, G_{out}^+, can be obtained by a procedure identical to the one presented above, simply by replacing the superscripts - by the superscript + in Eqs. 2-40 to 2-41a. We can thus show that

$$G_{out}^+ = G_{out}^- + (\rho_2^+ - \rho_2^-)\frac{dZ_{LEV}}{dt}$$

Thus we see that there will be a discontinuity in the value of the mass flux at the swollen mixture level if this level is moving and there is a discontinuity in the void fraction at that level. A method for estimating the discontinuity in void fraction across the swollen liquid level is presented in the following section. Since, however, in the present version of the code the assumption of total entrainment, E=1, is made as soon as the conditions for onset of entrainment are satisfied, any discontinuities across the swollen liquid level are ignored and

$$G_{out}^{+} = G_{out}^{-}$$

The mixture velocity in C.V.3 is high and this results in very short transit times. It is therefore reasonable to assume that quasi-steady-state conditions hold in that volume. Thus the channel exit flow rate is set to be equal to the flow rate above the swollen liquid level.

In summary, the continuous variation of the mass flux along the channel can be approximated by a two-step variation. The mass flux is constant in each of the main control volumes, as shown in Fig. 2-5. Presently, following the onset of entrainment, discontinuities across the swollen liquid level are ignored; this results in a single-step variation of the mass flux.

2.2.5 Velocity of the Swollen Liquid Level

The swollen liquid level velocity, dZ_{LEV}/dt, can be calculated by a mass and momentum balance at this level. The superscript + will be used again to designate quantities just above the level.

Figure 2-6 shows the mass and momentum fluxes crossing the swollen liquid level which moves with a velocity $U_{LEV} = dZ_{LEV}/dt$, Since there is no storage of mass at the interface, we can write for the mass continuity of liquid:

$$\rho_\ell(1-\alpha^-)(u_\ell^- - U_{LEV}) = \rho_\ell(1-\alpha^+)(u_\ell^+ - U_{LEV})$$

or

$$j_\ell^- - j_\ell^+ = (\alpha^+ - \alpha^-)U_{LEV} \qquad (2\text{-}42)$$

where, by definition $j_\ell^- = (1-\alpha^-)u_\ell^-$ and $j_\ell^+ = (1-\alpha^+)u_\ell^+$

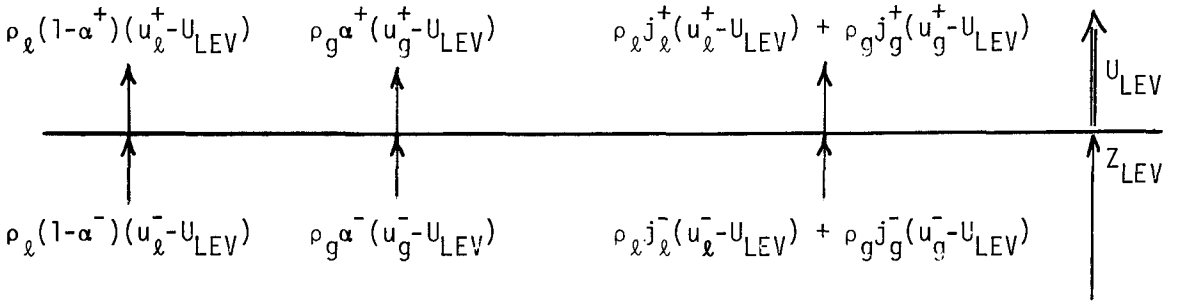

Figure 2-6. Mass and Momentum Fluxes Crossing the Swollen Liquid Level

Mass continuity of vapor yields

$$\rho_g\alpha^-(u_g^- - U_{LEV}) = \rho_g\alpha^+(u_g^+ - U_{LEV})$$

or

$$j_g^- - j_g^+ = -(\alpha^+ - \alpha^-)U_{LEV} \tag{2-43}$$

where, by definition also, $j_g^- = \alpha^- u_g^-$ and $j_g^+ = \alpha^+ u_g^+$. Adding Eqs. 2-42 and 2-43 results in

$$j^- = j_\ell^- + j_g^- = j_\ell^+ + j_g^+ = j^+ \tag{2-44}$$

Assuming that there are no outside forces acting on the mixture as it crosses the level, conservation of the mixture momentum yields

$$\rho_\ell j_\ell^-(u_\ell^- - U_{LEV}) + \rho_g j_g^-(u_g^- - U_{LEV}) = \rho_\ell j_\ell^+(u_\ell^+ - U_{LEV}) + \rho_g j_g^+(u_g^+ - U_{LEV})$$

or

$$\frac{\rho_\ell j_\ell^{+2}}{(1-\alpha^+)} + \frac{\rho_g j_g^{+2}}{\alpha^+} = \left[\rho_\ell(j_\ell^+ - j_\ell^-) + \rho_g(j_g^+ - j_g^-)\right]U_{LEV} + \frac{\rho_\ell j_\ell^{-2}}{(1-\alpha^-)} + \frac{\rho_g j_g^{-2}}{\alpha^-}$$

Using Eqs. 2-44 and 2-42 results in

$$\frac{\rho_\ell j_\ell^{+2}}{(1-\alpha^+)} + \frac{\rho_g j_g^+}{\alpha^+} = -(\rho_\ell - \rho_g)(\alpha^+ - \alpha^-)U_{LEV}^2 + \frac{\rho_\ell j_\ell^{-2}}{(1-\alpha^-)} + \frac{g j_g^{-2}}{\alpha^-} \tag{2-45}$$

All quantities just below the level, namely α^-, j_ℓ^-, and j_g^- are obtained by the methods described in Sections 2.2.1 and 2.2.4. Four quantities are left to be calculated, namely j_ℓ^+, j_g^+, α^+, and U_{LEV}. The entrainment fraction E can be calculated from Eq. 2-38, as a function of the velocity difference just below the liquid level, $\Delta u^- = j_g^-/\alpha^- - j_\ell^-/(1-\alpha^-)$; then

$$E = \frac{G_\ell^{ent}}{G_\ell^-} = \frac{j_\ell^+}{j_\ell^-} \qquad \text{and} \qquad j_\ell^+ = E j_\ell^- \tag{2-46}$$

The value of j_g^+ can be calculated from Eq. 2-44, i.e.

$$j_g^+ = j^+ - j_\ell^+ = j^- - j_\ell^+ \tag{2-47}$$

The remaining two unknowns, α^+ and U_{LEV}, can then be calculated from Eqs. 2-42 and 2-45. Inserting Eq. 2-42 into Eq. 2-45 to eliminate U_{LEV}, results after some manipulation in

$$\alpha^{+3} + a_1\alpha^{+2} + a_2\alpha^+ + a_3 = 0 \tag{2-48}$$

where

$$a_1 = \frac{1}{p^-}\left[\rho_\ell j_\ell^{+2} - \rho_g j_g^{+2} - (\rho_\ell - \rho_g)(j_\ell^- - j_\ell^+)^2\right] - (1+\alpha^-)$$

$$a_2 = \frac{1}{p^-}\left[(1+\alpha^-)\rho_g j_g^{+2} - \alpha^-\rho_\ell j_\ell^{+2} + (\rho_\ell - \rho_g)(j_\ell^- - j_\ell^+)^2\right] + \alpha^-$$

$$a_3 = -\frac{\alpha^-}{p^-}\rho_g j_g^{+2}$$

with

$$p^- = \frac{\rho_\ell j_\ell^{-2}}{(1-\alpha^-)} + \frac{\rho_g j_g^{-2}}{\alpha^-}$$

The three roots of Eq. 2-48 can be easily found, however, the desired solution must be real and satisfy the following condition:

$$1 - E(1-\alpha^-) \leqslant \alpha^+ \leqslant 1$$

Once α^+ and j_ℓ^+ are known, the swollen liquid level velocity can be calculated from Eqs. 2-43 and 2-44 as

$$U_{LEV} = \frac{j_\ell^- - j_\ell^+}{\alpha^+ - \alpha^-} \tag{2-49}$$

The swollen liquid level position is then calculated at any time from

$$Z_{LEV}(t+\Delta t) = Z_{LEV}(t) + U_{LEV}\,\Delta t \tag{2-50}$$

as long as $0 \leqslant E < 1$. When $E = 1$, i.e., $j_\ell^+ = j_\ell^-$, there is no mass flux discontinuity at the level, Eq. 2-48 yields $\alpha^+ = \alpha^-$, and U_{LEV} is undetermined. In this case the swollen liquid level is taken as the position in the channel where Δu^- is equal to Δu_{TE}.

When $E = 0$, i.e. $j_\ell^+ = 0$, there is no liquid leaving the level and Eq. 2-48 yields $\alpha^+ = 1$.

The level velocity is then obtained from Eq. 2-49 as

$$U_{LEV} = \frac{j_g^-}{1-\alpha^-} = u_\ell^-$$

as expected. This condition corresponds to the "filling up" of the channel before the onset of liquid carryover.

2.2.6 Characteristics of the Droplets in the Dispersed-Flow Region

If the liquid core in inverse-annular flow breaks up into liquid slugs due to an interface instability, the length of these slugs should be comparable to the radial channel dimensions. This was experimentally confirmed by photographs taken during FLECHT experiment [25] and during the quenching of a glass tube cooled by internal flow [26]. These slugs then probably form large drops that travel some distance before further breaking down into smaller drops. The stability of the drops to fragmentation is governed by the droplet Weber number,

$$We_\delta = \frac{\rho_g (u_g - u_\ell)^2 \delta}{\sigma} \tag{2-51}$$

where δ is the droplet diameter. Droplets have been observed to fragment for values of the Weber number, We_δ between 10 and 20 [27,28]. Thus a droplet Weber number of the order of 15 could be used to define the maximum possible droplet diameter. In reality droplets of all diameters up to the maximum droplet diameter may be present. Thus a value below 15 may have to be used to properly account for the hydrodynamic and heat transfer behavior of the droplets in the dispersed-flow region.

Smith [29] measured droplet diameters and velocities from FLECHT films. Clearly, only visible droplets could be considered, and the droplets that were considered were flowing in the partly unheated area around the rod bundle. Assuming that these droplets had a terminal velocity with respect to the surrounding steam, and using the value of 0.45 for the drag coefficient, Smith obtained droplet Weber numbers in the range 1.5 to 3. This corresponds to droplets having a range of diameters between 1.5 and 4 mm.

In the present work it is assumed that all the droplets leaving the swollen liquid level have a diameter δ_o determined by $We_\delta \cong 2$, with u_g and u_ℓ taken to be the calculated values just above the swollen liquid level, i.e. at Z_{LEV}^+. However, from terminal-velocity considerations, there is a limiting droplet size δ_{max} above which carryover will not be possible. This maximum droplet size can be calculated by equating the drag and gravity forces acting on a drop,

$$\delta_{max} = \frac{3C_D \rho_g (u_g^+ - u_\ell^+)^2}{4(\rho_f - \rho_g)g}$$

If the value of the initial droplet diameter calculated from Eq. 2-51 is larger than δ_{max}, δ_o is set equal to δ_{max}. This procedure is needed to insure that if liquid entrainment is calculated to occur, liquid carryover will be possible. Details of the droplet equation of motion and a correlation for the drag coefficient C_D are given in Section 2.3.2.

2.3 DISPERSED-FLOW FILM-BOILING REGION

The flow pattern in this region is characterized by dispersed liquid droplets flowing in a continuous vapor medium. It is usually encountered at void fractions well above 80% and is often referred to as the liquid-deficient regime. This kind of flow regime usually appears downstream of an annular or inverted-annular flow regime, when the liquid film or core disappear as a result of evaporation, detachment from the wall, and/or droplet entrainment.

Heat transfer in this flow regime is generally poor but might be sufficient to turn around the fuel rod temperature transient during reflooding.

Dispersed-Flow Film-Boiling (DFFB) heat transfer can be predicted from empirical correlations or from semi-analytical models based on consideration of the heat transfer mechanisms between the wall, the vapor, and the droplets.

Groeneveld [30,31] gives a complete list of the existing empirical correlations; these are accurate for the ranges where data are available, but they lack the fundamental physical basis needed for extrapolation to conditions outside the data base.

The semi-analytical mechanistic models attempt to evaluate separately the various modes of heat transfer. The wall is cooled by radiation, by forced convection to the vapor, and by interaction with the droplets. Such models require specification of a number of flow parameters, e.g., droplet diameters and velocities that are not readily available but must be adjusted to fit the data.

Experimental evidence [32] of high vapor superheat exists. The vapor temperature is controlled both by wall-to-vapor and vapor-to-liquid heat transfer, therefore thermal non-equilibrium may be present. Visual observations [29] have shown that the droplets are moving at a lower velocity than the vapor, proving the existence of non-homogenous flow.

Since the point of onset of DFFB was considered to be at the end of the sputtering zone for the low-flooding-rate cases and at the swollen mixture level for the high-flooding-rate cases, heat transfer by direct contact of the droplets with the wall is not expected to play a major role downstream of this point. Indeed the wall

temperature will have reached a high enough value to forbid direct contact above this point.

Direct heat transfer between the droplets and the heated wall was added by Groeneveld [33] in Bennett's semi-analytical model [34] to account for the underpredictions of low-quality data. Groeneveld's new term has a variable parameter δ_{film} which accounts for the effects of increased convection due to the disturbance of the vapor boundary layer produced by the droplets approaching the wall. Groeneveld's model was used to predict the steam-water data of Bennett and the results were very insensitive to δ_{film}. Also Cumo [35] observed droplet trajectories in the post-dryout region, and noticed that they were virtually parallel to the wall. All these observations point to the conclusion that droplet-wall interaction at very high wall temperatures is negligible under steam-water high-void-fraction conditions.

Since contact heat transfer to the droplets is probably not important, two main modes of heat transfer to the droplets remain: conduction/convection from the steam and direct radiation from the walls. The details of radiative heat transfer to the droplets have been examined in a recent paper [36]. A simple radiative heat transfer model is used for the following development.

A modified version of a simple semi-analytical model for DFFB proposed by Saha [7,37] is used in this work. The main characteristics of this model, that includes radiative heat transfer to the droplets are described below:

- an axial profile for the rate of vapor generation that satisfies the proper boundary conditions is postulated. This profile can be adjusted according to the prevailing flow conditions by modifying the values of two parameters that could be obtained from experimental data. A method to estimate these two parameters analytically is presented in Appendix C.
- radiative heat transfer between the wall and the liquid is accounted, as a first approximation, by a simple model. A more advanced treatment of the radiative exchanges [36] could be included later.
- direct-contact heat transfer between the droplets and the heated surface is neglected.
- the liquid velocity is calculated either by solving the droplet equation of motion or by assuming that the droplets acquire immediately their terminal velocity.
- the quality and phase velocities at the upstream boundary of the DFFB region are required boundary conditions.

- it is assumed that the presence of liquid droplets and the radiative exchanges do not affect the heat transfer capability of the vapor phase, and Heineman's correlation [38] is used to evaluate the wall-to-vapor heat transfer.

2.3.1 Vapor Generation Rate

It is assumed that at the onset of DFFB, $z = Z_{LEV}$, the actual quality is equal to the equilibrium quality and that both phases are saturated. Downstream of this point, however, due to poor thermal conductivity of the vapor, the efficiency of the heat transfer to the droplets deteriorates, resulting in a reduction of the rate of vapor generation and an increase in the vapor temperature.

As mentioned previously, postulation of a profile for the rate of vapor generation requires the knowledge of the proper boundary conditions, i.e., the vapor generation rate, Γ_g, as well as its derivatives at the point of onset of DFFB and for $x_{eq} >> 1$. At steady state:

$$\Gamma_g = G \frac{dx}{dz} \quad , \qquad \frac{d\Gamma_g}{dz} = G \frac{d^2x}{dz^2} \tag{2-52}$$

where x is the true vapor quality and G is here the total mass flux leaving the liquid level.

A non-dimensional rate of vapor generation per unit volume, Γ_g^+, is defined as:

$$\Gamma_g^+ = \frac{\Gamma_g}{\Gamma_{g,eq}} = \frac{G}{\Gamma_{g,eq}} \frac{dx}{dz} = \frac{dx}{dx_{eq}} \tag{2-53}$$

where x_{eq} is the equilibrium quality.

Groeneveld [31,39] and others [7,37] assume that direct cooling of the wall by droplets and radiative heat transfer are negligible and that near the dryout point, since the vapor is not superheated yet, there is no vapor-to-droplets heat transfer. With these assumptions, near the point of onset of DFFB, the entire wall heat flux is used to superheat the vapor. Downstream of this point heat transfer from the vapor to the droplets increases since the vapor becomes progressively superheated.

This assumption is modified by retaining some form of heat transfer to the droplets at the upstream boundary of the DFFB regime; this could be either direct-contact

heat transfer or more likely radiative heat transfer to the droplets. Therefore at $x_{eq} = x_o$

$$\frac{dx}{dz} = \Gamma_g^+ Q = \gamma Q$$

where

$$Q \equiv \frac{dx_{eq}}{dz} = \frac{\Gamma_{g,eq}}{G} = \frac{q'}{GA_c h_{fg}}$$

$$\text{or} \quad \Gamma_g^+ = \gamma \qquad \text{with} \qquad 0 \leq \gamma \leq 1 \tag{BC-1}$$

For $\gamma = 0$ we have "frozen" flow, i.e., no heat transfer to the droplets, while $\gamma = 1$ implies thermodynamic equilibrium.

Figure 2-7 shows qualitatively the distributions of vapor temperature, actual quality, and of the non-dimensional rate of vapor generation along the heated channel. In order to specify the form of the profile for Γ_g^+ it is necessary to specify at least its first derivative at $x_{eq} = x_o$. $d\Gamma_g^+/dx_{eq}$ can be evaluated analytically if an assumption for the heat transfer to the droplets at the upstream boundary of the DFFB region is made, as shown in Appendix C. Since this assumption might be too restrictive for the case of reflooding, the value of this derivative, β, can be left as a parameter to be obtained from experimental data. Therefore

$$\left.\frac{d\Gamma_g^+}{dx_{eq}}\right|_{x_o} = \beta \tag{BC-2}$$

At the other boundary of the DFFB region, i.e., for $x \to 1$ or for $x_{eq} >> 1$, the vapor generation must necessarily be reduced progressively to zero,

$$\Gamma_g^+ = 0 \qquad \text{as} \qquad x_{eq} \to \infty \tag{BC-3}$$

Calculations show that the diameter of the droplets and the actual quality may tend to zero with a large negative slope as $x \to 1$. This is due to the fact that heat transfer and consequently the evaporation of very small droplets are accelerated as the diameter of the droplets decreases. This, however, seems to be true

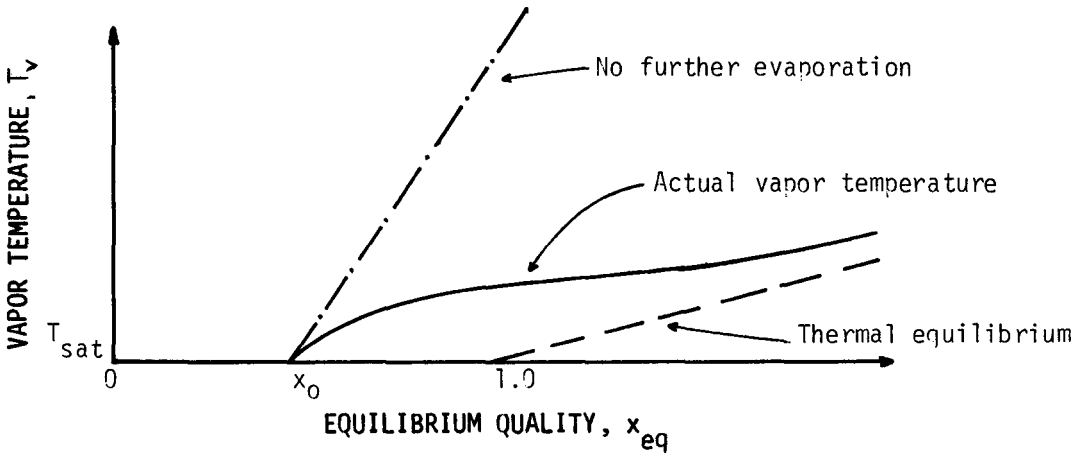

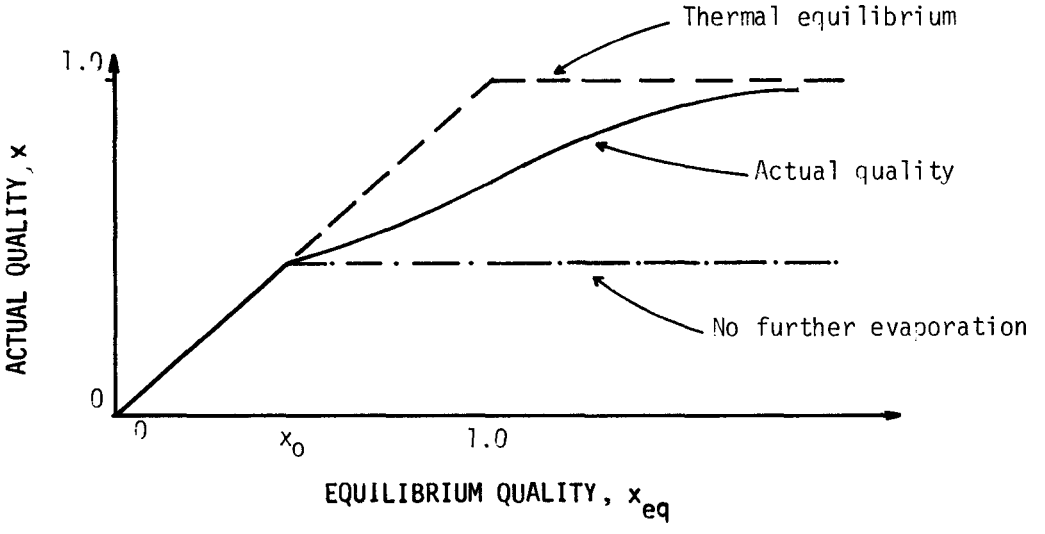

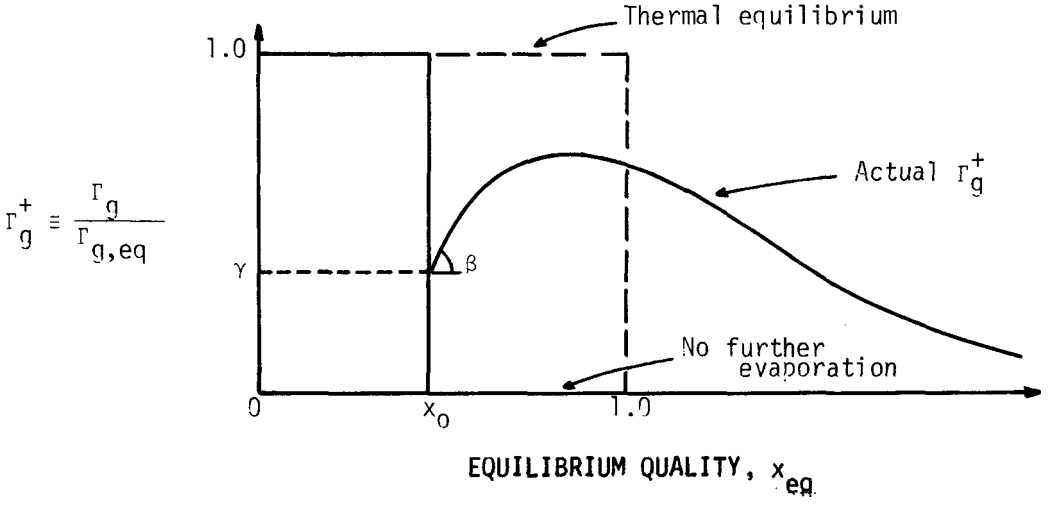

Figure 2-7. Variation of the vapor temperature, actual quality and of the non-dimensional rate of vapor generation along the heated channel.

only at the very end of the range of the droplets, and it would have been true on the average only if all the droplets had the same diameter. It seems physically more realistic to assume that

$$\frac{d\Gamma_g^+}{dx_{eq}} \to 0 \qquad \text{as} \qquad x_{eq} \to \infty \tag{BC-4}$$

Note that it is in principle possible to specify a small negative slope at $x_{eq} \to \infty$ but this introduces another unknown parameter.

Since all the droplets must be evaporated between x_o and infinity

$$\int_{x_o}^{\infty} \Gamma_g^+ \, dx_{eq} = 1 - x_o \tag{BC-5}$$

The following functional form is considered for Γ_g^+

$$\Gamma_g^+ = \exp[-a(x_{eq}-x_R)] - \exp[-b(x_{eq}-x_R)] \tag{2-54}$$

where a, b and x_R are positive constants. The function automatically satisfies boundary conditions 3 and 4. The constants a, b and x_R are then chosen such that the three remaining conditions, 1, 2 and 5, are satisfied. This yields

$$\begin{cases} \exp[-a(x_o-x_R)] - \exp[-b(x_o-x_R)] = \gamma \\ -a \exp[-a(x_o-x_R)] + b \exp[-b(x_o-x_R)] = \beta \\ \frac{1}{a} \exp[-a(x_o-x_R)] - \frac{1}{b} \exp[-b(x_o-x_R)] = 1 - x_o \end{cases} \tag{2-55}$$

The values of β and γ can be either specified as input, or calculated as shown in Appendix C. The system of Eqs. 2-55 must be solved to obtain the values of a, b and x_R. The actual quality is obtained by integrating Eq. 2-54 from $x_{eq} = x_o$ to x_{eq},

$$x = 1 - \frac{1}{a} \exp[-a(x_{eq}-x_R)] + \frac{1}{b} \exp[-b(x_{eq}-x_R)] \tag{2-56}$$

where $x_{eq}(z)$ is given by

$$x_{eq}(z) = x_o + \int_{z_o}^{z} \frac{q''(z')P_H}{GA_c h_{fg}} dz' \tag{2-57}$$

Once the actual quality x is determined, the vapor bulk temperature, T_v, can be calculated from:

$$x[h_{fg} + c_{pv}(T_v - T_{sat})] = x_{eq} h_{fg} \tag{2-58}$$

where the subscript v denotes superheated vapor conditions.

2.3.2 Void Fraction Model

Besides knowing the actual quality and the bulk vapor temperature, it is also necessary to determine the phase velocities and the void fraction in order to calculate the local heat transfer coefficient.

At the point of onset of DFFB all the liquid is assumed to be in the form of spherical droplets with diameter δ_o. As the droplets move downstream they are evaporated and accelerated by the vapor; it is however assumed that they do not further coalesce or breakup, i.e., the droplet number flux is constant. In the actual physical situation a spectrum of droplet sizes exists with some coalescence and breakup taking place. These physical phenomena could have been accounted for in the present model but this would have represented another degree of sophistication with questionable advantages.

The equation of motion for a droplet moving in an accelerating vapor medium is*

$$\frac{\pi}{6}\delta^3\rho_f \frac{du_f}{dt} = C_D \frac{\pi\delta^2}{4} \frac{\rho_v(u_v-u_f)^2}{2} - \frac{\pi}{6}\delta^3 (\rho_f-\rho_v)g \tag{2-59}$$

Time and space variations can be related by

$$\frac{d}{dt} = u_f \frac{d}{dz}$$

*The liquid is denoted by the subscript f since the droplets are assumed to remain saturated.

and Eq. 2-54 can be written as

$$\frac{\pi}{6}\delta^3 \rho_f u_f \frac{du_f}{dz} = C_D \frac{\pi\delta^2}{4} \frac{\rho_v(u_v-u_f)^2}{2} - \frac{\pi}{6}\delta^3 (\rho_f-\rho_v)g \tag{2-60}$$

By definition, the droplet and vapor velocities are

$$u_f = \frac{(1-x)G}{(1-\alpha)\rho_f} \quad , \qquad u_v = \frac{xG}{\alpha\rho_v} \tag{2-61}$$

where G now is the mass flux in control volume 3, assumed constant.

Eliminating α from Eqs. 2-61 results in

$$u_v = \frac{\rho_f}{\rho_v} \frac{u_f xG}{[\rho_f u_f - (1-x)G]} \tag{2-62}$$

Assuming that the droplet number flux, N, remains constant, a mass balance yields

$$(1-x)G = N \frac{\pi}{6}\delta^3\rho_f \tag{2-63}$$

From Eq. 2-63, a relationship between the actual vapor quality and the droplet size can be written as

$$\delta = \left(\frac{1-x}{1-x_o}\right)^{1/3} \delta_o \tag{2-64}$$

where δ_o is the initial droplet diameter calculated as described in Section 2.2.6.

Inserting Eqs. 2-62 and 2-64 into Eq. 2-60 results after some rearrangement in

$$\frac{du_f}{dz} = 0.75\, C_D\, u_f \left(\frac{1-x_o}{1-x}\right)^{1/3} \frac{\rho_f}{\delta_o\rho_v} \left[\frac{xG}{\rho_f u_f - (1-x)G} - \frac{\rho_v}{\rho_f}\right]^2 - \frac{(\rho_f-\rho_v)g}{\rho_f u_f} \tag{2-65}$$

A correlation developed by Ingebo [40] for the drag coefficient of accelerating particles is a proper choice for C_D:

$$C_D = \frac{27}{Re_\delta^{0.84}} \tag{2-66}$$

where

$$Re_\delta = \frac{\rho_v(u_v-u_f)\delta}{\mu_v} \tag{2-67}$$

Over the range of Re_δ tested by Ingebo, no minimum value of C_D, as predicted by the well-established drag laws, was found. However, under the present conditions, it is occasionally necessary to calculate C_D at somewhat higher Reynolds numbers than those used by Ingebo in his experiments. Therefore, in the present work, a minimum value of 0.44 is used for the drag coefficient.

Equation 2-65 can be integrated along the channel, with the quality x specified by the methods of Section 2.3.1 and Eq. 2-56. The droplet diameter at the onset of DFFB regime δ_o, and the initial conditions for u_f and u_v are obtained by the method of Section 2.2.6 and on the basis of a droplet Weber number.

An alternative to integration of Eq. 2-65 can be provided by assuming that the droplets acquire immediately the terminal velocity (i.e. the relative velocity with respect to the vapor) corresponding to their diameter and the local conditions in the channel. This approximation is probably acceptable in view of the fact that the droplet diameter spectrum was represented by a single droplet size. The local terminal velocity is obtained by solving the steady-state form of the droplet momentum equation, Eq. 2-59,

$$u_v - u_f = \left[\frac{4}{3}\frac{\delta(\rho_f-\rho_v)g}{C_D\rho_v}\right]^{1/2} \tag{2-68}$$

Since C_D is a function of $u_v - u_f$, this equation must be solved together with Eq. 2-65, with the droplet diameter provided by Eq. 2-64. If the calculated value of C_D is less than 0.44, it should be set equal to 0.44.

Equations 2-68 and 2-62 can then be solved to provide the phase velocities u_f and u_v. Finally, with the actual vapor quality and the phase velocities known, the local void fraction is calculated from

$$\alpha = \frac{1}{1 + \frac{1-x}{x}\frac{\rho_v}{\rho_f}\frac{u_v}{u_\ell}} \tag{2-69}$$

2.3.3 Heat Transfer

To calculate heat transfer from the wall to the vapor, the Heineman [38] correlation derived from superheated steam data is a proper choice:

$$h_c = 0.0157 \frac{k_{f\ell}}{D_H}\left(\frac{\rho_v u_v D_H}{\mu_{f\ell}}\right)^{0.84} Pr_{f\ell}^{0.33}\left(\frac{L}{D_H}\right)^{-0.04} \quad \text{for} \quad \frac{L}{D_H} < 60$$

$$h_c = 0.0133 \frac{k_{f\ell}}{D_H}\left(\frac{\rho_v u_v D_H}{\mu_{f\ell}}\right)^{0.84} Pr_{f\ell}^{0.33} \quad \text{for} \quad \frac{L}{D_H} > 60 \tag{2-70}$$

with L taken to be equal to $z - Z_{LEV}$. The subscript $f\ell$ denotes that the properties are evaluated at the film temperature.

To account for radiation which might contribute a small fraction of the total wall heat flux, a model proposed by Sun et al. [41] is used. The model considers the three radiation heat fluxes, namely wall to drops, vapor to drops, and wall to vapor, and assumes that the vapor-drop mixture is an optically thin medium. For typical reflooding conditions, however, it can be shown that the only significant contribution on the total wall heat flux is radiation from the wall to the droplets. Therefore only this component is considered in the present model. According to Sun's model:

$$h_r = \mathcal{I}_{w-d}\,\sigma_R\,\frac{(T_w^4 - T_{sat}^4)}{(T_w - T_{sat})} \tag{2-71}$$

where

$$\mathcal{I}_{w-d} = \frac{\varepsilon_f}{(1-\varepsilon_f)\left(1 + \frac{\varepsilon_v}{\varepsilon_w} + \frac{\varepsilon_f}{\varepsilon_w(1-\varepsilon_f)}\right)} \tag{2-72}$$

with ε_f, ε_v, and ε_w denoting the emissivities of the liquid, vapor and wall, respectively.

For an optically thin medium the liquid and vapor emissivities can be calculated from

$$\varepsilon_f = 1 - e^{-a_f D_H} \quad , \quad \varepsilon_v = 1 - e^{-a_v D_H} \tag{2-73}$$

where a_f and a_v are the liquid and vapor absorption coefficients, respectively. For the geometries under consideration, the hydraulic diameter D_H is the proper choice for the radiation mean beam length.

The absorption coefficient for water droplets is given by

$$a_f = 0.74 \left(\frac{\pi\delta^2}{4}\right) n$$

where $n = N/u_f$ is the droplet number density. Using Eqs. 2-61 and 2-63 to eliminate N results in

$$a_f = 1.11 \frac{(1-\alpha)}{\delta} \tag{2-74}$$

For an optically thin medium, the Planck mean absorption coefficient is a proper choice for a_v. Using 0.05 ft (15 mm) as a typical hydraulic diameter, 30 psia (2 bar-a) as a typical pressure, and a vapor temperature in the range of 500-1500°F (260-815°C) yields a vapor emissivity of about 0.1. This value is adopted for ε_v. It should be noticed that Eq. 2-72 is a very weak function of ε_v.

The total wall heat flux is given by

$$q'' = h_c(T_w - T_v) + h_r(T_w - T_{sat}) \tag{2-75}$$

Summarizing, the calculational procedure to follow at any given time is:

- all parameters at the onset of DFFB and the values of β and γ must be specified.
- the channel is subdivided axially in nodes with node number one at the point of onset of DFFB; conditions at the downstream nodes are found by stepwise integration along the heated channel.

- at each node the following steps are taken: Equation 2-57 is integrated along the node to produce the equilibrium quality; then Eq. 2-56 is used to find the actual quality. Knowing the equilibrium and and the actual quality, Eq. 2-58 gives the vapor temperature, Eqs. 2-65 or 2-68 and 2-62 the phase velocities, and finally Eq. 2-69 gives the void fraction. With the vapor velocity, void fraction, local wall and vapor temperatures known, Eqs. 2-70 through 2-74 give the heat transfer coefficient.
- the calculations proceed from node to node until the exit of the channel is reached.

It should be noticed that, in the absence of liquid entrainment, the above procedure can be used to calculate convective heat transfer to superheated steam by simply setting x and α equal to one all the way up to the channel exit.

2.4 OVERALL CALCULATIONAL PROCEDURE

The sequence of calculations used in the UCFLOOD computer code is now described briefly. As mentioned before, the main objective of this model is to calculate the cladding temperature history of a single fuel pin at all axial positions.

The fuel pin is subdivided axially in a number of fuel nodes and the transient radial conduction equation is solved at every node, except at the nodes that happen to be in the quench front region. This region is defined as a sliding axial length covering at most two fuel nodes and containing the quench front. The cladding temperature drops dramatically from values typical of post-CHF heat transfer to values typical of nucleate boiling across the length of the quench-front region. Heat transfer in the quench front region is treated separately, as discussed in Chapter 3. Nodes downstream of the quench-front region provide the necessary temperature boundary conditions for the quench-front-region model. The temperatures at nodes uncovered upstream, after the passage of the quench front, are updated by the quench front-region-model. Transient-conduction calculations resume than in these nodes.

To solve the heat conduction equation in the fuel pin, and calculate the cladding temperature, the distribution of local heat transfer coefficients along the pin is required. The selection of heat transfer coefficient correlations was described in Sections 2.1.2, 2.2.2, and 2.3.3 and is based on position with respect to the swollen liquid level and to the quench front, local clad temperature, and local flow conditions. The cladding temperature distribution at the previous time step is used in calculating the treat transfer coefficients for the next time step.

The local flow conditions required to calculate the heat transfer coefficients are produced by solving the continuity and energy conservation equations along the channel as described in Sections 2.1.1, 2.2.1, 2.2.4, and 2.3.2.

With the inlet flow rate and coolant temperature specified externally at all time steps, the calculational procedure described in Section 2.1.3 is followed to calculate the location of the point of net vapor generation (Z_{NVG}) and the coolant temperature at that point. The swollen liquid level position is calculated as described in Section 2.2.5.

In the quench-front region, treated in Chapter 3, a local calculational procedure is used to obtain the quench front velocity, and the heat input to the coolant. Knowing the quench front velocity, the quench front position is updated every time step.

The mass flux distribution along the channel is approximated by a two-level distribution, as shown in Fig. 2-5, and discussed in Section 2.2.4. The details of the procedure outlined above are given in Appendix E.

Chapter 3

QUENCH-FRONT-REGION MODEL

In this chapter, a brief description of the quench phenomena and the technique used to calculate the quench front velocity and the wall axial temperature distribution in the quench region are presented.

Experimental evidence [2-5, 19] shows the existence of steep axial temperature gradients in the quench region, with an associated narrow spike of heat flux to the coolant (0.2 - 1.5 in.) just behind the quench front. The quench front moves at a velocity determined by the combined effects of axial conduction in the fuel rod and convective cooling of the wall downstream (precursory cooling). The axial temperature gradient and the axial heat flux are important only in the immediate vicinity of the quench front. In this quench region very fine axial and radial nodalizations are necessary in order to correctly calculate numerically the temperature distribution. For this reason, it is difficult to calculate the temperature distribution in the entire rod and simultaneously account for the large local temperature gradients in the narrow quench region.

The various published [21] axial-conduction-limited quench-front propagation models consider the rewetting of infinitely long rods. In practice, however, the "points at infinity" are not spaced apart further than half an inch, since the axial temperature profile flattens very rapidly.

The steep axial temperature gradient in the quench-front region is due to the sharp discontinuity of the heat transfer coefficient distribution. This steep axial temperature gradient creates in turn the axial-conduction effect. Thus axial conduction cannot be controlling except when the quench front region is narrow.

The facts recalled above allow the decoupling of the quench-front problem from the calculation of the temperature field in the rod outside the quench-front region. Indeed, outside this region, the temperature distribution in the fuel rod or in a heated wall, can be calculated using a conventional radial-conduction routine for a number of axial nodes. The temperature at the nodes at the extremities of the quench-front region will provide the boundary conditions "at infinity" for

the quench-front-region model. This procedure is detailed in Section 3.6.1.

3.1 QUENCH PHENOMENA

If a hot surface whose temperature is above the quenching temperature is suddenly immersed in a coolant, stable film boiling develops. Convective and radiative heat transfer remove heat from the rod, decreasing its temperature, and after some time the film becomes unstable. Local intermittent wetting of the surface in the transition-boiling regime that follows increases the cooling rate and a wet patch is formed. This wet patch spreads and results in the formation of a stable quenching front.

A similar succession of heat transfer regimes can be found along a rod undergoing quenching. Visual observations have revealed the existence of a quench front that progresses along the rod at a slowly-varying velocity.

Below the quench front heat is removed by transition and nucleate boiling and by convective heat transfer to the liquid. The dry portion of the rod is cooled by free and forced convection to steam, by dispersed-flow and/or inverted-annular film boiling, and by axial conduction of heat within the surface, from the dry to the wetted side, where the heat transfer coefficient can be many orders of magnitude larger than the one on the dry side. The cooling of the dry portion of the rod by direct convection and radiation to the cooolant is usually referred to as precursory cooling [57].

The relative importance of these two cooling mechanisms, namely axial conduction and precursory cooling, depends on the physical situation. With top-spray emergency cooling very poor heat transfer may exist downstream of the quench front and axial conduction is likely to be the dominant mechanism driving the quench front propagation. With bottom flooding, the cooling of the dry surface ahead of the quench front may be significant and both heat transfer mechanisms may be important.

Some investigators [42, 43] have neglected axial conduction in the case of bottom flooding and assumed that the wall temperature all along the rod can be calculated by considering radial conduction only. Reasonable results were obtained [42] by using an elevated quench temperature, which may actually be compensating for the absence of axial conduction in the model.

3.2 MODELING OF THE QUENCH FRONT REGION

A significant amount of theoretical and analytical work has been done recently to better understand the quenching phenomena. In all the proposed analytical models

the heat conduction equation for the wall is solved by assuming a distribution of heat transfer coefficients as a function of surface temperature. The major differences among these models are in the distribution of heat transfer coefficients considered and in the number of dimensions used in solving the heat conduction equation in the wall (one- and two-dimensional models). The results are usually presented in the form of explicit or implicit relationships between a dimensionless quench velocity, local wall temperature (which contains the quench temperature), and Biot numbers characterizing heat transfer in the various heat transfer zones.

Most models were developed for the case of top spray but they should in principle be applicable for bottom flooding also. A review of these models can be found in references [21, 44, 45].

A recently developed model that neglects axial conduction in the fuel pellets and radial conduction in the cladding [46, 47] was used in the present work with some limited amount of success. This model has produced satisfactory results in predicting quench front propagation in thin tubular test sections where the Biot and Peclet numbers are smaller than one. Under these conditions the temperature distributions in the wall are indeed one-dimensional (i.e. the radial temperature gradients are negligible) and therefore any discrepancies between predictions and data can be attributed with reasonable certainty to a poor choice of heat transfer coefficients.

However, at high quenching rates, and for fuel rods or tubular test sections with reasonably thick wall, the one-dimensional solutions are not applicable. Therefore, the only alternative left is to solve the two-dimensional (r, z) time-dependent heat conduction equation in the quench-front region. Since very steep temperature gradients are known to exist in the neighborhood of the quench front, a very fine axial grid is required for a finite-difference solution. This fine spatial grid, together with the very small time step required for accuracy, and the fact that the reflooding transient lasts several minutes, makes this solution very demanding in computation time. This high computational cost has lead many investigators to discard this solution as a viable alternative. Indeed to carry out this full two-dimensional solution continuously during the whole reflooding period would cause the computational cost to rise significantly.

Analysis of reflooding data, e.g. [2, 19], shows that the quench front velocity is a slowly varying function of time, as the quench front propagates along the fuel rod. This experimental observation opens the possibility of updating the quench front velocity at rather sparse time intervals only, and using a constant value

in between. This approach alleviates considerably the computational cost and can be adopted in the present work.

The solution for the two-dimensional conduction equation using a variable axial grid and a procedure to calculate the quench front velocity are described in the next section.

3.3 ANALYTICAL FORMULATION

Figure 3-1 shows schematically a section of a fuel rod and typical surface temperature and heat transfer coefficient profiles. The solution is described for the case of a fuel rod but it is applicable with appropriate adjustments also to the case of a heated tube.

The two-dimensional time-dependent heat conduction equation determining the fuel pin temperature field is

$$\frac{1}{r}\frac{\partial}{\partial r}\left[rk(r,T)\,\frac{\partial T(r,z,t)}{\partial r}\right]+\frac{\partial}{\partial z}\left[k(r,T)\,\frac{\partial T(r,z,t)}{\partial z}\right]+q'''(r,z,t)=$$

$$\rho(r,T)c(r,T)\,\frac{\partial T(r,z,t)}{\partial t} \qquad (3\text{-}1)$$

where

$T(r,z,t)$ - temperature

$\rho(r,T)$ - density

$k(r,T)$ - thermal conductivity

$c(r,T)$ - specific heat

$q'''(r,z,t)$ - volumetric heat source

The boundary conditions imposed to solve Eq. 3-1 are:

$$-k\,\frac{\partial T}{\partial r}\bigg|_{r=r_c} = h\Big(T(r_c,z,t),G,x,p,\ldots\Big)(T-T_s) \qquad (B.C.1)$$

where $h(T,G,x,p,\ldots)$ is the surface heat transfer coefficient and T_s is a reference coolant temperature. It was assumed here that the heat transfer coefficient

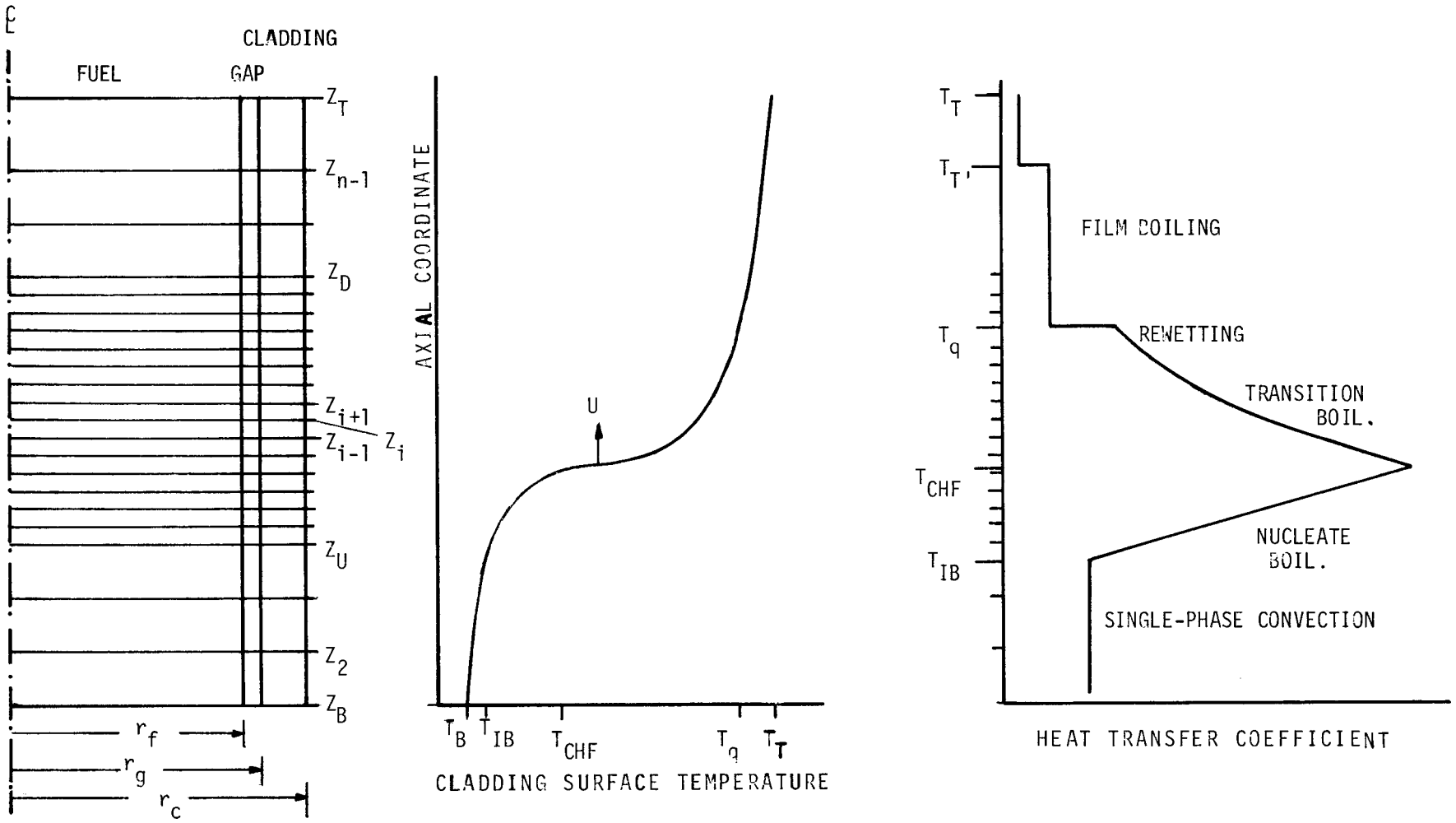

Figure 3-1. Axial grid, surface temperature and heat transfer coefficient profiles in the quench front region.

is a function of wall temperature and local flow conditions in the vicinity of the quench front. At the rod centerline, by symmetry:

$$\left.\frac{\partial T}{\partial r}\right|_{r=0} = 0 \qquad \text{(B.C.2)}$$

At the gap between the fuel and cladding,

$$-r_F k \left.\frac{\partial T}{\partial r}\right|_{r=r_F} = -r_g k \left.\frac{\partial T}{\partial r}\right|_{r=r_g} = h_g\left[T(r_F,z,t) - T(r_g,z,t)\right] \qquad \text{(B.C.3)}$$

where h_g is the gap heat transfer coefficient, possibly a function of the adjoining wall temperatures.

At both extremities of the fuel rod, the temperature gradients are specified, i.e.,

$$\left.\frac{\partial T}{\partial z}\right|_{z=Z_B} \quad \text{and,} \quad \left.\frac{\partial T}{\partial z}\right|_{z=Z_T} \qquad \text{(B.C.4,5)}$$

are given. In practice, since the extremities of the fuel rod represent points at infinity, these gradients are taken as zero.

In addition, prescription of the initial temperature field $T(r,z,0)$ uniquely defines the solution of Eq. 3-1.

In the case of a wall or rod with internal heat generation, the wall temperature at infinity can also be specified by adjusting the value of the heat transfer coefficient at infinity. Indeed, since at infinity a steady state exists and axial conduction is negligible,

$$q''_g - q''_\ell = h_T(T_T - T_s)$$

Where q''_g and q''_ℓ are the steady-state heat fluxes corresponding to internal heat generation and losses, in the case of internally-cooled tubular test sections.

Subroutines QFADI and QFADIT were written to perform the numerical calculations described above for fuel rods and tubular test sections, respectively. A detailed description of the numerical scheme used in these subroutines is presented in Appendix D. QFADI and QFADIT are listed in Appendix E.

As can be seen in Figure 3-1 the axial temperature profile is very steep in a fairly narrow axial region, $z_U < z < z_D$. Therefore, only in this region a very fine axial grid is necessary to properly describe the temperature field; a much sparser grid is suitable elsewhere. Since this stiff gradient in the temperature profile is moving with a velocity U, it is highly desirable from the point of view of computational cost to keep the fine grid moving together with the steep profile. This procedure is used in the present work. After each time step, the surface temperature field is scanned and the fine grid is reset in the proper place. Details of this moving-grid technique are described in Appendix E.

By recalling the fact that the quench-front propagation is a slow transient, that the quench velocity, the boundary conditions at the points "at infinity", and the heat transfer coefficient distribution vary slowly in time, it is possible to use quasi-steady-state values of the quench-front velocity. These values can be obtained by running the solution of the quench-front problem described above, with constant boundary conditions, only for the time necessary to achieve steady-state within a given tolerance. The solution is then extrapolated, i.e., the quench front velocity is assumed to remain constant, until changes in the boundary conditions make an update of the quench velocity necessary. In practice, a similar goal can be achieved by reevaluating the quench velocity at fixed time intervals.

The transient model described here can also be used, however, to perform a truly transient solution by running the solution continuously.

Note that the time step used for axial conduction calculations is much smaller than the time step used for channel hydrodynamics, heat transfer, and radial conduction in the fuel.

3.3.1 Quench Front Velocity

The velocity of the quench front can be obtained by monitoring the displacement of the fine axial grid that follows it. In practice for quasi-steady-state calculations the integral procedure outlined below has yielded good results, and is preferred since it fits well with the overall calculational scheme.

We will assume that the progression of the quench front has reached an asymptotic state, i.e., that the conditions away from the quench front do not change and that the temperature field translates while preserving its shape with a quench-front velocity U.

A heat balance for a fuel-rod segment delimited by planes at Z_T and Z_B, Fig. 3-1, yields

$$\frac{\partial}{\partial t}\int_{Z_B}^{Z_T}\int_{0}^{r_c}\rho(r,T)c(r,T)T(r,z,t)2\pi r dr dz =$$

$$\int_{Z_B}^{Z_T}\int_{0}^{r_c} q'''(r,z,t)2\pi r dr dz - \int_{Z_B}^{Z_T} 2\pi r_c q''(z,t) dz$$

or

$$\bar{U}[Q_b - Q_a] = \dot{Q}_s - \dot{Q}_g \tag{3-2}$$

where Q_b and Q_a are the amounts of heat stored in the fuel rod per unit length at locations ahead and behind the quench front, respectively,

$$Q_b = \int_{0}^{r_c}\rho(r,T)c(r,T)T(r,Z_T,t)2\pi r dr \tag{3-3}$$

$$Q_a = \int_{0}^{r_c}\rho(r,T)c(r,T)T(r,Z_B,t)2\pi r dr \tag{3-4}$$

and are assumed to remain constant. $\dot{Q}_g$ is the rate of heat generation in the segment

$$\dot{Q}_g = \int_{Z_B}^{Z_T}\int_{0}^{r_c} q'''(r,z,t)2\pi r dr dz \quad , \tag{3-5}$$

while $\dot{Q}_s$ is the rate of heat transfer to the coolant,

$$\dot{Q}_s = \int_{Z_B}^{Z_T} P_H q''(z,t) dz \tag{3-6}$$

where $q''(z,t)$ is the surface heat flux, and P_H the heat transfer perimeter.

Integrating Eq. 3-2 from t_1 to t_2 yields the average quench front velocity over this time interval

$$\overline{U} = \frac{Q_s + Q_\ell - Q_g}{(Q_b - Q_a)(t_2 - t_1)} \tag{3-7}$$

where $Q_s = \int_{t_1}^{t_2} \dot{Q}_s \, dt$

$$Q_g = \int_{t_1}^{t_2} \dot{Q}_g \, dt \tag{3-8}$$

and the quantity Q_ℓ was added to represent the heat losses from the external surface of a tubular test section. Q_ℓ is zero in the case of a fuel rod,

$$Q_\ell = \int_{t_1}^{t_2} \int_{Z_B}^{Z_T} q''_\ell(z,t) P_L \, dz dt \tag{3-9}$$

where $q''_\ell(z,t)$ is the heat flux due to losses (calculated on the basis of the corresponding wall temperature) and P_L is the corresponding outside perimeter. In this case, P_H in Eq. 3-6 is the tube inner perimeter, and the lower limit of integration in Eqs. 3-3 to 3-6 is r_g instead of zero.

A convergence criterion for the quasi-steady-state quench-front velocity is defined as

$$\left| \frac{\overline{U}'' - \overline{U}'}{\overline{U}'} \right| < \varepsilon \tag{3-10}$$

where $\overline{U}'$ and $\overline{U}''$ are the average quench front velocities over two consecutive time intervals $(t_2 - t_1)$ and ε is a small quantity defining convergence.

The time interval $t_2 - t_1$ must be sufficiently small to avoid running the solution unnecessarily, but also sufficiently large so that steady state can actually be

achieved. A proper order of magnitude for this time interval is provided by the inverse of the fuel rod time constant defined as

$$\tau = \frac{h_{max} P_H}{\rho c A} \tag{3-11}$$

where A is the fuel rod (or tube wall) cross sectional area, h_{max} is the maximum value of the heat transfer coefficient, and ρc is the average heat capacity evaluated at $(T_B + T_T)/2$.

The advantage of this indirect method for determining the quench front velocity is that it is based on integral calculations and for this reason yields relatively noise-free quench velocity variations. Furthermore the quantity $Q_b - Q_a$ is needed in calculating the enthalpy variation across the quench-front region.

3.3.2 Length of the Quench Front Region, ΔZ_{QF}

The axial locations Z_U and Z_D in Fig. 3-1, bracketing the very find axial grid, are defined by scanning the surface temperature profile, starting from the wetted end and locating the position Z_U where the axial temperature gradient first exceeds a critical value, and the position Z_D where it first drops below this critical value. Sensitivity studies have shown that 1000 °F/ft (6°C/mm) is a proper choice for this critical temperature gradient.

For the purpose of determining the conditions at the points "at infinity" upstream and downstream (temperature and temperature gradient), it is necessary to define a somewhat longer width for the quench front region. Experience has shown that this can be defined as

$$\Delta Z_{QF} = 1.2(Z_D - Z_U) \tag{3-12}$$

3.4 HEAT TRANSFER COEFFICIENT IN THE QUENCH FRONT REGION

The variation of the heat flux along the quench region, calculated by simple approximate methods, indicates that the heat flux--wall temperature relationship resembles the classical pool boiling characteristic. This is not surprising since one finds the heat transfer regimes similar to those encountered in pool boiling succeeding one another along the rod. The discontinuity of the heat transfer coefficient distribution that is needed to create the steep axial temperature profile is provided by the rapid variation of the heat transfer coefficient in the transition-boiling regime.

An attempt was made initially to describe the variation of the heat transfer coefficient in the quench region using conventional pool and flow-boiling correlations. This approach is successful only at low flooding rates and subcoolings. Indeed, experimental evidence reveals that the quench front velocity is a strong function of subcooling and flooding rate at elevated flooding rates and subcoolings. Unfortunately the subcooled nucleate-boiling correlations do not include any mass-flux effect. Furthermore, the peak value of the heat flux must be obtained from pool-boiling correlations since flow-boiling critical heat flux correlations applicable under reflooding conditions do not exist. This pool-boiling CHF can be corrected for subcooling, but there is no established procedure for correcting for the effect of mass flux. Section 3.4.1 describes the effort made in this direction.

Several authors [21] attempted to account for the effects of mass flux and subcooling on the quench velocity by correlating empirically either the quench velocity itself, or the peak value of the heat transfer coefficient versus subcooling and mass flux.

Correlations of the quench velocity itself are applicable only to the particular test section geometry from which they were derived. This is because they implicitly include the effects of axial conduction in the wall and the conduction characteristics of the wall.

If we knew perfectly well the variation of the heat transfer coefficient distribution as a function of local conditions near the quench front, any correlation of this distribution would have been expected to have universal validity. In this case the effects of axial conduction in the rod or tubular test section would have been taken care of by an appropriate axial-conduction model of the hot wall utilizing the heat transfer coefficient distribution as a boundary condition.

Unfortunately, it is presently impossible to measure accurately the surface temperature profile and the heat transfer coefficient distribution in the narrow quench front region, where very strong axial and radial temperature gradients exist. For this reason the variation of the heat transfer coefficient is often idealized as a one or two-step function, as shown in Fig. 3-2. With two-dimensional analytical axial-conduction models, we are in practice limited to a single step since the solution becomes unmanageable for more complex variations of the heat transfer coefficient.

When a simple, idealized heat transfer coefficient distribution is used, the peak value of the heat transfer coefficient can be correlated in terms of local conditions at the quench front. Because of the idealization of the heat transfer

coefficient distribution, some of the axial conduction effects may be absorbed in the correlation. Thus the correlation may not apply very well to a variety of test section configurations having different axial conduction characteristics. The success of the method can only be tested by applying it to rods as well as to tubular test sections. An approach based on this method was adopted for the present work and is described in Section 3.4.2.

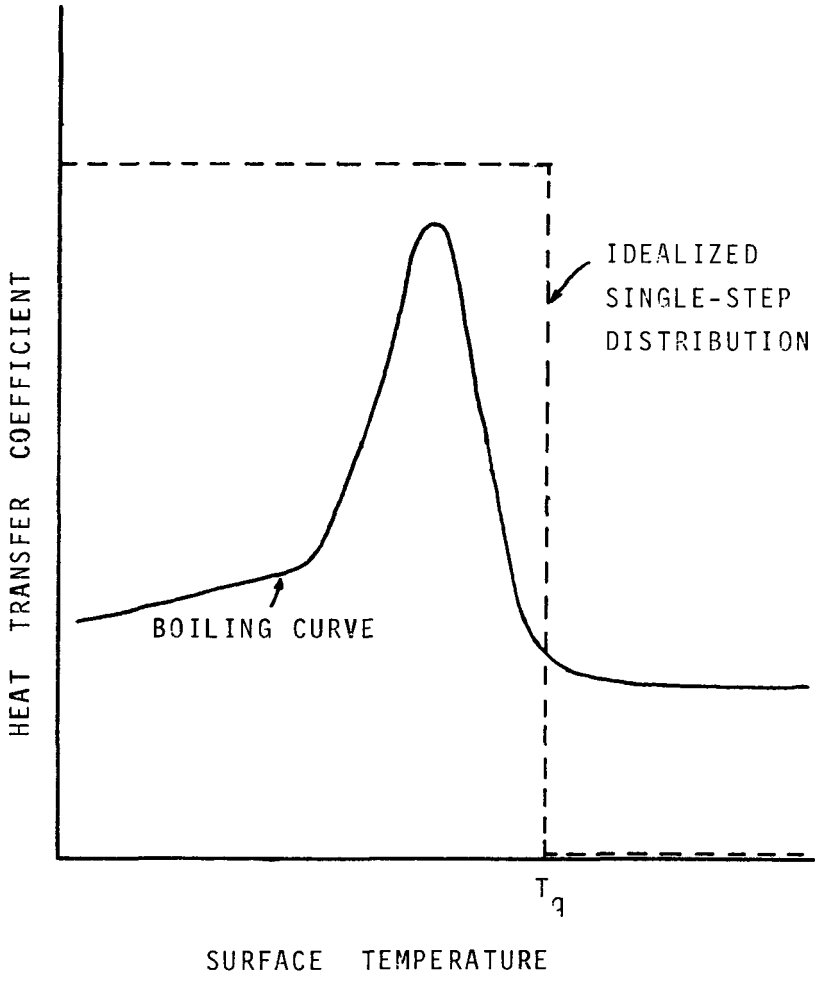

Figure 3-2. Variation of the Heat Transfer Coefficient in the Quench Front Region

3.4.1 Boiling-Curve Approach

As mentioned above, the heat-flux versus wall-temperature relationship along the quench front region resembles the classical pool boiling characteristics. This observation led to the approach that consists in defining the heat transfer coefficient accordingly.

The flow conditions may change substantially along the quench front region. To evaluate these changes properly, a very find axial grid would be necessary in the flow channel. Given, however, the high turbulence and axial mixing of the two-phase flow near the quench front, the calculation of a very fine axial distribution of flow conditions is not justified on physical grounds. Thus flow conditions in the quench front region are probably sufficiently well specified by average or reference local flow conditions there.

Initially a heat transfer coefficient distribution based on the local wall temperature only was adopted. This is because the correlations that were readily available and were believed to be applicable had no dependence or only a weak dependence on flow conditions, i.e., local quality or subcooling and mass flux. The heat transfer coefficient distribution tested and the limitations of this method are described below. A sketch of the heat transfer coefficient distribution in the quench front region is shown in Fig. 3-1. In agreement with the proposal by Kirchner [42], this distribution is anchored by the wall temperature at the critical heat flux (CHF) point and by the quench temperature. Kirchner has, however, ignored any effects of axial conduction.

Unfortunately, there is no information in the open literature on CHF at very low pressures and flow rates. Kirchner [42] suggested the use of Zuber's pool boiling correlation [49] to evaluate the critical heat flux under reflooding conditions and this procedure was adopted.

The Zuber CHF correlation together with the nucleate-boiling component of Chen's correlation are used to calculate the wall superheat at the point of CHF:

$$\Delta T_{w_{CHF}} = \frac{q''_{CHF}}{h_{NB}}$$

where

$$q''_{CHF} = 0.131\, h_{fg}\rho_g^{1/2}\left[\sigma g(\rho_f-\rho_g)\right]^{1/4}\left[\frac{\rho_f}{\rho_f+\rho_g}\right]^{1/2} \qquad (3\text{-}13)$$

and h_{NB} is given by Eq. 2-28.

As the CHF is exceeded, transition boiling will develop. Transition boiling, as the name implies, is a combination of unstable film boiling and unstable nucleate boiling. It is characterized by the fact that an increase in surface temperature usually results in a decrease in surface heat flux, as shown in Fig. 3-1.

At surface temperatures in excess of the CHF value, the heated surface will be partially covered with unstable vapor patches. The formation of these dry patches is accompanied by a drastic reduction in heat transfer coefficient; the corresponding reduction in local vapor generation will permit the liquid to momentarily rewet the heated surface. As the wall superheat increases, the frequency of liquid contacts with the wall decreases rapidly. The liquid will be able to rewet the wall occasionally up to a temperature T_q, which in pool boiling is known as the minimum film-boiling temperature. In flow boiling, this temperature has been referred to as the quenching, rewetting, or Leidenfrost temperature but the mechanisms that produce rewetting and the parameters that determine the value of the rewetting temperature are not well known.

The quench temperature, T_q in Fig. 3-1, is left as a free parameter because the inferred experimental values as well as correlations proposed to predict it show a very wide scattering of results. However, for atmospheric-pressure data the inferred experimental values are clustered around 500°F (260°C) and this value is in principle recommended.

Several authors have proposed correlations for the heat transfer coefficient in the transition boiling region. A good review of the literature is presented by Groeneveld [50].

A transition-boiling correlation proposed by Ramu and Weisman [23,24] was adopted in the present work, with the maximum value of the boiling component taken as h_{CHF}. This procedure insures heat flux continuity. According to these authors:

$$h_{TB} = h_b + h_c \tag{3-14}$$

$$h_b = h_{CHF}\left\{\exp[-0.0078(T-T_{CHF})] + \exp[-0.0698(T-T_{CHF})]\right\}$$

$$h_c = 0.023\,\frac{k_f}{D_H}\left(\frac{\mu_g}{\mu_w}\right)^{0.14} Pr_f^{1/3}\left(\frac{GD_H}{\mu_g}\right)^{0.8}(0.15+0.86x) \quad \text{for} \quad x < 0.2$$

$$h_c = 0.023 \frac{k_f}{D_H} \left(\frac{\mu_g}{\mu_w}\right)^{0.14} Pr_f^{1/3} \left(\frac{GD_H x}{\mu_g}\right)^{0.8} \left(1 + \frac{1-x}{x} \frac{\rho_g}{\rho_f}\right)^{0.8} \quad \text{for} \quad x > 0.2$$

where h_{CHF} is evaluated from Eqs. 2-28 and 3-13.

For the high-flooding-rate cases, Fig. 1-3B, an inverted-annular flow regime will exist ahead of the quench front. The modified Bromley correlation discussed in Section 2.2.2.2 can be used in this region.

The heat transfer coefficient selection criteria based on the local cladding temperature only resulting from the above discussion are summarized below:

a) Single-phase convection, $T \leq T_{IB}$

If the cladding temperature drops below the incipence-of-boiling value T_{IB}, defined by the Bergles and Rohsenow [9] criterion, Eq. 2-10, the single-phase forced-convection heat transfer coefficient at the axial node just below the quench front region is used.

b) Nucleate Boiling, $T_{IB} < T \leq T_{CHF}$

Chen's correlation [15] was used to define the wall superheat at CHF. Below CHF, instead of using Chen's correlation, and for the sake of simplicity, the heat transfer coefficient is calculated from

$$h = h_{CHF} \frac{T - T_b}{T_{CHF} - T_b}$$

where h_{CHF} is the heat transfer coefficient at CHF and T_b is the coolant reference temperature in the quench front region.

c) Transition-Boiling region, $T_{CHF} < T \leq T_q$

In the transition-boiling region the boiling component of the Ramu and Weisman correlation [51], Eq. 3-14 is used. The convective component, represents a small contribution and is dropped for simplicity.

d) Film Boiling region, $T_q < T \leq T_T'$

In the film boiling region the modified Bromley correlation, Eqs. 2-30 is used. T_T' is defined as

$$T_T' = T_T - 5°F$$

where T_T is the cladding temperature at the quench-region upper boundary. The reason for defining T'_T is discussed below.

e) Dry Region away from Quench Front, $T > T'_T$

In this region the value of the heat transfer coefficient is defined as

$$h = \frac{q''_g - q''_\ell}{T - T_b} \tag{3-15}$$

in order to achieve steady state at "infinity". q''_g and q''_ℓ are the steady-state heat fluxes due to heat generation and to losses, in the case of a tubular test section. These are defined later in Section 3.6.2. The 5°F limit puts this region sufficiently far from the quench front so that it does not influence its progression.

It should be pointed out, that for typical reflooding conditions the dominant factors in determining the quench front velocity are the surface heat transfer coefficient distribution and the state of the fuel rod before and after the passage of the quench front. The magnitude, distribution and time dependence of the heat source has therefore a minor effect on the calculated quench front velocity.

The use of the heat transfer distribution described above produced reasonable agreement with quench front velocity data only for low flooding rates and subcoolings. Tong [53] presents several corrections that have been proposed to account for the effect of subcooling on CHF. Increasing the CHF value with subcooling improved the predicted values. However inspection of the UC-B data [19] shows that besides subcooling there is a strong effect of mass flux on the quench front velocity. Therefore, to better estimate the feasibility of the pool boiling approach it is necessary to have at least a CHF correlation that accounts for the effects of subcooling and mass flux. The non-availability of such a correlation led to the adoption of a semi-empirical approach described in the next section.

3.4.2 Idealized-Boiling-Curve Approach

The two-dimensional axial conduction problem in a lamina undergoing rewetting was solved analytically by Coney [54], who used an one-step distribution for the heat transfer coefficient. The heat transfer coefficient was taken as zero on the hot wall. The value of the heat transfer coefficient on the wetted side and the rewetting temperature are inputs to this model. Yu et al. [55] used a variety of atmospheric-pressure bottom-reflooding rewetting data to correlate the value of Coney's heat transfer coefficient and rewetting temperature as follows:

$$T_q = T_{sat} + 144°F$$

$$h = 7.18627 \times 10^8 \; V^{0.3} \left[\frac{0.4839\left(1 + 0.0941 \; V \; \Delta T_{cq}^2\right)^{0.346}}{T_q - T_{cq}} \right]^2 \quad \text{for}$$

$$1 + 0.0941 \; V \; \Delta T_{cq}^2 \geqslant 40$$

and

$$h = 7.18627 \times 10^8 \; V^{0.3} \left[\frac{\left(1 + 0.0941 \; V \; \Delta T_{cq}^2\right)^{0.13}}{T_q - T_{cq}} \right]^2 \quad \text{for} \quad 1 + 0.0941 \, V \, \Delta T_{cq}^2 < 40$$

(3-16)

where

T_q - quench temperature (°F)

h - wet-side heat transfer coefficient (Btu/ft^{2}hr°F)

V - channel-inlet (reflooding) velocity (ft/s)

T_{cq} - coolant temperature at quench front (°F)

ΔT_{cq} - $T_{sat} - T_{cq}$ = subcooling at quench front (°F)

The values of h according to Yu et al. are plotted in Fig. 3-3. This correlation predicted very well UC-Berkeley bottom reflooding data [19] (see Section 3.5) and, in the absence of a more realistic model, was adopted for inclusion in the UCFLOOD code. The approach that should be taken for fuel rods or fuel rod simulators is discussed in Section 3.5.

In all cases, axial conduction calculations can be performed using the two-dimensional axial conduction routines QFADI or QFADIT developed and described in Section 3.3 and in Appendices D and E. For unheated or heated tubular test sections Coney's analytical results [54] can be also used instead of a numerical calculation. Indeed the heat fluxes due to internal heat generation and heat losses are generally negligible compared to the heat spike at the quench front due to the evacuation of the heat stored in the wall. Coney presents a table of

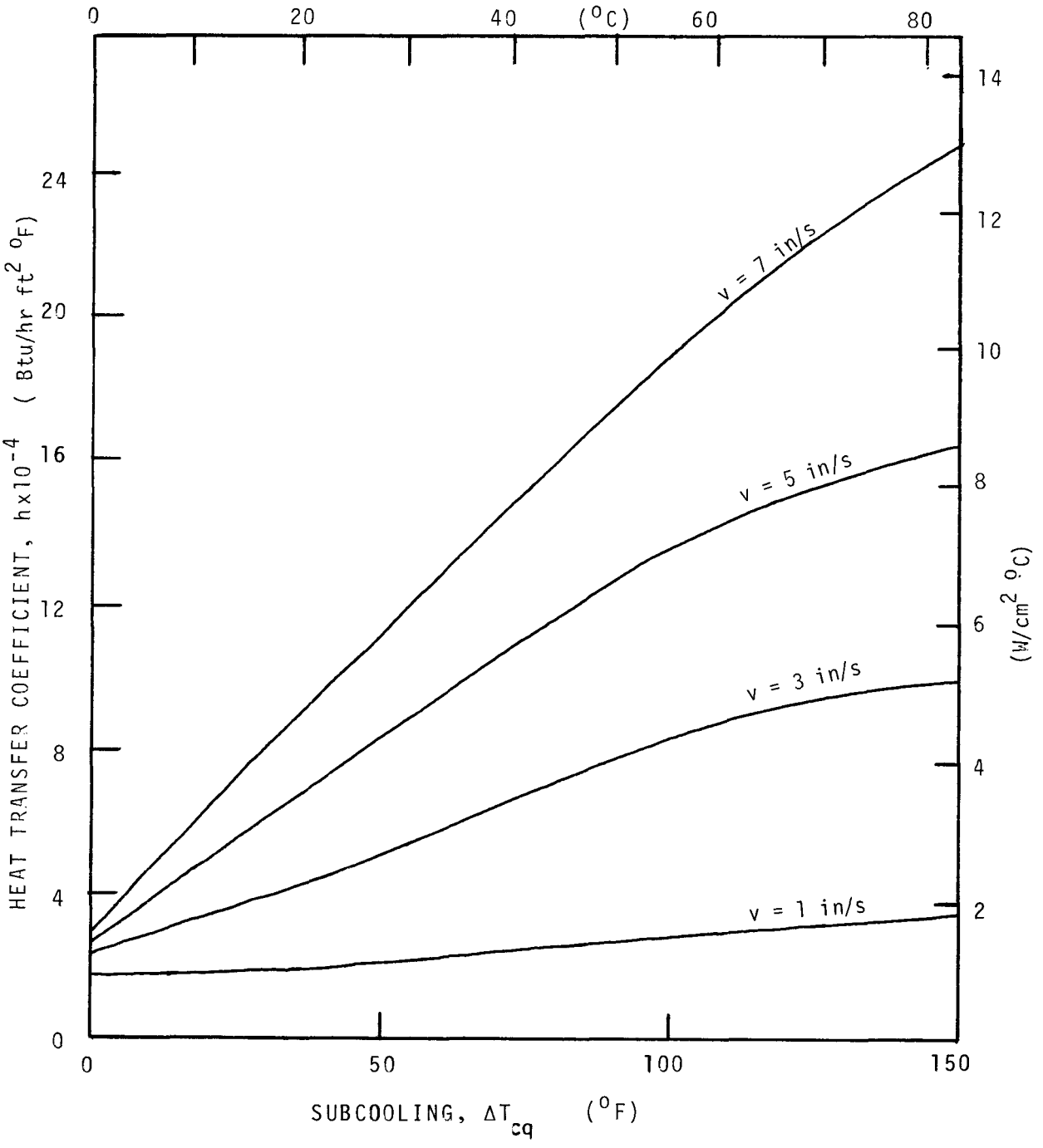

Figure 3-3. Heat transfer coefficient calculated by Yu et al. correlation for bottom-reflooding.

calculated values of the Peclet number versus the Biot number and the dimensionless wall temperature. This table is stored in UCFLOOD and is interpolated in two-dimensions to calculate the Peclet number for values of h obtained from Eq. 3-16 and initial wall temperatures obtained according to the method that will be presented in Section 3.6. The values of h and of the initial wall temperature determine the Biot number and the dimensionless wall temperature.

Recently, Dua and Tien [59] proposed a simple numerical fit that describes fairly accurately their two-dimensional axial-conduction results, as well as, of course, those of Coney. This simple equation was also programmed in UCFLOOD as described in Appendix E.

3.5 MODEL VERIFICATION

The boiling-curve approach for calculating the quench front velocity does not account for the effects of subcooling and flow rate revealed by the experimental results. However, by considering the case of no subcooling and low flooding rate, the feasibility of such an approach can be assessed.

A UC-B experimental data point [19], characterized by the conditions shown in Fig. 3-4, was selected for this assessment. The quench front velocity was calculated using the boiling curve described in Section 3.4.1 and the two-dimensional conduction routine QFADIT, for various values of the quench temperature. Even under these favorable conditions, i.e., no subcooling and low mass flux, the experimental value was underestimated. Increasing the quench temperature does yield higher quench front velocities, as expected. However, the present analysis implicitly assumes that the quench front propagation is conduction-controlled, i.e., the quench front region is always below the swollen liquid level, therefore the prescribed quench temperature must be less than the wall temperature ahead of the quench front (T_w). Figure 3-4 shows that the experimental quench front velocity is not achieved as values approaching T_w are assigned to T_q. Figure 3-4 also shows the significant effect of axial conduction on the quench front velocity. The no-axial-conduction point was obtained by setting the value of the thermal conductivity in the axial direction equal to zero in QFADIT.

Figure 3-5 shows the surface temperature and heat flux profiles obtained during the calculation of the quench front velocity shown in Fig. 3-4. Note that the whole boiling curve is confined to a length of approximately 0.05 feet.

Precursory cooling and axial conduction are the two mechanisms driving the propagation of the quench front, and the relative importance of each of these is a function of local flow conditions and of the thermal characteristics of the wall. Yu

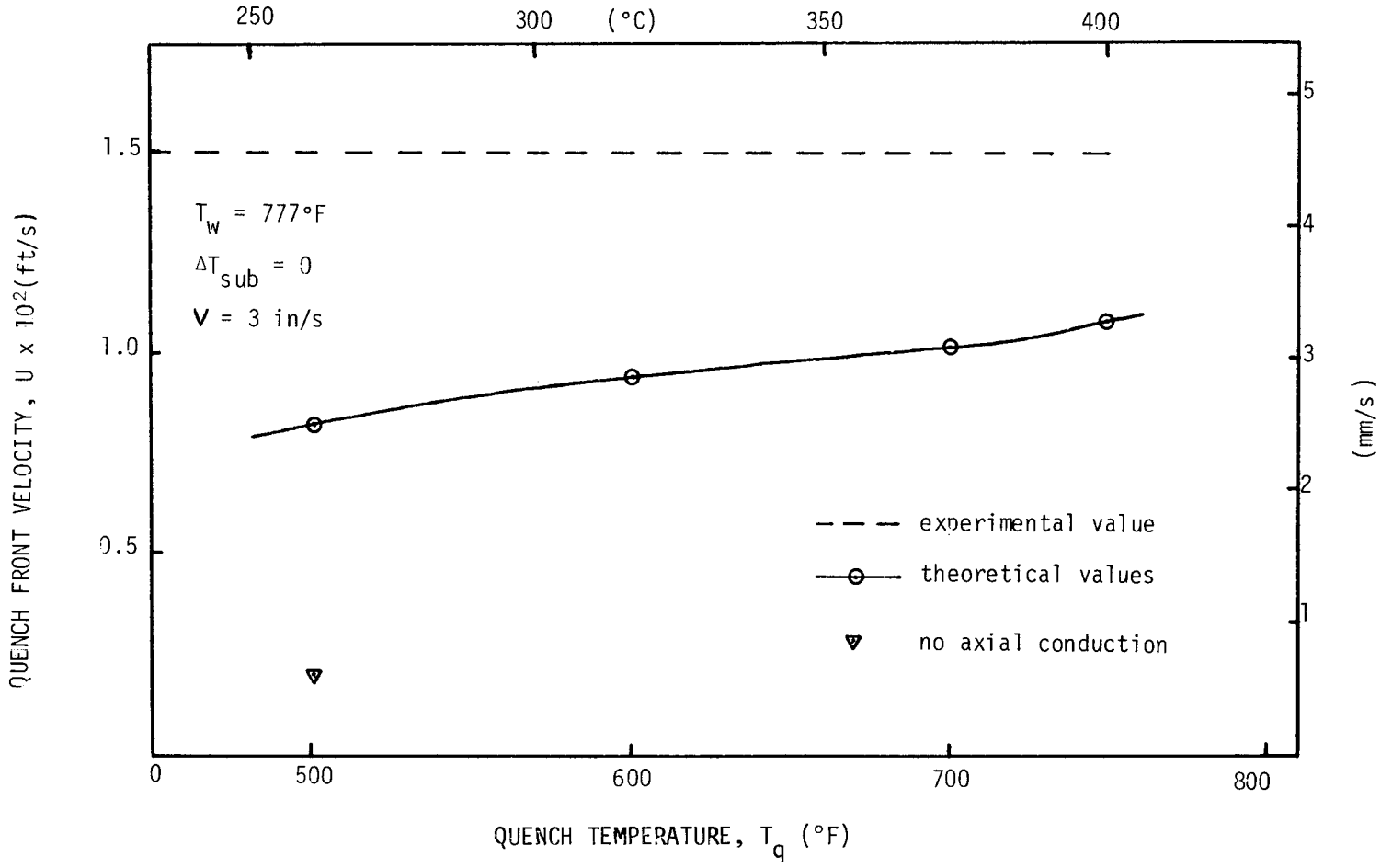

Figure 3-4. Effect of the quench temperature on the quench front velocity.

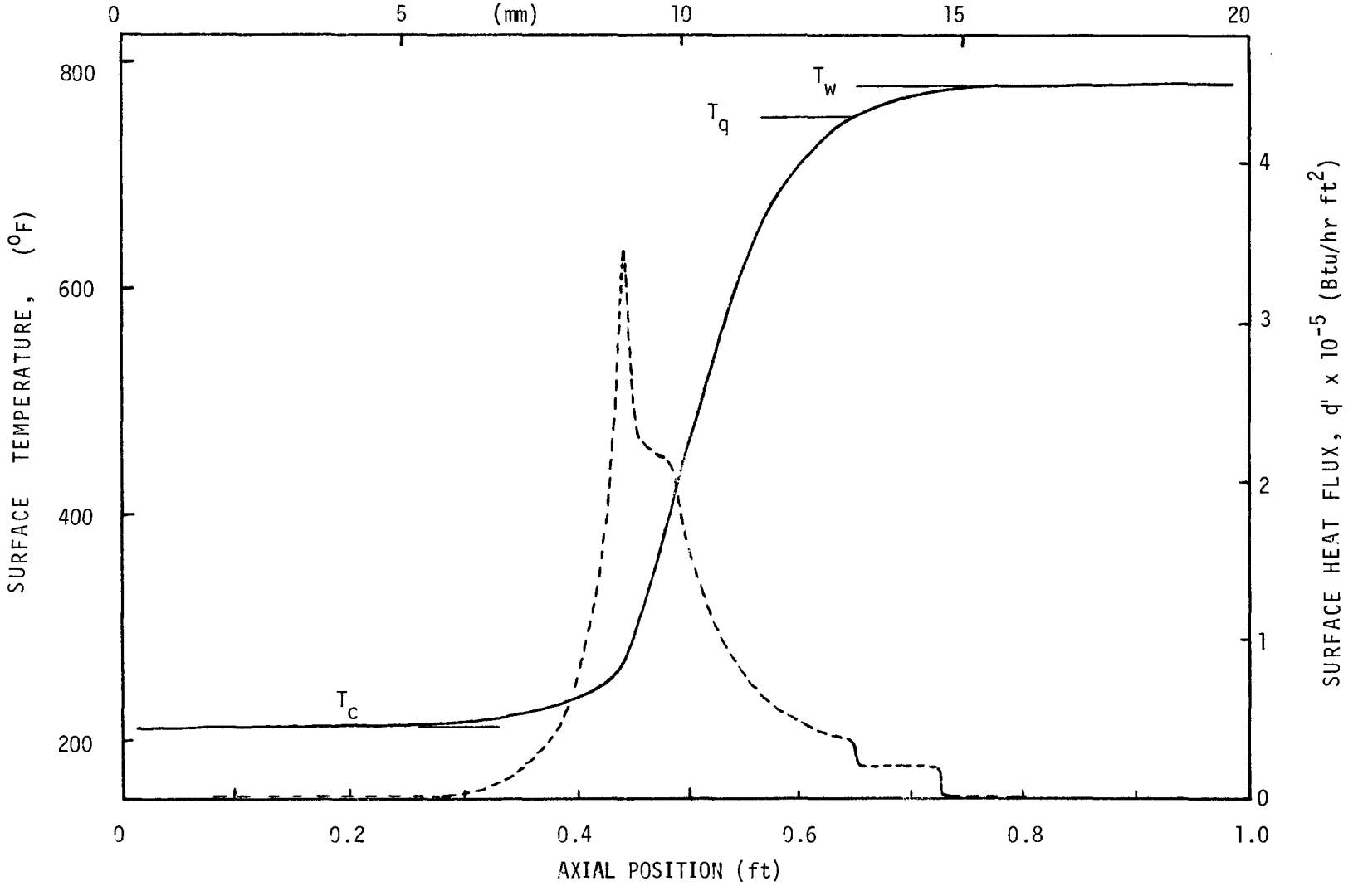

Figure 3-5. Surface temperature and heat flux in the quench front region.

et al. [55], by assuming a zero heat transfer coefficient ahead of the quench front, included the effect of precursory cooling in the idealized constant heat transfer coefficient on the wet side. Therefore they have enhanced artificially the effect of axial conduction to account for the absence of precursory cooling. The main advantage of correlating the heat transfer coefficient as a single step function is the availability of analytical solutions relating this heat transfer coefficient to the quench front velocity. Indeed the problem of rewetting a lamina or tubular test section was solved analytically by Coney [54] as noted earlier, while Yeh [56] solved the same problem for a solid rod.

However, for the case of an actual reactor fuel rod including fuel, a gap, and cladding, no analytical solution is available. In principle, the heat transfer coefficient and quench temperature correlated by Yu et al. [55] could be used as the boundary condition to solve numerically the conduction equation in the fuel rod as described in Section 3.3. However, the very sharp discontinuity of the heat transfer coefficient, which is an idealization and not physically sound, places a heavy burden on the numerical solution. Specifically, it yields extremely steep axial temperature gradients and therefore an extremely fine axial grid is necessary. Moreover, it is not clear that the approximations involved in the approach by Yu et al. would remain valid when drastic changes in geometry (thin tubular test section to rod) are made, since some effects of axial conduction and precursory cooling are lumped in the artificial value of the heat transfer coefficient used, as noted above.

Since for actual fuel rods a numerical solution seems inevitable, it is desirable to generate numerical solutions using a simplified boiling-curve approach and tabulating the quench velocity or Peclet number as a function of the Biot number at the CHF point, and the quench and wall temperatures. These tables could then be used, together with experimental data, to correlate the heat transfer coefficient or the heat flux at CHF and the quench temperature as a function of subcooling and mass flux. This approach is demanding in computational cost but seems inevitable for achieving a better modeling of the quench region; therefore, it is recommended for future work.

Figure 3-6 shows the comparison of UC-B quench velocity data with the correlation by Yu et al. [55]. The general agreement is quite good, however, a few high-velocity data points show a large discrepancy. It is likely that these data points are not conduction-controlled and therefore the correlation is not applicable to these. A new version of the correlation by Yu et al. derived from the UC-B reflooding data is under development [20].

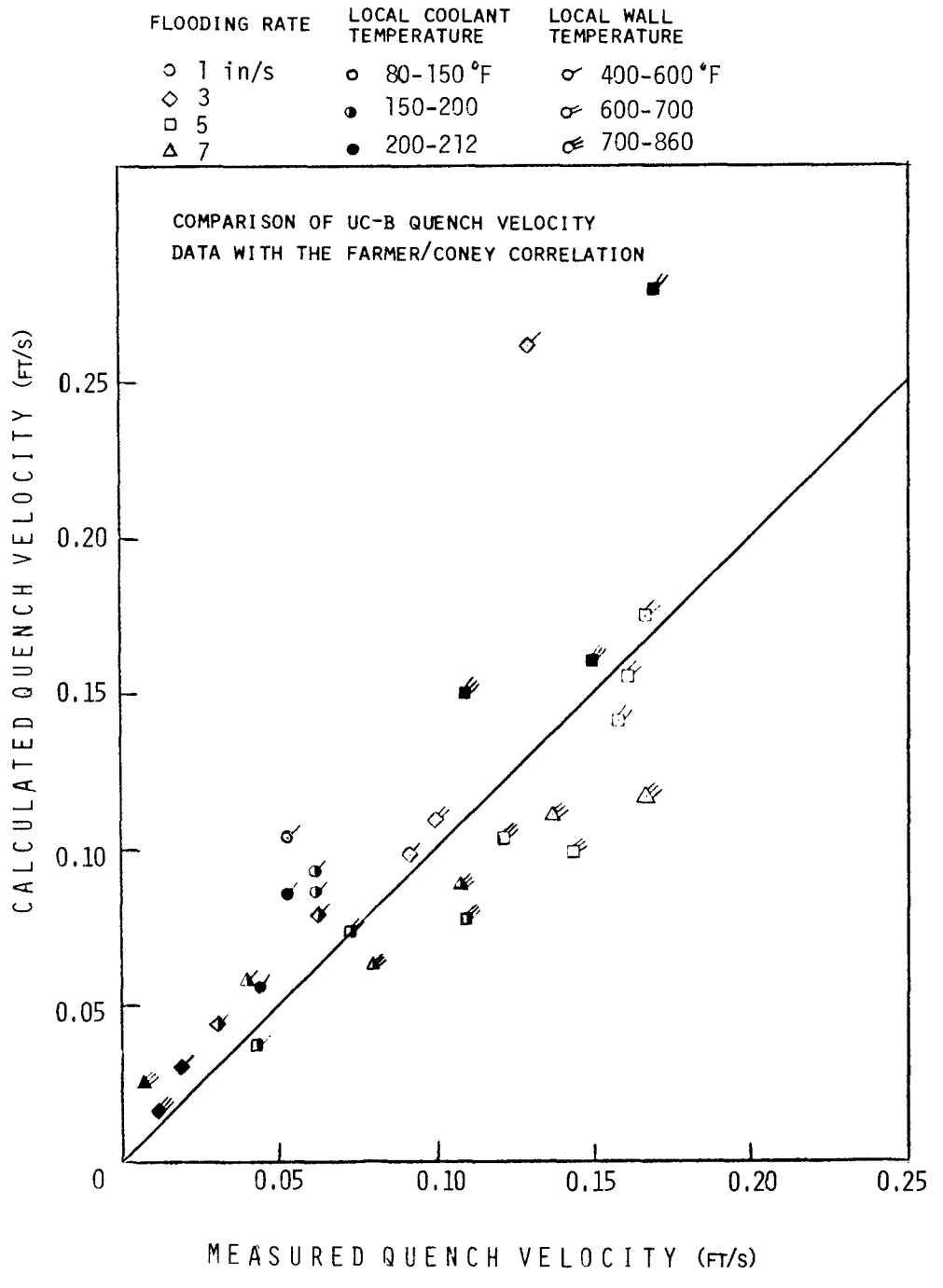

Figure 3-6. Comparison of UC-B quench velocity data with the results of the Yu et al. correlation method.

3.6 INTEGRATION OF THE QUENCH-FRONT REGION MODEL IN THE OVERALL CALCULATIONAL SCHEME

3.6.1 Boundary Conditions

The quench-front-region model described in the previous sections requires boundary conditions provided by the channel thermo-hydraulic model and returns the position of the quench front $Z_q(t)$ and the heat flux in the quench front region.

The width of the quench front region ΔZ_{QF}, defined in Section 3.3.2, is normally smaller than the width of an axial fuel node (the overall channel length of 12 ft is typically divided into 40 nodes of 0.3 ft each, while the length of the quench front region rarely exceeds 0.1 ft). Thus the quench front region covers part of at most two fuel nodes.

In the overall calculational scheme the width of the quench-front region is taken to be equal to the width of a fuel node, ΔZ. The coordinates of the upstream and downstream boundaries of this region are denoted by $Z_{U'}$, and $Z_{D'}$, as shown in Fig. 3-7.

The surface temperature and the surface axial temperature gradients at the "infinity points" for the quench-front model, i.e. at $Z_{U'}$ and $Z_{D'}$, are calculated by linear extrapolation as follows:

$$\frac{dT_B}{dZ} = \frac{(T_{m-1} - T_{m-2})}{\Delta Z} \tag{3-17}$$

$$T_B = T_{m-1} + \frac{dT_B}{dZ}(Z_{U'} - Z_{m-1}) \tag{3-18}$$

and

$$\frac{dT_T}{dZ} = \frac{(T_{m+3} - T_{m+2})}{\Delta Z} \tag{3-19}$$

$$T_T = T_{m+2} - \frac{dT_T}{dZ}(Z_{m+2} - Z_{D'}) \tag{3-20}$$

where Z_m is the axial position of node m and ΔZ is the size of the axial nodes along the fuel rod.

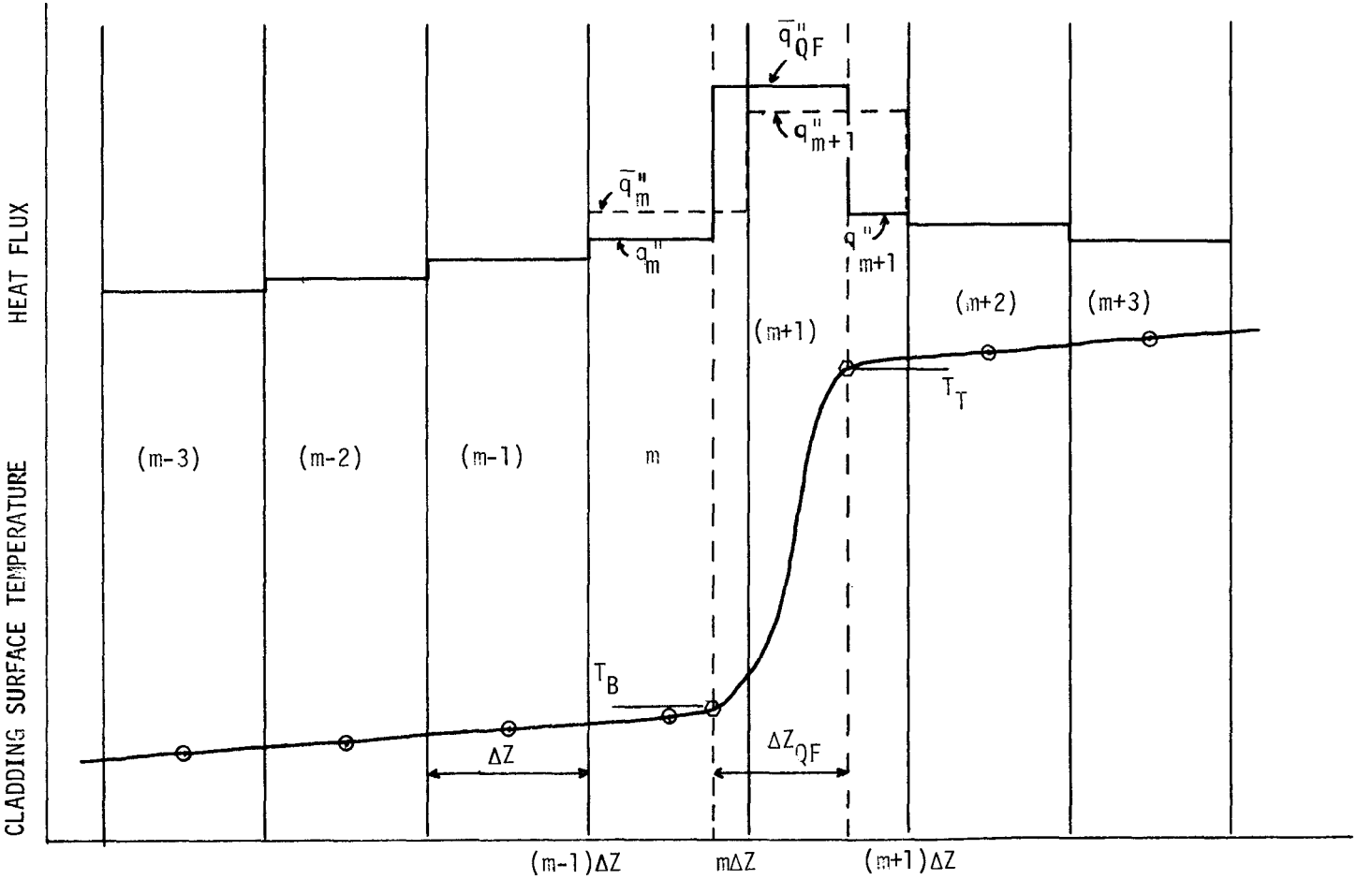

Figure 3-7. Cladding surface temperature and heat fluxes in the neighborhood of the quench front.

The gradients at interior radial mesh points are assigned values equal to the surface gradients; the fact that these axial gradients are very small makes this approximation quite acceptable.

Usually ΔZ_{QF} is a small fraction of ΔZ as noted above; however, to simplify the programming logic, if ΔZ_{QF} is calculated to be larger than ΔZ it is set equal to ΔZ. There is no great loss of accuracy by this requirement because of the relative flatness of the temperature profiles outside the quench-front region.

The quench front position $Z_q(t)$ is updated according to

$$Z_q(t + \ t) = Z_q(t) + \Delta Z_q$$

where Z_q is either obtained from the advance of the fine axial grid, when a fully transient axial-conduction solution is performed, or is calculated as

$$\Delta Z_q = U\Delta t$$

In this case the quasi-steady-state value of the quench velocity U is supplied as described in Section 3.4. The upstream and downstream boundaries of the quench front region are given by

$$Z_{U'} = Z_q - \Delta Z_{QF}/2$$

and

$$Z_{D'} = Z_q + \Delta Z_{QF}/2 \qquad (3\text{-}21)$$

The local flow conditions in the vicinity of the quench front are needed to establish the heat transfer coefficient distribution in the quench-front region. The mass flux at the quench front is taken to be equal to the inlet mass flux. In reality the mass flux at the quench front could be slightly lower, as discussed in Section 2.2.4, but this approximation is consistent with the derivation of the heat transfer correlations in the quench region discussed in Section 3.4.2.

The quality or subcooling at the quench front are taken to be the values at the node immediately upstream (m-1), c.f. Fig. 3-7. A slightly more accurate value could have been calculated by extrapolating upstream conditions, but this is not necessary since the variation of flow conditions below the quench front is generally very slow.

3.6.2 Average Heat Flux in the Quench Front Region

The cladding surface heat flux in the quench front region has the form of a very narrow spike compared to the channel length. Therefore, to calculate the flow conditions in the neighborhood of the quench front, a very fine axial grid in the flow channel would have been necessary to properly account for this distribution of the surface heat flux. Such a detailed computation, however, would have increased the computational cost and is really not necessary within the present framework.

An alternative, which is adopted in this work, is to calculate flow conditions in the quench-front region using an average value of the heat flux. This average heat flux is calculated by the axial-conduction routine when a fully transient axial-conduction calculation is performed.

When the quench-front model is used in its quasi-steady-state form, this average heat flux is calculated by a heat balance and is given by

$$\bar{q}''_{QF} = \frac{(Q_b - Q_a)U}{P_H(Z_{U'} - Z_{D'})} + q''_g - \bar{q}''_\ell \qquad (3\text{-}22)$$

The first term represents the contribution of the stored heat being released by the passage of the quench front, the second term is the contribution due to the power input, and the last term represents the average heat losses. Q_a and Q_b are given by Eqs. 3-3 and 3-4, while

$$q''_g = \frac{Q_g}{P_H(Z_{U'} - Z_{D'})(t_2 - t_1)}$$

and

$$q''_\ell = \frac{Q_\ell}{P_L(Z'_U - Z'_D)(t_2 - t_1)}$$

where Q_g and Q_ℓ are given by Eqs. 3-8 and 3-9, respectively.

3.6.3 Average Heat Flux in the Fuel Nodes Affected by the Quench Front Region

The average value of the cladding surface heat flux over the fuel node lengths is needed to calculate the heat input into the coolant. Special care must be taken

when calculating this average heat flux for nodes partly under the quench front length ΔZ_{QF}.

With reference to Fig. 3-7, the average heat fluxes in nodes m and m+1, $\bar{q}''_m$ and $\bar{q}''_{m+1}$, are calculated as

$$\bar{q}''_m = \frac{1}{\Delta Z}\left\{q''_m[Z_{U'} - (m-1)\Delta Z] + \bar{q}''_{QF}[m\Delta Z - Z_{U'}]\right\} \tag{3-23}$$

$$\bar{q}''_{m+1} = \frac{1}{\Delta Z}\left\{\bar{q}''_{QF}[Z_{D'} - m\Delta Z] + q''_{m+1}[(m+1)\Delta Z - Z_{D'}]\right\} \tag{3-24}$$

The heat fluxes q''_m and q''_{m+1} are calculated as follows. The surface temperature at the middle of node m, i.e., at $z = (m-1/2)\Delta Z$, is calculated first by a linear forward extrapolation based on T_{m-2} and T_{m-1}. With this temperature and the flow conditions at node (m-1), i.e., the flow quality x_{m-1} and $T_{b,m-1}$, a heat transfer coefficient h_m is calculated (using either the Chen or the Dittus Boelter correlations presented in Sections 2.1 and 2.2). Then

$$q''_m = h_m(T_m - T_{b,m-1})$$

Similarly for node (m+1), the surface temperature T_{m+1} at $z = (m+1/2)\Delta Z$, is calculated first by a linear backward extrapolation based on T_{m+2} and T_{m+3}. The heat transfer coefficient h_{m+1} is based on this temperature and flow conditions in the middle of node m+2, and

$$q''_{m+1} = h_{m+1}(T_{m+1} - T_{b,m+2})$$

Use of flow conditions at the nodes immediately upstream and downstream of the nodes in question (i.e., (m-1) instead of m, and m+2 instead of m+1) is justified by the slow variation of flow conditions outside the quench front region.

3.6.4 Reinitialization of the Radial Temperature Distribution for Nodes Swept by the Quench Front

When a fuel node emerges completely from underneath the quench front length, i.e., with reference to Fig. 3-7, as soon as $Z_{U'} > m\Delta Z$, the radial temperature profile in this node is reinitialized by a forward extrapolation of the temperature fields in nodes m-1 and m-2, i.e.

$$T_{i,m} = 2T_{i,m-1} - T_{i,m-2} \qquad i = 1,2,\ldots,NR$$

where NR is the number of radial nodes.

This is necessary because when a large time step is used, the quench front region is moving in discrete steps. Note that the rate of heat release from axial node m is given by Eq. 3-23. Therefore if the quench front velocity U were such that the quench front region took an integer number of time steps to sweep node m, the reinitialization would not have been necessary, since to calculate $\bar{q}''_m$ a proper heat balance would have been performed. Since the time step is not defined according to the instantaneous quench front velocity U, there is a need to reinitialize the temperature profile of node m after the passage of the quench front.

Chapter 4

PREDICTION OF UC-BERKELEY REFLOODING DATA

Predictions of UC-B reflooding data [19] obtained using the UCFLOOD code will be presented and discussed in this chapter.

At the beginning of this work there were plans to use PWR-FLECHT reflooding data [2-5] for model verification, since at this time these were the only readily available, well documented data. Recently, however, UC-B reflooding data obtained with internal flow in a single tube became available, and were used for the first phase of model verification presented here.

There are clear advantages in using single-tube data instead of rod-bundle data for model verification. Indeed the rod bundle data are occasionally obscured by bundle and housing effects that are not germane to the basic heat transfer and two-phase flow phenomena occuring during reflooding. Conduction in the rod heaters, and through the gap between the heaters and the cladding, and rod-heat-storage effects further complicate the data analysis. The UC-B data had the additional advantage of including careful measurements of test section exit liquid and vapor flows.

The UC-B experimental setup consists of a 12-ft (3.66 m) long Inconel-600 bare tube, heated directly by a DC source. The tube thickness and inner diameter are 0.030 and 0.565 inches (0.76 and 14.35 mm), respectively. Thermocouples are attached on the outside wall at selected elevations to record the wall temperature histories. A differential pressure transducer is used to estimate the amount of liquid stored in the test section as a function of time. A separator is attached at the channel top, as well as various collection chambers and flow meters, to measure the effluent masses of vapor and liquid as a function of time. The test section is brought to the desired initial wall temperature by adjusting the power input with no flow going through the channel. Once the selected initial conditions are achieved, bottom flooding starts at constant velocity and subcooling, while the power input is kept constant. A detailed description of the UC-B experimental setup and data acquisition can be found in reference [19].

4.1 PREDICTIONS AND DISCUSSION

The UCFLOOD code, version-2 was used to obtain the predictions presented in this

chapter. The code is designated as version-1, 2 or 3 according to the method used to calculate the quench front velocity, as described in Section E.1.3. The input data used for each comparison run are presented in Appendix E.

For all the predictions presented in this section, the following values of the parameters and/or options were used:

- time step	DT = 1.0 s
- number of axial ("fuel") nodes in the wall	NA = 40
- number of radial nodes in the wall (lumped-parameter conduction solution)	NR = 2
- minimum number of coolant axial nodes per fuel node in control volume 1	XNCPFN = 4
- number of coolant axial nodes per fuel node in control volume 2	NCPFN1 = 2
- number of coolant axial nodes per fuel node in control volume 3	NCPFN = 1
- Weber number for the onset of and for total entrainment	WE = 10
- droplet initial Weber number	WED = 2
- distribution parameter for the inverted-annular flow regime	COB = 1.1
- vapor drift velocity in the inverted-annular regime	VGJB = 1.0 ft/s
- in the dispersed-flow region the droplets are assumed to acquire immediately the terminal velocity corresponding to their local diameter	ITVOPT = 0
- the quench front velocity is calculated using the method proposed by Yu et al. (UCFLOOD version 2)	
- system pressure	PSAT = 14.7 psia

Predictions of only three UC-B experimental runs were carried out; therefore these should be considered as only the first step in the process of model verification. However the very good general agreement with the data shows that the various assumptions made were reasonable. Table 4.1 shows the experimental conditions under which these runs were made.

In order to obtain the UCFLOOD predictions, some information had to be extracted from the experimental data themselves, namely the heat transfer coefficient in the inverted-annular and transition-flow regime, as discussed in Section 2.2.2.2. Since the empirical correlation of UC-B data obtained by Yu [20] was not available at the time when the comparison runs were made, preliminary simpler expressions were used as discussed below.

Table 4-1

UC-B RUN CONDITIONS

UC-B Run Number	114	120	188
Initial wall temperature, °F (°C)	1000 (538)	1000 (538)	1000 (538)
Reflooding rate, in/s (mm/s)	5.00 (127)	4.85 (123)	2.96 (75)
Inlet subcooling, °F (°C)	139 (59)	63 (17)	78 (134)
Power input, kW/ft (kW/m)	0.28 (0.92)	0.28 (0.92)	0.31 (1.02)
Ambient temperature, °F (°C)	70 (21)	70 (21)	70 (21)

For each run, the experimental and predicted values of the following quantities have been plotted, in Figs. 4-1 through 4-12:

a) Temperature histories at the 2, 6 and 10-ft elevations. These plots give integral information on how well the heat transfer coefficients as a function of time have been predicted at the various elevations.

b) Stored mass in the channel and integral collected exit liquid and vapor masses as a function of time. These plots provide information about the overall liquid and vapor mass balances. Regarding model development, the prediction of the wall temperature histories by itself is not very significative if the liquid and vapor mass balances do not agree reasonably well with the data.

c) Total carryover fraction and exit quality as a function of time. These plots yield information about the instantaneous mass balance.

d) Quench-front and swollen-liquid-level positions as a function of time. These plots show the extent of the regions of the channel above the quench front under the inverted-annular or transition-flow regime and the dispersed-flow regime. This information can be very useful for "tuning" the model.

4.1.1 Run Number 114

The UCFLOOD predictions for this run are shown in Figs. 4-1 to 4-4. The heat transfer coefficient in the inverted-annular and transition-flow region was extracted from the experimental data of this run and correlated very well by the following functional form

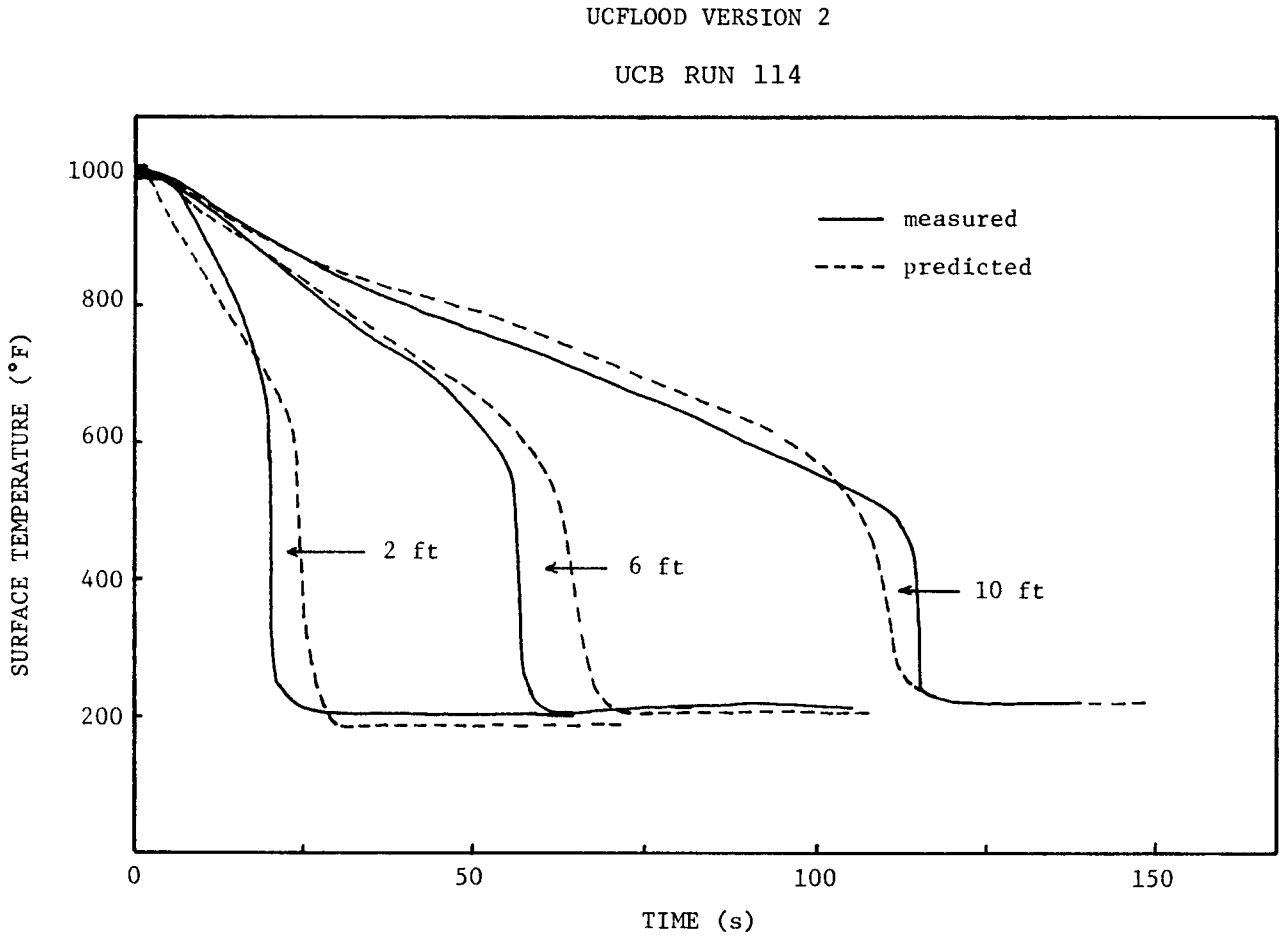

Figure 4-1. Temperature histories at the 2, 6 and 10 ft elevations -- run 114.

UCFLOOD VERSION 2

UCB RUN 114

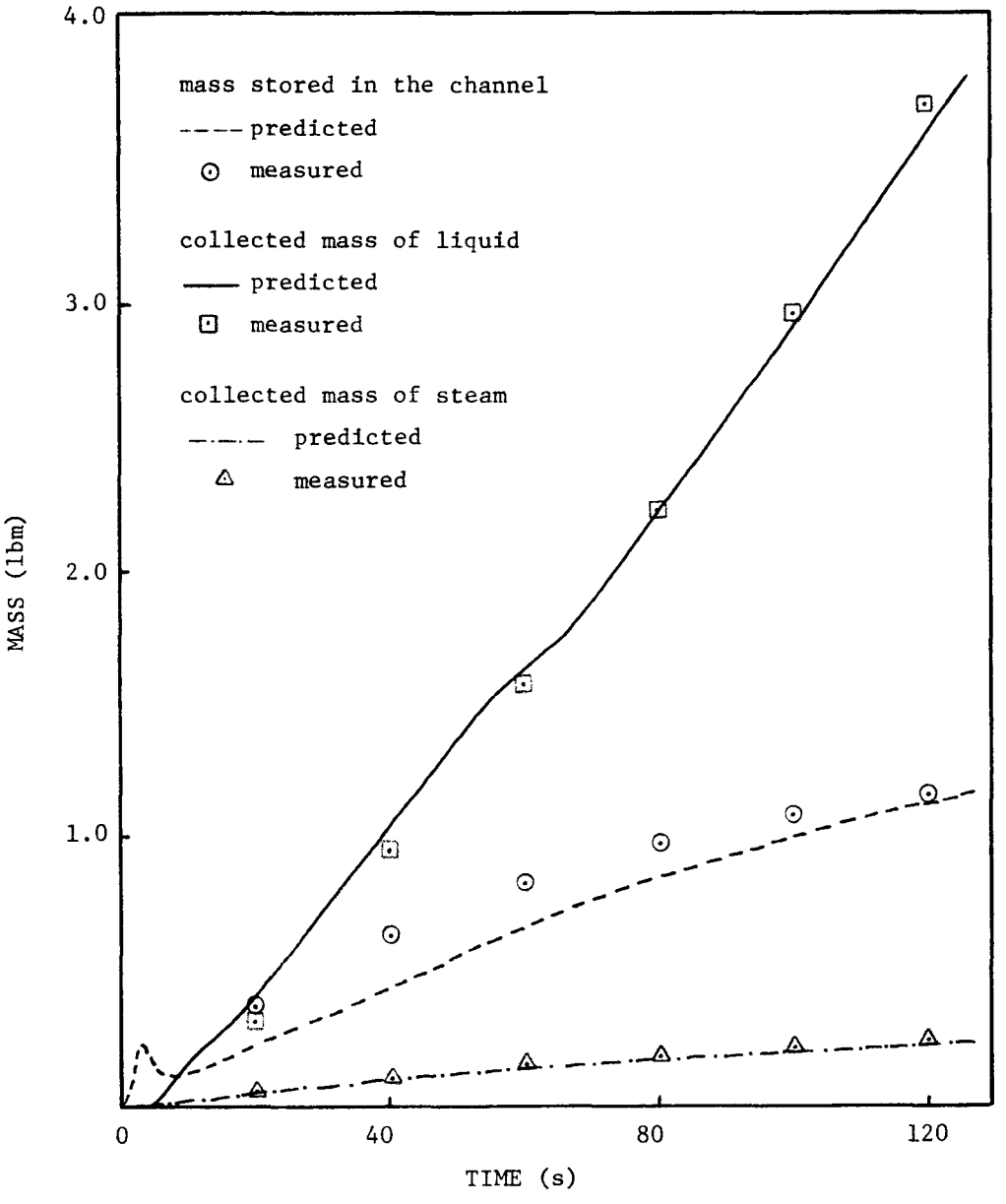

Figure 4-2. Mass stored in the channel and collected masses of liquid and steam -- run 114.

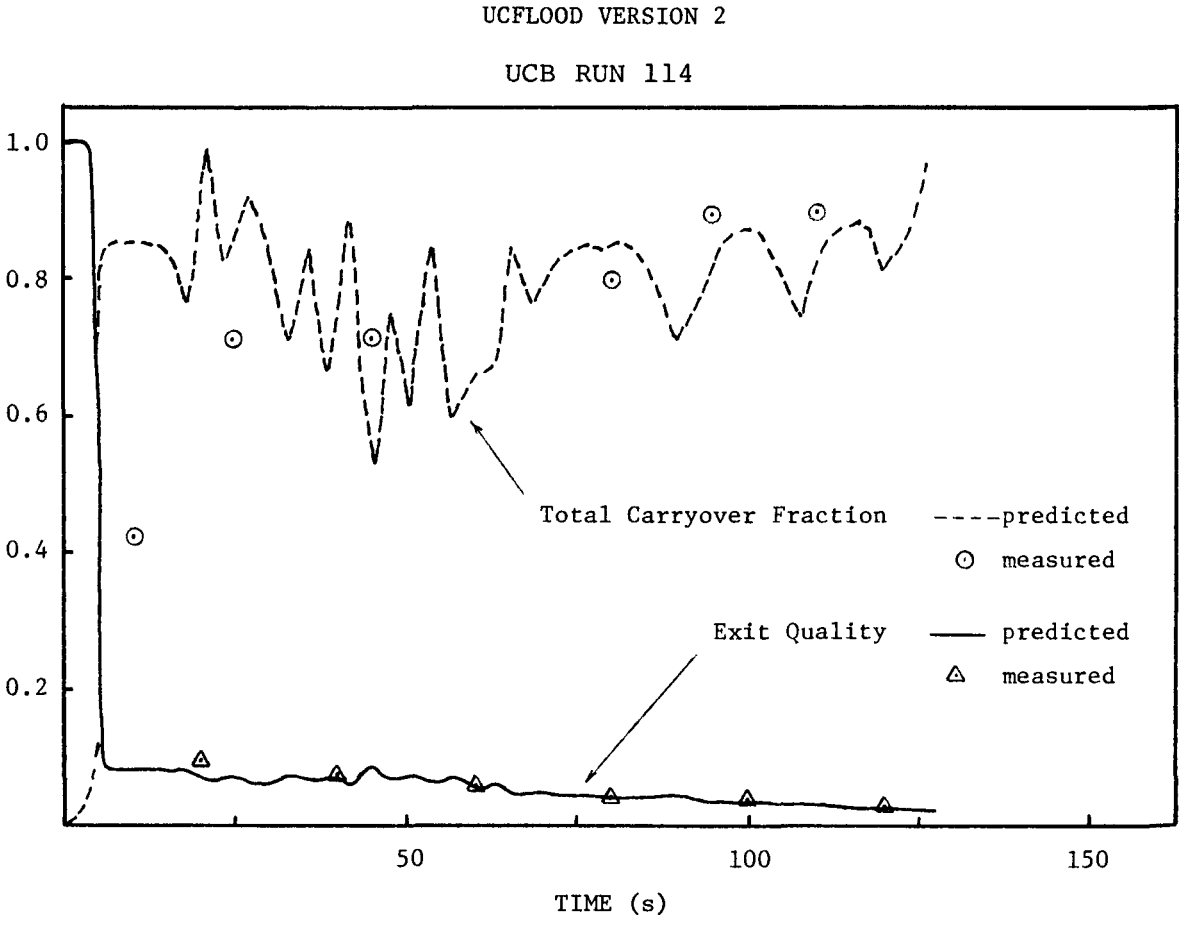

Figure 4-3. Exit quality and total carryover fraction -- run 114.

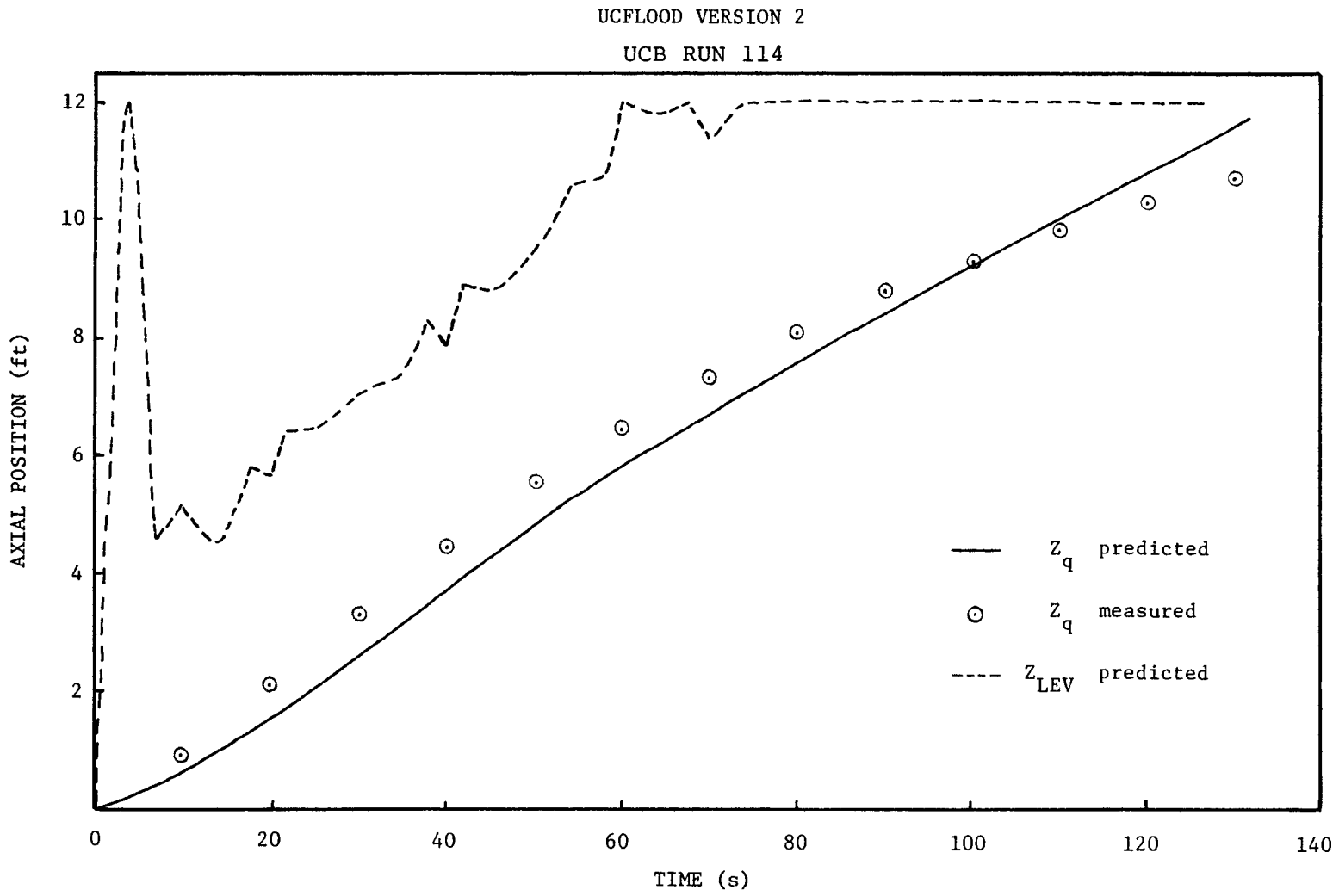

Figure 4-4. Quench front and swollen liquid level positions -- run 114.

$$h = \exp\left(2.974\ \Delta Z_q^{-0.174}\right) \quad (\text{Btu/hr ft}^2\text{°F}) \tag{4-1}$$

where ΔZ_q is the distance from the quench front in feet. The heat transfer coefficient is based on the coolant saturation temperature. Since the above correlation yields $h \to \infty$ as $\Delta Z \to 0$, it was necessary to define an upper bound for h, and the value h_{IAFB} obtained from Bromley's correlation, Eq. 2-30, was a proper choice. Therefore for $Z_q < z < Z_{LEV}$ the heat transfer coefficient is calculated from Eq. 4-1 as long as $h \leq h_{IAFB}$ and it is set equal to h_{IAFB} otherwise.

Figure 4-1 shows that the quench times of the 2- and 6-ft elevations are overpredicted while the quench time of the 10-ft elevation is slightly under predicted. With the exception of the 2-ft elevation, the general trend of the predicted temperature histories is in very good agreement with the data. Dispersed flow is predicted to exist in the channel up to about 80 seconds, time at which the swollen liquid level reaches the channel exit as shown in Fig. 4-4. Up to this time the length of the inverted-annular and transition-flow region is roughly 3 feet.

Figure 4-2 shows that the mass stored in the channel is somewhat underpredicted, especially at early times. This discrepancy may be explained by the fact that the pressure transducer measures the total pressure drop which includes gravity head, friction, and acceleration components. At intermediate and later times the gravity head is the major component; however, at early times, friction may represent an appreciable additional contribution to the total measured pressure drop.

The integral collected liquid mass is very slightly overpredicted at early times and under predicted at later times. Considering that liquid is stored in the channel mostly below the quench front this discrepancy is probably due to the fact that quench front velocity is slightly under predicted at early times and overpredicted at later times.

In Fig. 4-3 the calculated instantaneous total carryover fraction shows oscillations which are caused by oscillations of the swollen liquid level. This results from the large node size used in the "fuel" (3.6 in.) and the coolant (1.8 in.) in control volume 2. Decreasing these quantities will certainly alleviate this problem. Considering that the integral collected liquid and vapor carryover masses are in very good agreement with the experimental data, it can be concluded that the oscillations in the total carryover fraction are about the actual values.

Figure 4-4 shows that the Yu et al. method predicts the quench-front velocity very well.

4.1.2 Run Number 120

The UCFLOOD predictions for this run are shown in Figs. 4-5 to 4-8. The heat transfer coefficient in the inverted-annular and transition-flow region was obtained from the experimental data for this run and was correlated well by

$$h = \exp\left(3.068\,\Delta Z_q^{-0.176}\right) \tag{4-2}$$

Figure 4-5 shows that the quench times of the 2- and 6-ft elevations are in very good agreement with the data, while the 10-ft-elevation quench time is slightly under predicted. The temperature history of the 10-ft elevation shows that the temperature decay rate increases at about 50 seconds, while inspection of Fig. 4-8 shows this to be about the time at which the swollen liquid level arrives at that elevation. Therefore the change of slope of the temperature trace is explained by the transition between the heat transfer coefficient given by Eq. 4-2 and the one calculated by the dispersed-flow film-boiling model. The latter seems to be somewhat under predicting the value of the heat transfer coefficient.

In Fig. 4-6 the predicted and measured values of the stored mass in the channel show about the same behavior as for Run #114. Again the integral collected liquid carryover mass is somewhat overpredicted. Note, however, that the experimental overall mass balances also showed a slight mass defect.

The only major difference between this run and Run #114 is in the inlet subcooling of the coolant. This, however, produces substantial differences in the quench time of the various elevations. In this run, the 10-ft elevation quenches at about 65 seconds while in Run #114 it takes about twice as long to quench. The carryover fractions and the quench-front progression predictions are in excellent agreement with the experimental data again.

4.1.3 Run Number 188

The UCFLOOD predictions for this run are presented in Figs. 4-9 to 4-12. To obtain the heat transfer coefficient in the inverted-annular and transition-flow region, i.e., for $Z_q < z < Z_{LEV}$, the procedure to find h versus Z_q outlined earlier was used again; however, data from several 3 in/s (75 mm/s) runs were used now. The results were then correlated in the following form:

$$h = h_q \exp\left(-a\Delta Z_q\right) \left(\frac{\text{Btu}}{\text{ft}^2\text{hr°F}}\right) \tag{4-3}$$

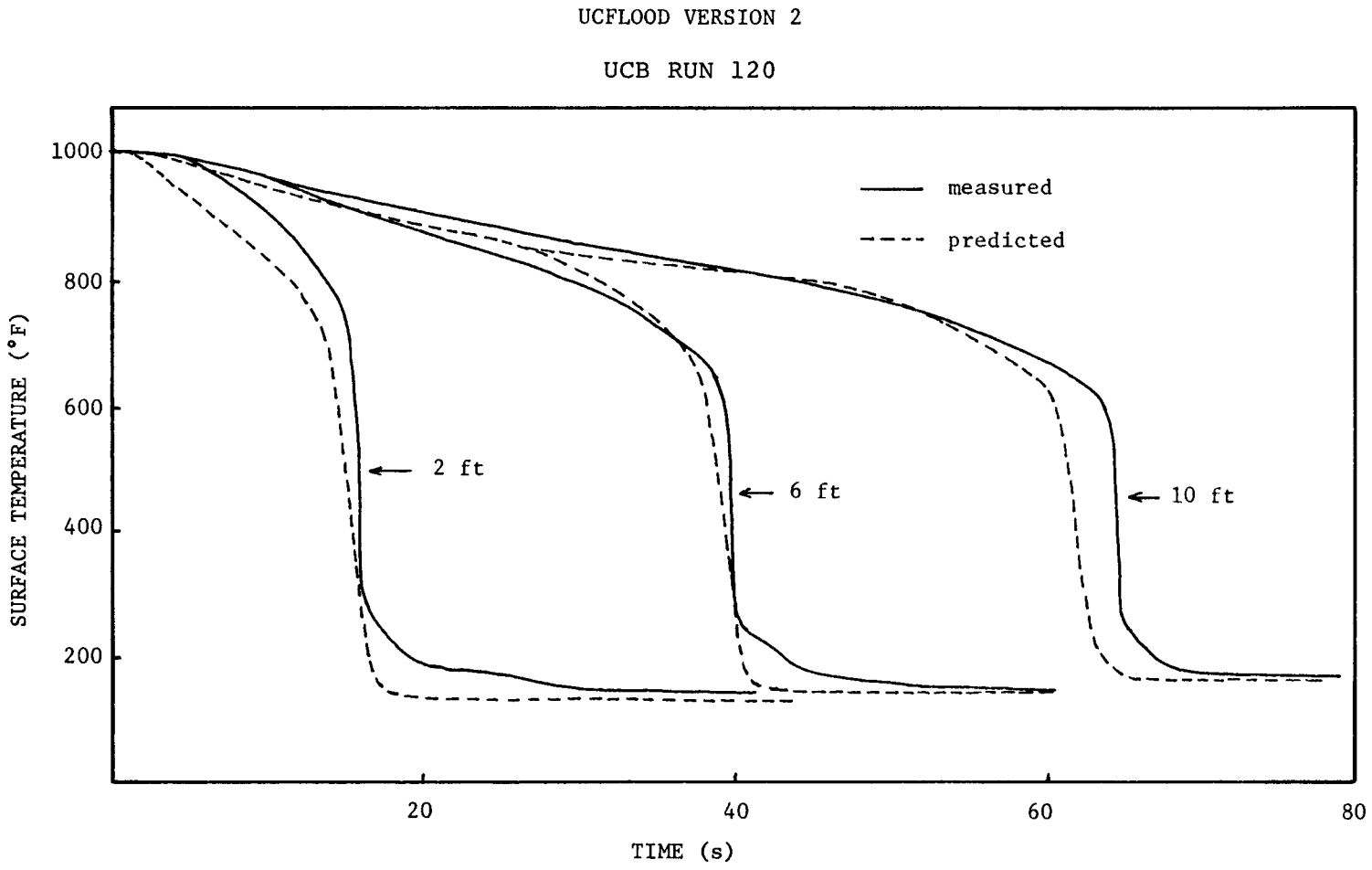

Figure 4-5. Temperature histories at the 2, 6, and 10 ft elevations -- run 120.

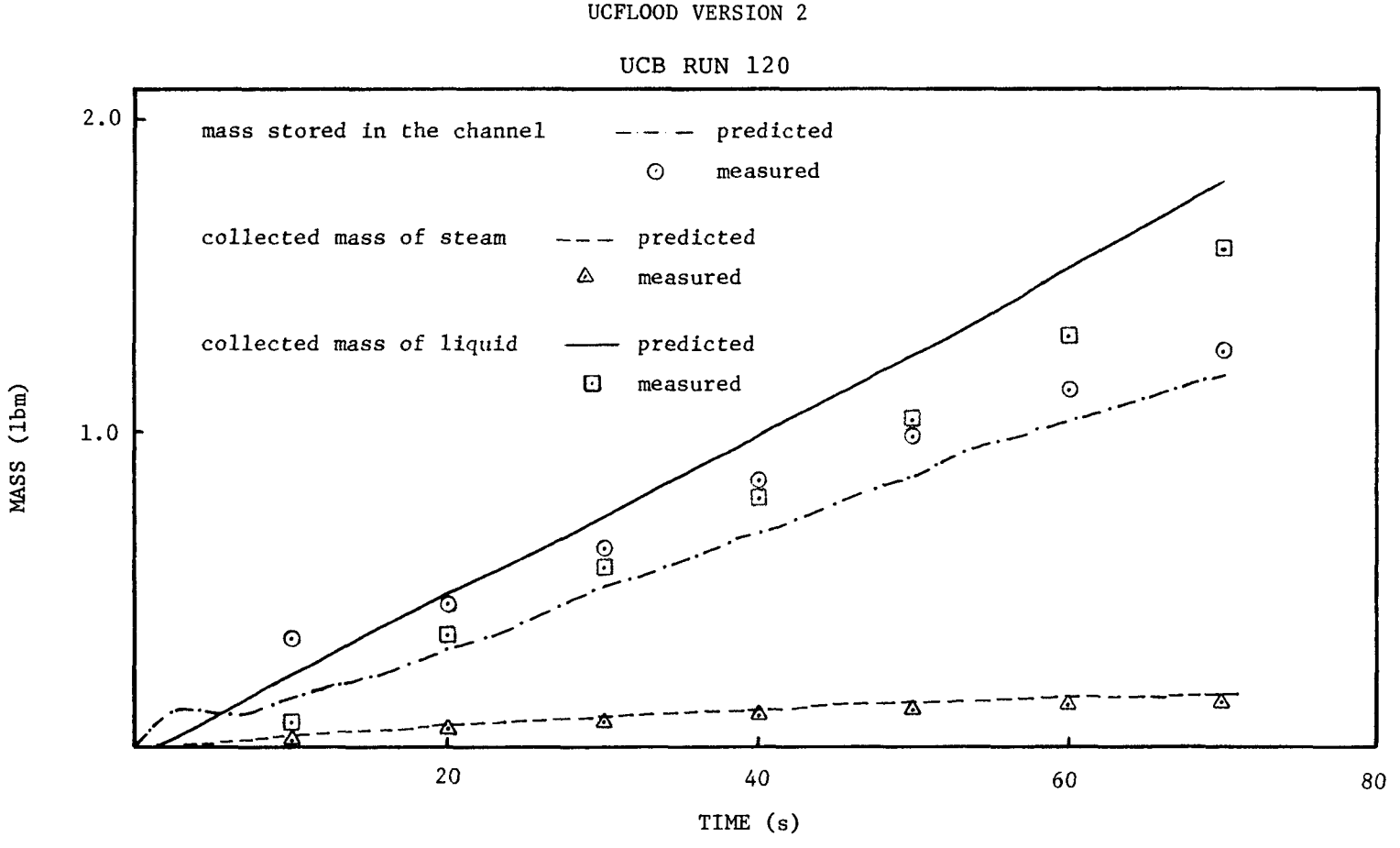

Figure 4-6. Mass stored in the channel and collected masses of liquid and steam -- run 120.

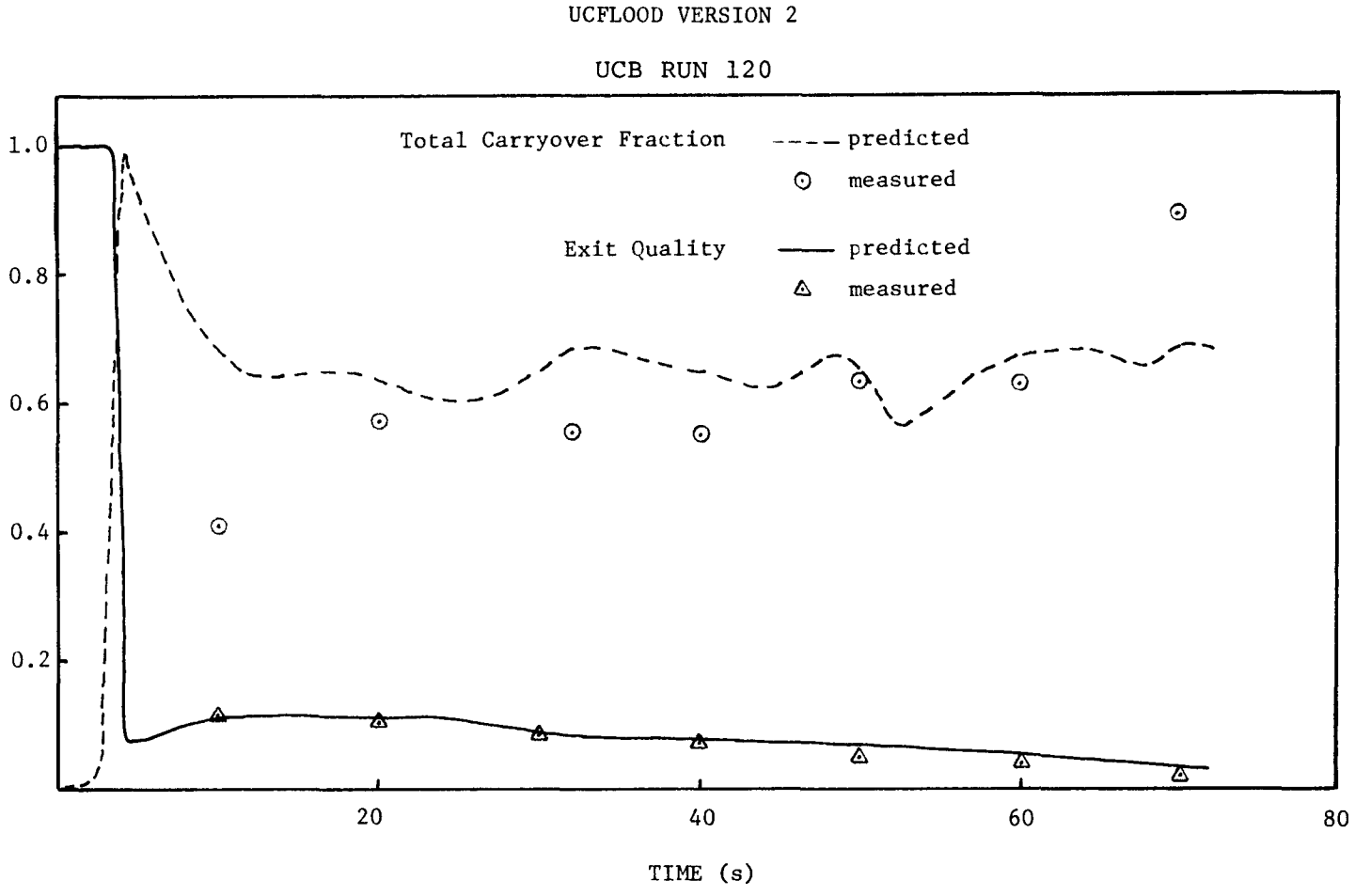

Figure 4-7. Exit Quality and total carryover fraction -- run 120.

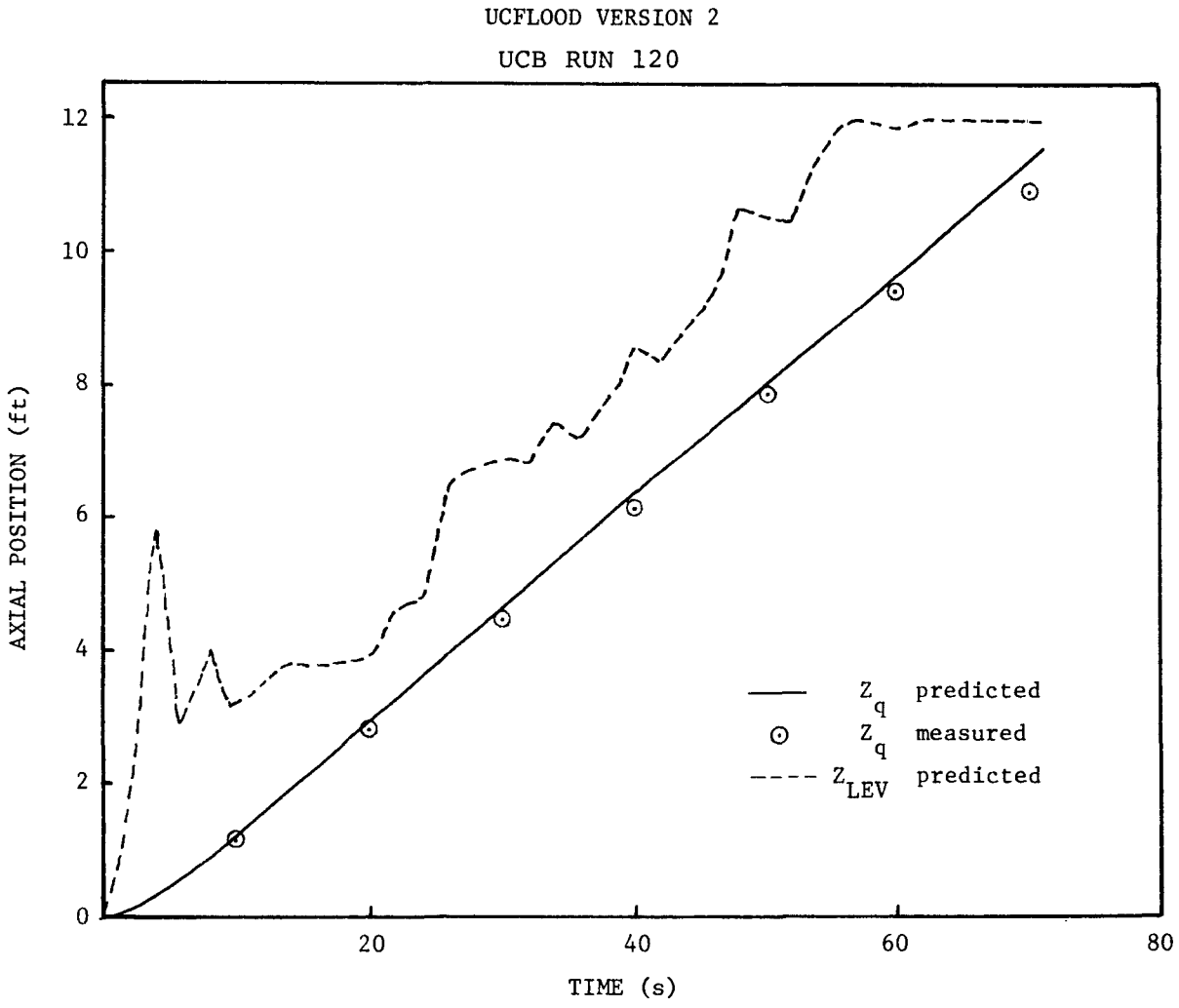

Figure 4-8. Quench front and swollen liquid level positions as a function of time -- run 120.

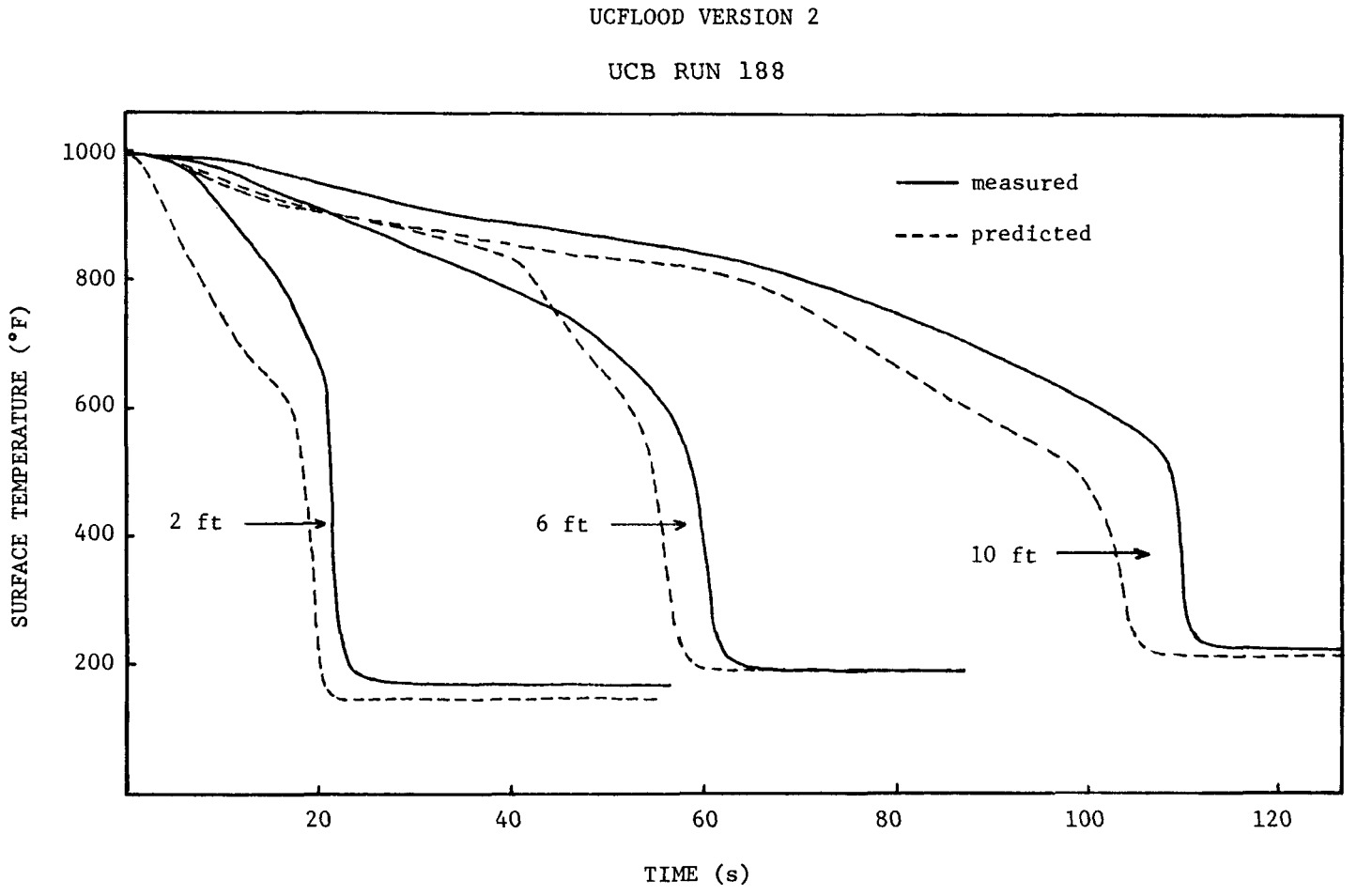

Figure 4-9. Temperature histories at the 2, 6 and 10 ft elevations -- run 188.

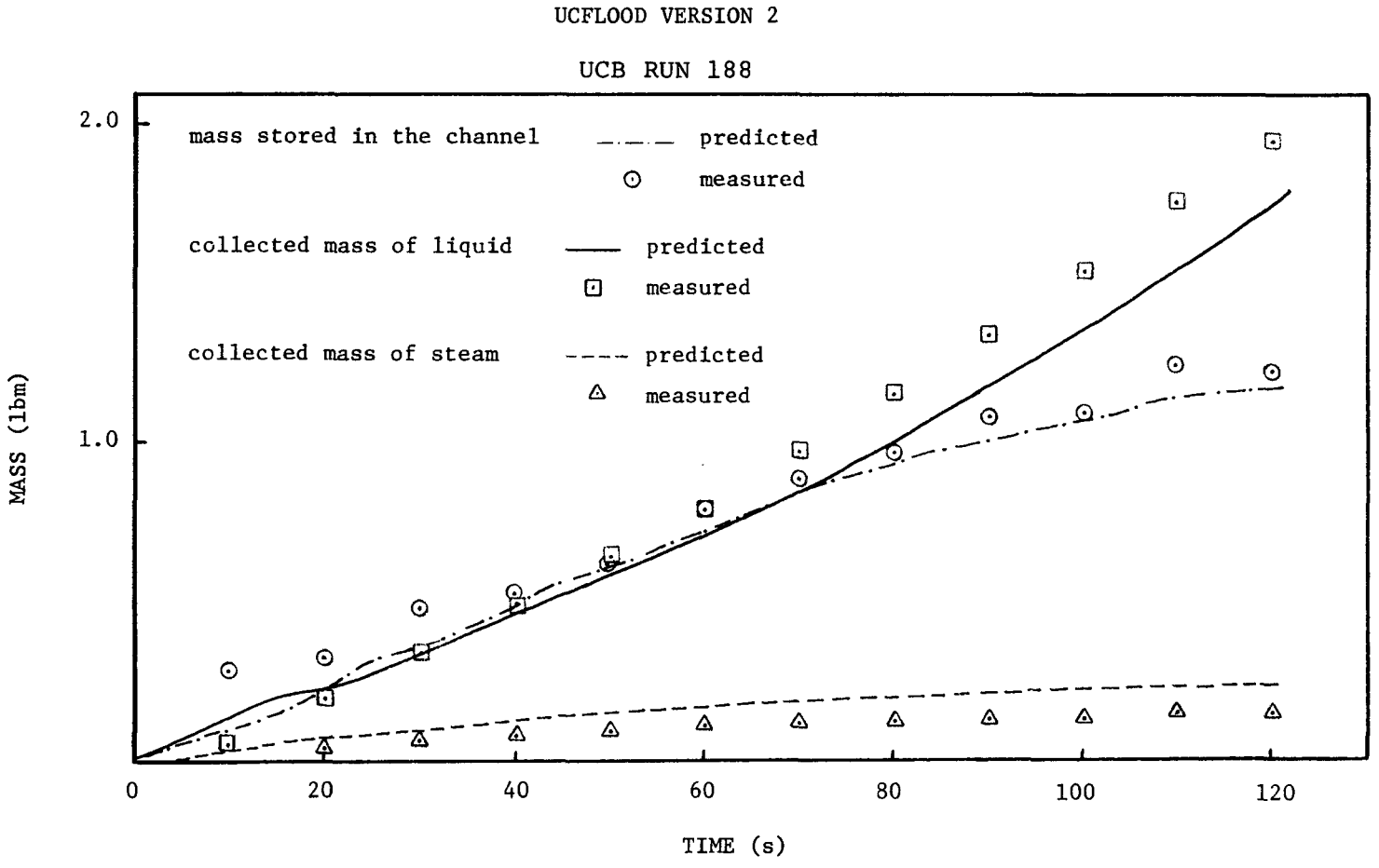

Figure 4-10. Mass stored in the channel and integrated masses of liquid and vapor at the channel exit.

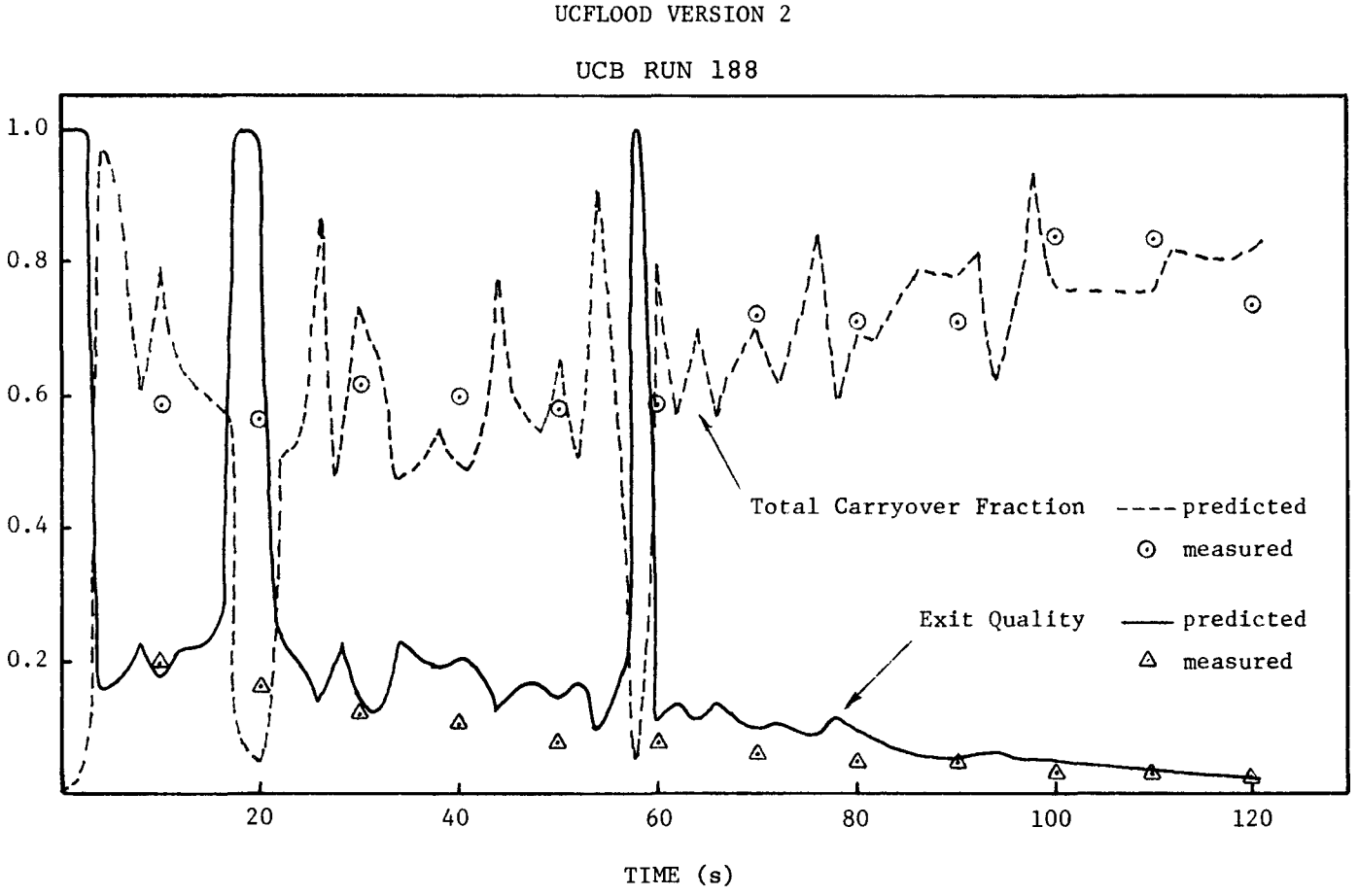

Figure 4-11. Exit quality and total carryover fraction -- run 183.

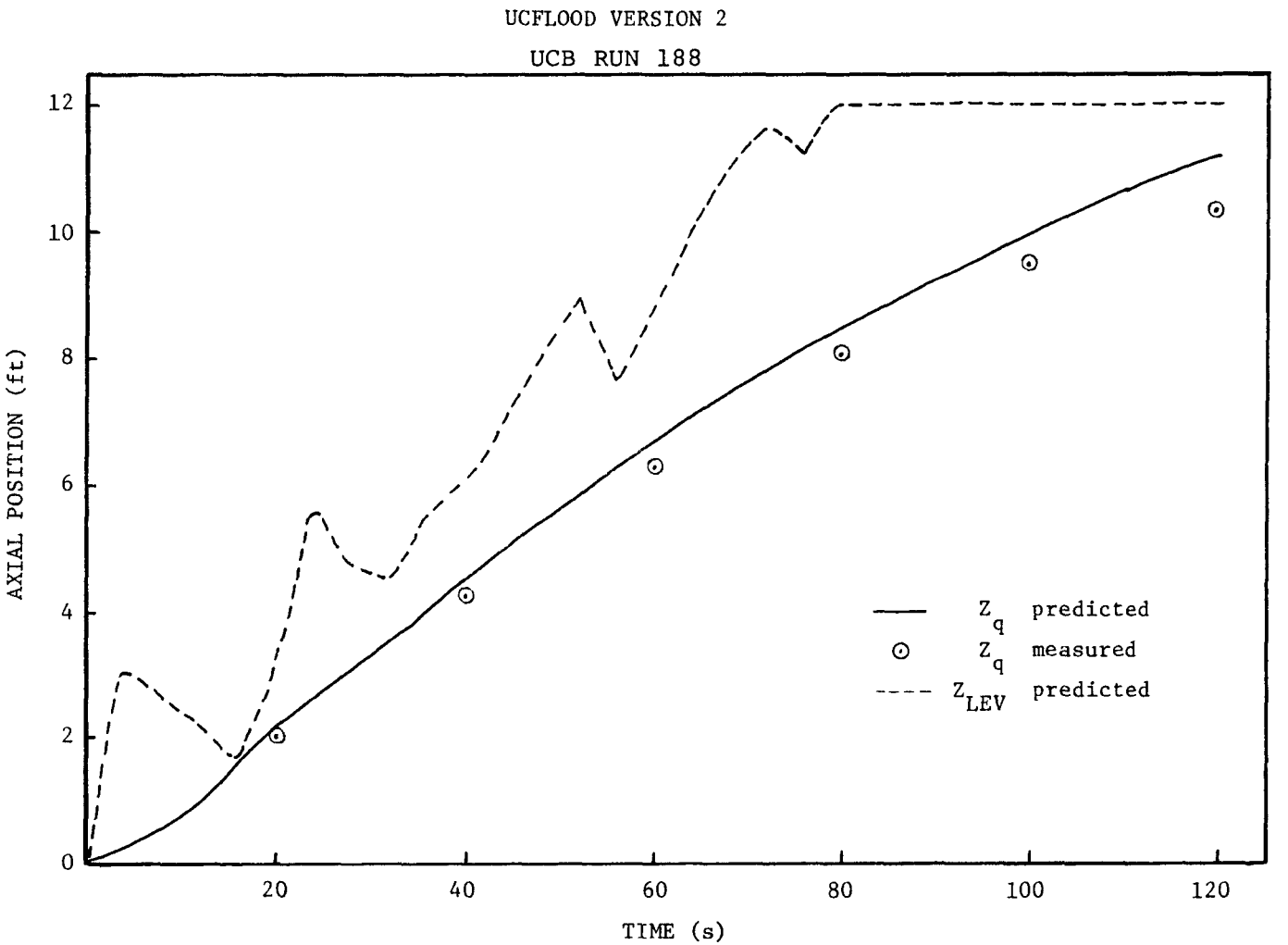

Figure 4-12. Quench front and swollen liquid level positions as a function of time -- run 188.

with h_q and a given in Table 4.2, where U_{in} and U_q are the inlet and quench-front velocities, respectively (in ft/hr). The quantity $\rho_f(U_{in} - U_q)$ is an estimate of the mass flux just ahead of the quench front, while x_q^+ is the calculated equilibrium quality just downstream of the quench front.

Table 4-2

CORRELATION OF THE HEAT TRANSFER COEFFICIENT
IN THE INVERTED-ANNULAR REGIME FOR 3 in/s RUNS

x_q^+	$\frac{h_q}{[\rho_f(U_{in}-U_q)]^{0.5}}$ Btu/ft°F/(lbm-hr)$^{0.5}$	x_q^+	$\frac{a}{(U_{in}-U_q)^{0.5}}$ (hr/ft)$^{0.5}$/ft
-0.0487	0.2707	-0.0270	46.8
-0.0380	0.2272	-0.0161	40.2
-0.0270	0.1963	0.0003	33.0
-0.0052	0.1490	0.0221	28.8
0.0112	0.1063	0.0440	26.4
0.0221	0.0828	0.0822	23.4
0.0331	0.0762	0.1423	21.0
0.0604	0.0772	0.2134	18.6
0.0986	0.0972		
0.1550	0.1117		
0.1423	0.1227		
0.1697	0.1317		
0.2134	0.1443		

This partial correlation of the data is superseded by the more general correlation of Section 2.2.2.2.

In Fig. 4-9, the predicted quench times of the 2, 6 and 10-ft elevations are slightly underestimated. The time at which the liquid level reached the 6 and 10-ft elevations can be easily identified by the change in the slope of the predicted

temperature history at each of these elevations. The dispersed-flow film-boiling model is predicting the heat transfer coefficient fairly well as evidenced by the temperature histories at early times, especially at the 10-ft elevation. The correlation discussed above is somewhat over predicting the heat transfer in the inverted-annular and transition-flow region as evidenced by the more rapid decrease of the predicted temperatures when compared to the data.

Figure 4-10 shows that the integral collected mass is somewhat under predicted and the vapor carryover is over predicted, while the mass storage in the channel is in very good agreement with the data.

The spikes of the predicted exit-quality curves shown in Fig. 4-11, are due to intermittent interruptions of liquid carryover during the calculations. These do not seem to influence adversely the overall results.

The major difference between this run and Run #120 is in the inlet velocity. This parameter has also a strong effect on the quench time of the various elevations. The quench front propagation predictions are again in excellent agreement with the experimental data.

4.2 SUMMARY OF RESULTS AND FINAL REMARKS

From these relatively limited comparisons with data the following conclusions may be drawn:

- the model predicts very well the quench time of the various elevations under all conditions considered. This is further evidenced by Fig. 3-6 covering a much broader range of experimental conditions.
- the mass balance for each phase is in very good agreement with the experimental data. The experimental data can probably be even better predicted if the number of axial nodes in the tube wall and in the flow channel is increased.
- the predictions of heat transfer in the dispersed-flow film-boiling region could be improved. Parametric studies using different values of the initial droplet Weber number and/or prescription of the values for the parameters γ and β (see Section 2.3.1) could possibly improve these predictions.

The results presented in this chapter show clearly that the overall model is capable of predicting the UC-B data (for intermediate and high reflooding velocities) provided that a correlation is supplied for the heat transfer coefficient in the inverted-annular and transition-flow region. Such a correlation is under development at Berkeley.

Chapter 5

CONCLUSION AND RECOMMENDATIONS FOR FUTURE WORK

5.1 CONCLUSION

A model to analyze the bottom reflooding of a single reactor core subchannel and its associated fuel rod or of a tubular test section with internal flow was developed. The computer code UCFLOOD was written to solve the finite difference approximations of the various equations.

A limited number of model verification runs, discussed in Chapter 4, using the UC-B single-tube data, has shown that the analytical model represents the reality fairly well. A systematic and comprehensive model verification and adjustment using various sources of data, including PWR-FLECHT data remains to be done. It is felt that the code parameters should be further adjusted using single channel tube data before attempting to analyze more complex rod bundle data. In fact it is much easier to detect model deficiencies with single-tube data which are not obscured by bundle and housing effects.

Among the various physical phenomena considered, two have proven to be especially difficult to model, namely the heat transfer coefficient distribution in the quench front region and in the inverted-annular and transition-flow region. The two alternatives available in UCFLOOD for calculating the quench front velocity are the Yu et al. correlation and the solution of the two-dimensional heat conduction equation in the fuel with a prescribed heat transfer coefficient distribution (boiling curve).

The first alternative, which was used to obtain the predictions of Chapter 4, yielded in general excellent agreement with the data. However, it should be kept in mind that it is based on a correlation, valid in principle only for tubular test sections at atmospheric pressure. Moreover, the assumed stepwise variation of the heat transfer coefficient is physically unrealistic.

The second method is much more general and physically sound, but requires knowledge of the heat transfer coefficient distribution in the quench-front region. This is poorly known at the present, as evidenced by the poor prediction of experimental data described in Section 3.5. It is felt that this approach should be, however,

pursued since success with such a procedure would shed light on the quench phenomenon.

The use of the modified Bromley correlation (Eq. 2-30) to calculate the heat transfer coefficient in the inverted-annular and transition-flow region has proven to be unsatisfactory. Photographic studies [26] have shown clearly the existence of a transition-flow region between the inverted-annular and the dispersed-flow film-boiling regions. Also the heat transfer coefficient inferred from UC-B data shows a more pronounced variation with distance from the quench front than the original or the modified Bromely correlation are able to predict. The procedure for obtaining the heat transfer coefficient in this region, described in Section 2.2.2.2 is partly unsatisfactory because of its empirical nature.

The model for liquid entrainment and carryover, discussed in Section 2.2.3 seems to be reasonable, considering the good agreement between the measured and predicted liquid carryover fractions. A revision of the initial droplet size and/or of the profile fit for the droplet evaporation rate could produce improved predictions of heat transfer in the dispersed flow region.

The criterion developed in Section 2.2.3 for the onset of liquid entrainment and carryover is based on the instability of the liquid core in the inverted-annular flow regime. Considering that for low reflooding rates the flow pattern likely to exist is that of Case A (see Fig. 1-3A), the criterion for liquid entrainment of Section 2.2.3 is in principle not applicable in this case. Therefore the possibility of introducing an alternative criterion for liquid entrainment for Case-A conditions needs to be investigated.

The prediction of the flow conditions and heat transfer below the quench front, namely in the single-phase liquid and nucleate-boiling regions, does not seem to need any refinement as evidenced by the good agreement of the measured and predicted wall temperatures below the quench front.

A thorough error analysis and estimation of error bounds for the various finite-difference approximations used could not be unfortunately performed within the time available. The selection of the various spatial mesh sizes and time steps was made based on numerical experiments rather than by a rigorous mathematical analysis.

Finally, it should be pointed out that the UCFLOOD code should not be regarded as a production code but rather as a useful working tool that could possibly be further improved in spite of the fact that it has already produced good results. The code seems to have good potential, but a comprehensive verification should be

conducted before a high degree of reliability is achieved. The modular nature of UCFLOOD, the various models and options already built in, and its relatively low running cost should make this task relatively simple.

5.2 RECOMMENDATIONS FOR FUTURE WORK

Considering the limitations and shortcomings of the present work, recommendations for future work follow naturally. In order of importance, the areas needing future development are:

1) Development of a general method for predicting heat transfer and hydrodynamic parameters in the inverted-annular and transition-flow regions. In order to develop such a model in terms of local flow conditions, modeling of the hydrodynamics of the inverted-annular regime and of the degree of thermal nonequilibrium between the phases should be included.

2) Development of a quench front velocity correlation for actual reactor fuel rods or rod simulators. A suggestion on how such a correlation could be developed, based on a boiling-curve approach, was made in Section 3.5.

3) Refinement of the entrainment correlation presented in Section 2.2.3 and development of a similar correlation for the case of low reflooding velocities is necessary.

4) The dispersed-flow film-boiling model of Section 2.3 has performed adequately during the limited number of predictions of UC-B data. There is a general lack of heat transfer data in this region under reflooding conditions. It is felt that this model should be further verified and adjusted using the available experimental data from Berkeley and elsewhere.

5) A comprehensive model verification using experimental data from various sources, together with a parametric sensitivity analysis, and wherever feasible, an error analysis are necessary.

6) Finally, expansion of the model to include bundle effects and to make it able to tacke fast inlet flow oscillations is the ultimate goal. It is felt, however, that such an expansion should not be attempted before the limitations described in the previous items are satisfactorily removed.

6. REFERENCES

1. G. Yadigaroglu, K. P. Yu, L. A. Arrieta, R. Greif, "Heat Transfer during the Reflooding Phase of the LOCA - State of the Art", EPRI Report 248-1 (September 1975); also: G. Yadigaroglu, "The Reflooding Phase of the LOCA in PWRs. Part I: Core Heat Transfer and Fluid Flow", Nuclear Safety, 19, 20-36 (1978).

2. F. F. Cadek, et al., "PWR FLECHT (Full Length Emergency Cooling Heat Transfer) - Final Report", WCAP-7665 (April 1971).

3. F. F. Cadek, et al., "PWR FLECHT Final Report Supplement", WCAP-7931 (October 1972).

4. J. A. Blaisdell, L. E. Hochreiter and J. P. Waring, "PWR FLECHT-SET Phase A Report", WCAP-8238 (December 1973).

5. J. P. Waring and L. E. Hochreiter, "PWR FLECHT-SET Phase B1 Evaluation Report", WCAP-8483 (August 1973).

6. P. Saha and N. Zuber, "Point of Net Vapor Generation and Vapor Void Fraction in Subcooled Boiling", Heat Transfer 1974, Proceedings of 5th International Heat Transfer Conference, Tokyo, Vol. IV, 175-179, Paper B 4.7 (1974).

7. P. Saha, General Electric, San Jose, CA, personal communication.

8. J. G. Collier, Convective Boiling and Condensation, McGraw-Hill (1972).

9. A. E. Bergles and W. M. Rohsenow, "The Determination of Forced-Convection Surface-Boiling Heat Transfer", J. Heat Transfer, Trans. ASME, 86, 365 (1964).

10. N. Zuber and J. A. Findlay, "Average Volumetric Concentration in Two-Phase Flow Systems", J. of Heat Transfer, Trans. ASME, 87, 453-468 (1965).

11. N. Zuber, F. W. Staub, and G. Bijward, "Vapor Void Fraction in Subcooled Boiling and Saturated Boiling Systems", Proceedings of the 3rd International Heat Transfer Conference, Chicago, Ill., Vol. 5, p. 24 (1966).

12. S. Levy, "Forced Convection Subcooled Boiling-Prediction of Vapor Volumetric Fraction", Int. J. Heat and Mass Transfer, 10, 951-965 (1967).

13. G. E. Dix, "Vapor Void Fraction for Forced Convection with Subcooled Boiling at Low Flow Rates", Ph.D. Thesis, University of California, Berkeley (1971).

14. M. Ishii, T. C. Chawla, and N. Zuber, "Constitutive Equation for Vapor Drift Velocity in Two-Phase Annular Flow", AIChE Journal, 22, 283-289 (1976).

15. J. C. Chen, "A Correlation for Boiling Heat Transfer to Saturated Fluids in Convective Flow", ASME Paper 63-HT-34 (1963).

16. L. A. Bromley, "Heat Transfer in Stable Film Boiling", Chem. Eng. Progr., 46, 221-227 (1950).

17. N. A. Bailey, "Film Boiling in Submerged Vertical Cylinders", AEEN-M-1051 (1971).

18. J. G. M. Andersen, "Low-Flow Film Boiling Heat Transfer on Vertical Surfaces, Part I: Theoretical Model", and J. E. Leonard, K. H. Sun, and G. E. Dix, "Part II: Empirical Formulations and Applications to BWR-LOCA Analysis", AIChE papers AIChE-53 and 54 (1976).

19. R. Seban et al., "UC-B Reflood Program: Experimental Data Report", EPRI Report NP-743 (April 1978).

20. K. P. Yu, Personal communication (November 1977).

21. E. Elias and G. Yadigaroglu, "Rewetting and Liquid Entrainment during Reflooding -- State of the Art", EPRI Report NP-435 (May 1977), also: "The Reflooding Phase of the LOCA in PWRs, Part II: Rewetting and Liquid Entrainment", Nuclear Safety, 19, 160-175 (1978).

22. G. B. Wallis, One Dimensional Two-Phase Flow, McGraw-Hill, New York (1969).

23. G. Collier et al., "Calculational Model for Core Reflooding after a Loss-of-Coolant Accident (WREFLOOD Code)", WCAP-8171 (June 1974).

24. D. N. Plummer, "Post Critical Heat Transfer to Flowing Liquid in a Vertical Tube", Sc.D. Thesis, Department of Mechanical Engineering, MIT (May 1974).

25. R. Jensen, "Inception of Liquid Entrainment during Emergency Cooling of Pressurized Water Reactors", Ph.D. Thesis, Utah State University, Mechanical Engineering (1972).

26. E. Elias, Personal communication (November 1977).

27. W. R. Lane, "Shatter of Drops in Streams of Air", Ind. Eng. Chem., 43, 1312-1317 (1951).

28. J. O. Hinze, "Critical Speeds and Sizes of Liquid Globules", Appl. Sci. Res., A.1., No. 4, 273-288 (1949).

29. T. A. Smith, "Heat Transfer and Carryover of Low Pressure Water in a Heated Vertical Tube", M. Sc. Thesis, Massachusetts Institute of Technology (1976); NUREG-0105 (August 1976).

30. D. C. Groeneveld, "Post-Dryout Heat Transfer of Reactor Operating Conditions", Proceedings of the Topical Meeting on Water Reactor Safety, CONF 730304, p. 321, Salt Lake City, March 26-28, 1973.

31. D. C. Groeneveld, "Post-Dryout Heat Transfer: Physical Mechanisms and Survey of Prediction Methods", Nucl. Eng. Des., 32, 283-294 (1975).

32. E. E. Polomik, "Transition Boiling Heat Transfer Program", Final Summary Report on Program for Feb. 1963 - October 1967, GEAP-5563 (1967).

33. D. C. Groeneveld, "The Thermal Behavior of a Heated Surface at and Beyond Dryout", AECL-4309 (1972).

34. A. W. Bennett, G. F. Hewitt, H. A. Kearsey, and R. K. F. Keeys, "Heat Transfer to Steam-Water Mixtures in Uniformly Heated Tubes in which the Critical Heat Flux has been Exceeded", AERE-R-5373 (1967).

35. M. Cumo, G. Ferrari, and G. E. Farello, "A Photographic Study of Two-Phase Highly Dispersed Flows", European Two-Phase Flow Group Meeting, Milan, June 1970.

36. R. Deruaz and B. Petitpain, "Modeling of Heat Transfer by Radiation during the Reflooding Phase of a LWR", Specialists' Meeting on the Behavior of Water Reactor Fuel Elements under Accident Conditions, Spatind, Mord-Torpa (Norway), September 13-16, 1976.

37. R. T. Lahey, Jr. and E. J. Moody, The Thermal-Hydraulics of a Boiling Water Nuclear Reactor, American Nuclear Society (1977).

38. J. B. Heineman, "An Experimental Investigation of Heat Transfer to Superheated Steam in Round and Rectangular Channels", ANL 6213 (1969).

39. D. C. Groeneveld and G. G. J. Delorme, "Prediction of Thermal Non-Equilibrium in the Post-Dryout Regime", Nucl. Eng. Des., 36, 17-26 (1976).

40. R. D. Ingebo, "Drag Coefficients for Droplets and Solid Spheres in Clouds Accelerating in Air Streams", NACO-Tech. Note 3762.

41. K. H. Sun, J. M. Gonzalez, and C. L. Tien, "Calculations of Combined Radiation and Convection Heat Transfer in Rod Bundles under Emergency Cooling Conditions", J. Heat Transfer, Trans. ASME, 98, 414-420 (1976).

42. W. L. Kirchner, "Reflood Heat Transfer in Light Water Reactors", Ph.D. Thesis, Massachusetts Institute of Technology (January 1976); NUREG-0106 (August 1976).

43. R. Martini and A. Premoli, "A Simple Model for Predicting ECC Transients in Bottom-Flooding Conditions", Proceedings of the CREST Specialists' Meeting on Emergency Core Cooling for Light Water Reactors, Garching/Muenchen, October 18-20, 1972, MRR 115, Vol. 2.

44. D. Butterworth and R. G. Owen, "The Quenching of Hot Surfaces by Top and Bottom Flooding - A Review", European Two-Phase Flow Group Meeting (AERE-R7992), Haifa, June 1975.

45. M. E. Sawan and M. W. Carbon, "A Review of Spray-Cooling and Bottom-Reflooding Work for LWR Cores", Nucl. Eng. Des., 32, 191 (1975).

46. E. Elias and G. Yadigaroglu, "A General One-Dimensional Model for Conduction-Controlled Rewetting of a Surface", Nucl. Eng. Des., 42, 185-194 (1977).

47. E. Elias, L. Arrieta, and G. Yadigaroglu, "An Improved Model for the Rewetting of a Hot Fuel Rod", Trans. ANS, 24, 299 (1976).

48. D. Andréoni, "Echanges Thermiques lors du Renoyage d'un Coeur de Réacteur à Eau", Thèse de Docteur-Ingénieur, L'Université Scientifique et Médicale de Grenoble et l'Institut National Polytechnique de Grenoble (1975).

49. N. Zuber et al., "The Hydrodynamic Crisis in Pool Boiling of Saturated and Subcooled Liquids", International Developments in Heat Transfer, International Heat Transfer Conference, Boulder, Colorado, Part II, Paper No. 27, pp. 230-236 (1961).

50. D. C. Groeneveld and K. K. Fung, "Forced Convective Transition Boiling - Review of Literature and Comparison of Prediction Methods", AECL-5543 (June 1976).

51. K. Ramu and J. Weisman, "Transition Boiling Heat Transfer to Water in a Vertical Annulus", National Heat Transfer Conference, San Francisco (1975).

52. K. Ramu and J. Weisman, "A Method for the Correlation of Transition Boiling Heat Transfer Data", Heat Transfer 1974, Proceedings of the 5th International Heat Transfer Conference, Tokyo, Vol. IV, 160-164, Paper B4.4 (1974).

53. L. S. Tong, Two Phase Flow and Boiling Heat Transfer, John Wiley & Sons (1965).

54. M. E. Coney, "Calculations of the Rewetting of Hot Surfaces", Nucl. Eng. Des., 31, 246-259 (1974).

55. S. W. Yu, P. R. Farmer and M. E. Coney, "Methods and Correlations for the Prediction of Quenching Rates of Hot Surfaces", Int. J. Multiphase Flow, 3, 415-433 (1977).

56. H. C. Yeh, "An Analysis of Rewetting of a Nuclear Fuel Rod in Water Reactor Emergency Core Cooling", Nucl. Eng. Des., 34, 317-322 (1975).

57. K. H. Sun, G. E. Dix, and C. L. Tien, "Effect of Precursory Cooling on Falling-Film Rewetting", ASME paper 74-WA/HT-52 (1974).

58. K. H. Sun and R. B. Duffey, "A Generalized Model for Predicting Mass Effluence during Reflooding", Trans. ANS, 27, 604 (1977).

59. S. S. Dua and C. L. Tien, "A Generalized Two-Parameter Relation for Conduction-Controlled Rewetting of a Hot Vertical Surface", Int. J. Heat Mass Transfer, 20, 174-176 (1977).

Appendix A

AN ASSESSMENT OF THE VALIDITY OF THE QUASI-STEADY-STATE ASSUMPTION FOR CALCULATING LOCAL HYDRODYNAMIC CONDITIONS

Recognition of reflooding as a very slow process, opens the possibility of using a quasi-steady-state assumption to evaluate local flow conditions. This assumption implies that the flow hydrodynamics accommodate instantaneously to new boundary conditions.

A straightforward way to assess the validity of this assumption is to solve sample problems with and without this assumption, and compare the two solutions.

The sample problem to be solved is: Given a 12 ft. long channel, prescribed heat flux and inlet flow rate, calculate the phase volumetric fluxes (j_f,j_g), the quality (x) and the void fraction (α) along the channel as a function of time. Assume, for the sake of simplicity, that the inlet flow is saturated and a negligible pressure drop along the heated length (i.e., no property variations).

This problem was first solved analytically by Zuber and Staub [A.1] by prescribing an oscillatory flow and heat flux variation. The present analysis extends these solutions for the general case of arbitrary flow and heat flux variations.

Starting with the conservation equations, Zuber and Staub derived the void propagation equation and solved it by the method of characteristics. Their solution is quite general and can be easily extended to the case of any arbitrary heat flux and flow rate variations by using numerical methods. However, the numerical computation cost becomes undesirably high. The quasi-steady-state assumption permits to reduce computer costs; the purpose of this Appendix is to assess the validity of the quasi-steady-state assumption under reflooding conditions.

A.1 GOVERNING EQUATIONS

Continuity of vapor

$$\frac{\partial \alpha}{\partial t} + \frac{\partial j_g}{\partial Z} = \Gamma_g \, v_g \qquad \text{(A-1)}$$

Continuity of liquid

$$\frac{\partial(1-\alpha)}{\partial t} + \frac{\partial j_f}{\partial Z} = \Gamma_f \, v_f \tag{A-2}$$

Mixture Continuity

$$\Gamma_f + \Gamma_g = 0 \tag{A-3}$$

Drift Flux Model

$$j_g = \alpha j + \alpha \, v_{gj} \quad . \tag{A-4}$$

By definition

$$j = j_f + j_g \tag{A-5}$$

$$x = \frac{\rho_g j_g}{\rho_g j_g + \rho_f j_f} = \frac{G_g}{G_g + G_f} = \frac{G_g}{G} \tag{A-6}$$

Inserting Eq. A-4 into Eq. A-1

$$\frac{\partial \alpha}{\partial t} + \frac{\partial}{\partial Z} (\alpha j + \alpha v_{gj}) = \Gamma_g / \rho_g \tag{A-7}$$

Since the volumetric flux and void fraction vary radially across the cross section, Zuber and Staub integrated the above equation; in terms of cross-sectional-average quantities

$$\frac{\partial \langle\alpha\rangle}{\partial t} + \frac{\partial}{\partial Z} (\langle\alpha j\rangle + \langle\alpha v_{gj}\rangle) = \langle\Gamma_g\rangle / \rho_g \tag{A-8}$$

Using the definition of V_{gj} and C_o, Eqs. 2-21 and 2-22, Eq. A-8 becomes

$$\frac{\partial \langle\alpha\rangle}{\partial t} + \frac{\partial}{\partial Z} [C_o \langle\alpha\rangle\langle j\rangle + \langle\alpha\rangle V_{gj}] = \langle\Gamma_g\rangle v_g \tag{A-9}$$

The average forms of Eqs. A-1 and A-2 are added and using Eq. A-3 to eliminate Γ_f results in

$$\frac{\partial \langle j \rangle}{\partial Z} = \frac{\partial \langle j_g \rangle}{\partial Z} + \frac{\partial \langle j_f \rangle}{\partial Z} = \Gamma_g \, v_{fg} \tag{A-10}$$

Integrating Eq. A-10

$$\langle j \rangle = V_{in}(t) + v_{fg} \int_0^Z \langle \Gamma_g \rangle dZ \tag{A-11}$$

carrying out the differentiation in Eq. A-9, and using Eqs. A-10 and A-11 to eliminate $\langle j \rangle$ and $\frac{\partial \langle j \rangle}{\partial Z}$,

$$\frac{\partial \langle \alpha \rangle}{\partial t} + C_k \frac{\partial \langle \alpha \rangle}{\partial Z} = (v_g - C_o v_{fg} \langle \alpha \rangle) \langle \Gamma_g \rangle \tag{A-12}$$

where

$$C_k \equiv C_o V_{in} + V_{gj} + \langle \alpha \rangle \frac{\partial V_{gj}}{\partial \langle \alpha \rangle} + C_o v_{fg} \int_0^Z \langle \Gamma_g \rangle dz \tag{A-13}$$

Equation A-12 is a first-order wave equation with the wave velocity given by C_k. Previous work by Zuber and Findlay [A.2] has shown that an average value $C_o = 1.13$ can be assumed over a wide range of void fractions. Taking this value for C_o and further assuming that $\frac{\partial V_{gj}}{\partial \langle \alpha \rangle} = 0$, Zuber and Staub solved Eq. A-12 for oscillatory power and flow variations.

For flows in thermodynamic equilibrium the vapor generation rate Γ_g is obtained from the mixture energy equation as

$$\Gamma_g = \frac{q'' P_H}{A_c h_{fg}} \tag{A-14}$$

Equation A-12 can be written in terms of a substantial derivative

$$\frac{D\alpha}{Dt} = (v_g - C_o\, v_{fg}\alpha)\Gamma_g \tag{A-15}$$

For the sake of simplicity the angle brackets (< >) will be dropped from here on, but it must be kept in mind that all symbols represent cross sectional averages. Then Eq. A-13 becomes

$$\frac{dZ}{dt} = C_k = C_o V_{in} + V_{gj} + C_o\, v_{fg} \int_0^Z \Gamma_g\, dz \tag{A-16}$$

Formally integrating Eq. A-15 with the boundary condition

$$t = t_o \quad , \qquad Z = 0 \quad , \qquad \alpha = \alpha_o$$

and using Eq. A-14 to eliminate Γ_g, we get

$$\alpha(t) = \frac{v_g}{C_o\, v_{fg}} + \left(\alpha_o - \frac{v_g}{C_o\, v_{fg}}\right) \exp\left[-\frac{C_o P_H v_{fg}}{A_c h_{fg}} \int_{t_o}^{t} q''(Z(t'),t')dt'\right] \tag{A-17}$$

where Z(t) is the solution of Eq. A-16. Equations A-16 and A-17 represent the Lagrangian description of the flow.

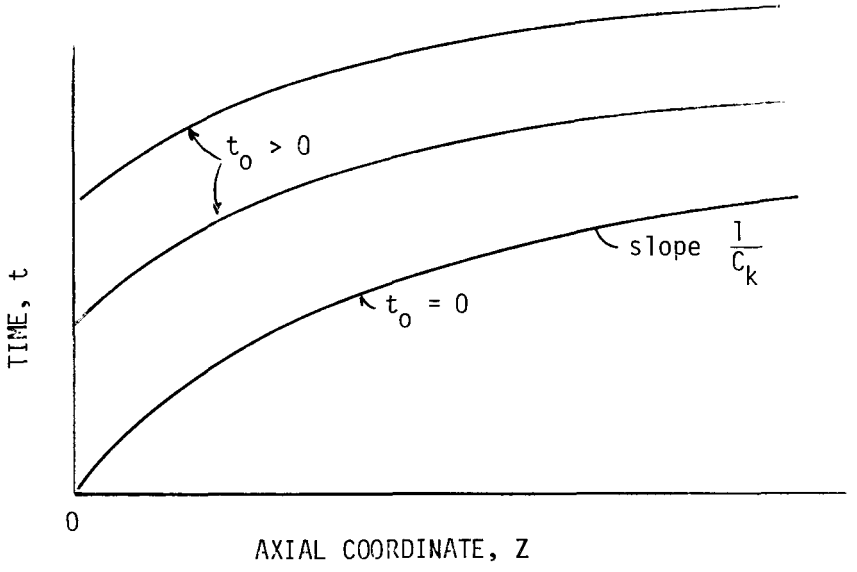

Figure A-1. Trajectories of Fluid Elements in the (Z,t) Plane.

Equation A-16 describes the trajectory (characteristic) in the (Z,t) plane of a fluid element that was at Z = 0, $\alpha = \alpha_o$ at time $t = t_o$. Figure A-1 shows the trajectories of some fluid elements.

Given the heat flux distribution q"(z,t) and the inlet velocity $V_{in}(t)$, the procedure to evaluate the local flow conditions is as follows:

1) Choose a spatial increment to define the spatial nodalization, and solve the inverse of Eq. A-16, i.e.,

$$\frac{dt}{dZ} = \frac{1}{C_k} = \frac{1}{C_o V_{in}(t) + V_{gj} + \frac{C_o v_{fg} P_H}{A_c h_{fg}} \int_0^Z q"(Z,t)dZ} \qquad \text{(A-18)}$$

with the boundary condition: $t = t_o$ at $Z = 0$

Solving this equation for different values of t_o, yields the family of characteristics shown in the Fig. A-1 above. For a given value of t_o, i.e., a given fluid element to be followed, the solution of Eq. A-18 gives a one-to-one correspondence between position Z and time t. A 4th order Runge-Kutta numerical scheme with $\Delta Z = 0.02$ ft was used to solve Eq. A-18.

2) Knowing t at every axial node for a given t_o, Eq. A-17 can be written as

$$\alpha(Z) = \frac{v_g}{C_o v_{fg}} + \left(\alpha_o - \frac{v_g}{C_o v_{fg}}\right) \exp\left[-\frac{C_o P_H v_{fg}}{A_c h_{fg}} \int_0^Z \frac{dt}{dZ} q"(Z,t)\, dZ\right] \qquad \text{(A-19)}$$

The integral in the exponential term of Eq. A-19 can be easily evaluated by a composite Simpson's rule, provided that the same spatial increment Z chosen to solve Eq. A-18 is used.

3) The total volumetric flux j is obtained by performing the integration on Eq. A-11, i.e.,

$$j = V_{in} + \frac{v_{fg} P_H}{A_c h_{fg}} \int_0^Z q"(Z,t)\, dZ \qquad \text{(A-20)}$$

4) The liquid and vapor volumetric fluxes are then calculated with the help of the cross-sectional averaged drift-flux model, i.e.,

$$j_g = (C_o j + V_{gj}) \tag{A-21}$$

$$j_f = j - j_g \tag{A-22}$$

The weighted mean drift velocity is calculated by a correlation suggested by Zuber and Findlay [A.2] namely

$$V_{gj} = 1.41 \left[\frac{\sigma g(\rho_f - \rho_g)}{\rho_f^2} \right]^{1/4} \tag{A-23}$$

5) The flow quality x and the flow rate G are calculated from Eq. A-6.

Repeating steps 1 to 5 with different values of t_o maps the local flow conditions as a function of Z and t.

A.2 QUASI-STEADY-STATE ASSUMPTION

When the time derivatives in Eqs. A-1 and A-2 are set to zero t becomes a parameter, and the conservation equations are reduced to:

Continuity of vapor:

$$\frac{d(\rho_g j_g)}{dZ} = \Gamma_g \tag{A-24}$$

$$\rho_g j_g = G_g = Gx \tag{A-25}$$

Mixture continuity:

$$G = G_{in}(t) \tag{A-26}$$

Energy Equation:

$$x = x_o + \int_0^Z \frac{q'' P_H}{G A_c h_{fg}} dZ \tag{A-27}$$

The procedure to calculate the local flow conditions is simplified to:

1) Calculate x at all axial nodes from Eq. A-27

2) Calculate the volumetric fluxes from

$$j_f = G(1-x)v_f$$

$$j_g = G \times v_g$$

3) Calculate the void fraction from

$$\alpha = \frac{j_g}{C_o(j_f + j_g) + V_{gj}}$$

A.3 PRESCRIPTION OF A HEAT FLUX PROFILE

By assuming a heat flux profile, the hydrodynamics and the heat transfer are decoupled. To have meaningful results, it is necessary to prescribe q"(Z,t) as close as possible to the profile expected to be found during reflooding conditions.

The prescribed heat flux profile is

$$q"(Z,t) = Q_o \sin\left[\frac{\pi(Z+\delta)}{L}\right] + Q_1 \operatorname{sech}^2[b(Z-Ut)] \qquad \text{(A-28)}$$

and is shown in Fig. A-2.

The chopped-sine in the profile represents the decay heat. The second term simulates the peak in heat flux in the neighborhood of the quench front. In the decay-heat term an exponential decay in time could have been included, however the time constant of this exponential is many times larger than the one of the transient under investigation. For $Z < Z_q$ the sine shape is quite good because all that the variations in flow rate can do is to raise or drop the fuel pin temperature field by a few degrees. For $Z > Z_q$ the surface heat flux is expected to be somewhat different than the sine shape since some points of the pin are heating up (away from Z_q) and some are cooling off (near Z_q).

The heat flux spike representing the quench front is moving with the velocity U of the quench front. The width 1/b of this spike is calculated by assuming that:

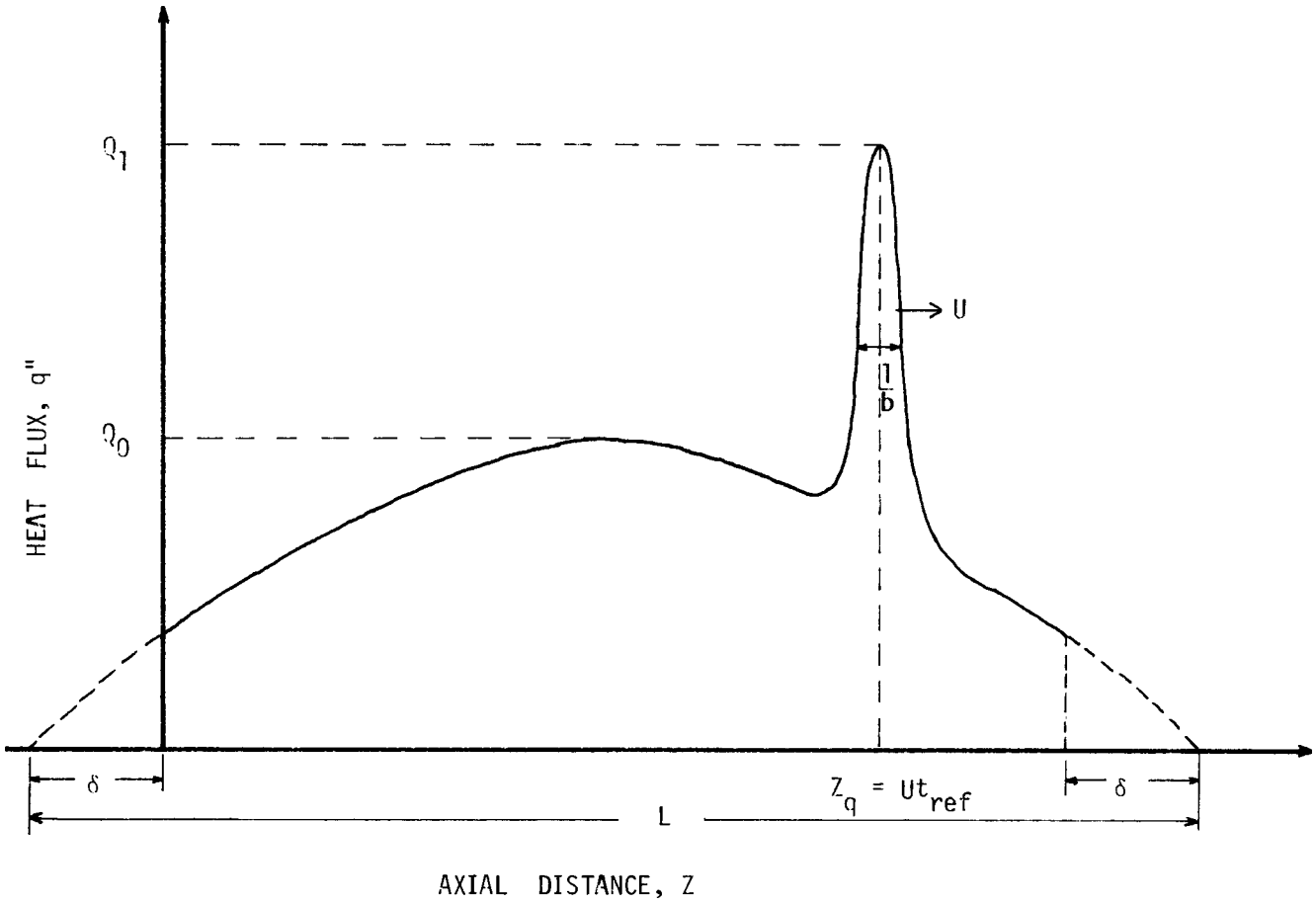

Figure A-2. Sketch of heat flux profile used for appendix A calculations.

- the passing quench front drops the pin temperature by ΔT
- the pin has a heat capacity $\rho_F c_{PF}$ and a radius R_F
- the maximum heat flux Q_1 is equal to q''_{CHF} and that $Q_1 >> Q_o$.

An energy balance then requires that the area under the heat flux spike be equal to the stored heat release by the fuel pin per unit time, i.e.,

$$\int_{-\infty}^{\infty} Q_1 \, \mathrm{sech}^2[b(Z-Ut)]dZ = \frac{\rho_F c_{PF} R_F U \Delta T}{2} \tag{A-29}$$

yields

$$b = \frac{4Q_1}{\rho_F c_{PF} R_F U \Delta T} \tag{A-30}$$

The prescribed inlet flow rate is shown in Fig. A-3, and it represents variations in the inlet velocity between 1 and 10 in/sec, with different slopes to simulate transients of different intensities.

Other numerical values used were:

ΔT = 700°F (390°C)

c_{PF} = 0.075 Btu/lbm °F (0.314 kJ/kg °C) (UO_2)

ρ_F = 623 lbm/ft^3 (9.98 g/cm^3)

U = 0.05 ft/s (15 mm/s)

R_F = 0.018 ft (5.5 mm)

D_H = 0.04525 ft (13.8 mm)

Q_o = 15,000 Btu/hr ft^2 (47.3 kW/m^2)

Q_1 = 350,000 Btu/hr ft^2 (1100 kW/m^2)

t_{ref} = 140 s

α_o = 0

t_{ref} is the time at which the transient begins and it essentially locates, together with U, the position of the heat spike at the beginning of the transient.

A.4 ANALYSIS OF RESULTS

Figures A-3 through A-8 show typical results; the local flow conditions are calculated by the method of characteristics and by using the quasi-steady-state assumption. In general, the two solutions are in very good agreement.

As expected, the error is smaller at the lower elevations (3 ft.). Also the quasi-steady-state solution falls further behind as the changes in the inlet flow rate become faster.

The void fraction was not plotted because both solutions agree within at least two significant figures at almost all times and elevations.

Comparing Fig. A-4 with Fig. A-7 and Fig. A-5 with Fig. A-8, it is clear that the increase in pressure makes the quasi-steady-state assumption less accurate. This is a result of the fact that C_k is proportional to v_{fg} (Eq. A-13) and therefore for the same heat flux profile, C_k decreases with increasing pressure, increasing the system time constant.

It should be noted that the correlation used to calculate V_{gj} was developed for bubbly flow and consequently is expected to give inaccurate results for medium and high values of quality. However at medium and high qualities (medium and high elevations) the dominant term in Eq. A-13 is the integral term and an error in V_{gj} has a negligible effect. Also in the void calculation the dominant term is $C_o j$ under these conditions.

The effect of assuming subcooled inlet flow instead of saturation conditions is to reduce the vapor generation rate and therefore results in a small decrease in C_k. However this effect should be small for low subcoolings and for low inlet flow rates.

REFERENCES

A.1 N. Zuber and F. W. Staub, "The Propagation and the Wave Form of the Vapor Volumetric Concentration in Boiling, Forced Convection System under Oscillatory Conditions", Int. J. Heat Mass Transfer, 9, 871 (1966).

A.2 N. Zuber and S. A. Findlay, "Average Volumetric Concentration in Two-Phase Flow Systems", J. of Heat Transfer, 87, 453-468 (1965).

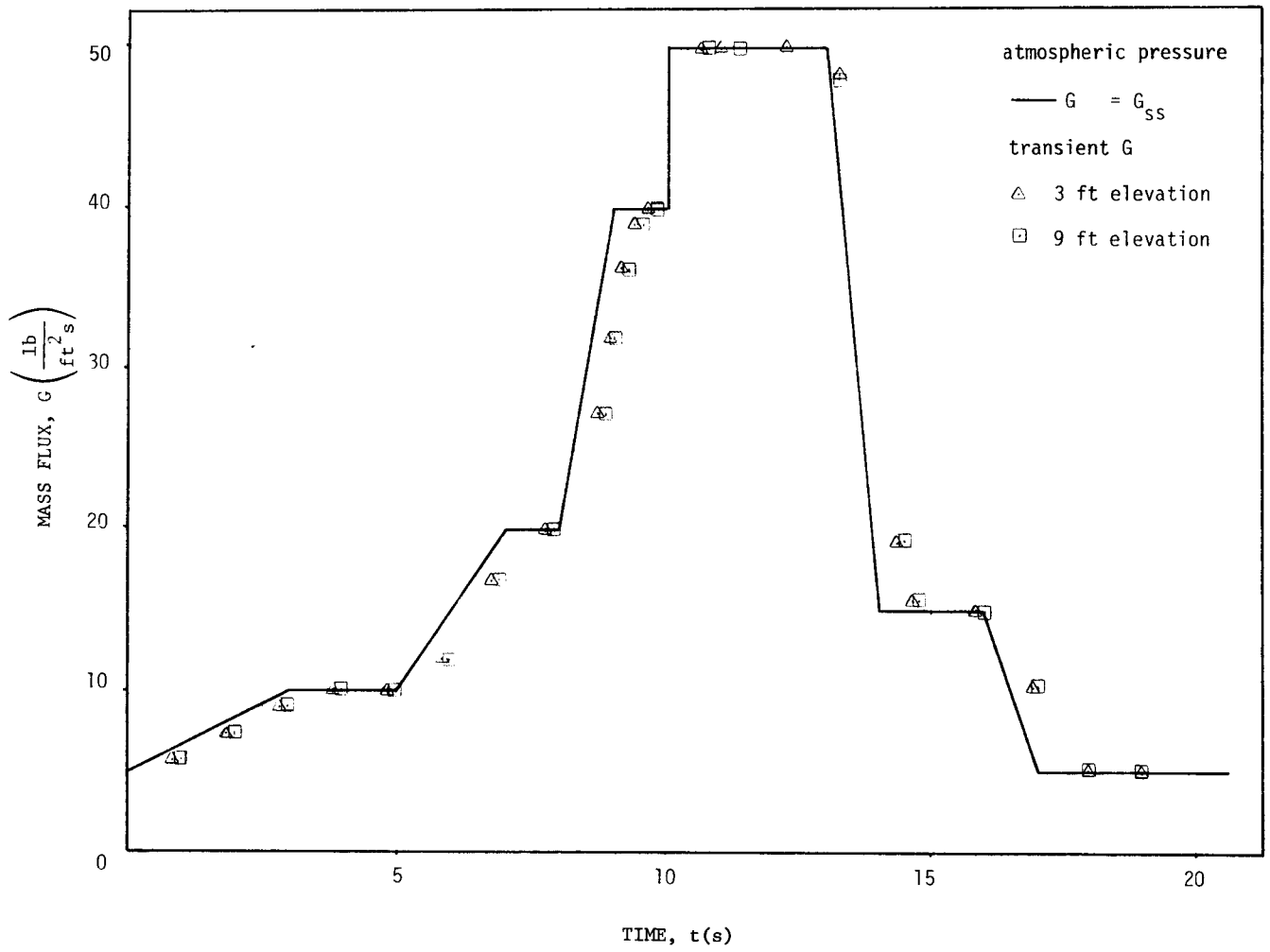

Figure A-3. Comparison of mass fluxes at atmospheric pressure.

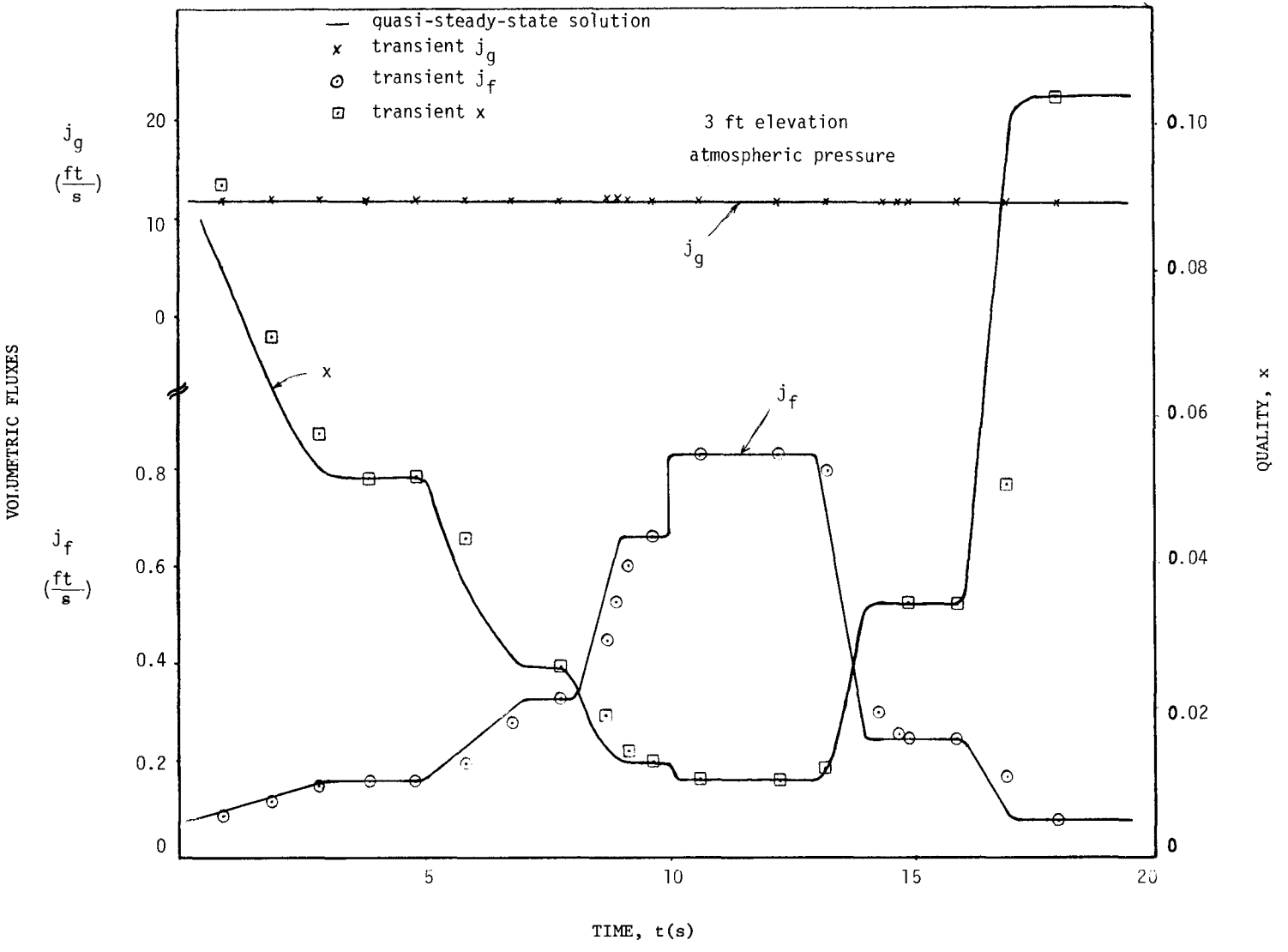

Figure A-4. Comparison of the volumetric fluxes and of the quality at atmospheric pressure and at the 3-ft elevation.

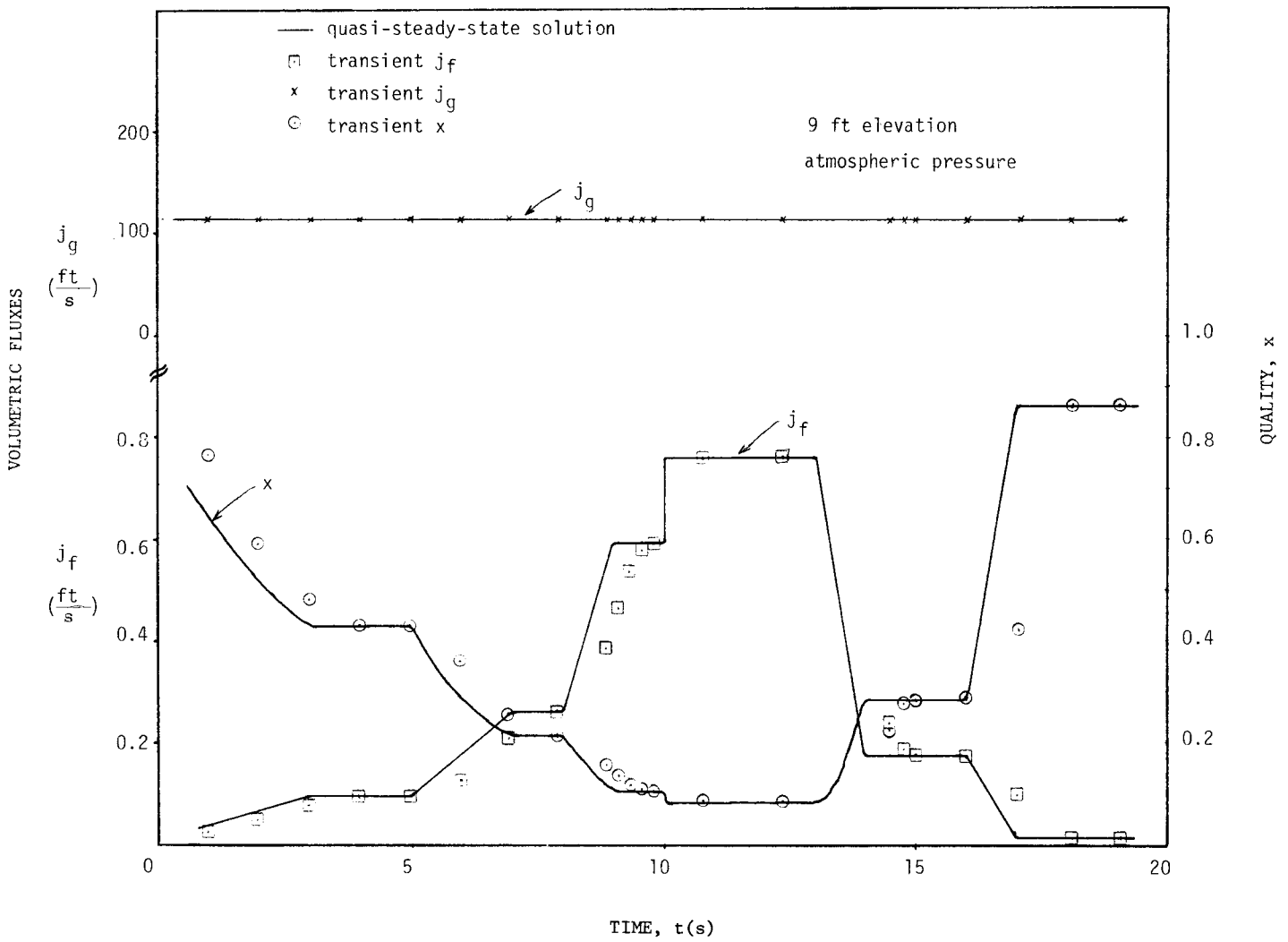

Figure A-5. Comparison of the volumetric fluxes and of the quality at atmospheric pressure and at the 9-ft elevation.

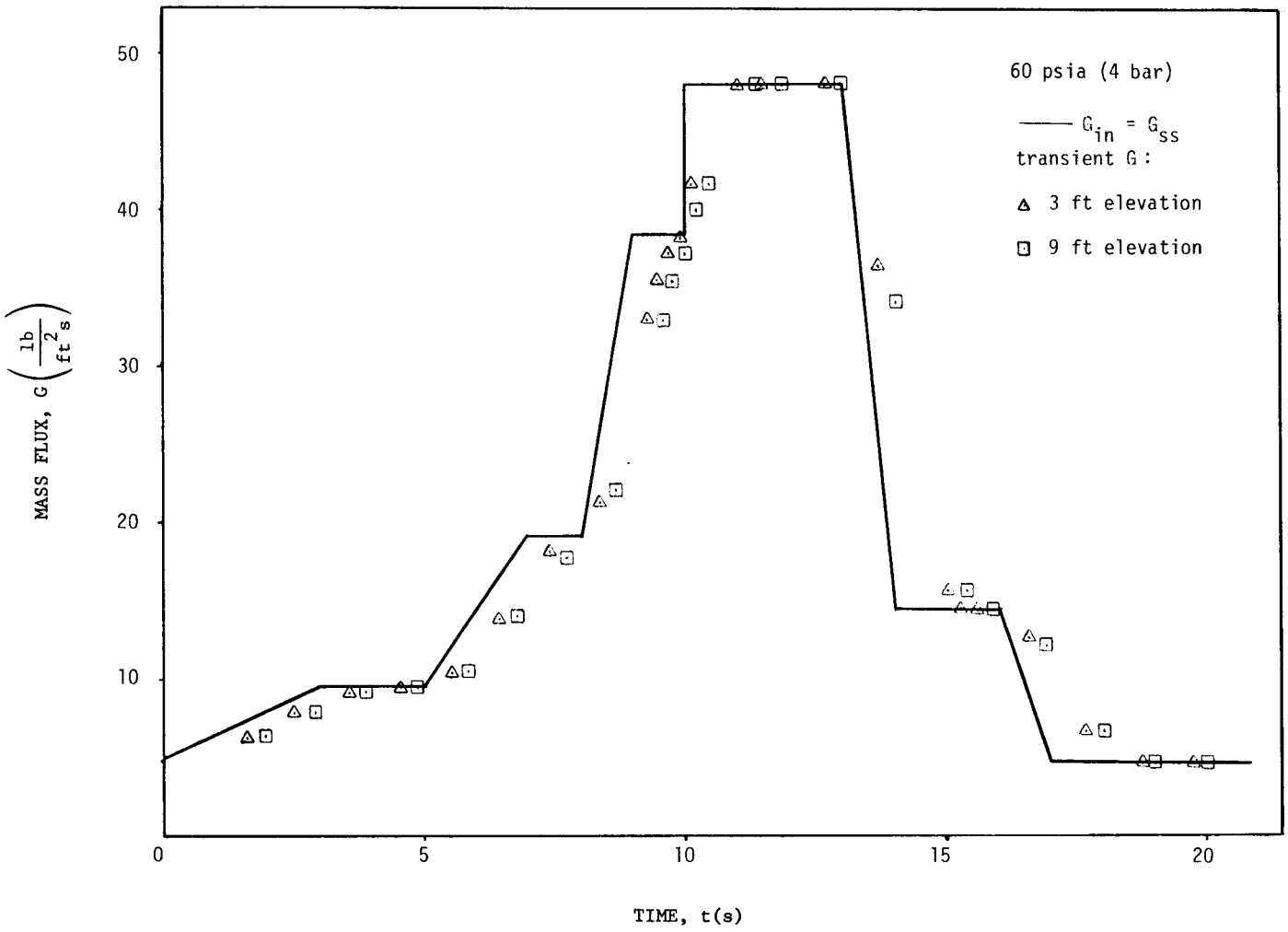

Figure A-6. Comparison of mass fluxes at elevated pressure.

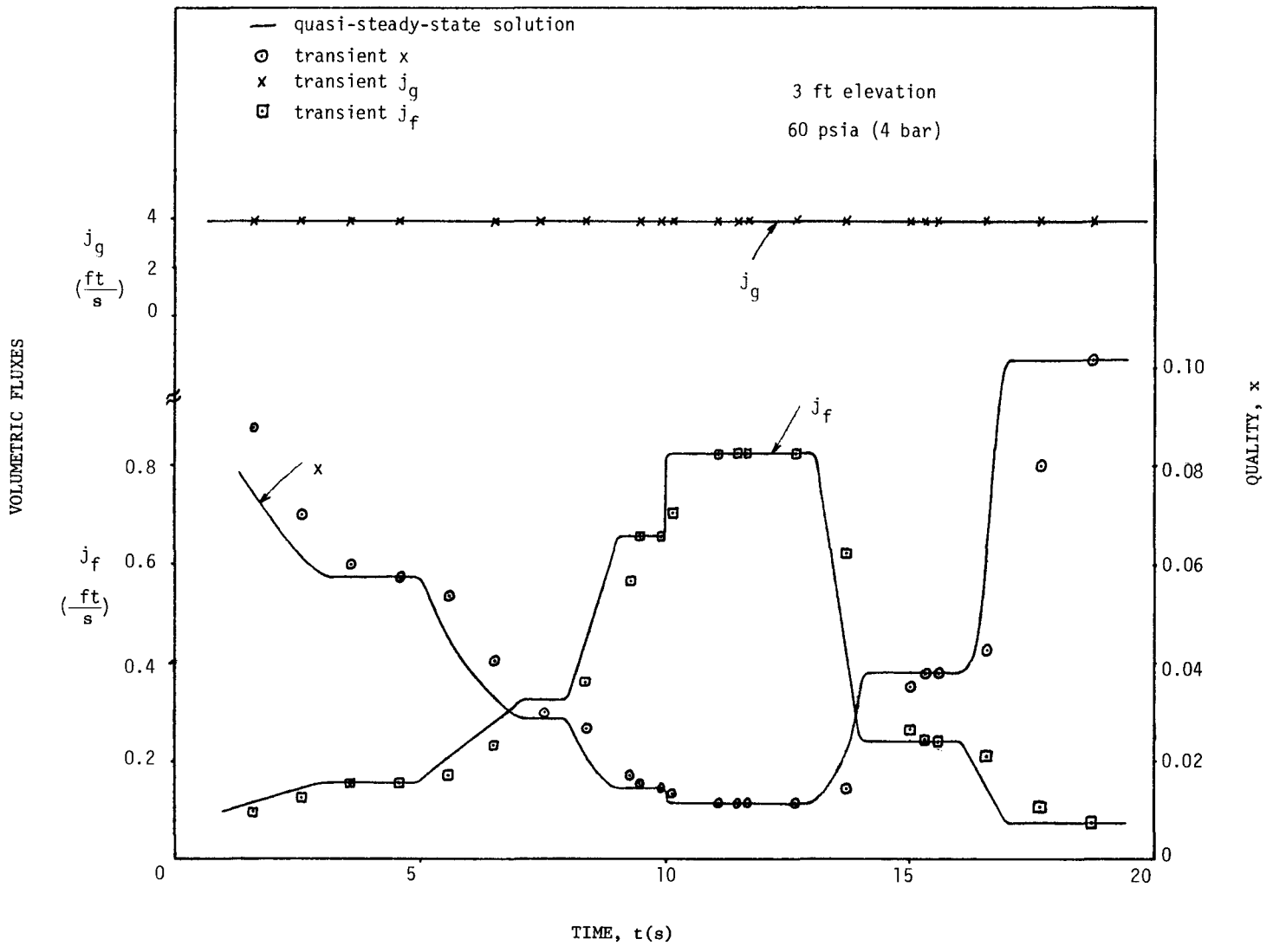

Figure A-7. Comparison of the volumetric fluxes and of the quality at elevated pressure and at the 3-ft elevation.

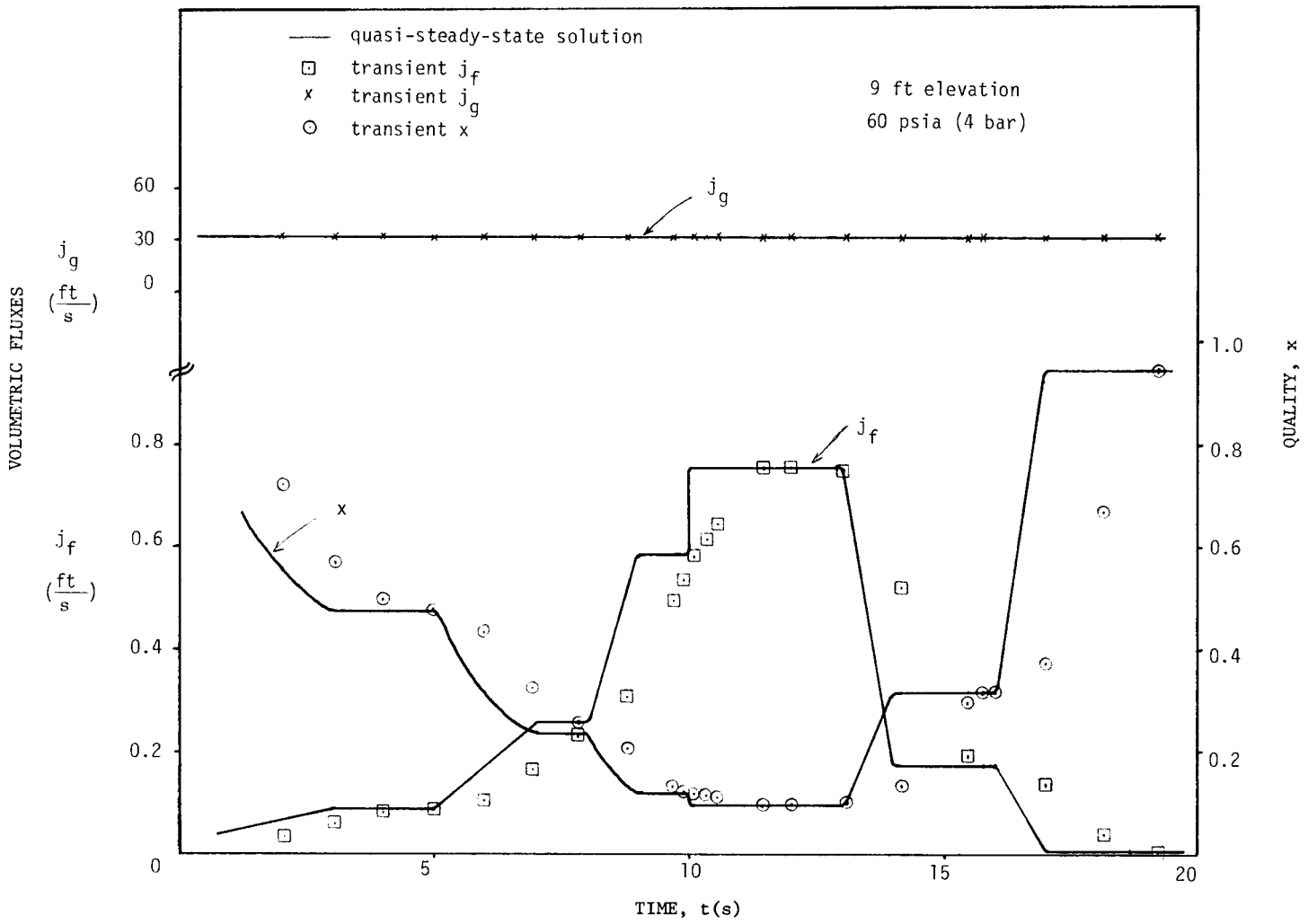

Figure A-8. Comparison of the volumetric fluxes and of the quality at elevated pressure and at the 9-ft elevation.

Appendix B

RADIAL HEAT CONDUCTION IN THE FUEL ROD

In order to calculate the cladding temperature history, the transient heat conduction equation must be solved in the fuel rod. The temperature dependence of the thermophysical properties eliminates the possibility of any analytical solution and therefore a finite-difference numerical approximation is required.

This Appendix describes the numerical procedure used for solving the heat conduction equation in actual reactor fuel rods, as well as in electrically heated rods or tubes used in various reflooding simulation experiments.

The numerical procedure was developed for the one-dimensional time-dependent or steady-state conduction equation in cylindrical geometry. Only heat conduction in the radial direction is considered; it is assumed that axial and circumferential temperature variations can be neglected. The thermophysical properties are considered as position and temperature dependent. The heat source can be space and time dependent. The gap between the fuel pellet and the cladding is considered as a simple resistance with no heat capacity. The variation of the gap conductance in time is externally specified. A finite-difference approximation of the partial differential equation is obtained from an integral method [B.1]. A two-step numerical scheme is used to ensure accuracy and avoid spurious results during fast transients.

B.1 FINITE-DIFFERENCE FORMULATION OF THE CONDUCTION EQUATION

The heat conduction equation for which a solution is required is:

$$\rho c_p \frac{\partial T(r,t)}{\partial t} = \nabla \cdot k(r,T)\, \nabla T(r,t) + S(r,t) \qquad \text{(B-1)}$$

where

$\rho c_p = g(r,T)$ - volumetric heat capacity

$k(r,T)$ - thermal conductivity

$S(r,T)$ - volumetric heat source

Figure B-1 illustrates the layout of mesh points and Fig. B-2 shows details of a typical interior mesh point. Subscripts are used to designate space indexes, and superscripts to indicate time indexes. The subscripts p and s designate quantities to the left and to the right, respectively, of a mesh point. The h's indicate the mesh point spacing which is not necessarily even. Between mesh points, k, g and S are assumed constant, but the values to the left and to the right of a given mesh point are not necessarily equal.

To obtain the spatial diffference approximation for the n^{th} mesh point an integral method is used. Equation B-1 is integrated over the volume indicated by the dashed line in Fig. B-2,

$$\iiint_V g(r,t)\,\frac{\partial T(r,t)}{\partial t}\,dV = \iiint_V \nabla.k(r,t)\,\nabla T(r,t)\,dV + \iiint_V S(r,t)dV \qquad \text{(B-2)}$$

Since only radial conduction is considered, the dimension of the volume in the axial direction is set equal to one. The volume is a ring formed by rotating Fig. B-2 about the r = 0 axis.

Using a forward difference for the time derivative, the first term of equation B-2 is approximated by

$$\iiint_V g(r,t)\,\frac{\partial T(r,t)}{\partial t}\,dV = \frac{T_n^{m+1} - T_n^m}{\Delta t}\left[g_{pn}\pi\{r_n^2-(r_n-\frac{h_{pn}}{2})^2\} + g_{sn}\pi\{(r_n+\frac{h_{sn}}{2})^2-r_n^2\}\right]$$

$$= 2\pi\,\frac{(T_n^{m+1} - T_n^m)}{\Delta t}\left[g_{pn}\,\frac{h_{pn}}{2}\,(r_n - \frac{h_{pn}}{4}) + g_{sn}\,\frac{h_{sn}}{2}\,(r_n + \frac{h_{sn}}{4})\right] \qquad \text{(B-3)}$$

where T_n^m indicates the temperature at $r = r_n$ at time $t = m\Delta t$.

The second term of equation B-2 is approximated by

$$\iiint_V \nabla\cdot k(r,T)\nabla T(r,t)dV = \iint_S k(r,T)\,\nabla T(r,t)\,.\,d\bar{s} \;\simeq$$

$$\simeq 2\pi\left[\frac{k_{sn}(T_{n+1}-T_n)}{h_{sn}}\,(r_n + \frac{h_{sn}}{2}) - \frac{k_{pn}(T_n - T_{n-1})}{h_{pn}}\,(r_n - \frac{h_{sn}}{2})\right] \qquad \text{(B-4)}$$

where $\bar{s}$ is the surface area of V, with the unit vector pointing outwards, i.e., the heat flux entering the control volume is negative and heat flux leaving the control volume is positive.

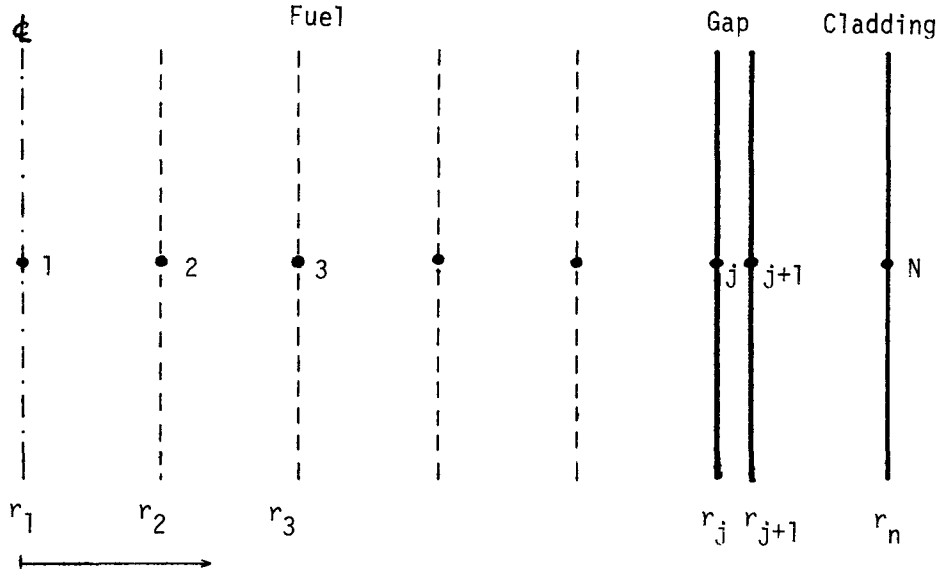

Figure B-1. Mesh point layout for one-dimensional (radial) conduction.

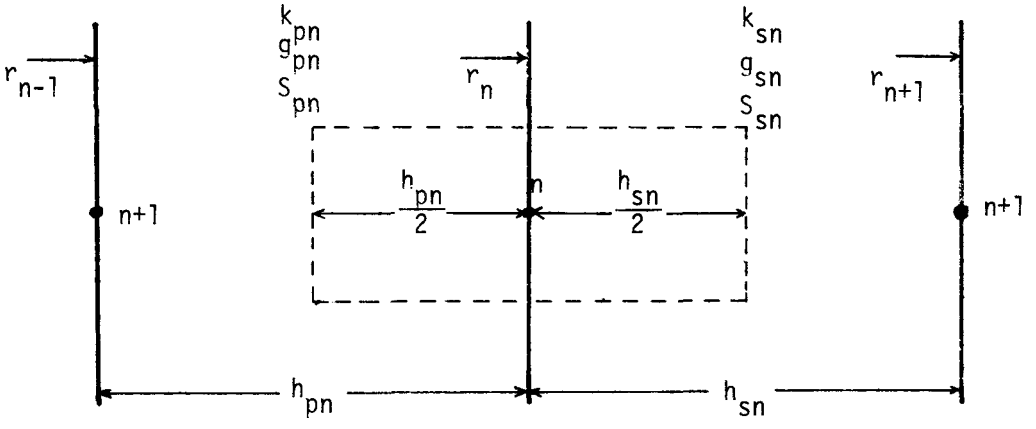

Figure B-2. Typical mesh points for one-dimensional (radial) conduction.

The space and time dependence of the source term is assumed to be separable, i.e.,

$$S(r,t) = P(t)\, Q(r)$$

The third term of Eq. B-2 is then approximated by

$$\iiint_V S(r,t)dV \simeq 2\pi\, P(t)\, \left[Q_{pn} \frac{h_{pn}}{2} \left(r_n - \frac{h_{pn}}{4}\right) + Q_{sn} \frac{h_{sn}}{2} \left(r_n + \frac{h_{sn}}{4}\right)\right] \qquad \text{(B-5)}$$

The following quantities are defined for convenience:

$$h^v_{pn} \equiv \frac{h_{pn}}{2} \left(r_n - \frac{h_{pn}}{4}\right) \quad , \qquad h^v_{sn} \equiv \frac{h_{sn}}{2} \left(r_n + \frac{h_{sn}}{4}\right)$$

$$h^s_{pn} \equiv \frac{1}{h_{pn}} \left(r_n - \frac{h_{pn}}{2}\right) \quad , \qquad h^s_{sn} \equiv \frac{1}{h_{sn}} \left(r_n + \frac{h_{sn}}{2}\right)$$

$$D_n \equiv g_{pn}\, h^v_{pn} + g_{sn}\, h^v_{sn}$$

$$Q_n \equiv \left(Q_{pn}\, h^v_{pn} + Q_{sn}\, h^v_{sn}\right)$$

Gathering together the approximations for the terms of B-2, the basic difference equation for the n^{th} mesh point becomes:

$$\left(\frac{T^{m+1}_n - T^m_n}{\Delta t}\right) D_n = (T_{n+1} - T_n) k_{sn} h^s_{sn} - (T_n - T_{n-1}) k_{pn} h^s_{pn} + Q_n\, P(t) \equiv \delta_n \qquad \text{(B-6)}$$

where δ_n denotes the second member of the equation.

B.2 CHOICE OF A SOLUTION SCHEME

So far, the time superscript for δ_n has been omitted and the procedure for approximating the temperature dependence of the thermophysical properties has not been mentioned. For a steady-state, the difference approximation becomes

$$\delta_n = 0 \qquad \text{(B-7)}$$

and no time superscripts are needed. For the time-dependent case, an equation of the type,

$$\frac{(T_n^{m+1} - T_n^m)}{\Delta t} D_n = \omega\delta_n^{m+1} + (1-\omega)\delta_n^m \quad , \qquad 0 \leq \omega \leq 1 \tag{B-8}$$

with $\omega = 0$, gives an explicit formula since the quantities in δ_n^m are given either by the initial temperatures or the results of the last time advancement, and thus T_n^{m+1} can be determined directly. However, in this case, the stability of the resulting difference equation depends on the choice of Δt and the truncation error is of the order of Δt. A difference equation is stable if any introduced error, such as truncation or roundoff error, is attenuated rather than amplified in successive time advancements. With $\omega \neq 0$, B-8 yields an implicit formula and leads to a set of simultaneous equations. The choice of $\omega = 0.5$ results in an implicit formulation (Crank-Nicholson scheme) that is unconditionally stable and has a truncation error of the order of $(\Delta t)^2$. This feature makes this formulation very attractive; however, it produces spurious results when used to calculate fast transients, such as those driven by a large step change in the value of the heat transfer coefficient, and is avoided for this reason.

A two-step scheme proposed by Miller [B.2] that is unconditionally stable, has a truncation error of the order of $(\Delta t)^2$, and also minimizes the numerical noise when applied to fast transients is adopted. All available radial conduction routines use Eq. B-8 in one form or another, however, cannot always handle adequately severe transients.

Miller's scheme requires the solution of two sets of simultaneous equations for every time advancement. The two steps to follow are:

First

$$\sigma \frac{(T_n^{m+1/3} - T_n^m)}{\frac{1}{3}\Delta t} D_n = \delta_n^{m+1/3} \tag{B-9}$$

and second

$$\frac{(T_n^{m+1} - T_n^m)}{\Delta t} D_n = \frac{3}{4}\delta_n^{m+1/3} + \frac{1}{4}\delta_n^{m+1} \tag{B-10}$$

where the superscript $m+1/3$ refers to values calculated at time $t = (m+1/3)\Delta t$, and σ is one for transient cases and zero for steady-state cases. Note that $\delta_n^{m+1/3}$ is immediately available as the left-hand side of Eq. B-9.

The temperature dependence of k and g is approximated by using at each time step the values of k and g corresponding to the average temperature (not weighted by volume) of the two mesh points obtained in the previous calculation, i.e., k_{pn} and g_{pn} are evaluated at $(T^m_{n-1} + T^m_n)/2$ and k_{sn} and g_{sn} at $(T^m_n + T^m_{n+1})/2$. The k's and g's calculated in this manner are used to evaluate both δ^m_n and δ^{m+1}_n. It would have been more accurate to iterate the solution at each time step, using the new values of T^{m+1} to determine the k's and g's for δ^{m+1}, but since the properties of most materials change slowly with temperature, this procedure would have given only a small increase in accuracy at the expense of considerable increase in computation time.

Writing Eqs. B-9 and B-10 in full, the difference approximation for the n^{th} interior mesh point for both transient or steady-state cases, for the first step becomes

$$a_n T^{m+1/3}_{n-1} + b_n T^{m+1/3}_n + c_n T^{m+1/3}_{n+1} = d_n \qquad \text{(B-11)}$$

where

$$a_n = -\frac{k_{pn} h^s_{pn} \Delta t}{3} \quad , \quad c_n = -\frac{k_{sn} h^s_{sn} \Delta t}{3} \quad , \quad b_n = \sigma D_n - a_n - c_n$$

$$d_n = \sigma D_n T^m_n + \frac{Q_n P^{m+1/3} \Delta t}{3}$$

and for the second step:

$$a'_n T^{m+1}_{n-1} + b'_n T^{m+1}_n + c'_n T^{m+1}_{n+1} = d'_n \qquad \text{(B-12)}$$

where

$$a'_n = \frac{3}{4} a_n \quad , \quad c'_n = \frac{3}{4} c_n \quad , \quad b'_n = D_n - a'_n - c'_n$$

$$d'_n = \left(\frac{9}{4} T_n^{m+1/3} - \frac{5}{4} T_n^m\right) D_n + Q_n P^{m+1} \frac{\Delta t}{4}$$

Note that for steady-state only the first step is needed.

B.3 DIFFERENCE APPROXIMATION FOR THE BOUNDARY MESH POINTS

A convective boundary condition is assumed to exist at the boundary mesh points, i.e.,

$$-k \frac{\partial T}{\partial r} = H(T-T_c) \qquad \text{at the boundaries}$$

where

H = heat transfer coefficient

T_c = coolant temperature

Equation B-2 is again used to obtain the difference approximation at the boundaries, with volumes of integration defined as indicated by the dashed lines in Fig. B-3 below

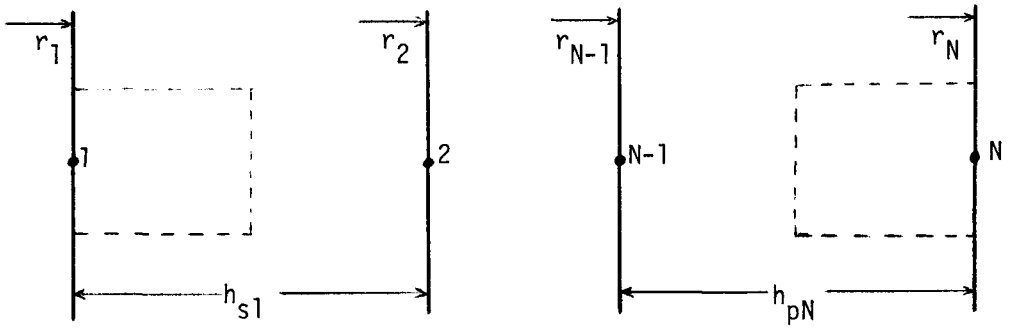

Figure B-3. Boundary Mesh Points

The second term of Eq. B-2 for the boundary condition at $r = r_1$ is

$$\iiint_V \nabla \cdot k(T,r)\nabla T(r,t)dV = \iint_S k(T,r)\nabla T(r,t)\cdot d\bar{s} \simeq$$

$$\simeq 2\pi[k_{s1}h^s_{s1}(T_2-T_1) + H_1(T_1-T_{c1})r_1]$$

The complete equation for the mesh point at $r = r_1$ becomes

$$\frac{(T_1^{m+1}-T_1^m)}{\Delta t} g_{s1} h_{s1}^v = H_1(T_1 - T_{c1})r_1 + k_{s1}(T_2 - T_1)h_{s1}^s + P(t)Q_{s1}h_{s1}^v \equiv \delta_1 \qquad \text{(B-13)}$$

For a solid fuel rod $r_1 = 0$, and the condition of zero temperature gradient at the center line is satisfied by Eq. B-13.

Writing Eq. B-13 in a two-step fashion, in the same manner as for the interior mesh points, results for the first step in

$$b_1 T_1^{m+1/3} + c_1 T_2^{m+1/3} = d_1 \qquad \text{(B-14)}$$

where

$$c_1 = -\frac{k_{s1}h_{s1}^v \Delta t}{3} \quad , \quad b_1 = \sigma g_{s1} h_{s1}^v - \frac{H_1 r_1 \Delta t}{3} - c_1$$

$$d_1 = \sigma g_{s1} h_{s1}^v T_1^m - \frac{H_1 r_1 \Delta t}{3} T_{c1}^m + \frac{P^{m+1/3} Q_{s1} h_{s1}^v \Delta t}{3}$$

and for the second step in

$$b_1' T_1^{m+1} + c_1' T_2^{m+1} = d_1' \qquad \text{(B-15)}$$

where

$$c_1' = \frac{3}{4} c_1 \quad , \quad b_1' = g_{s1} h_{s1}^v - \frac{H_1 r_1 \Delta t}{4} - c_1'$$

$$d_1' = g_{s1}^v h_{s1} \left(\frac{9}{4} T_1^{m+1/3} - \frac{5}{4} T_1^m\right) - \frac{H_1 r_1 \Delta t}{4} T_{c1}^m + \frac{\Delta t}{4} P^{m+1} Q_{s1} h_{s1}^v$$

Similarly for the boundary mesh point at $r = r_N$, for the first step:

$$a_N T_{N-1}^{m+1/3} + b_N T_N^{m+1/3} = d_N \qquad \text{(B-16)}$$

where

$$a_N = -\frac{k_{pN}\, h^s_{pN}\, \Delta t}{3} \quad , \quad b_N = \sigma g_{pN}\, h^v_{pN} + \frac{H_N r_N \Delta t}{3} - a_N$$

$$d_N = \sigma g_{pN}\, h_{pN}\, T^m_N + \frac{H_N r_N \Delta t}{3}\, T^m_{cN} + \frac{P^{m+1/3} Q_{pN} h^v_{pN} \Delta t}{3}$$

and for the second step

$$a'_N\, T^{m+1}_{N-1} + b'_N\, T^{m+1}_N = d'_N \tag{B-17}$$

where

$$a'_N = \frac{3}{4}\, a_N \quad , \quad b'_N = g_{pN}\, h^v_{pN} + \frac{H_N r_N \Delta t}{4} - a'_N$$

$$d'_N = g_{pN}\, h^v_{pN}\, \left(\frac{9}{4}\, T^{m+1/3}_N - \frac{5}{4}\, T^m_N\right) + \frac{H_N r_N \Delta t}{4}\, T^m_{CN} + \frac{P^{m+1} Q_{pN}\, h^v_{pN} \Delta t}{4}$$

B.4 SOLUTION OF THE ALGEBRAIC EQUATIONS

The difference approximations for the first step, Eq. B-11 together with Eqs. B-14 and B-16, lead to a tri-diagonal set of N equations.

$$\begin{vmatrix} b_1 & c_1 & & & & \\ a_2 & b_2 & c_2 & & & \\ & a_3 & b_3 & c_3 & & \\ & & & & & \\ & & & & & \\ & & & & & \\ & & a_{N-1} & b_{N-1} & c_{N-1} & \\ & & & a_N & b_N & \end{vmatrix} \begin{vmatrix} T^{m+1/3}_1 \\ T^{m+1/3}_2 \\ T^{m+1/3}_3 \\ \\ \\ \\ T^{m+1/3}_{N-1} \\ T^{m+1/3}_N \end{vmatrix} = \begin{vmatrix} d_1 \\ d_2 \\ d_3 \\ \\ \\ \\ d_{N-1} \\ d_N \end{vmatrix}$$

For the second step, Eqs. B-12, B-15, and B-16 result in a similar set where m+1/3 is replaced by m+1 and the coefficients are primed.

A Gaussian Elimination method [B.4] is used to solve the two resulting sets or tri-diagonal equations; the following calculational procedure is used.

1) $\beta_1 = b_1 \quad , \quad \gamma_1 = d_1/\beta_1$

2) $\beta_i = b_i - \frac{a_i\, c_{i-1}}{\beta_{i-1}} \qquad i = 2,3, \ldots N$

3) $\gamma_i = b_i \frac{d_i - a_i\gamma_{i-1}}{\beta_i} \qquad i = 2,3, \ldots N$

4) $T_N = \gamma_N$

5) $T_i = \gamma_i - \frac{c_i\, T_{i+1}}{\beta_1} \qquad i = N-1, N-2, \ldots 1$

It can be shown [B.3] that this method of solution introduces little roundoff error if the off-diagonal elements are negative and the diagonal is greater than the sum of the magnitudes of the off-diagonal elements. From the form of the difference equations, these conditions are satisfied for any values of the mesh point spacing, time step, and thermo-physical properties.

B.5 GAP CONDUCTANCE

As mentioned previously, the gap conductance, H_{gap}, has to be externally specified. If j is the mesh point of the surface of the fuel pellet, H_{gap} is introduced as

$$k_{sj} = k_{p(j+1)} = H_{gap}\,(r_{j+1} - r_j)$$

For the case of a closed gap having, however, a finite contact resistance, $1/H_{cont}$, the gap is represented by a local resistance at mesh point j. The thermal conductivity at this j^{th} mesh point is substituted by an effective thermal conductivity given by

$$k_{sj}^{eff} = \frac{k_{sj}}{1 + \frac{k_{sj}}{H_{cont}(r_{j+1} - r_j)}}$$

B.6 LUMPED-PARAMETER RADIAL CONDUCTION FOR THE CASE OF A THIN TUBE

For the case of a thin tubular test section, the radial temperature gradient across the tube wall is very small and therefore a simple lumped-parameter heat balance at each axial node describes adequately the wall temperature history.

A heat balance per unit length yields

$$g\pi(r_N^2 - r_1^2)\frac{dT}{dt} = -2\pi r_1 H_1(T - T_{c1}) - 2\pi r_N H_N(T - T_{cN}) + \pi(r_N^2 - r_1^2)S \qquad \text{(B-18)}$$

Rearranging and grouping similar terms results in

$$\frac{dT}{dt} = -(AH_1 + BH_N)T + AH_1\,T_{c1} + BH_N\,T_{cN} + Q \equiv \delta \qquad \text{(B-19)}$$

where

$$A = \frac{2r_1}{g(r_N^2 - r_1^2)} \quad , \qquad B = \frac{2r_N}{g(r_N^2 - r_1^2)} \quad , \qquad Q = \frac{S}{g}$$

The heat source S is assumed to be radially uniformly distributed, and therefore a function of time and axial coordinate only. The volumetric heat capacity g is now a function of temperature only.

Using the two-step numerical difference scheme described in Eqs. B-9 and B-10 and further assuming that $S^{m+1/3} \approx S^{m+1}$ results in

$$T^{m+1} = \left[\frac{(1 - \frac{5}{12}\lambda\Delta t)}{(1 + \frac{1}{3}\lambda\Delta t)(1 + \frac{1}{4}\lambda\Delta t)}\right]T^m + \left[\frac{\frac{1}{12}\lambda\Delta t}{1 + \frac{1}{3}\lambda\Delta t}\right](AH_1T_{c1} + BH_NT_{cN} + Q)\Delta t \qquad \text{(B-20)}$$

where

$$\lambda = AH_1 + BH_N$$

This simple lumped-parameter solution is very economical to run compared to the fully transient solution.

REFERENCES

B.1 Wagner, R. J., "Heat 1 - A One Dimensional Time Dependent or Steady-State Heat Conduction Code for the IBM-650", IDO-16867 (1963).

B.2 Miller, K., "Advanced Numerical Analysis", Class Notes, University of California-Berkeley (Winter 1974).

B.3 Carnahan, B., Luther, H. A., and Wilke, J. O., Applied Numerical Methods, John Wiley & Sons, Inc. (1969).

B.4 Gatewood, F. E., "A Round-off Error Study on an IBM-650 Computer", Master's Thesis, University of Idaho, Moscow (1961).

Appendix C

HEAT TRANSFER IN DISPERSED-FLOW FILM BOILING

C.1 HEAT BALANCE IN DISPERSED FLOW

Assuming a steady state and that the liquid phase remains saturated, an elementary heat balance over a channel length dz yields

$$Gx\, c_{pv} \frac{dT_v}{dz} = \frac{q'' P_H}{A} - G[h_{fg} + c_{pv}(T_v - T_{sat})] \frac{dx}{dz} \tag{C-1}$$

Defining

$$h'_{fg} \equiv h_{fg} + c_{pv}(T_v - T_{sat}) \tag{C-2}$$

$$Q \equiv \frac{q'' P_H}{AG\, h_{fg}} = \frac{dx_{eq}}{dz} = \frac{\Gamma_{g,eq}}{G} \tag{C-3}$$

Eq. C-1 becomes

$$\frac{dT_v}{dz} = \frac{Q\, h_{fg}}{x\, c_{pv}} - \frac{h'_{fg}}{x\, c_{pv}} \frac{dx}{dz} \tag{C-4}$$

C.2 VAPOR GENERATION

A non-dimensional vapor generation rate is defined as

$$\Gamma_g^+ \equiv \frac{\Gamma_g}{\Gamma_{g,eq}} = \frac{dx}{dx_{eq}} = \frac{\Gamma_g}{GQ} \tag{C-5}$$

Note that Eq. C-5 may also be written in terms of the partial heat fluxes as

$$\Gamma_g^+ = \frac{\frac{dx}{dz}}{\frac{dx_{eq}}{dz}} = \frac{q''_{w-d} + q''_{v-d}}{q''_{w-v} + q''_{w-d}} = \frac{q''_{w-d} + q''_{v-d}}{q''} \tag{C-6}$$

where

q''_{w-d} - heat flux from the wall to all droplets

q''_{v-d} - heat flux from the vapor to all droplets

q''_{w-v} - heat flux from the wall to the vapor

The derivative of Γ_g^+ with respect to x_{eq} will be calculated now. Note first that

$$\frac{d}{dz} = \frac{dx_{eq}}{dz}\frac{d}{dx_{eq}} = Q\frac{d}{dx_{eq}} \tag{C-7}$$

Thus

$$\frac{d\Gamma_g^+}{dx_{eq}} = \frac{1}{Q}\frac{d\Gamma_g^+}{dz} \tag{C-8}$$

Assuming for simplicity that the total wall heat flux is uniform, Eq. C-8 can be written as

$$\frac{d\Gamma_g^+}{dx_{eq}} = \frac{1}{Q\,q''}\left[\frac{dq''_{w-d}}{dz} + \frac{dq''_{v-d}}{dz}\right] \tag{C-9}$$

C.3 EVAPORATION OF THE DROPLETS

As mentioned previously, it is assumed that the droplet flux N remains constant, therefore a mass balance yields

$$(1-x)G = N\,\rho_f\,\frac{\pi}{6}\,\delta^3 \tag{C-10}$$

Differentiation of this equation yields

$$\frac{dx}{dz} = -\frac{\pi}{2}\frac{N\rho_f\delta^2}{G}\frac{d\delta}{dz} \tag{C-11}$$

Since the variations in space and time of the droplet diameter can be related by

$$\frac{d\delta}{dz} = \frac{1}{u_\ell} \frac{d\delta}{dt} \tag{C-12}$$

$$\frac{dx}{dz} = - \frac{\pi}{2} \frac{N\rho_f \delta^2}{u_\ell G} \frac{d\delta}{dt} \tag{C-13}$$

A heat balance on a droplet, assumed to be saturated, yields

$$q_{drop} = \pi\sigma^2 \, q''_{drop} = - h_{fg} \frac{d}{dt} \left(\rho_f \frac{\pi\delta^3}{6} \right) \tag{C-14}$$

or

$$\frac{d\delta}{dt} = - \frac{2 \, q_{drop}}{\pi h_{fg} \rho_f \delta^2} = - \frac{2 \, q''_{drop}}{h_{fg} \rho_f} \tag{C-15}$$

Combining Eqs. C-13 and C-15 and using Eq. C-10 results in

$$\frac{dx}{dz} = \frac{N \, q_{drop}}{u_\ell G \, h_{fg}} = \frac{\pi\delta^2 N q''_{drop}}{u_\ell G \, h_{fg}} = \frac{6(1-x) q''_{drop}}{u_\ell h_{fg} \rho_f \, \delta} \tag{C-16}$$

C.4 HEAT TRANSFER TO THE DROPLETS

Lee and Ryley [C.1] developed a correlation for the average Nusselt number of liquid droplets flowing in a superheated vapor medium

$$\overline{Nu} = \frac{h\delta}{k_v} = 2 + 0.74 \, Re_\delta^{0.5} \, Pr_v^{0.33}$$

The heat flux from the vapor to the droplets can then be written as

$$q''_{vapor \text{ to } drop} = \frac{k_v}{\delta} (2 + 0.74 \, Re_\delta^{0.5} \, Pr_v^{0.33}) \, (T_v - T_{sat})$$

where Re_δ is the droplet Reynolds number defined as

$$Re_\delta \equiv \frac{\rho_v |u_v - u_\ell| \delta}{\mu_v}$$

and Pr_v is the Prandtl number for the superheated vapor.

Since the Nusselt number for a droplet sitting in a pool of stagnant vapor is 2, the vapor-to-droplet convective/conductive heat flux may be written as

$$q''_{\text{vapor to drop}} = \frac{2k_v}{\delta}(T_v - T_{sat})F \tag{C-17}$$

where $F \equiv 1 + 0.37\ Re_\delta^{0.5}\ Pr_v^{0.33}$ is considered as a ventilation factor that accounts for the enhancement of heat transfer due to the relative velocity between the droplets and the surrounding vapor phase.

The radiative heat flux to a droplet is written as:

$$q''_{\text{rad. to drop}} = E\ \sigma_R(T_w^4 - T_{sat}^4) \tag{C-18}$$

where E is a factor including all effects of geometry, emissivities, etc., and must be of the order of magnitude but less than one. E will be calculated later.

The total heat flux to a droplet is then written as

$$q''_{\text{drop}} = q''_{\text{vapor to drop}} + q''_{\text{rad. to drop}}$$

$$= \frac{2k_v}{\delta}(T_v - T_{sat})F + E\ \sigma_R(T_w^4 - T_{sat}^4) \tag{C-19}$$

C.5 RATE OF VAPORIZATION γ AT THE UPSTREAM BOUNDARY OF THE DFFB REGION

At the onset of DFFB the vapor is assumed to be saturated and therefore heat transfer to the droplets will take place only via radiation and direct contact with the wall. Assuming that the major contribution is radiative, results in

$$\Gamma_g^+\Big|_{x_{eq}=x_o} = \gamma = \frac{q''_{w-d}}{q''}\Big|_{x_{eq}=x_o} \tag{C-20}$$

As discussed in Section 2.3.3 the radiative heat flux to all the droplets is given by

$$q''_{w-d} = \mathcal{F}_{w-d}\ \sigma_R(T_w^4 - T_{sat}^4) \tag{C-21}$$

where

$$\mathcal{F}_{w\text{-}d} = \frac{\varepsilon_\ell}{(1-\varepsilon_\ell)\left(1 + \frac{\varepsilon_v}{\varepsilon_w} + \frac{\varepsilon_\ell}{\varepsilon_w(1-\varepsilon_\ell)}\right)} \tag{C-22}$$

with

$$\varepsilon_v = 0.1 \quad , \qquad \varepsilon_\ell = 1 - e^{-a_\ell D_H}$$

and

$$a_\ell = 1.11\,\frac{(1-\alpha)}{\delta}$$

So, the non-dimensional vapor generation rate at the onset of DFFB is given by

$$\gamma = \frac{\mathcal{F}_{w\text{-}d}\ \sigma_R(T_{wo}^4 - T_{sat}^4)}{q''} \tag{C-23}$$

with $x = x_o$, $\delta = \delta_o$, $\alpha = \alpha_o$, $T_w = T_{wo}$ and the total wall heat flux calculated from

$$q'' = q''_{w\text{-}v} + q''_{w\text{-}d} = h_c(T_{wo} - T_{sat}) + \mathcal{F}_{w\text{-}d}\ \sigma_R(T_{wo}^4 - T_{sat}^4) \tag{C-23a}$$

where h_c is calculated from the Heineman correlation with $u_v = u_{vo}$.

In the following development an expression for the heat flux received on the surface of a droplet, q''_{drop}, will also be needed. Writing a radiative heat transfer balance yields,

$$P_H\ q''_{w\text{-}d} = A\ n\ \pi\delta^2\ q''_{\text{rad. to drop}}$$

Using Eq. C-10 to eliminate the droplet number density, $n = N/u_\ell$, yields

$$q''_{\text{rad. to drop}} = \frac{2}{3}\,\frac{\rho_f u_\ell \delta}{G(1-x)D_H}\,q''_{w\text{-}d} = \frac{2}{3}\,\frac{\delta}{D_H}\,\frac{1}{(1-\alpha)}\,q''_{w\text{-}d} \tag{C-24}$$

Inserting Eqs. C-18 and C-21 into Eq. C-24 results in

$$E = \frac{2}{3}\mathcal{F}_{w\text{-}d}\,\frac{\delta}{(1-\alpha)D_H}$$

and

$$q''_{\text{rad. to drop}} = \frac{2}{3}\mathcal{F}_{w\text{-}d}\,\frac{\delta}{(1-\alpha)D_H}\,\sigma_R\,(T_w^4 - T_{sat}^4) \tag{C-25}$$

and finally

$$q''_{drop} = \frac{2k_v}{\delta}\,(T_v - T_{sat})F + \frac{2}{3}\mathcal{F}_{w\text{-}d}\,\frac{\delta}{(1-\alpha)D_H}\,\sigma_R\,(T_w^4 - T_{sat}^4) \tag{C-26}$$

Writing a convective heat transfer balance

$$P_H q''_{v\text{-}d} = A\,\frac{N}{u_\ell}\,\pi\delta^2\,q''_{\text{vapor to drop}}$$

and using Eq. C-10 to eliminate N, results in

$$q''_{v\text{-}d} = \frac{3D_H(1-\alpha)}{\delta^2}\,k_v\,(T_v - T_{sat})F \tag{C-27}$$

C.6 $d\Gamma_g^+/dx_{eq}$ AT THE UPSTREAM BOUNDARY OF THE DFFB REGION

In section C.2, an equation relating $d\Gamma_g^+/dx_{eq}$ to the axial derivative of the partial heat fluxes was derived. Equation C-9 will be used here to calculate $d\Gamma_g^+/dx_{eq}$ at $x_{eq} = x_o$.

Starting from

$$\frac{dq''_{w\text{-}d}}{dz} = \frac{\partial q''_{w\text{-}d}}{\partial \mathcal{F}_{w\text{-}d}}\,\frac{d\mathcal{F}_{w\text{-}d}}{dz} + \frac{\partial q''_{w\text{-}d}}{\partial T_w}\,\frac{dT_w}{dz}$$

$$= \frac{\partial q''_{w\text{-}d}}{\partial \mathcal{F}_{w\text{-}d}}\left[\frac{d\mathcal{F}_{w\text{-}d}}{d\varepsilon_\ell}\,\frac{d\varepsilon_\ell}{da_\ell}\right]\left[\frac{\partial a_\ell}{\partial \alpha}\,\frac{d\alpha}{dz} + \frac{\partial a_\ell}{\partial \delta}\,\frac{d\delta}{dz}\right] + \frac{\partial q''_{w\text{-}d}}{\partial T_w}\,\frac{dT_w}{dz}$$

carrying out all derivatives, and evaluating the results at $z = z_o$, yields

$$\frac{1}{q''}\left.\frac{dq''_{w-d}}{dz}\right|_{z=z_o} = \gamma\left\{\mathcal{F}_{w-d}\left(1+\frac{\varepsilon_v}{\varepsilon_w}\right)\frac{a_\ell D_H}{\varepsilon_\ell^2}\, e^{-a_\ell D_H}\left[\frac{1}{1-\alpha_o}\left.\frac{d\alpha}{dz}\right|_o + \frac{1}{\delta_o}\left.\frac{d\delta}{dz}\right|_o\right]\right.$$

$$\left. + \frac{4T_{wo}^3}{T_{wo}^4 - T_{sat}^4}\left.\frac{dT_w}{dz}\right|_o\right\} \qquad \text{(C-28)}$$

where

$$\left.\frac{d\delta}{dz}\right|_o = \left.\frac{d\delta}{dz}\right|_{z=z_o} = -\left.\frac{2\, q''_{drop}}{u_{\ell o} h_{fg} \rho_f}\right|_{z=z_o} = -\frac{4}{3}\mathcal{F}_{w-d}\,\frac{\delta_o}{(1-\alpha_o)D_H}\,\frac{\sigma_R(T_{wo}^4 - T_{sat}^4)}{u_{\ell o}\, h_{fg}\, \rho_f} \qquad \text{(C-29)}$$

Since, for separated flow

$$(1-\alpha) = \frac{G(1-x)}{u_\ell \rho_f}$$

$$\frac{d(1-\alpha)}{dz} = \frac{\partial(1-\alpha)}{\partial x}\frac{dx}{dz} + \frac{\partial(1-\alpha)}{\partial u_\ell}\frac{du_\ell}{dz}$$

or

$$\left.\frac{d\alpha}{dz}\right|_o = \left.\frac{d\alpha}{dz}\right|_{z=z_o} = \frac{G}{u_{\ell o}\rho_f}\left.\frac{dx}{dz}\right|_{z=z_o} + \frac{G(1-x_o)}{u_{\ell o}^2 \rho_f}\left.\frac{du_\ell}{dz}\right|_{z=z_o} \qquad \text{(C-30)}$$

Assuming that at the onset of DFFB the droplets have zero acceleration

$$\left.\frac{du_\ell}{dz}\right|_{z=z_o} = 0 \qquad \text{(C-31)}$$

Inserting Eq. C-26 into Eq. C-16 and evaluating the result at $z = z_o$ yields

$$\left.\frac{dx}{dz}\right|_{z=z_o} = \frac{4\mathcal{F}_{w-d}}{G h_{fg} D_H}\,\sigma_R(T_{wo}^4 - T_{sat}^4) \qquad \text{(C-32)}$$

Inserting Eqs. C-31 and C-32 into Eq. C-30 yields,

$$\left.\frac{d\alpha}{dz}\right|_o = \frac{4\mathcal{F}_{w-d}}{u_{\ell o}\rho_f h_{fg} D_H}\,\sigma_R(T_{wo}^4 - T_{sat}^4) \tag{C-33}$$

The next term to be evaluated is

$$\frac{dq''_{v-d}}{dz} = \frac{\partial q''_{v-d}}{\partial\alpha}\frac{d\alpha}{dz} + \frac{\partial q''_{v-d}}{\partial\delta}\frac{d\delta}{dz} + \frac{\partial q''_{v-d}}{\partial F}\frac{dF}{dz} + \frac{\partial q''_{v-d}}{\partial T_v}\frac{dT_v}{dz}$$

$$= \frac{\partial q''_{v-d}}{\partial\alpha}\frac{d\alpha}{dz} + \left(\frac{\partial q''_{v-d}}{\partial\delta} + \frac{\partial q''_{v-d}}{\partial F}\frac{\partial F}{\partial\delta}\right)\frac{d\delta}{dz} + \frac{\partial q''_{v-d}}{\partial F}\frac{\partial F}{\partial(u_v - u_\ell)}\frac{d(u_v - u_\ell)}{dz}$$

$$+ \frac{\partial q''_{v-d}}{\partial T_v}\frac{dT_v}{dz}$$

Again, carrying out all derivations and evaluating the result at $z = z_o$, yields

$$\left.\frac{1}{q''}\frac{dq''_{v-d}}{dz}\right|_{z=z_o} = \frac{3\,D_H(1-\alpha_o)k_v F}{\delta_o^2 q''}\left.\frac{dT_v}{dz}\right|_{z=z_o} \tag{C-34}$$

Starting from Eq. C-1 that can be written as

$$\frac{dT_v}{dz} = \frac{Q}{xc_{pv}}\left\{h_{fg} - [c_{pv}(T_v - T_{sat}) + h_{fg}]\Gamma_g^+\right\}$$

results in

$$\left.\frac{dT_v}{dz}\right|_{z=z_o} = \frac{Qh_{fg}}{x_o c_{pv}}(1-\gamma)$$

and inserting this expression into Eq. C-34 results in

$$\left.\frac{1}{q''}\frac{dq''_{v-d}}{dz}\right|_{z=z_o} = \frac{3D_H(1-\alpha_o)k_v F}{\delta_o^2 q''}\frac{Qh_{fg}}{x_o c_{pv}}(1-\gamma) \tag{C-35}$$

Finally inserting Eqs. C-28 and C-35 into Eq. C-9 yields,

$$\beta \equiv \frac{1}{Q}\left.\frac{d\Gamma_g^+}{dz}\right|_{z=z_o} = \frac{\gamma}{Q}\left\{\mathcal{F}_{w\text{-}d}\left(1+\frac{\varepsilon_v}{\varepsilon_w}\right)\frac{a_\ell D_H}{\varepsilon_\ell^2}\, e^{-a_\ell D_H}\left[\frac{1}{1-\alpha_o}\left.\frac{d\alpha}{dz}\right|_o + \frac{1}{\delta_o}\left.\frac{d\delta}{dz}\right|_o\right]\right.$$
$$\left. + \frac{4T_{wo}^3}{T_{wo}^4 - T_{sat}^4}\left.\frac{dT_w}{dz}\right|_o\right\} + \frac{3D_H(1-\alpha_o)k_v F}{\delta_o^2 q''}\frac{h_{fg}}{x_o c_{pv}}(1-\gamma) \qquad \text{(C-36)}$$

where $\left.\frac{d\alpha}{dz}\right|_o$ and $\left.\frac{d\delta}{dz}\right|_o$ are given by Eqs. C-33 and C-29 respectively.

REFERENCE

C.1 D. J. Ryley and K. Lee, "The Evaporation of Water Droplets in Superheated Steam", J. of Heat Transfer, 90, 445-451 (1968).

Appendix D

NUMERICAL SOLUTION OF THE TWO-DIMENSIONAL HEAT CONDUCTION EQUATION IN A FUEL PIN

In the neighborhood of the quench front very steep axial temperature gradients may develop, and in this case axial conduction plays an important role regarding quench front propagation.

This Appendix describes the finite difference technique used to solve the two-dimensional, time-dependent heat conduction equation in an actual nuclear fuel pin configuration. The procedure is general enough to handle fuel pin simulators as well as tubular test sections with internal flow as a particular case.

The temperature dependence of the thermophysical properties is considered, but circumferential temperature variations are neglected. The gap between fuel and cladding is modeled as a simple heat resistance with no heat capacity, and the heat source can be position and time dependent.

The alternating-direction implicit (ADI) numerical scheme developed by Peaceman and Rachford [D.1] is used. This scheme is unconditionally stable but a small time step is required for accurate results.

D.1 FINITE-DIFFERENCE FORMULATION

The heat conduction equation for which a solution is sought is:

$$\frac{1}{r}\frac{\partial}{\partial r}\left(r\, k(r,T)\,\frac{\partial T(r,z,t)}{\partial r}\right) + \frac{\partial}{\partial z}\left(k^*(r,T)\,\frac{\partial T(r,z,t)}{\partial z}\right) + S(r,z,t) = \rho c\,(r,T)\,\frac{\partial T(r,z,t)}{\partial t} \qquad \text{(D-1)}$$

where

$\rho c = g(r,T)$ - volumetric heat capacity

$k(r,T)$ - thermal conductivity

$S(r,z,t)$ - volumetric heat source

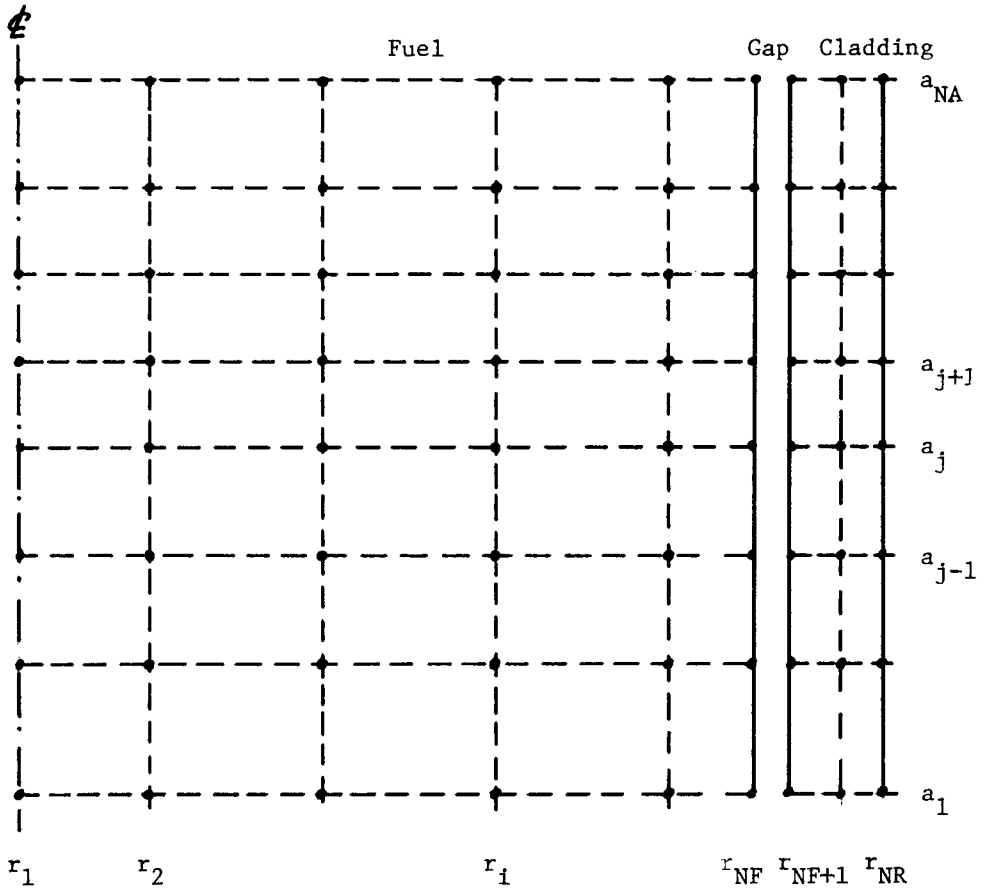

Figure D-1. Mesh point layout for two-dimensional conduction.

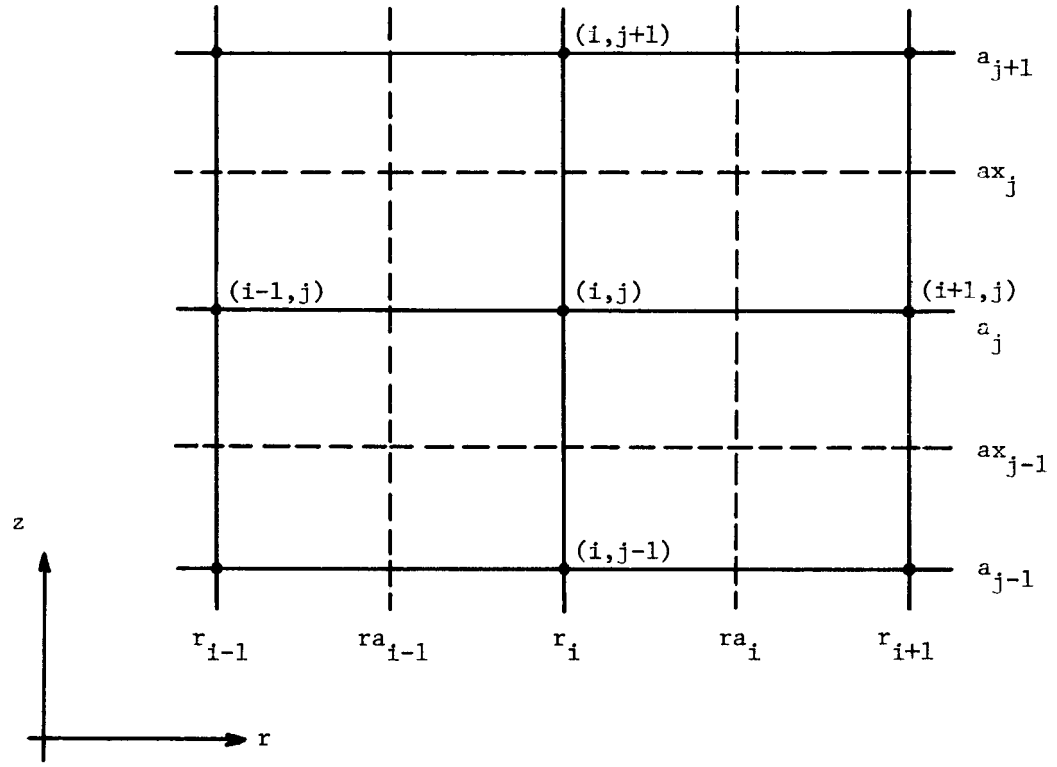

Figure D-2. Typical mesh points for two-dimensional conduction.

Figure D-1 illustrates the layout of mesh points and Fig. D-2 shows details of a typical interior mesh point. The mesh points are represented by dots and the grid by the dashed lines. Subscripts are used to designate space indexes, and superscripts to indicate time indexes. An asterix superscript is used to distinguish the axial from the radial thermal conductivities.

To solve Eq. D-1 numerically, values to each term in the equation are sought at every point in the mesh. Terms containing spatial derivatives are approximated by forward derivatives of the temperatures at adjacent points. The quantities in parentheses in Eq. D-1 are evaluated first at the grid line between the mesh points. It can be shown that a forward difference of the temperatures at adjacent points approximates the first derivative at the grid line by making both forward and backward Taylor expansions of the temperatures at the grid line and subtracting these [D.2]. The thermal conductivity evaluated at the grid line represents a mean value between the two mesh points, as can be obtained by assuming steady, one-dimensional heat conduction to be valid. The approximation of the space derivatives is completed by making a forward difference of the quantities in parentheses which is then evaluated at the mesh points.

Therefore, if $k_{i,j}$ is the mean thermal conductivity in the r-direction between the points (i,j) and (i+1,j) and $T_{i,j}$ is the mean temperature of the area represented by the point (i,j), then

$$r\, k \left.\frac{\partial T}{\partial r}\right|_{\substack{ra_i \\ a_j}} \approx k_{i,j} \frac{T_{i+1,j} - T_{i,j}}{\ell n(r_{i+1}/r_i)} \qquad \text{(D-2)}$$

similarly,

$$r\, k \left.\frac{\partial T}{\partial r}\right|_{\substack{ra_{i-1} \\ a_j}} \approx k_{i-1,j} \frac{T_{i,j} - T_{i-1,j}}{\ell n(r_i/r_{i-1})} \qquad \text{(D-3)}$$

and

$$\frac{1}{r}\frac{\partial}{\partial r}\left(r\,k\,\frac{\partial T}{\partial r}\right)\Bigg|_{\substack{r_i\\a_j}} \approx k_{i,j}\,\frac{T_{i+1,j}-T_{i,j}}{r_i\,\ell n(r_{i+1}/r_i)(ra_i-ra_{i-1})}$$

$$-\,k_{i-1,j}\,\frac{T_{i,j}-T_{i-1,j}}{r_i\,\ell n(r_i/r_{i-1})(ra_i-ra_{i-1})} \equiv \delta_{i,j} \qquad \text{(D-4)}$$

Similarly for the space derivatives in the z-direction

$$k^*\,\frac{\partial T}{\partial z}\Bigg|_{\substack{r_i\\ax_j}} \approx k^*_{i,j}\,\frac{T_{i,j+1}-T_{i,j}}{a_{j+1}-a_j} \qquad \text{(D-5)}$$

$$k^*\,\frac{\partial T}{\partial z}\Bigg|_{\substack{r_i\\ax_{j-1}}} \approx k^*_{i,j-1}\,\frac{T_{i,j}-T_{i,j-1}}{a_j-a_{j-1}} \qquad \text{(D-6)}$$

and

$$\frac{\partial}{\partial z}\left(k^*\,\frac{\partial T}{\partial z}\right)\Bigg|_{\substack{r_i\\a_j}} \approx k^*_{i,j}\,\frac{T_{i,j+1}-T_{i,j}}{(a_{j+1}-a_j)(ax_j-ax_{j-1})}$$

$$-\,k^*_{i,j-1}\,\frac{T_{i,j}-T_{i,j-1}}{(a_j-a_{j-1})(ax_j-ax_{j-1})} \equiv \gamma_{i,j} \qquad \text{(D-7)}$$

The space and time dependence of the source is assumed to be separable, i.e.,

$$S(r,z,t) = P(t)\,R(t)\,Q(z)$$

where P(t) accounts for time changes in the source strength and R(t) and Q(z) are spatial distribution factors in the r and z directions, respectively.

If RDP_i and RDS_i are the radial source distributions at $r = ra_{i-1}$ and $r = ra_i$, respectively, and Q_j is the axial source distribution at $z = a_j$, the volume-averaged finite difference approximation for the source term is,

$$S_{i,j} = P\ Q_j \left[RDP_i \frac{r_i^2 - ra_{i-1}^2}{ra_i^2 - ra_{i-1}^2} + RDS_i \frac{ra_i^2 - r_i^2}{ra_i^2 - ra_{i-1}^2} \right] \tag{D-8}$$

D.2 PEACEMAN-RACHFORD METHOD

In solving two-dimensional partial differential equations, efficiency is a crucial factor. It is therefore highly desirable to be able to take relatively large time steps while maintaining accuracy and stability.

All implicit schemes do remove stability considerations from the time step selection; however, most of these generate a five-diagonal system of algebraic equations to be solved at each time step, resulting in a very time consuming procedure. The implicit alternating-direction scheme developed by Peaceman-Rachford, requires solution of only tri-diagonal systems of algebraic equations and was selected for the present work.

In this scheme, two difference equations are written at each time step, each valid over one-half of the interval. Over the first half of the time step, the space derivative in the z-direction is written as an implicit difference, while the r-space derivative is written as an explicit difference. The difference form of Eq. D-1 for the first half time step then is

$$\frac{T_{i,j}^{n+1/2} - T_{i,j}^{n}}{\frac{\Delta t}{2}} = \delta_{i,j}^{n} + \gamma_{i,j}^{n+1/2} + S_{i,j}^{n} \tag{D-9}$$

For the second half-step the procedure is reversed, i.e., the space derivative in the r-direction is written as an implicit difference, while the z-space derivative is written as an explicit difference resulting in

$$\frac{T_{i,j}^{n+1} - T_{i,j}^{n+1/2}}{\frac{\Delta t}{2}} = \delta_{i,j}^{n+1} + \gamma_{i,j}^{n+1/2} + S_{i,j}^{n+1} \tag{D-10}$$

where Δt is the time step, and the γ and δ's are defined by Eqs. D-4 and D-7 above. Writing Eq. D-9 in full and rearranging, yields

$$A_{i,j}\ T_{i,j-1}^{n+1/2} + B_{i,j}\ T_{i,j}^{n+1/2} + C_{i,j}\ T_{i,j+1}^{n+1/2} = D_{i,j} \tag{D-11}$$

where

$$A_{i,j} = - \frac{k^*_{i,j-1}\Delta t}{2\, g_{i,j}(ax_j - ax_{j-1})(a_j - a_{j-1})}$$

$$C_{i,j} = - \frac{k^*_{i,j}\Delta t}{2\, g_{i,j}(ax_j - ax_{j-1})(a_{j+1} - a_j)}$$

$$B_{i,j} = 1 - A_{i,j} - C_{i,j}$$

$$D_{i,j} = T^n_{i,j} + \frac{k_{i,j}(T^n_{i+1} - T^n_{i,j})\Delta t}{2\, g_{i,j}\, r_i\, \ell n(r_{i+1}/r_i)(ra_i - ra_{i-1})}$$

$$- \frac{k_{i-1,j}(T^n_{i,j} - T^n_{i-1,j})\Delta t}{2\, g_{i,j}\, r_i\, \ell n(r_i/r_{i-1})(ra_i - ra_{i-1})} + \frac{S_{i,j}\Delta t}{2\, g_{i,j}}$$

In writing the above equations, it was implicitly assumed that the thermophysical properties are a slowly varying function of temperature, in the sense that evaluating these using previous-time step temperatures is a good approximation. More specifically, $k^*_{i,j}$ is evaluated at $(T^n_{i,j+1} + T^n_{i,j})/2$, $k_{i,j}$ at $(T^n_{i+1,j} + T^n_{i,j})/2$ and $g_{i,j}$ at $T^n_{i,j}$.

Noting that Eq. D-11 contains unknowns only along column i, and letting j = 1,2,...NA generates a tridiagonal system of equations to be solved for $T^{n+1/2}_{i,j}$ with j = 1,2,...NA. This system of equations is solved by Gaussian elimination as described in Appendix B. Thus, the axial sweeping of each column i generates a system of equations and consequently the computational effort involved in the first half step is to solve NR (i=1,...NR) systems of algebraic equations with NA(j=1,...NA) unknowns each.

Similarly, writing Eq. D-10 in full and rearranging, yields

$$A'_{i,j}\, T^{n+1}_{i,j-1} + B'_{i,j}\, T^{n+1}_{i,j} + C'_{i,j}\, T^{n+1}_{i,j+1} = D'_{i,j} \qquad \text{(D-12)}$$

where

$$A'_{i,j} = - \frac{k_{i-1,j}\Delta t}{2\, g_{i,j}\, r_i\, \ell n(r_i/r_{i-1})(ra_i - ra_{i-1})}$$

$$C'_{i,j} = - \frac{k_{i,j}\Delta t}{2\, g_{i,j}\, r_i\, \ell n(r_{i+1}/r_i)(ra_i - ra_{i-1})}$$

$$B'_{i,j} = 1 - A'_{i,j} - C'_{i,j}$$

$$D'_{i,j} = T^{n+1/2}_{i,j} + \frac{k^*_{i,j}(T^{n+1/2}_{i,j+1} - T^{n+1/2}_{i,j})\Delta t}{2\, g_{i,j}(ax_j - ax_{j-1})(a_{j+1} - a_j)}$$

$$- \frac{k^*_{i,j-1}(T^{n+1/2}_{i,j} - T^{n+1/2}_{i,j-1})\Delta t}{2\, g_{i,j}(ax_j - ax_{j-1})(a_j - a_{j-1})} + \frac{S^{n+1}_{i,j}\,\Delta t}{2\, g_{i,j}}$$

Analogously, the radial sweeping of each row j generates a system of equations and consequently the computational effort involved in the second half step is to solve NA (j=1,...NA) systems of algebraic equations with NR (i=1,...NR) unknowns each.

D.3 FINITE DIFFERENCE APPROXIMATION FOR THE BOUNDARY NODES

In this section the boundary conditions allowed, as well as the finite-difference approximation of these conditions are described

D.3.1 Cladding Outer-Surface Nodes

At the cladding outer surface a convective boundary condition of the form

$$k \left.\frac{\partial T}{\partial r}\right|_{r=r_{NR}} = - H(T - T_c) \qquad \text{(BC-1)}$$

is assumed to exist, where H is a heat transfer coefficient and T_c the coolant temperature.

Therefore, for all nodes in the column i = NR the space derivative in the r-direction is approximated by

$$rk \left.\frac{\partial T}{\partial r}\right|_{\substack{r_{NR} \\ a_j}} = - r_{NR} HO_j\, (T_{NR,j} - TCO_j)$$

where HO_j and TCO_j are the heat transfer coefficient and coolant temperature, respectively, in front of axial node j. Also, as before

$$r\ k\ \frac{\partial T}{\partial r}\bigg|_{\substack{r_{NR-1}\\ a_j}} \approx k_{NR-1,j}\ \frac{T_{NR,j} - T_{NR-1,j}}{\ell n(r_{NR}/r_{NR-1})}$$

and therefore

$$\delta_{NR,j} \equiv \frac{1}{r}\frac{\partial}{\partial r}\left(r\ k\ \frac{\partial T}{\partial r}\right)\bigg|_{\substack{r_{NR}\\ a_j}} \approx -\ HO_j\ \frac{T_{NR,j} - TCO_j}{r_{NR} - ra_{NR-1}}$$

$$- \frac{k_{NR-1,j}(T_{NR,j} - T_{NR-1,j})}{r_{NR}\ell n(r_{NR}/r_{NR-1})(r_{NR} - ra_{NR-1})} \qquad \text{(D-13)}$$

Thus, for the cladding outer-surface nodes, Eq. D-13 is inserted into Eqs. D-9 and D-10 with the proper time superscript to generate the complete finite-difference equation for these nodes.

D.3.2 Top and Bottom Nodes of the Fuel Rod

At the top and bottom ends of the fuel rod the temperature gradients as a function of radial position are required boundary conditions. These boundary conditions can be expressed as

$$\frac{\partial T}{\partial z}\bigg|_{\substack{r_i\\ a_i}} = SLOPB_i \qquad i = 1,2,\ldots NR \qquad \text{(BC-2)}$$

and

$$\frac{\partial T}{\partial z}\bigg|_{\substack{r_i\\ a_{NA}}} = SLOPT_i \qquad i = 1,2,\ldots NR \qquad \text{(BC-3)}$$

where $SLOPB_i$ and $SLOPT_i$ are the prescribed temperature gradients at $z = a_1$ and $z = a_{NA}$ respectively. Thus, at the bottom-end (j=1) the space derivatives in the z-direction are approximated by

$$k^* \frac{\partial T}{\partial z}\bigg|_{\substack{r_i \\ a_1}} = k^*_{i,1}\ SLOPB_i$$

$$k^* \frac{\partial T}{\partial z}\bigg|_{\substack{r_i \\ ax_i}} \approx k^*_{i,1}\ \frac{T_{i,2} - T_{i,1}}{a_2 - a_1}$$

and

$$\gamma_{i,1} \equiv \frac{\partial}{\partial z}\left(k^* \frac{\partial T}{\partial z}\right)\bigg|_{\substack{r_i \\ a_1}} \approx k^*_{i,1}\ \frac{T_{i,2} - T_{i,1}}{(ax_1 - a_1)(a_2 - a_1)} - k^*_{i,1}\ \frac{SLOPB_i}{(ax_1 - a_1)} \qquad \text{(D-14)}$$

Similarly, at the top end (j=NA) the space derivatives in the z-direction are approximated by

$$k^* \frac{\partial T}{\partial z}\bigg|_{\substack{r_i \\ a_{NA}}} = k^*_{i,NA-1}\ SLOPT_i$$

$$k^* \frac{\partial T}{\partial z}\bigg|_{\substack{r_i \\ ax_{NA-1}}} \approx k^*_{i,NA-1}\ \frac{T_{i,NA} - T_{i,NA-1}}{a_{NA} - a_{NA-1}}$$

and

$$\gamma_{i,NA} \quad \frac{\partial}{\partial z}\left(k^* \frac{\partial T}{\partial z}\right)\bigg|_{\substack{r_i \\ a_{NA}}} \approx k^*_{i,NA-1}\ \frac{SLOPT_i}{a_{NA} - ax_{NA-1}} - k^*_{i,NA-1}\ \frac{T_{i,NA} - T_{i,NA-1}}{(a_{NA} - a_{NA-1})(a_{NA} - ax_{NA-1})}$$

(D-15)

D.3.3 Fuel Outer-Surface Nodes

As mentioned previously, the gap between the fuel and the cladding is treated as a simple thermal resistance with no heat capacity. If HG_j is the gap heat transfer coefficient in front of axial node j, the following condition must hold

$$k \frac{\partial T}{\partial r}\bigg|_{\substack{r_{NF} \\ a_j}} = \frac{r_{NF+1}}{r_{NF}} k \frac{\partial T}{\partial r}\bigg|_{\substack{r_{NF+L} \\ a_j}} = - HG_j(T_{NF,j} - T_{NF+1,j}) \qquad \text{(BC-4)}$$

Therefore, for all nodes in column i = NF the space derivatives in the r-direction are approximated by

$$rk \frac{\partial T}{\partial r}\bigg|_{\substack{r_{NF} \\ a_j}} = - r_{NF}\, HG_j(T_{NF,j} - T_{NF+1,j})$$

$$rk \frac{\partial T}{\partial r}\bigg|_{\substack{ra_{NF-1} \\ a_j}} \approx k_{NF-1,j} \frac{T_{NF,j} - T_{NF-1,j}}{\ell n(r_{NF}/r_{NF-1})}$$

and

$$\delta_{NF,j} \equiv \frac{1}{r} \frac{\partial}{\partial r}\left(rk \frac{\partial T}{\partial r}\right)\bigg|_{\substack{r_{NF} \\ a_j}} \approx HG_j \frac{T_{NF,j} - T_{NF+1,j}}{r_{NF} - ra_{NF-1}}$$

$$- k_{NF-1,j} \frac{T_{NF,j} - T_{NF-1,j}}{r_{NF}\ell n(r_{NF}/r_{NF-1})(r_{NF} - ra_{NF-1})} \qquad \text{(D-16)}$$

D.3.4 Cladding Inner-Surface Nodes

Using Eq. BC-4, the space derivatives in the r-direction for all nodes in column i = NF + L are approximated by

$$rk \left.\frac{\partial T}{\partial r}\right|_{\substack{r_{NF+1} \\ a_j}} = r_{NF+1}\ HG_j (T_{NF+1,j} - T_{NF,j})$$

$$rk \left.\frac{\partial T}{\partial r}\right|_{\substack{ra_{NF+1} \\ a_j}} \approx k_{NF+1,j}\ \frac{T_{NF+2,j} - T_{NF+1,j}}{\ell n(r_{NF+2}/r_{NF+1})}$$

and

$$\delta_{NF+1,j} \equiv \frac{1}{r}\frac{\partial}{\partial r}\left(rk\frac{\partial T}{\partial r}\right)\Bigg|_{\substack{r_{NF+1} \\ a_j}} \approx k_{NF+1,j}\ \frac{T_{NF+2,j} - T_{NF+1,j}}{r_{NF+1}\ell n(r_{NF+2}/r_{NF+1})(ra_{NF+1} - r_{NF+1})}$$

$$- HG_j\ \frac{T_{NF+1,j} - T_{NF,j}}{ra_{NF+L} - r_{NF+1}} \qquad \text{(D-17)}$$

D.3.5 Fuel Center-Line Nodes

At the fuel center line the following symmetry boundary condition must hold

$$\left.\frac{\partial T}{\partial r}\right|_{\substack{r_1=0 \\ a_j}} = 0 \qquad \text{(BC-5)}$$

The space derivative in the r-direction can be expanded as

$$\delta \equiv \frac{1}{r}\frac{\partial}{\partial r}\left(rk\frac{\partial T}{\partial r}\right) = k\left(\frac{\partial^2 T}{\partial r^2} + \frac{1}{r}\frac{\partial T}{\partial r}\right) + \frac{\partial k}{\partial r}\frac{\partial T}{\partial r}$$

and at $r = 0$ the second term in the above equation yields an indetermination. Expanding $\frac{\partial T}{\partial r}$ in Taylor series around $r = 0$, yields

$$\frac{\partial T}{\partial r}(r) = \frac{\partial T}{\partial r}(0) + r\frac{\partial^2 T}{\partial r^2}(0) + r^2\frac{\partial^3 T}{\partial r^3}(0) + \ldots$$

thus, for small values of r, since $\frac{\partial T}{\partial r}(0) = 0$ by Eq. BC-5, $\frac{\partial T}{\partial r}(r) \approx r \frac{\partial^2 T}{\partial r^2}(0)$. Therefore,

$$\delta_{1,j} \equiv \frac{1}{r}\frac{\partial}{\partial r}\left(rk\frac{\partial T}{\partial r}\right)\Bigg|_{\substack{r_1 \\ a_j}} \approx 2\,k\,\frac{\partial^2 T}{\partial r^2}\Bigg|_{\substack{r_1 \\ a_j}} \approx 2\,\frac{k_{1,j}}{ra_1}\left[\frac{\partial T}{\partial r}\Bigg|_{\substack{ra_1 \\ a_j}} - \frac{\partial T}{\partial r}\Bigg|_{\substack{r_1 \\ a_j}}\right]$$

but

$$\frac{\partial T}{\partial r}\Bigg|_{\substack{ra_1 \\ a_j}} \approx \frac{T_{2,j} - T_{1,j}}{r_2 - r_1}$$

which finally results in

$$\delta_{1,j} \approx 2\,k_{1,j}\,\frac{T_{2,j} - T_{1,j}}{ra_1(r_2 - r_1)} \qquad \text{(D-18)}$$

D.4 CASE OF A TUBULAR TEST SECTION WITH INTERNAL FLOW

The solution technique described in the previous sections can be easily particularized for the case of a tubular test section with internal flow by simply ignoring the fuel nodes and imposing a convective boundary condition at the cladding inner surface, i.e.,

$$k\frac{\partial T}{\partial r}\Bigg|_{\substack{r_{NF+1} \\ a_j}} = -\,HI_j(T_{NF+1,j} - TCI_j)$$

where NF is set to zero and HI_j and TCI_j are the interior heat transfer coefficient and coolant temperature, respectively, in front of axial node j.

Therefore, for all nodes in column i = NF+1 = 1 the space derivative in the r-direction is approximated by

$$\delta_{1,j} \equiv \frac{1}{r}\frac{\partial}{\partial r}\left(r\,k\,\frac{\partial T}{\partial r}\right)\Bigg|_{\substack{r_1 \\ a_j}} \approx k_{1,j}\,\frac{T_{2,j} - T_{1,j}}{r_1 \ell n(r_2/r_1)(ra_1 - r_1)}$$

$$- HI_j\,\frac{T_{1,j} - TCI_j}{ra_1 - r_1} \qquad \text{(D-19)}$$

Everything else remains the same and as before Eq. D-19 should be inserted into Eqs. D-9 and D-10 with the proper time superscripts to generate the finite-difference equation for the nodes in column i = 1.

REFERENCES

D.1 Peaceman, D. W. and Rachford, H. H., "The Numerical Solution of Parabolic and Elliptic Differential Equations", J. Soc. Indust App. Math., 3, 28-41 (1955).

D.2 McClure, J. A., "TOODEE - A Two-Dimensional, Time-Dependent Heat Conduction Program", IDO-17227 (1967).

Appendix E

THE UCFLOOD COMPUTER CODE

This appendix contains a description of the FORTRAN computer program UCFLOOD and a user's manual. UCFLOOD is a transient thermal-hydraulic code designed to analyze the behavior of a single fuel pin and its associated flow channel under reflooding conditions. It can also be used to analyze a tubular test section with internal flow.

The required boundary conditions are the reflooding velocity and the inlet subcooling of the coolant as a function of time, and also the fuel pin power density as a function of time and position.

The code calculates local flow conditions such as phase velocities and temperatures, quality, void fraction, and heat transfer coefficients throughout the channel, as well as the fuel pin temperature history.

UCFLOOD consists of a main program (FLOOD), fourteen major subroutines (twelve for version 2), eight auxiliary subroutines, and twenty-one functions. It requires about 120,000 words of core memory to load and execute in a CDC system.

In Section E.1 of this appendix a description of the code is presented. Section E.2 gives all the input instructions.

E.1 CODE DESCRIPTION

UCFLOOD was written in modular form in the sense that all major calculations are performed by subroutines. The job of the main program is essentially to call the major subroutines and to print out results.

Figure E-1 shows the sequence of calculations performed by the code, while Fig. E-2 illustrates the calling hierarchy among the various subroutines.

The flow channel is divided in three major control volumes as shown in Fig. E-3. Inside the control volumes the hydrodynamic equations are solved in their quasi-steady-state form, except in the single-phase region (control volume 1) where a transient calculation is performed. The local flow conditions, together with the cladding surface temperature and the positions of the swollen liquid level and of the quench front define the heat transfer coefficients everywhere along the fuel

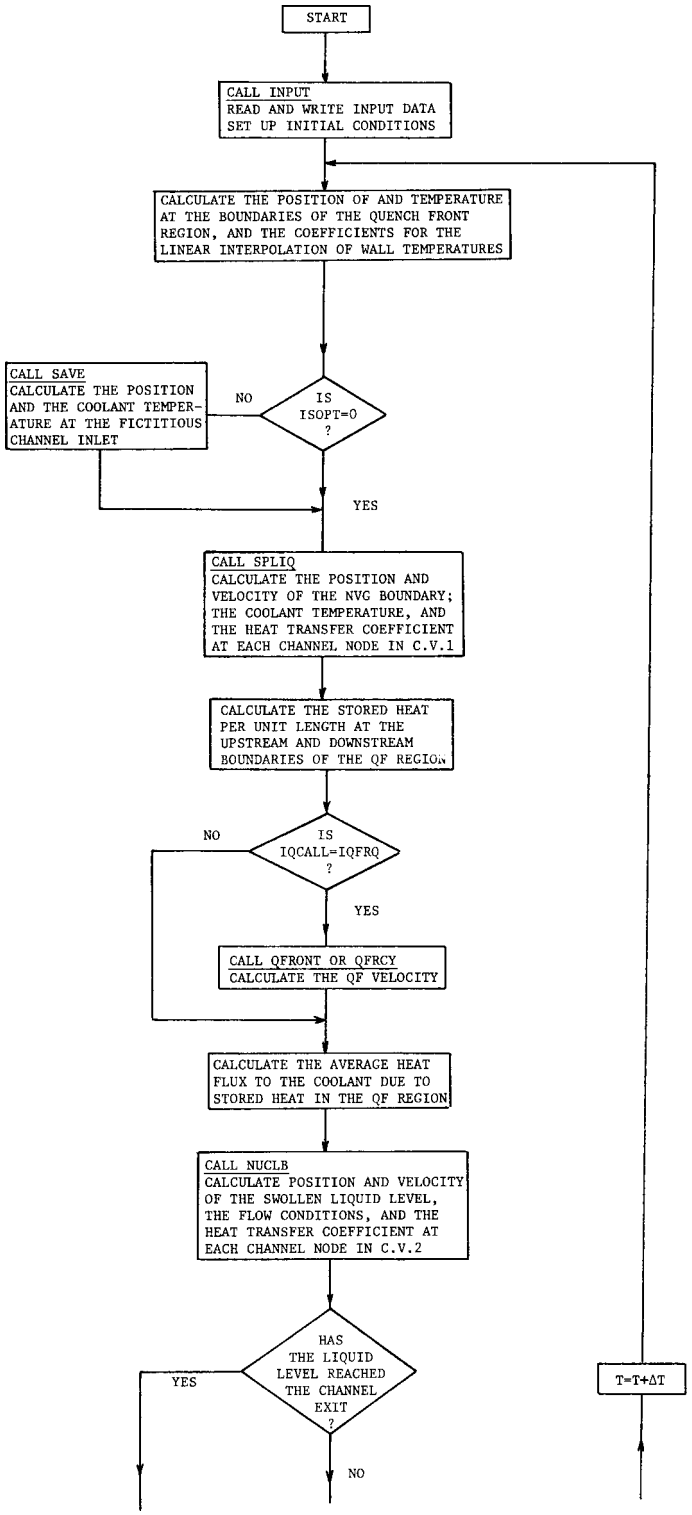

Figure E-1. UCFLOOD flow chart.(Continued in next page).

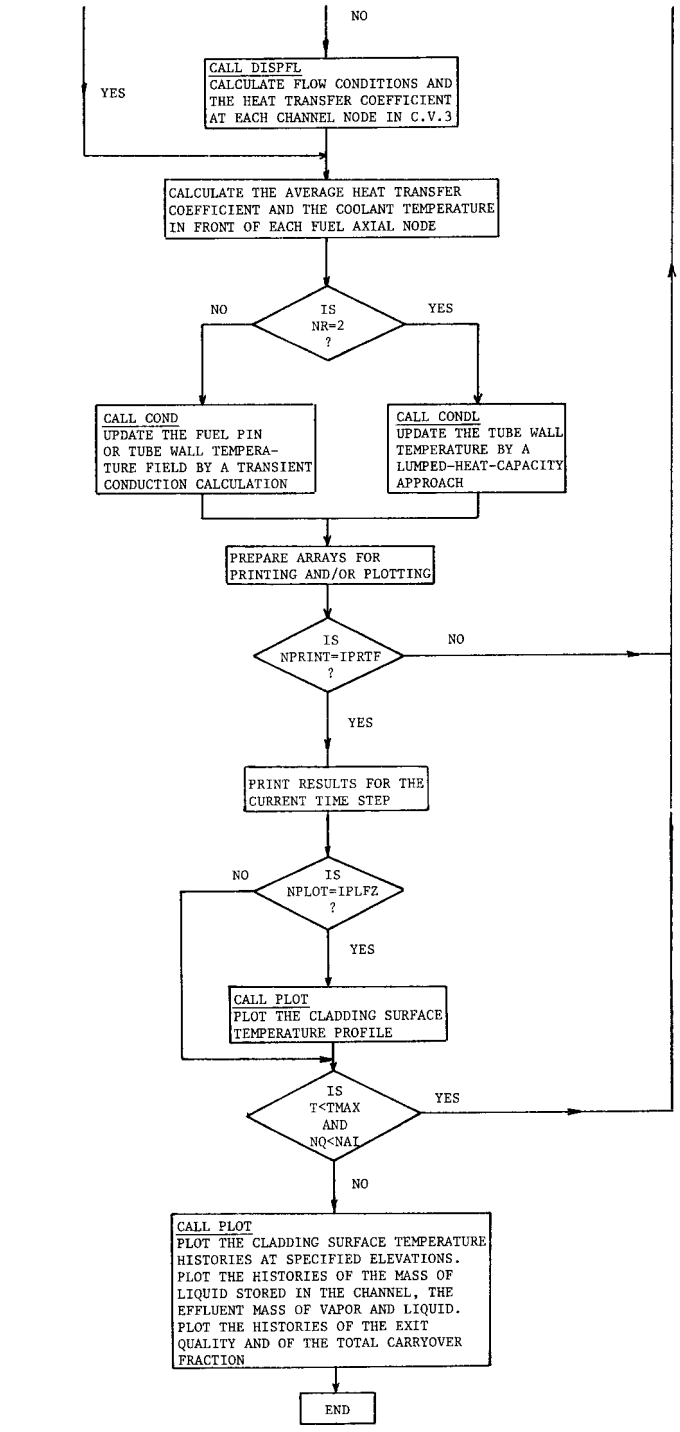

C.V. - CONTROL VOLUME

QF - QUENCH FRONT

Figure E-1. UCFLOOD flow chart. (Continued from previous page)

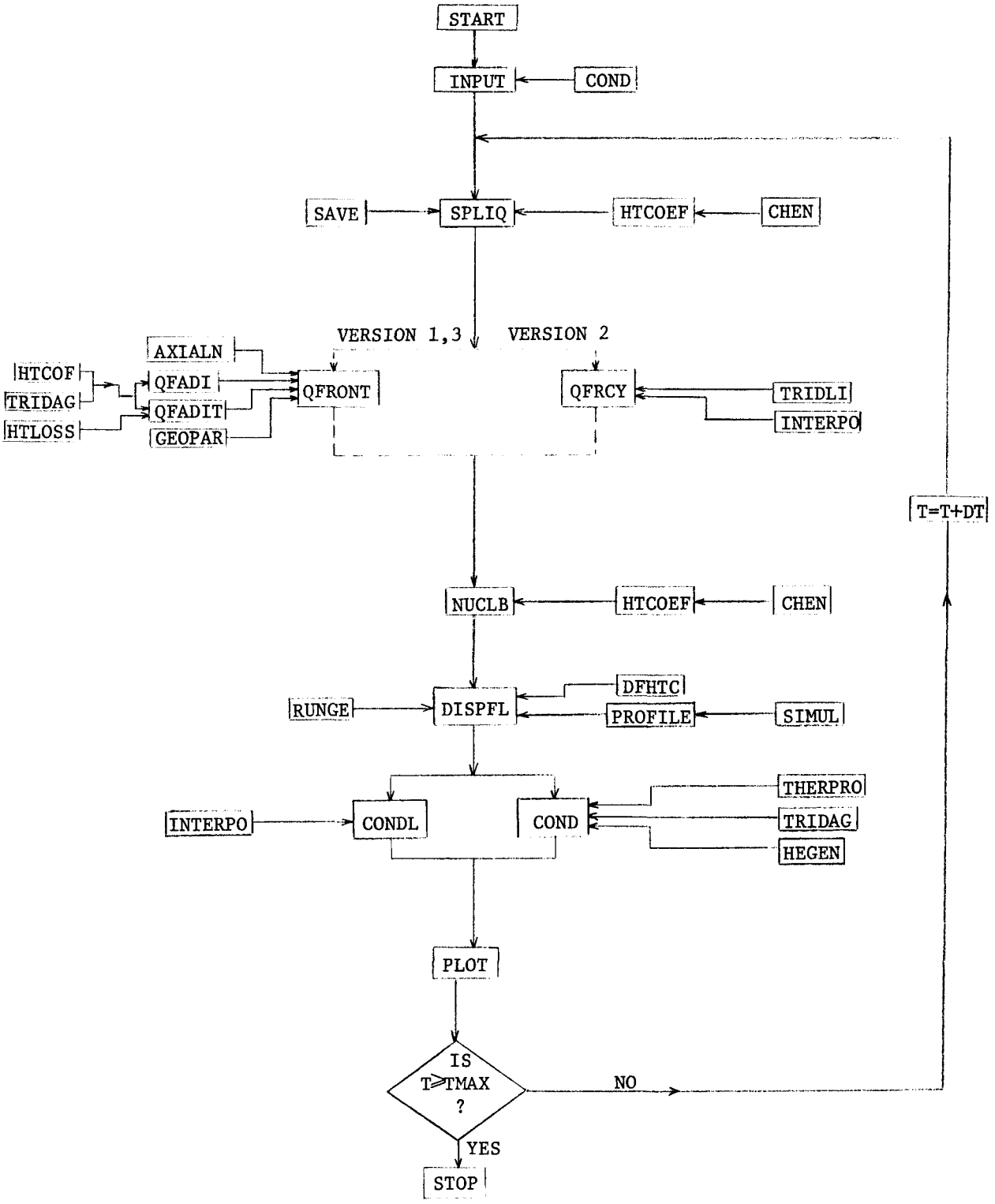

Figure E-2. Code structure and subroutine hierarchy in UCFLOOD.

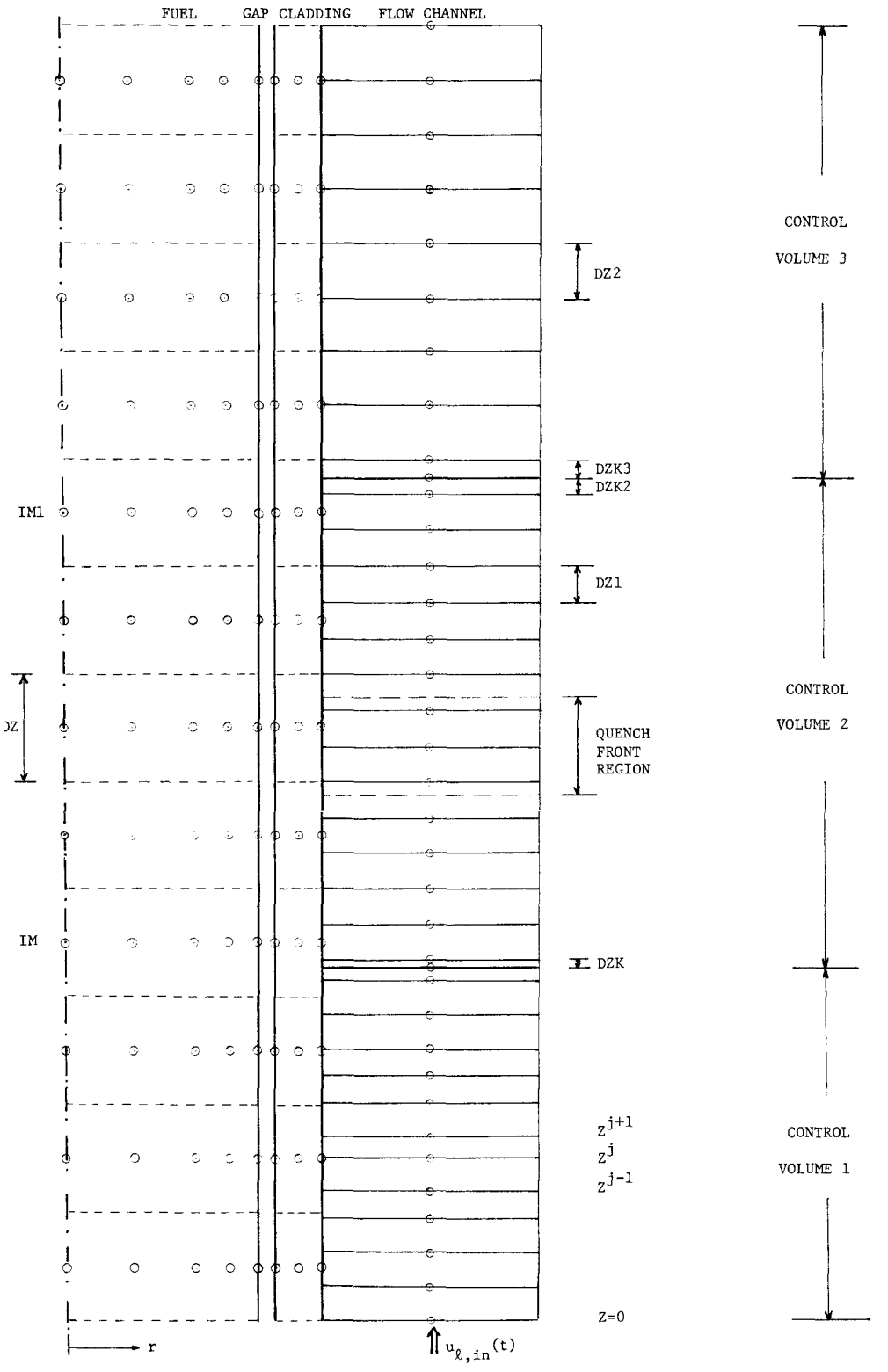

Figure E-3. Nodalization.

pin. These heat transfer coefficients are used as boundary conditions for the radial conduction calculations to update the fuel-pin temperature field. In the quench-front region, however, the special procedure of Chapter 3 is used to calculate the quench front velocity and an average surface heat flux in that region. The updated fuel pin temperature field is used to calculate new local flow conditions which in turn generate new heat transfer coefficients that are used to obtain a new temperature field. These looped calculations are repeated for as many time steps as desired or until the fuel pin is completely quenched.

E.1.1 Hydrodynamic Calculations

E.1.1.1 Control Volume 1 (Subroutine SPLIQ). The Lagrangian equations describing the flow in this control volume were presented in Section 2.1. Since the heat flux, q", is calculated in terms of the local wall and liquid temperatures, Eq. 2-4 is rewritten as

$$c_{pl} \frac{DT_\ell}{Dt} = \frac{P_H h}{\rho_l A_c} (T_w - T_\ell) \qquad \text{(E-1)}$$

where the liquid specific heat is assumed constant and equal to the arithmetic average of the inlet and saturation values.

The heat transfer coefficient h, based on the local liquid temperature is defined from Eq. 2-11 as

$$h = \frac{h_c(T_w - T_\ell) + h_{NB}(T_w - T_{sat})}{(T_w - T_\ell)} \qquad \text{(E-2)}$$

and is calculated by Chen's correlation with x = 0 and F = 1 (Subroutine CHEN). Note that h_{NB} is zero for $T_w < T_{IB}$.

Equations 2-5 and E-1 are then written in the following finite-difference form,

$$\frac{Z^j(t+\Delta t) - Z^j(t)}{\Delta t} = \frac{1}{2}\left[u_\ell^{in}(t+\Delta t) + u_\ell^{in}(t)\right] \qquad \text{(E-3)}$$

and

$$\frac{T_\ell^j(t+\Delta t) - T_\ell^j(t)}{\Delta t} = \frac{1}{2} s\left[T_w^j - T_\ell^j(t+\Delta t)\right] + \frac{1}{2} s\left[T_w^j - T_\ell^j(t)\right] \qquad \text{(E-4)}$$

where

$T_\ell^j(t)$ - temperature of the liquid element j at time t

$Z^j(t)$ - position of the liquid element j at time t

T_w^j - wall temperature at $[Z^j(t+\Delta t) + Z^j(t)]/2$

and

$$s \equiv \frac{P_H h}{\rho_l A_c c_{pl}} = \frac{P_H}{\rho_l A_c P_{cpl}} \left[h_c + h_{NB} \frac{T_w^j - T_{sat}}{T_w^j - T_\ell^j(t)}\right]$$

Rearranging Eqs. E-3 and E-4 results in

$$Z^j(t+\Delta t) = Z^j(t) + \frac{\Delta t}{2}\left[u_\ell^{in}(t+\Delta t) + u_\ell^{in}(t)\right] \qquad \text{(E-5)}$$

and

$$T_\ell^{j+1}(t+\Delta t) = \frac{\left(1 - \frac{s\Delta t}{2}\right)}{\left(1 + \frac{s\Delta t}{2}\right)} T_\ell^j(t) + \frac{s}{\left(1 + \frac{s\Delta t}{2}\right)} T_w^j \quad , \quad j = 1,2,\ldots M \qquad \text{(E-6)}$$

where M is the order of appearance of the liquid elements at the channel entrance, i.e., $Z^M(L) = 0$ and $T_\ell^M(t) = T_\ell^{in}(t)$.

Therefore, if the position and temperature of a liquid element is known at time t, Eqs. E-5 and E-6 give its new position and temperature at time $t + \Delta t$.

At every time step Δt, a new liquid element enters the channel. The liquid elements are numbered according to their chronological order of appearance. Since the liquid is assumed incompressible, all the liquid elements move upwards by the same distance during a time step Δt.

In a Lagrangian description of the flow, where the reflooding velocity $u_\ell^{in}(t)$ is an independent variable, the only way to control the coolant axial grid spacing

(position of the liquid elements) is by adjusting the time step according to the instantaneous liquid velocity. Calling DT the code time step (time step used to update the fuel pin temperature field by radial conduction) and requiring the existence of XNCPFN coolant nodes per fuel axial node (DZ), the maximum time step allowed for subroutine SPLIQ is

$$(\Delta t)_{max} = \frac{DZ}{XNCPFN \cdot u_{\ell}^{in}(t + DT/2)} \tag{E-7}$$

If $(\Delta t)_{max} \geqslant DT$, DT is used as the time step in subroutine SPLIQ. However, if $(\Delta t)_{max} < DT$, the time step to be used by subroutine SPLIQ is defined from

$$NSTEP = INT\left[\frac{DT}{(\Delta t)_{max}} + 1\right]$$

and

$$\Delta t = \frac{DT}{NSTEP}$$

In this case subroutine SPLIQ will perform NSTEP time steps each time it is called by the main program; a new liquid element enters control volume 1 at every time step Δt.

E.1.1.2 Definition of the NVG Boundary. The net vapor generation boundary (Z_{NVG}) is defined by Eq. 2-12 as the axial location where the Nusselt number reaches a critical value, namely 455. As previously mentioned, the liquid elements are numbered according to their order of entrance in the channel. Whenever a liquid element crosses the NVG boundary, i.e., leaves control volume 1, all the elements are reordered so that the position of liquid element number one always coincides with the NVG boundary.

In the process of updating the position and temperature of each liquid element, via Eqs. E-5 and E-6, the local Nusselt number, Nu, is also calculated by Eq. 2-12. After each time step, Δt, the new position of and the liquid temperature at the NVG boundary are obtained as follows.

The fluid elements are scanned and the position of the first fluid element IK for which the Nusselt number exceeds 455 (ZU(IK)) and the corresponding value of the

	XNUN01 < 455 No subcooled boiling in C.V.1	XNUN01 ⩾ 455 NVG boundary in C.V.1
ZU(1) < CPFT(1) Quench front region above C.V.1	LK = 0 No subcooled boiling yet NVG set at downstream boundary of C.V.1	LK = 1 Find exact location of NVG point by linear interpolation (with Nusselt number)
ZU(1) ⩾ CPFT(1) Quench front region overlaps with C.V.1	LK = 2 NVG is set at the upstream boundary of the quench front region.	LK = 3 Find exact location of NVG point by linear interpolation (with liquid temperature). If NVG found to be above CPFT(1) set at CPFT(1).

Figure E-4. Program logic for defining location of and conditions at NVG.

Nusselt number (XNUNO1) are noted. Four cases are then distinguished according to Nu $\gtrless$ 455 and the relative position of ZU(IK) with respect to the position of the quench front CPFT(1), as shown in Fig. E-4.

Case 0: (LK = 0) The Nusselt number associated with liquid element number 1 is less than 455 (XNUNO1 < 455) and the position of this element is below the upstream boundary of the quench-front region defined in Section 3.6.1 (i.e. ZU(1) < CPFT(1)).

This means that subcooled boiling has not started yet. In this case the NVG boundary is set at the downstream limit of control volume 1 and the position (ZNVG) and the liquid temperature (TLNVG) of the NVG boundary are defined as ZNVG = ZU(1) and TLNVG = TCU(1), where TCU(1) is the temperature of liquid element 1.

Case 1: (LK = 1) The Nusselt number associated with liquid elements 1,2,...,IK is larger than 455 and the position of element IK is below the upstream boundary of the quench front region, i.e. XNUNO1 $\geqslant$ 455 and ZU(IK) $\leqslant$ CPFT(1).

In this case the position and the liquid temperature of the NVG boundary are calculated by linear interpolation as shown below:

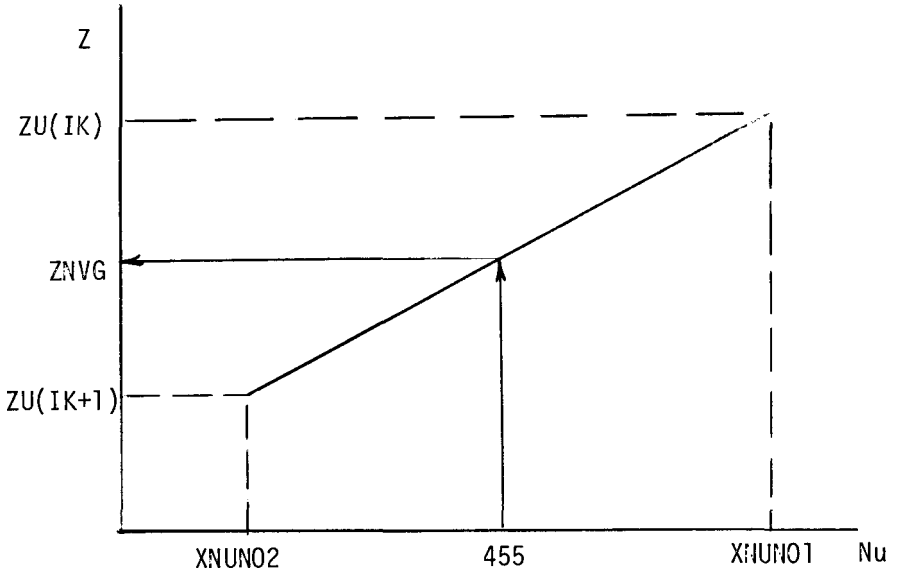

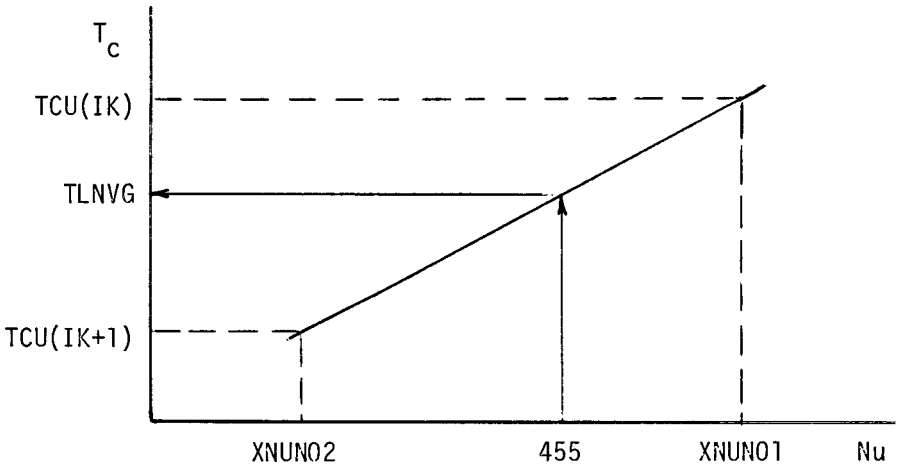

Case 2: (LK = 2) The Nusselt number associated with liquid element number 1 is less than 455 and the position of this element is above the upstream boundary of the quench front region, i.e., XNUO1 < 455 and ZU(IK) > CPFT(1).

In this case the NVG boundary is set at the location of the quench front, i.e. ZNVG = CPFT(1). The liquid temperature at the NVG boundary is calculated by linear interpolation as shown below:

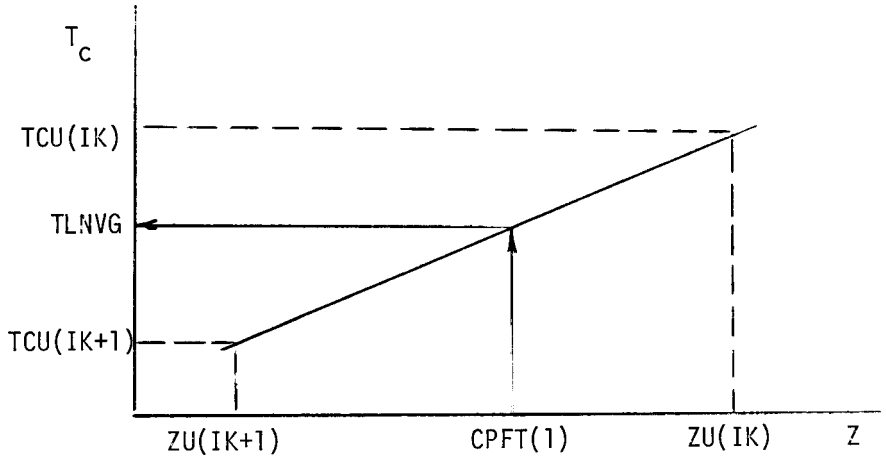

Case 3: (LK = 3) This case is similar to Case 1, with the exception that the element is now above the upstream boundary of the quench front region, i.e., XNUNO1 $\geqslant$ 455 and ZU(IK) $\geqslant$ CPFT(1). In this case the liquid temperature at the NVG boundary is calculated from

$$TLNVG = T_{sat} - \frac{q"(IK)\ D_H}{455\ k_\ell(IK+1)}$$

where q"(IK) is the heat flux to the liquid at node IK. The position of the NVG boundary is calculated by linear interpolation as shown below:

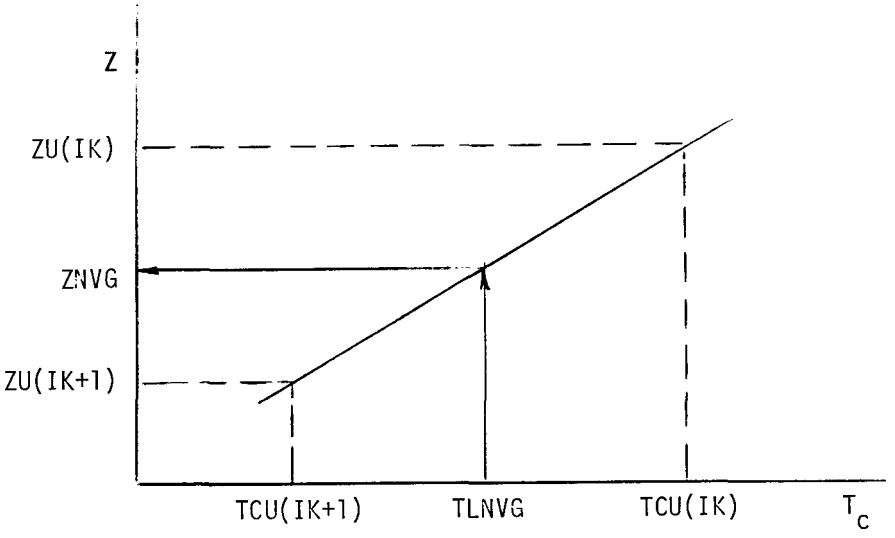

If the position of the NVG boundary, calculated by the procedure above, results in ZNVG > CPFT(1) this becomes a LK = 2 case, and the NVG boundary is set at the location of the upstream boundary of the quench front.

If ZNVG1 is the axial position of the NVG boundary at time t and ZNVG is the position at time t + DT, the velocity of this boundary is defined by

$$DZNVG = \frac{ZNVG - ZNVG1}{DT} \qquad \text{(E-8)}$$

The local cladding surface temperature, T_w^j in Eq. E-6, is calculated by linear interpolation between the cladding surface nodes which are spaced by DZ, as shown in Fig. E-3. Function TWL(Z) performs this operation.

At any time, the number of coolant nodes (i.e. the number of liquid elements) in control volume 1 is called M, and the fuel axial node in which the NVG boundary is located is denoted by IM, i.e., $(IM-1)*DZ \leq ZNVG \leq IM*DZ$.

E.1.1.3 Calculation of the Fictitious Channel Inlet. For the particular cases of constant reflooding rate (inlet velocity) and constant inlet subcooling, a fictitious channel inlet is defined in order to take advantage of the existence of near-steady-state conditions below the NVG boundary, as mentioned in Section 2.1.1.

Subroutine INPUT, while reading-in the input data, selects one of the following three options for calculating the position of the fictitious channel inlet. This selection is based on the number of input data points supplied to the code. The code interprets tabular data input with more than one data point as meaning that the dependent variable is not constant.

ISOPT = 0 - the reflooding rate and/or the inlet subcooling change in time. In this case a true transient will exist all along the channel and the fictitious channel inlet is set at the actual channel inlet (i.e. there is no fictitious channel inlet).

ISOPT = 1 - the reflooding rate and the inlet subcooling are constant, but the power input is a function of time (usually a power decay). In this case the position of the fictitious channel inlet is set at

$$ZBT = DZ*(IM - NA10 - 1)$$

with

$$NA10 = MAX(NA/20, 2)$$

where NA is the number of axial nodes in the fuel and IM is the index of the fuel axial node where the NVG boundary is located. If ZBT is calculated to be less than zero, it is set equal to zero. The liquid velocity at this fictitious channel inlet is equal to the reflooding velocity since the liquid was assumed to be incompressible; the liquid temperature, however, is calculated from

$$T_{\ell}(ZBT,t) = T_{\ell,in} + \frac{\Delta t_o}{\rho_l c_{pl} A_c ZBT} \int_0^{ZBT} q'(t'_o,z)dz$$

where:

Δt_o - liquid transit time from z = 0 to z = ZBT, $\Delta t_o = ZBT/u_{\ell}$

$q'(t'_o,z)$ - linear power input at time t'_o and position z, with $t'_o = t - \Delta t_o/2$.

The evaluation of $T_{\ell}(ZBT,t)$ by the expression above is a good approximation only when the liquid transit time, Δt_o, is only a small fraction of the time constant for the power-input decay. The execution of this option (ISOPT = 1) can be avoided by giving more than one point for the inlet-velocity-versus-time tabular data. (See input CARD(S) #18).

ISOPT = 2 - the reflooding rate, the inlet subcooling, and the linear power input are constant in time. In this case the position of the fictitious channel inlet is calculated as in the ISOPT = 1 case; however, the liquid temperature is simply calculated from:

$$T_{\ell}(ZBT,t) = T_{\ell}(M) + \frac{T_{\ell}(M-1) - T_{\ell}(M)}{Z(M-1) - Z(M)} (ZBT - Z(M))$$

where:

M - index of the first liquid element below ZBT.

$T_{\ell}(M)$ - temperature of liquid element M.

Note that M is also the number of liquid elements in control volume 1, which is now defined as extending from ZBT to ZNVG.

If ISOPT $\neq$ 0, the MAIN program calls subroutine SAVE, which calculates the position of and the liquid temperature at the fictitious channel inlet, before calling subroutine SPLIQ.

E.1.1.4 Control Volume 2 (Subroutine NUCLB). The limits of this control volume are the positions of the NVG boundary and of the swollen liquid level (or onset of

liquid carryover point). The local flow conditions are obtained by solving Eqs. 2-18 to 2-20, and 2-23 to 2-25.

Equation 2-18 is integrated in a stepwise manner as

$$H(Z+\Delta Z) = H(Z) + \frac{P_H \Delta Z}{GA_c} q''\left(Z + \frac{\Delta Z}{2}\right) \tag{E-9}$$

where H(Z) is the bulk enthalpy*.

In this control volume, the saturation liquid properties (ρ_f and c_{pf}) are used since the liquid subcooling at the NVG boundary is already small. Subroutine NUCLB solves Eqs. 2-20 and 2-19 in the following forms

$$T_\ell = T_{sat} - (T_{sat} - T_{\ell,NVG})\ EXP\left[-\frac{H - H_{NVG}}{H_f - H_{NVG}}\right] \tag{E-10}$$

and

$$x = \frac{(H - H_f) + c_{pf}(T_{sat} - T_\ell)}{(H_g - H_f) + c_{pf}(T_{sat} - T_\ell)} \tag{E-11}$$

With this local flow quality, and the void fraction calculated from Eq. 2-23, the local liquid and vapor velocities are calculated from

$$u_\ell = \frac{(1-x)G}{(1-\alpha)\rho_f} \qquad \text{and} \qquad u_g = \frac{xG}{\alpha\rho_g} \tag{E-12}$$

The heat flux from the wall to the coolant needed in Eq. E-9, is calculated from

$$q''\left(Z + \frac{\Delta Z}{2}\right) = h\left[T_W\left(Z + \frac{\Delta Z}{2}\right) - T_\ell(Z)\right] \tag{E-13}$$

where the local heat transfer coefficient h is defined as a function of local flow conditions and relative position with respect to the quench front as follows:

---

*Capital H will be used in this appendix to designate the bulk enthalpy to avoid confusion with the heat transfer coefficient, lower case h.

1) ZNVG < Z < CPFT(1) - In this nucleate-boiling and/or forced-convection-evaporation region, the heat flux is calculated from Eq. 2-29, with the heat transfer coefficient given by Chen's correlation, Eqs. 2-26 to 2-28.

2) CPFT(1) $\leq$ Z $\leq$ CPFT(2) - The boundaries of this quench-front region, namely CPFT(1) and CPFT(2), correspond to $Z_{U'}$, and $Z_{D'}$, respectively, defined by Eq. 3-21. The width of this region ($\Delta Z_{QF} = Z_{D'} - Z_{U'}$) is arbitrarily set equal to the size of the fuel axial nodes DZ (see Fig. E-3).

In the quench front region, the heat flux is calculated from Eq. 3-22, as described in Section 3.6.

3) CPFT(2) < Z < Z_{LEV} - In this inverted-annular and transition-flow region, the heat transfer coefficient is calculated according to the procedure outlined in Section 2.2.2.2.

In all regions, the heat transfer coefficient is calculated by subroutine HTCOEF, except at quench-front region. The local $T_W(Z)$ is provided by the function TWL(Z), by linear interpolation, using the calculated cladding surface temperatures at the adjacent fuel axial nodes.

E.1.1.5 Nodalization in Control Volume 2. After calculating at a given time step, the positions of the NVG boundary (Z_{NVG}) and of the swollen liquid level (Z_{LEV}), the channel nodalization in control volume 2 is obtained by the following procedure:

The size of the coolant nodes, DZ1, is defined by

$$DZ1 = \frac{DZ}{FLOAT(NCPFN1)}$$

where NCPFN1 is an integer larger or equal to one, specified as input, and DZ is the size of the axial nodes in the fuel. For the illustrative case shown in Fig. E-3, NCPFN1 = 3. As a consequence of asking for an integer number of coolant nodes in front of each fuel axial node, in general the first (DZK) and the last (DZK2) coolant nodes in control volume 2 will have a length which is a fraction of DZ1, as shown in Fig. E-3.

The size of the first coolant node is

$$DZK = DELZ - DZ1*INT\left(\frac{DELZ}{DZ1}\right)$$

with

DELZ = DZ*IM - ZNVG

where IM is the index of the fuel axial node at the NVG boundary.

Similarly, the size of the last coolant node is

$$DZK2 = DELZ1 - DZ1*INT\left(\frac{DELZ1}{DZ1}\right)$$

with

DELZ1 = ZLEV - IM*DZ

Note that since ZNVG and ZLEV are time dependent, the coolant nodalization is redefined at every time step.

The number of coolant nodes in control volume 2 is denoted by NNP1, and the fuel axial node at the swollen liquid level is called IM1, i.e., (IM1-1)*DZ $\leqslant$ ZLEV $\leqslant$ IM1*DZ.

E.1.1.6 Swollen Liquid Level, Z_{LEV}. As mentioned in Section 2.2.3, the entrainment correlation being presently used is a step function, i.e. the entrainment fraction E is zero for $\Delta u^- < \Delta u_{crit}$ and one for $\Delta u^- \geqslant \Delta u_{crit}$, where Δu^- is the phase velocity difference just below the liquid level and Δu_{crit} is the critical velocity difference calculated from Eq. 2-35.

First the velocity and the updated position of the swollen liquid level are estimated by Eq. 2-51 and by

$$ZBSU = ZBS + UL(NNP1)*DT \qquad \text{(E-14)}$$

where

ZBS - swollen liquid level position at time t, i.e., ZBS = $Z_{LEV}(t)$

ZBSU - updated position of the swollen liquid level, i.e., ZBSU = $Z_{LEV}(t + DT)$

UL(NNP1) - liquid velocity just below the level at time t, i.e., UL(NNP1) = $\bar{u}_{\ell}(t)$

DT - code time step.

With the updated position of the level, ZBSU, and the position of the NVG boundary $Z_{NVG}(t+DT)$ the procedure described in Section E.1.1.5 is used to define the channel nodalization in control volume 2. Then the flow conditions at all nodes (i = 2,...,NNP1) are calculated using Eqs. E-9 through E-13, plus Eq. 2-33 for the local void fraction.

In calculating these local flow conditions two cases are considered:

1) $\Delta u_i = (u_g - u_\ell)_i < \Delta u_{crit}$, i = 2,...,NNP1

This is the case of no liquid carryover (E = 0) and therefore the initial estimate of the level position remains valid.

2) $\Delta u_{ik} > \Delta u_{crit}$ where $ik \leqslant NNP1$

This is the case of total liquid carryover (E = 1) and the updated position of the swollen liquid level is calculated by linear interpolation as

$$ZBSU = Z_{ik-1} + \frac{Z_{ik} - Z_{ik-1}}{\Delta u_{ik} - \Delta u_{ik-1}} (\Delta u_{crit} - \Delta u_{ik-1}) \qquad \text{(E-15)}$$

where: Z_{ik} - axial position of coolant node IK

and

$$\Delta u_{ik} = (u_g - u_\ell) \quad \text{at} \quad z = Z_{ik}$$

Note that by definition $\Delta u_{ik-1} < \Delta u_{crit}$, and IK becomes the number of coolant nodes in control volume 2, i.e. NNP1 = IK. The flow conditions at ZBSU are calculated similarly by linear interpolation as

$$x_{NNP1} = x_{ik-1} + \frac{x_{ik} - x_{ik-1}}{Z_{ik} - Z_{ik-1}} (ZBSU - Z_{ik-1}) \qquad \text{(E-16)}$$

$$\alpha_{NNP1} = \alpha_{ik-1} + \frac{\alpha_{ik} - \alpha_{ik-1}}{Z_{ik} - Z_{ik-1}} (ZBSU - Z_{ik-1}) \qquad \text{(E-17)}$$

The phase velocities are given by

$$u_{\ell,NNP1} = \frac{(1 - x_{NNP1})G}{(1 - \alpha_{NNP1})\rho_f} \quad , \qquad u_{g,NNp1} = \frac{x_{NNP1}G}{\alpha_{NNP1}\rho_g} \tag{E-18}$$

The above flow conditions correspond to the conditions just below the level, as defined in Section 2.2.5.

E.1.1.7 Mass Flux in Control Volume 2. The mass flux G, used to calculate the flow conditions in control volume 2 is calculated from Eq. 2-41 as G^{-}_{out}.

To calculate G at t + DT, the velocity of the NVG boundary is calculated from Eq. E-8, and the velocity of the swollen liquid level is approximated by a backward difference as

$$\left.\frac{dZ_{LEV}}{dt}\right|_{t+DT} \approx \frac{Z_{LEV}(t) - Z_{LEV}(t - DT)}{DT} \tag{E-19}$$

The last term remaining to be approximated in Eq. 2-41 is the derivative of the integral M(t) that represents the rate of change of the mass contents of control volume 2 per unit of channel cross-sectional area. The integral is approximated by

$$M(t) = \int_{Z_{NVG}(t)}^{Z^{-}_{LEV}(t)} \rho(z,t)dz = \rho_f(Z_{LEV} - Z_{NVG}) - (\rho_f - \rho_g)\int_{Z_{NVG}(t)}^{Z_{LEV}(t)} \alpha(z,t)dz$$

$$\approx \rho_f(Z_{LEV} - Z_{NVG}) - (\rho_f - \rho_g)\left(DZK\,\frac{\alpha_2}{2} + DZ1 \sum_{i=3}^{NNP1-1} \frac{(\alpha_i + \alpha_{i-1})}{2}\right.$$

$$\left. + DZK2\,\frac{(\alpha_{NNP1} + \alpha_{NNP1-1})}{2}\right) \tag{E-20}$$

The time derivative of the integral is again approximated by a backward difference. Gathering together the finite-difference approximations for the various terms of Eq. 2-41 results in

$$G^{-}_{out}(t+DT) = G_{in}(t+DT) - \rho_l \frac{Z_{NVG}(t+DT) - Z_{NVG}(t)}{DT}$$

$$+ \rho_{NNPl} \frac{Z_{LEV}(t) - Z_{LEV}(t-DT)}{DT} - \frac{M(t) - M(t-DT)}{DT} \qquad \text{(E-21)}$$

where

$$\rho_{NNPl} = \rho_f(1-\alpha_{NNPl}) + \rho_g\alpha_{NNPl} \qquad \text{(E-22)}$$

and M(t) is given by Eq. E-20.

The value of $G^{-}_{out}(t+DT)$ calculated above is used together with Eqs. E-9 through E-13, plus Eq. 2-33 to calculate $Z_{LEV}(t+DT)$, $M(t+DT)$, $\rho_{NNPl}(t+DT)$, and the local flow conditions along control volume 2 at t + DT. These new values could have have then been used to obtain a better estimate of the third and fourth terms on the right-hand-side of Eq. E-21 and consequently a better estimate of $G^{-}_{out}(t+DT)$. The process could have then been repeated until convergence was achieved. This procedure was not adopted because, first, the third and fourth terms in Eq. E-21 are usually small compared to the first two terms, and second, an iterative procedure would have increased the computational cost.

E.1.1.8 Mass Flux Leaving Control Volume 2, G_{out}. Two cases are considered again:

1) $\Delta u_{NNPl} < \Delta u_{crit}$ - in this case only vapor is leaving control volume 2 and therefore the mass flux is given by

$$G_{out}(t+DT) = x_{NNPl}G^{-}_{out}(t+DT) = G_{v,out} \qquad \text{(E-23)}$$

2) $\Delta u_{NNPl} \geq \Delta u_{crit}$ - this is the case of total carryover since a step function is being used for the entrainment correlation, i.e. E = 1. Therefore, there is no mass flux discontinuity at the level, and the mass flux calculated from Eq. E-21 is used as the value of G_{out}. However, since now the new position of the swollen liquid level and the mass contents of control volume 2 are available, a better estimate for G_{out} is given by forward finite differences:

$$G_{out}(t+DT) = G_{in} - \rho_l \frac{Z_{NVG}(t+DT) - Z_{NVG}(t)}{DT}$$

$$+ \rho_{NNPl} \frac{Z_{LEV}(t+DT) - Z_{LEV}(t)}{DT} - \frac{M(t+DT) - M(t)}{DT} \qquad \text{(E-24)}$$

The mass fluxes of liquid and vapor leaving control volume 2 and therefore entering control volume 3 are given by

$$G_{v,out} = x_{NNPl}\, G^{-}_{out} \tag{E-25}$$

$$G_{\ell,out} = G_{out} - G_{v,out} \tag{E-26}$$

Note that when Z_{LEV} reaches the channel exit, control volume 3 vanishes and the third term of Eq. E-24 becomes zero.

E.1.1.9 Control Volume 3 (Subroutine DISPFL). The limits of this control volume are defined by the position of the swollen liquid level and the channel exit. The first task performed by subroutine DISPFL is to calculate the flow conditions at the upstream boundary of control volume 3, i.e., just above the swollen liquid level. A subscript o is used in this section to identify quantities at this location.

The mass flux entering control volume 3 is given either by Eq. E-23 or E-24, and it is equal to the mass flux leaving the channel, since it was assumed that there is no mass accumulation in control volume 3.

For the case when liquid carryover is calculated to occur (KENT = 1) the mass fluxes of liquid and vapor entering control volume 3 are given by Eqs. E-25 and E-26, respectively. The flow conditions at the upstream boundary are calculated from:

$$\alpha_o = \alpha_{NNPl} \tag{E-27}$$

$$x_o = \frac{G_{v,out}}{G^{+}_{out}} \tag{E-28}$$

$$u_{\ell o} = \frac{(1 - x_o)G_{out}}{(1 - \alpha_o)\rho_f} \tag{E-29}$$

$$u_{vo} = \frac{x_o G_{out}}{\alpha_o \rho_g} \tag{E-30}$$

where G_{out} is given by Eq. E-24.

The initial droplet size δ_o is calculated from Eq. 2-51 with the liquid and vapor velocities calculated from Eqs. E-29 and E-30, respectively. The vapor temperature of this boundary is assumed to be saturated, i.e., $T_{vo} = T_{sat}$.

For the case of no liquid carryover (KENT = 0) only vapor will flow throughout control volume 3; the quality and the void fraction will be equal to one all along this region. The initial vapor velocity, u_{vo}, is calculated from Eq. E-30 with $\alpha_o = 1$.

The wall heat flux at the upstream boundary is calculated from Eq. 2-75. Function DFHTC calculates the convective heat transfer coefficient h_c as a function of the vapor Reynolds and Prandtl numbers using Heineman's correlation, Eq. 2-70. The radiation heat transfer coefficient is calculated from Eqs. 2-71 through 2-74 with $\delta = \delta_o$, $\alpha = \alpha_o$, and the wall and vapor emissivities, $\varepsilon_w, \varepsilon_v$, given as input. The local wall temperature is provided by the function TWL.

The next step carried out by subroutine DISPFL is to calculate the boundary conditions for the non-dimensional evaporation rate profile Γ_g^+, namely the coefficients γ and β. The following options are available for calculating these two parameters:

1) IDFP = 0 - in this case subroutine EXTPF is called to calculate γ and β. Subroutine EXTPF must be provided by the user.

2) IDFP = 1 - in this case, γ and β are calculated by subroutine DISPFL using the procedure described in detail in Appendix C.

Once γ, β and x_o are known, subroutine PROFILE is called to solve the system of transcendental equations, Eqs. 2-55, yielding a, b and x_R which uniquely define the relationship between the equilibrium and actual qualities through Eq. 2-56.

The computations concerning the non-dimensional evaporation-rate are bypassed in the case of no liquid carryover (KENT = 0).

E.1.1.10 Nodalization in Control Volume 3. The channel nodalization in control volume 3 is similar to that in control volume 2. The size of the coolant nodes DZ2, is defined as

$$DZ2 = \frac{DZ}{FLOAT(NCPFN)} \qquad \text{(E-31)}$$

where NCPFN is an integer number larger or equal to one, specified as input. In the example shown in Fig. E-3, NCPFN = 2.

The number of coolant nodes, of size DZ2, is calculated from

$$NTOT = INT\left(\frac{FLENGT - ZLEV}{DZ2} + 1\right) \tag{E-32}$$

where FLENGT is the length of the entire flow channel and Z_{LEV} is the instantaneous position of the swollen liquid level.

Since again the total number of nodes is not necessarily an integer, a fractional-size first node is defined as

$$DZK3 = FLENGT - ZLEV - NTOT*DZ2 \tag{E-33}$$

The total number of coolant nodes in this control volume is NTOT1 = NTOT + 1.

E.1.1.11 Local Flow Conditions in Control Volume 3. Once the axial nodalization is defined, Eq. 2-57 is integrated in a stepwise fashion, i.e.

$$x_{eq}(Z + DZ2) = x_{eq}(Z) + \frac{P_H DZ2}{G_{out} A_c h_{fg}} q''\left(Z + \frac{DZ2}{2}\right) \tag{E-34}$$

The wall heat flux is calculated from Eq. 2-75 as

$$q''(Z + DZ2) = h_c\left[T_w\left(Z + \frac{DZ2}{2}\right) - T_v(Z)\right] + h_r\left[T_w\left(Z + \frac{DZ2}{2}\right) - T_{sat}\right]$$

where:

T_w - cladding (wall) surface temperature provided by interpolation by the function TWL

T_v - bulk vapor temperature

First, h_c is calculated by the function DFHTC, and h_r from Eqs. 2-71 through 2-74 using the local flow conditions at the immediately upstream coolant node.

Next, with the equilibrium quality calculated from Eq. E-34, the actual quality, the bulk vapor temperature, and the droplet diameter are calculated from Eqs. 2-56, 2-58, and 2-64, respectively.

Two options are available for calculating the droplet velocity u_f:

1) ITVOPT = 0 - in this case the liquid velocity is calculated by assuming that the droplets acquire immediately the terminal velocity (i.e. the relative velocity with respect to the vapor) corresponding to their local diameter. First the drag coefficient is calculated by combining Eqs. 2-66, 2-67, and 2-68 , resulting in

$$C_D = \left\{ \frac{27}{\left[\frac{\rho_v \delta}{\mu_v}\right]^{0.84} \left[\frac{4}{3} \frac{\delta(\rho_f - \rho_v)g}{\rho_v}\right]^{0.42}} \right\}^{1.7241} \qquad \text{(E-35)}$$

where δ is the local droplet diameter, ρ_v and μ_v are the local density and viscosity of the vapor calculated at the local vapor bulk temperature. If the value of the drag coefficient calculated from Eq. E-35 is less than 0.44, C_D is set equal to 0.44. Next, Eqs. 2-62 and 2-68 are combined and solved for the liquid velocity, resulting in

$$u_f = 0.5\left(B + \sqrt{B^2 + 4C}\right) \qquad \text{(E-36)}$$

where

$$B = \frac{(1-x)G_{out}}{\rho_f} + \frac{x\, G_{out}}{\rho_v} - \sqrt{\frac{4}{3} \frac{\delta(\rho_f - \rho_v)g}{C_D \rho_v}}$$

$$C = \frac{x\, G_{out}}{\rho_v} \sqrt{\frac{4}{3} \frac{\delta(\rho_f - \rho_v)g}{C_D \rho_v}}$$

2) ITVOPT = 1 - in this case the liquid velocity is calculated by integrating the droplet equation of motion. Combining Eqs. 2-56, 2-64, E-35, and C-3 with Eq. 2-65, the droplet equation of motion is written in terms of u_f and x_{eq} only, i.e.,

$$\frac{du_f}{dx_{eq}} = f(x_{eq}, u_f) \qquad \text{(E-37)}$$

Knowing $u_g(Z)$, $x_{eq}(Z)$ and $x_{eq}(Z + DZ2)$, Eq. E-37 is integrated to find $u_f(Z + DZ2)$ by the function RUNGE, which uses a 4th-order Runge-Kutta method.

Finally, with the liquid velocity calculated from Eq. E-36 or Eq. E-37, the vapor velocity is calculated from Eq. 2-62 and the void fraction from Eq. 2-69.

For the case of no liquid carryover (KENT = 0) or for the coolant nodes at which the actual quality $x > 0.999$, the above sequence of calculations is simplified. In this case the wall heat flux is still calculated from Eq. E-34 but with $h_r = 0$. The vapor temperature is then calculated by a stepwise integration of Eq. C-1, i.e.

$$T_v(Z + DZ2) = T_v(Z) + \frac{P_H DZ2}{G_{out} A_c c_{pv}} q''\left(Z + \frac{DZ2}{2}\right) \tag{E-38}$$

where c_{pv} is the vapor specific heat evaluated at $T_v(z)$. The local vapor velocity is then calculated from

$$u_v(Z + DZ2) = \frac{G_{out}}{\rho_v} \tag{E-39}$$

The sequence of calculations described above is repeated for all coolant nodes in control volume 3.

E.1.1.12 Average Heat Transfer Coefficient and Coolant Temperature at Fuel Axial Nodes. As shown in Fig. E-3, the number of coolant nodes in the flow channel is larger than the number of axial nodes in the fuel pin. Therefore, for the purpose of updating the fuel pin temperature field by radial conduction, it is necessary to define an average heat transfer coefficient and an average coolant temperature for each fuel axial node.

The time-dependent number of coolant nodes in control volumes 1, 2 and 3 were denoted by M, NNP1 and NTOT1, respectively; therefore the total number of coolant nodes in the flow channel is given by

$$IT = M + NNP1 + NTOT1 \tag{E-40}$$

In the process of calculating the local flow conditions, the position, coolant temperature, and wall heat flux associated with each of these nodes were stored in arrays ZAXL(I), TCZ(I), QFLUXZ(I), for I = 1,...,IT, respectively. Early during execution, the array ZZT(I) = J*DZ, J = 1,...,NA is created to define the axial positions of the boundaries of the NA fuel axial nodes.

The average coolant temperature and wall heat flux in front of fuel axial node I are calculated from

$$TCO(I) = \frac{\sum_{J=NL}^{NT} \frac{TCZ(J) + TCZ(J-1)}{2} \left(ZAXL(J) - ZAXL(J-1)\right)}{ZAXL(NL-1) - ZAXL(NT)} \tag{E-41}$$

$$QM(I) = \frac{\sum_{J=NL}^{NT} QFLUXZ(J-1) \left(ZAXL(J) - ZAXL(J-1)\right)}{ZAXL(NL-1) - ZAXL(NT)} \tag{E-41a}$$

where NL is the index of the first coolant node for which ZAXL(NL) > ZZT(I-1). Similarly, NT is the index of the first coolant node for which ZAXL(NT) $\geqslant$ ZZT(I).

The average heat transfer coefficient for fuel axial node I is then calculated from

$$HO(I) = \frac{QM(I)}{TW(I) - TCO(I)} \tag{E-42}$$

where TW(I) is the cladding surface temperature of fuel axial node I. The values of HO and TCO are supplied to subroutine COND for the radial conduction calculations.

E.1.2 Radial Conduction Calculations

In this section, details concerning the one-dimensional radial conduction solution used to obtain the fuel pin (or tube wall) temperature history are presented. The numberical scheme used to solve the one-dimensional conduction equation is described in Appendix B. As far as geometry is concerned, two cases are allowed:

1) IGEOM = 1 - the fuel pin is a cylindrical rod consisting of fuel, gap and cladding with heat removal at the cladding outer surface;

2) IGEOM = 0 - the heater is a tubular test section with heat removal by the coolant at the inner surface and heat losses at the outer surface.

E.1.2.1 Heat Generation in the Fuel Pin. The heat generation in the fuel pin is considered as a function of time and space. The time and space dependences in each direction (r and z) are assumed to be separable, i.e.

$$S(r,z,t) = S_{max}P(t)R(r)Z(z) \qquad \text{(E-43)}$$

where S_{max} is the maximum source strength (PO), P(t) (SD) is a normalized power decay curve, and R(r) and Z(z) (RDP,RDS) are normalized source distribution factors in the r and z directions, respectively.

The normalized time and space distributions are inputed as two-dimensional tables of normalization factors versus spatial or time coordinate. The spatial distribution factors are calculated at the actual node locations by linear interpolation of these tables. The power-decay normalization factor, however, is calculated by an exponential interpolation. Subroutine INTERPO performs these interpolations, linearly if IFLAG = 0 or exponentially if IFLAG = 1.

The power decay curve can also be calculated internally using the proposed ANS-Standard decay heat curves [E1] (LOPT = 1). In the ANS decay heat curve the energy release is considered to come from two sources: fission product decay and actinide decay.

The fission-product decay heat is given by:

$$\frac{P_{FP}}{P_o}(t_o,t_s) = \frac{P_{FP}}{P_o}(\infty,t_s) - \frac{P_{FP}}{P_o}(\infty,t_o+t_s) \qquad \text{(E-44)}$$

where

$\frac{P_{FP}}{P_o}$ - fraction of the reactor operating power

t_s - cooling time after shutdown in seconds (TBLOW)

t_o - reactor operating time in seconds (TOPER)

and

$$\frac{P_{FP}}{P_o}(\infty,t) = At^{-a} \qquad \text{(E-45)}$$

with the coefficients A and a obtained from,

Time Interval (s)	A	a
$10^{-1} \leq t \leq 10^{1}$	0.0603	0.0639
$10^{1} < t \leq 15 \times 10^{2}$	0.0766	0.181
$15 \times 10^{2} < t \leq 4 \times 10^{6}$	0.130	0.283
$4 \times 10^{6} < t \leq 2 \times 10^{8}$	0.266	0.335

The actinides considered by the ANS Standard are Uranium-239 and Neptunim-239; their contribution to the decay heat is calculated from:

For ^{239}U:

$$\frac{P_{29}}{P_o} = 2.28 \times 10^{-3}\, C\, \frac{\sigma_{25}}{\sigma_{f25}} \left[1 - \exp\left(-4.91\times10^{-4} t_o\right)\right] \exp\left(-4.91\times10^{-4} t_s\right) \qquad \text{(E-46)}$$

For ^{239}Np:

$$\frac{P_{39}}{P_o} = 2.17 \times 10^{-3}\, C\, \frac{\sigma_{25}}{\sigma_{f25}} \left\{7.0\times10^{-3}\left[1 - \exp\left(-4.9\times10^{-4} t_o\right)\right]\right.$$
$$\times \left[\exp\left(-3.4\times10^{-6} t_s\right) - \exp\left(-4.91\times10^{-4} t_s\right)\right]$$
$$\left. + \left[1 - \exp\left(-3.41\times10^{-6} t_o\right)\right]\left[\exp\left(-3.41\times10^{-6} t_s\right)\right]\right\} \qquad \text{(E-47)}$$

where

C - conversion ratio, atoms of ^{239}Pu produced per atom of ^{235}U consumed (CR)

σ_{25} - effective neutron absorption cross section of ^{235}U (CS25)

σ_{f25} - effective neutron fission cross section of ^{235}U (FCS25)

Therefore the total ANS normalized power decay curve is given by

$$P(t) = \frac{P_{FP}}{P_o}(\infty, t_s) - \frac{P_{FP}}{P_o}(\infty, t_o + t_s) + \frac{P_{29}}{P_o} + \frac{P_{39}}{P_o} \qquad \text{(E-48)}$$

where P_o is the reactor operating power density (equal to S_{max} in terms of Eq. E-43). Subroutine HEGEN calculates the heat generation rate (Btu/ft^{3}s) in the fuel as a function of time and position by the procedure described above.

E.1.2.2 Thermal Properties of the Fuel Pin. The fuel pin or heater thermal properties, namely the thermal conductivity and the specific heat, are considered to be functions of temperature. Subroutine THERPRO calculates these thermal properties in the fuel and in the cladding (or tube wall) by one of the following alternatives:

1) By linear interpolation of input tables of temperature versus thermal property (IOPT = 0).

2) By using internally available numerical fits of the thermal properties (IOPT $\neq$ 0). Numerical fits are available for the following fuel pin models:

A) UO_2--Zircalloy-4 fuel pin model (IOPT = 1)

Thermal Conductivities (Btu/ft s °F)

- $$k_{UO_2} = \frac{1}{3600}\left[\frac{3978.1}{T+629.61} + (6.0237\times10^{-12})(T+460)^3\right] \qquad \text{(E-49)}$$

  for $77°F < T < 5072°F$

- $$k_{Zr} = \frac{1}{3600}\left[4.14 + 1.044\times10^{-2}T - 5.26\times10^{-6}T^2 + 1.536\times10^{-9}T^3\right] \qquad \text{(E-50)}$$

Specific Heats (Btu/lbm °F)

- $$c_{p,UO_2} = 7.26 \times 10^{-2} + 3.33 \times 10^{-6}T - \frac{4.74\times10^3}{(T+460)^2} \qquad \text{(E-51)}$$

  for $77°F < T < 2240°F$

$$c_{p,UO_2} = -0.18426 + 3.8303 \times 10^{-4}T - 2.0447 \times 10^{-7}T^2 + 4.6457 \times 10^{-11}T^3 - 3.6289 \times 10^{-15}T^4 \qquad \text{(E-51a)}$$

for $2240°F \leq T \leq 5072°F$

- $c_{p,Zr} = 6.80 \times 10^{-2} + 1.33 \times 10^{-5}T$ (E-52)

  for $77°F < T < 1376°F$

  $c_{p,Zr} = 8.60 \times 10^{-2}$ $T > 1376°F$ (E-52a)

Densities (lbm/ft^3)

- $\rho_{UO_2} = 623.0$

- $\rho_{Zr} = 409.0$

All the above numerical fits were obtained from reference [E2].

B) Boron Nitride (BN) - Stainless Steel (SS) FLECHT fuel pin model (IOPT = 2)

Thermal Conductivities (Btu/ft s °F)

- $k_{BN} = (14.778-0.0008889T)/3600$ (E-53)

- $k_{SS} = (8.4+0.0042T)/3600$ (E-54)

Specific Heats (Btu/lbm °F)

- $c_{p,BN} = 0.48193 - 0.333492 \exp(-0.0013611T)$ (E-55)

- $c_{p,SS} = 0.106 + 3.833 \times 10^{-5}T$ for $T < 599°F$ (E-56)

  $c_{p,SS} = 0.1157 + 2.2143 \times 10^{-5}T$ for $T \geqslant 599°F$ (E-56a)

Densities (lbm/ft^3)

- $\rho_{BN} = 124.8$

- $\rho_{SS} = 501.0$

All the above properties were obtained from reference [E3].

C) Boron Nitride - Zircalloy FLECHT fuel pin model (IOPT = 3)

In this case the thermal properties are calculated from Eqs. E-53, E-55, E-50 and E-52,52a.

E.1.2.3 External Loss Heat Transfer Coefficient. For the case of a tubular test section with internal flow (IGEOM = 0), the loss heat transfer coefficient at the outer surface of the tube is calculated by the function HTLOSS as

$$HTLOSS(T_w) = CLOSS(1) + CLOSS(2)T_w + CLOSS(3)T_w^2 + CLOSS(4)T_w^3 \qquad (E\text{-}57)$$

where

T_w - wall outer-surface temperature (°F)

CLOSS(I), I = 1,4 - polynomial fit coefficients

The dimensions of CLOSS(I) must be such that HTLOSS results in Btu/ft^2 s °F.

E.1.2.4 Fuel-Pin Temperature-Field Initialization and Update. The instantaneous fuel pin temperature field is stored in the array TF(I,J), I = 1,NR, J = 1,NA where NR and NA are the number of radial and axial fuel nodes, respectively.

Three options are available for initializing this temperature field:

1) The initial fuel pin temperatures are read in as input (JOPT = 0). In this case, three suboptions are available:

A) INTF = 1 - in this case the temperature field is radially and axially uniform. Only the value of TF(1,1) needs to be read in; subroutine INPUT will initialize the entire field with this value.

B) INTF = 2 - in this case the temperatures in each axial node are radially uniform. Only the values TF(I,J), J = 1,NA need to be read in; subroutine INPUT will initialize the radial profile at each axial node using TF(I,J), J = 1,NA.

C) INTF = 3 - in this case the temperature value at each node is read in.

2) Initialization based on the axial power input profile (JOPT = 1). This option is only available for fuel rod geometry (IGEOM = 1).

First, a steady-state heat transfer coefficient at the midplane elevation is defined as

$$h_{6ft} = \frac{q'_{6ft}}{\pi D_r (T_{w,6ft} - T_{sat})} \qquad \text{(E-58)}$$

where

q'_{6ft} - initial linear power input at midplane elevation (PO)

D_r - fuel rod diameter

$T_{w,6ft}$ - initial fuel pin surface temperature at the midplane elevation (TW6FT)

The above heat transfer coefficient is then used to initialize the radial temperature profile at each fuel pin axial node by a steady-state conduction calculation.

3) Initialization based on a chopped-sine distribution (JOPT = 2). This option is also only available for IGEOM = 1.

In this case the heat transfer coefficient defined by Eq. E-58 is used to obtain the radial temperature profile at the midplane-elevation axial node. Then the temperature profile at all other locations is obtained from

$$T_{i,j} = T_{i,\frac{NA}{2}} \sin\left[\frac{\pi(j\Delta Z + \delta)}{L}\right] \qquad \begin{matrix} i = 1,2,\ldots NR \\ j = 1,2,\ldots NA \end{matrix}$$

where

NR - number of radial nodes in the fuel pin

NA - number of axial nodes in the fuel pin

L - total fuel-pin length (usually 12 ft)

$T_{i,NA/2}$ - initial temperatures in node (i,NA/2) obtained by a steady-state calculation

Note that $T_{NR,NA/2} = T_{w,6ft}$. The quantity is calculated from

$$\delta = \frac{L \sin(T_{w,oft}/T_{w,6ft})}{\pi - 2 \sin(T_{w,oft}/T_{w,6ft})} \qquad \text{(E-59)}$$

where $T_{w,oft}$ is the surface temperature at elevation zero, and is given as input (TWOFT).

The fuel pin temperature field is updated by calling subroutines COND or CONDL that solve the radial conduction equation using the numerical schemes described in Appendix B. Subroutine CONDL is only called if IGEOM = 0 and NR = 2.

The solution is performed independently for each axial node. COND first calls subroutine THERPRO to calculate the thermal properties at the various radial nodes, then calls subroutine HEGEN to obtain the heat generation rate distribution. With this information, it calculates the coefficients of the resulting system of tridiagonal equations and calls subroutine TRIDAG to solve this system, as described in Appendix B.

E.1.3 Quench Front Velocity

Three methods are available in UCFLOOD for calculating the quench-front velocity. These vary in their degree of sophistication, and consequently of computational effort.

E.1.3.1 First Version. The quench front position as a function of time is given as input. This method is useful for investigating the effect of various heat transfer coefficient correlations in predicting temperature histories above and below the actual location of the quench front region. Also, it is useful for carrying out parametric studies of the effect of the various adjustable parameters used to predict the local flow conditions without interference from uncertainties due to quench front position.

The quench front position as a function of time is read in as described in Section E.2, CARD(s) #31. To use this method, the option parameter IQFRQ (subroutine QFRONT calling frequency) should be specified as zero in input CARD #2. Subroutine QFRONT will calculate the quench front velocity at every code time step from

$$U(t) = \frac{Z_q(t+2) - Z_q(t-2)}{4} \qquad \text{(ft/s)} \qquad \text{(E-60)}$$

where $Z_q(t)$ is the quench front position (ft) and t is the current time (s). The values of $Z_q(t+2)$ and $Z_q(t-2)$ are calculated by linear interpolation of the input table of quench front position versus time.

E.1.3.2 Second Version. The quench front velocity is calculated using the Yu/Farmer/Coney [54,55] method described in Section 3.4.2. This method as presently programmed is only applicable to tubular test sections at atmospheric pressure.

Yu et al. correlated the heat transfer coefficient at the quench front as a function of the average coolant velocity and subcooling at the quench front. They assumed that heat losses and heat generation rate in the wall have no effect on the quench front propagation. This assumption is proven to be reasonable by the favorable comparison of UC-B quench-front data with their correlation, as shown in Fig. 3-6.

From Coney's theoretical results the Peclet number (which is a non-dimensional quench front velocity) was plotted versus a non-dimensional wall temperature, with the Biot number as a parameter, as shown in Fig. E-5.

The three non-dimensional parameters are defined as

$$w \equiv \frac{1}{Pe} \equiv \frac{k}{\rho c\ \varepsilon\ U} \tag{E-61}$$

$$Bi \equiv \frac{h\varepsilon}{k} \equiv \frac{\varepsilon\ F_q^2}{k(T_q - T_{cq})^2} \tag{E-62}$$

and

$$\eta \equiv \frac{T_w - T_{cq}}{F_q}\sqrt{\frac{k}{\varepsilon}} = \frac{T_w - T_{cq}}{T_q - T_{cq}}\sqrt{\frac{1}{Bi}} \tag{E-63}$$

where

k - wall thermal conductivity (Btu/ft s °F)

ρ - wall density (lbm/ft^3)

ε - wall thickness (ft)

U - quench front velocity (ft/s)

Figure E-5. Coney's two-dimensional axial conduction results.

T_q - quench temperature (°F)

T_{cq} - coolant temperature at the quench front (°F)

T_w - wall temperature ahead of the quench front (°F)

F_q - correlation parameter ((Btu °F/s)$^{1/2}$/ft)

F_q was correlated empirically in terms of coolant velocity V (ft/s) and subcooling ΔT_{cq} (°F) at the quench front

$$F_q = 4.46787 \times 10^2 \; V^{0.15} \left(1 + 0.0941 \; V\Delta T_{cq}^2\right)^{0.13}$$

for

$$\left(1 + 0.0941 \; V \; T_{cq}^2\right) \leqslant 40$$

$$F_q = 2.162 \times 10^2 \; V^{0.15} \left(1 + 0.0941 \; V\Delta T_{cq}^2\right)^{0.346} \qquad \text{(E-64)}$$

for

$$\left(1 + 0.0941 \; V\Delta T_{cq}^2\right) > 40$$

The value of the quench temperature used to derive Farmer's correlation of F_q is

$$T_q = T_{sat} + 144°F = 356°F \qquad \text{(atmospheric pressure)}$$

IN UCFLOOD, the inlet reflooding velocity is used as the average coolant velocity at the quench front. The coolant subcooling at the quench front is taken as the subcooling at the coolant axial node just below the lower boundary of the quench-front region, (see Fig. E-3). The wall temperature ahead of the quench front is obtained as described in Section 3.6.1.

Subroutine QFRCY calculates the quench front velocity U by the method described above for given values of T_w, T_{cq}, and V. The eight curves shown in Fig. E-5 are

supplied to QFRCY as the discrete data points represented by the dots in this figure. The values of F_q, Bi and η are calculated first from Eqs. E-62 and E-63, respectively; next subroutine TRIDI is called to perform a linear interpolation in two dimensions and provide w. This value of w is used with Eq. E-61 to calculate the quench front velocity.

For small values of η, the plots are clearly non linear, therefore, for $\eta < 0.5$, a numerical fit of the results, suggested by Farmer, is used instead of the linear interpolation, namely

$$w = \kappa\left(\eta^2 - \frac{\eta}{\sqrt{Bi}}\right)$$

where the slow variation of the coefficient κ with $\eta\sqrt{Bi}$ is given by

$\eta\sqrt{Bi}$	1.0	1.2	1.5	2.0	2.5	3.0	4.0	5.0	6.0	7.0
κ	1.570	1.478	1.395	1.315	1.256	1.220	1.172	1.139	1.117	1.094

This table is also supplied to subroutine QFRCY. The values of κ for values of $\eta\sqrt{Bi}$ between the data points are calculated by linear interpolation.

To avoid the table interpolation procedure needed to obtain Coney's analytical solution results, a simple analytical fit of the solution proposed by Dua and Tien [59] that approximates the results of Fig. E-5 within approximately 10% can also be used. In this case the Peclet number, Pe, is given as a simple function of a modified Biot number $\overline{Bi}$,

$$Pe = [\overline{Bi}(1 + 0.40\ \overline{Bi})]^{1/2}$$

where

$$\overline{Bi} = \frac{Bi}{\theta_w(\theta_w - 1)}$$

with

$$\theta_w = \frac{T_w - T_{cq}}{T_q - T_{cq}}$$

For the calculation of U from Eq. E-65 the wall thermal conductivity and specific heat are calculated at $(T_w + T_{cq})/2$. However, to calculate the Biot number and η, the wall thermal conductivity is evaluated at the quench temperature. If the calculated value of Bi is larger than 200, the curve Bi = 200 is used to calculate w. Similarly if Bi is less than 0.5, the curve Bi = 0.5 is used to calculate w.

Note that any other correlation (such as the empirical fits derived from FLECHT data) could be easily substituted to the above for obtaining the velocity of the quench front.

E.1.3.3 Third Version. The quench front velocity is calculated by solving the two-dimensional heat conduction equation as described in Section 3.3. The finite-difference numerical scheme used to solve this equation was described in Appendix D.

Subroutine QFRONT calculates the quench-front velocity by this method; a flow diagram of this routine is shown in Fig. E-6.

Figure E-7 shows the nodalization in the quench front region. The positions of the radial nodes $r_1,\ldots,r_{NR}$ are read-in as input and do not change in time. There are NF radial nodes in the fuel and NC in the cladding (NR = NF + NC).

The axial grid moves in time by following the steep part of the axial temperature gradient. There is an inner region of fine axial nodes of node length DZ, sandwiched between two regions of sparse nodes of node length DZM. DZM is a multiple of DZ. Two fractional-length sparse nodes, one on each side, may exist between the fine and sparse-node regions. The maximum number of axial nodes is NA.

Inspection of the surface temperature profile, obtained by solving the conduction equation with a uniform fine grid throughout the quench-front region and the heat transfer coefficient distribution described in Section 3.4, has shown that the surface temperature gradient changes slowly with distance up to a point where this gradient takes a value (GRAM) of about 1000°F/ft. This number is therefore used to define the extent of the region where a fine axial grid is necessary. This region extends in Fig. E-7 from a_U to a_D.

Specifically, the axial location $Z = a_U$ is defined as the node for which the fuel pin centerline (or outer surface in the case of a tubular test section) temperature gradient just exceeded GRAM. Similarly, $Z = a_D$ is defined as the wet surface node for which the surface axial temperature gradient just dropped below GRAM.

Five fine axial nodes downstream of $Z = a_D$ are always maintained in order to make sure that after one time step the new position of node a_D will not "fall" in the sparse grid.

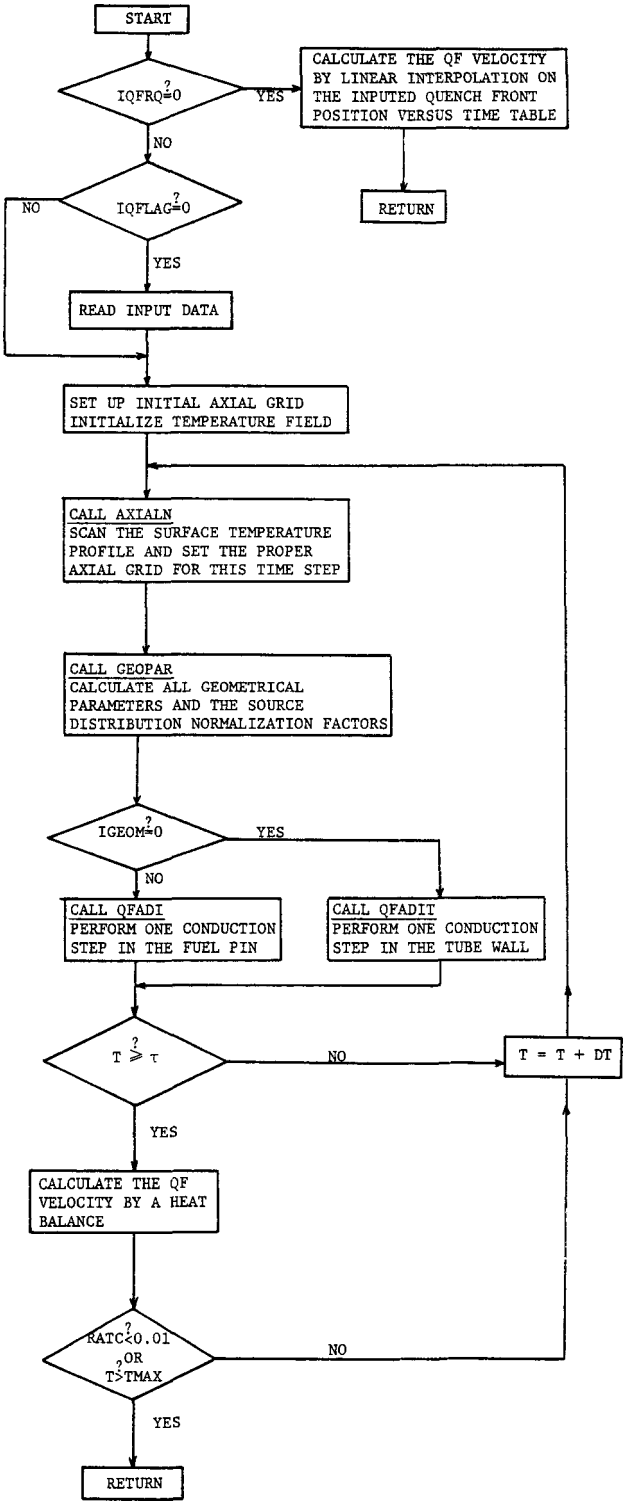

Figure E-6. Flow chart for subroutine QFRONT.

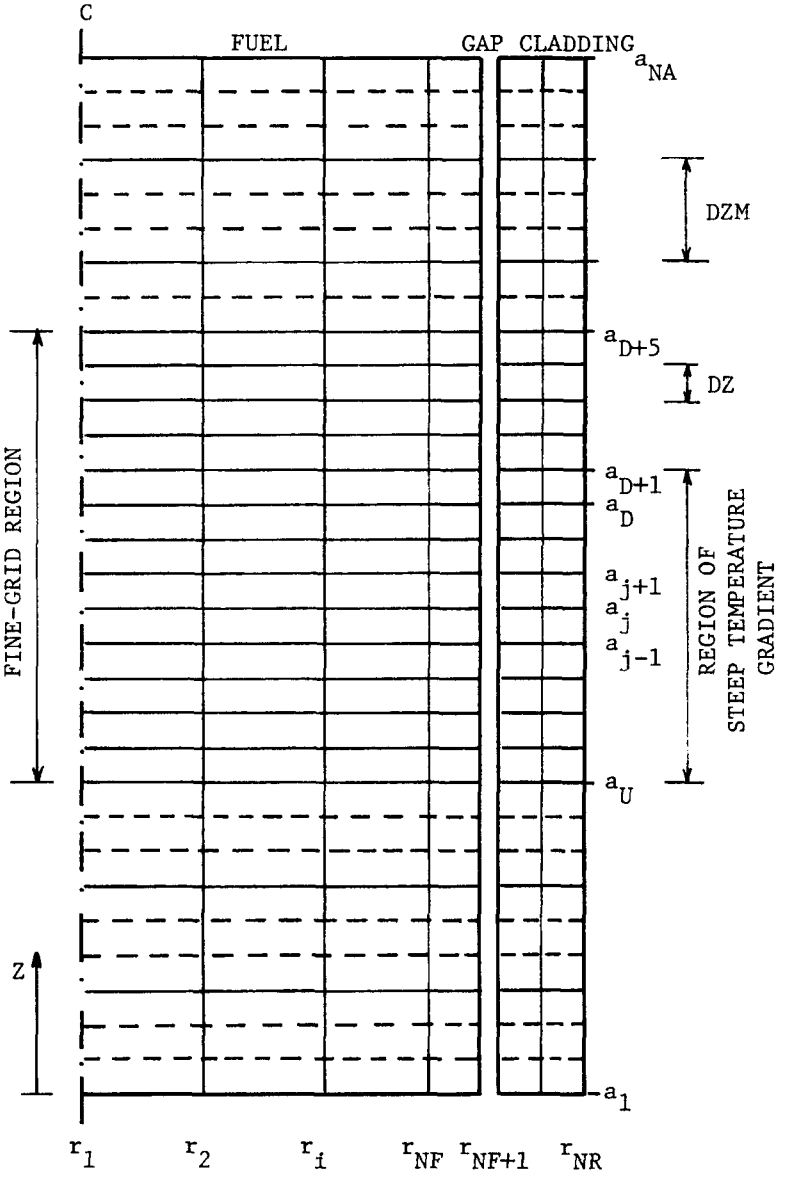

Figure E-7. Fuel pin nodalization in the quench front region.

Subroutine QFADI, or QFADIT if IGEOM = 0, performs one time step integration of the two-dimensional conduction equation, as described in Appendix D. Following this time advancement, a new temperature field exists and subroutine AXIALN is called to reset the axial grid. AXIALN scans the temperature profiles from bottom to top setting an axial grid in such a way that all nodes embraced by the region $a_U < Z < a_{D+5}$ have size DZ (fine grid) and all other nodes upstream and downstream of this region have size DZM. Two fractional-length large nodes may be created by this procedure, as mentioned above, and shown in Fig. E-7. During the solution, subroutine AXIALN creates new fine nodes downstream, so that five fine axial nodes are always maintained downstream of node a_D. The temperature initialization for these newly created fine nodes is obtained by linear interpolation, using the temperatures at the existing neighboring large nodes.

If node a_{D+5} reaches node a_{NA} the quench front region is extended by a length DZL. A fine or a sparse grid is set in this new length according to the requirements imposed by the moving temperature field.

Similarly, when the distance between upstream nodes a_1 and a_U exceeds DZL, the position of the first node a_1 is shifted upstream by a distance DZL. DZL must be specified as a multiple of DZM.

Initialization of the calculations is obtained as follows:

The first call of subroutine QFRONT sets a uniformly-fine axial grid of NA nodes:

$$a_j = Z_B + (j-1)DZ \quad , \qquad j = 1,2,...NA \tag{E-65}$$

where Z_B is the upstream location of the QF region.

Then the temperature field is initialized as

$$T_{i,j} = \frac{T_T + T_B}{2} + \frac{T_T - T_B}{2} \tanh\left[\frac{12(j-1)}{NA} - 6\right] \tag{E-66}$$

for

$$i = 1,2,...,NR \quad \text{and} \quad j = 1,2,...,NA$$

where T_B and T_T are the cladding surface temperatures at the upstream and downstream boundaries of the quench front region, respectively, and are calculated from Eqs. 3-18 and 3-20.

Once the initial grid and temperature field have been set by Eqs. E-66 and E-67, subroutine AXIALN is called, as usual, to redefine the axial nodalization. Figure E-7 shows the resulting axial grid after the first call of subroutine AXIALN. The dashed lines represent the initial nodes that have been discarded.

The heat generation rate distribution is treated in the same manner as described in Appendix B. However, since subroutine QFRONT runs for only a few seconds (2 or 3 s) each time it is called, it is assumed that there is no power decay during this period.

Subroutine GEOPAR calculates all the geometrical parameters used by QFADI (or QFADIT) and the heat source distribution at each time step.

The selection of heat transfer coefficients for the QF region, was discussed in Section 3.4; these are calculated by the function HTCOF.

In Section 3.3.1, an average quench front velocity $\bar{U}$ was defined by a heat balance over a short time period $t_2 - t_1 = \tau$, where τ is given by Eq. 3-11. To determine when a quasi-steady-state condition is achieved, a criterion is necessary. In principle, it would have been possible to define this convergence criterion using the definition of the instantaneous quench front velocity given by Eq. 3-2, i.e.

$$\left| \frac{U(t+\Delta t) - U(t)}{U(t)} \right| < \varepsilon$$

where ε is a small quantity defining convergence.

To calculate U(t) however, it is necessary to integrate the cladding surface heat flux along the quench front region numerically. This integration, due to its numerical nature, has some error associated with it. Since the time step Δt used by subroutine QFRONT and its associated routines is very small, the difference of the cladding-surface heat flux integrals at time t and $t + \Delta t$ could be distorted by the numerical error associated with those integrals.

Therefore, to avoid this problem, an average quench front velocity $\bar{U}$ was defined by Eq. 3-7. Subroutine QFRONT calculates the average quench front velocity over two consecutive time periods, i.e. over $(t, t+\tau)$ and over $(t+\tau, t+2\tau)$ and uses Eq. 3-10 with $\varepsilon = 0.01$ to check for convergence. When convergence is achieved, subroutine QFRONT returns the average quench front velocity calculated over the last time interval as the quasi-steady-state quench front velocity. A maximum running time (TMAX) for subroutine QFRONT is defined to stop execution if convergence is not achieved.

The input parameter IQFRQ determines how often the quench front velocity is going to be calculated. Three cases are considered:

1) IQFRQ = 0 - the quench front velocity is calculated at every code time step. This option should be used with UCFLOOD versions 1 and 2.

2) IQFRQ = 1 - the quench front velocity is calculated as often as the non-dimensional wall temperature ahead of the quench front changes by more than five percent with respect to its value at the previous quench front velocity calculation, i.e., if

$$\left|\frac{\theta - \theta_R}{\theta}\right| > 0.05$$

The non-dimensional wall temperature θ was defined as

$$\theta = \frac{T_w - T_{cq}}{T_q - T_{cq}}$$

and θ_R is the value of θ at the time of the previous quench-front-velocity calculation. This criterion arises from the fact that for a given fuel rod or test section, the wall temperature ahead of the quench front and the coolant temperature at the quench front are the two major variables influencing the quench front velocity. This option should be used with UCFLOOD version 3.

3) IQFRQ > 1 - the quench front velocity is calculated at every IQFRQ code time step. This option can also be used with UCFLOOD version 3.

The alternative that consists in running continuously the two-dimensional axial-conduction calculation has not been programmed in the present version of the code.

E.2 INPUT INSTRUCTIONS FOR UCFLOOD

Only four different formats are used for input as shown below. All two-dimensional tables made up of independent (X) and dependent (Y) variable pairs are inputed as follows. Each pair is punched on a card preceded by a running index K and followed by a flag KFLAG, and is read in as

```
READ (5,400) K,X,Y,KFLAG
FORMAT (I5,2F15.0,I5)
```

KFLAG is zero except on the last card, where the punched value of 1 terminates table input. For constant Y, a single card with KFLAG = 1 may be used. The cards must be ordered so that the independent variable increases monotonically.

E.2.1 Input Data Read in by Subroutine INPUT

CARD #1 - Format (I5,18A4) - Title Card

Variables: IPRO, TITLE

IPRO - specifies the input data level (used when more than one case is to be executed in the same run).

= 0 for the first case; all the input data must be read in.

= 1 for the subsequent cases; reading resumes at CARD #14.

= 2 reading resumes at CARD #17.

TITLE - title of the case.

CARD #2 - Format (16I5) - Options

Variables: ISIGI, IOPT, LOPT, JOPT, IGEOM, IQFRQ, KGAP, INTF, ITVOPT, IDFP, IPRTF, IPLTF, IPLFZ, III

ISIGI = 0 power input is constant in time

= 1 power input is variable in time

IOPT = 0 the fuel pin thermal properties are calculated by linear interpolation of tabular data

≠ 0 the fuel-pin thermal properties are calculated internally. Three fuel-pin models are available:

IOPT = 1 - UO_2 - Zr fuel pin model

= 2 - FLECHT pin model with SS-cladding

= 3 - FLECHT fuel pin model with Zircaloy-cladding

LOPT = 1 the power input is calculated according to the ANS Standard decay heat curve

= 2 the power input is calculated by linear interpolation of tabular data.

JOPT = 0 the fuel pin temperature initialization is supplied externally. Three options are available for this initialization:

INTF = 1 - the temperature is radially and axially uniform, only one value is given as input

= 2 - the temperature is uniform in the radial direction; the temperature at each axial node is given as input

= 3 - the temperature at each node is given as input

(See also card(s) #20)

JOPT = 1 the fuel pin temperature initialization is calculated by a steady-state conduction calculation based on the axial power profile. Available only for IGEOM = 1

= 2 the fuel pin temperature initialization is calculated by a mid-plane steady-state conduction calculation assuming a chopped-sine distribution. Available only for IGEOM = 1

IGEOM = 0 circular-tube geometry

= 1 fuel-rod geometry

IQFRQ - subroutine QFRONT calling frequency, number of time steps per call. If the quench front position as a function of time is given as input, IQFRQ must be specified as zero.

KGAP = 1 the gap heat transfer coefficient is constant along the pin.

= NA the gap heat transfer coefficient is specified at each axial node. NA is the number of axial nodes.

INTF - See under JOPT above

ITVOPT = 0 the droplet velocity is calculated as the terminal velocity.

= 1 the droplet velocity is calculated by integrating the droplet equation of motion.

IDFP = 0 the parameters γ and β for the nondimensional vaporization rate profile are calculated by subroutine EXTPF (to be supplied by user).

= 1 the parameters γ and β are calculated by subroutine DISPFL, (see Appendix C).

IPRFT - printing frequency, number of time steps per printing.

IPLTF - number of time steps between plotted points in the time plots. IPLTF $\geqslant$ TMAX/100.

IPLFZ - number of time steps between plots of the surface temperature profile. IPLFZ $\geqslant$ TMAX/100.

III - If IT is the number of axial nodes in the flow channel, the local flow conditions are printed for the nodes (I = 1,IT,III)

IF IOPT = 0 SKIP CARDS #3 to 8

CARD #3 - Format (8F10.0) - Fuel Pin Densities

Variables: DENF, DENC

DENF - fuel density (if IGEOM = 1) or tube wall density (if IGEOM = 0) (lbm/ft^3)

DENC - cladding density (lbm/ft^3)

CARD(S) #4 - Format (I5,2F15.0,I5) - Table of Fuel Pin Specific Heat

Variables: K, TEMP1(K), PROP1(K), KFLAG

TEMP1(K) - temperature (°F)

PROP1(K) - fuel specific heat (if IGEOM = 1) or tube wall specific heat (if IGEOM = 0) (Btu/lbm°F)

CARD(S) #5 - Format (I5,2F15.0,I5) - Table of Cladding Specific Heat

Variables: K, TEMP2(K), PROP2(K), KFLAG

TEMP2(K) - temperature (°F)

PROP2(K) - cladding specific heat (Btu/lbm°F). If IGEOM = 0 provide one card with KFLAG = 1 only.

CARD(S) #6 - Format (I5,2F15.0,I5) - Table of Fuel Pin Thermal Conductivity

Variables: K, TEMP3(K), PROP3(K), KFLAG

TEMP3(K) - temperature (°F)

PROP3(K) - fuel thermal conductivity (if IGEOM = 1) or tube wall thermal conductivity (if IGEOM = 0) (Btu/ft s °F)

CARD(S) #7 - Format (I5,2F15.0,I5) - Table of Cladding Thermal Conductivity

Variables: K, TEMP4(K), PROP4(K), KFLAG

TEMP4(K) - temperature (°F)

PROP4(K) - cladding thermal conductivity (Btu/ft s °F). If IGEOM = 0 one card with KFLAG = 1 suffices.

IF IGEOM = 1 SKIP CARD #8

CARD #8 - Format (4E15.0) - External Losses

Variables: CLOSS(I), I = 1,4

Coefficients for the third-order polynomial fit of the loss heat transfer coefficient. (Btu/ft^2 s °F, $°F^2$,$°F^3$,$°F^4$) (See Section E.1.2.3.)

CARD(S) #9 - Format (I5,2F15.0,I5) - Table of Axial Power Input Distribution

Variables: K, ZSOUR(K), SOUR(K), KFLAG

ZSOUR(K) - axial location (ft)

SOUR(K) - axial power input normalization factor

CARD(S) #10 - Format (I5,2F15.0,I5) - Table of Radial Power Distribution

Variables: K, RP(K), RD(K), KFLAG

RP(K) - radial location (ft)

RD(K) - radial power input normalization factor. (See Section E.1.2.1.)

IF LOPT = 1 OR ISIGI = 0 SKIP CARD #11

CARD(S) #11 - Format (I5,2F15.0,I5) - Table of Power Decay Factors

Variables: K, TIME(K), SS(K), KFLAG

TIME(K) - time (s)

SS(K) - power input decay normalization factor. (See Section E.1.2.1.)

IF LOPT ≠ 1 SKIP CARD #12

CARD #12 - Format (8F10.0) - Decay Heat Calculation

Variables: TBLOW, TOPER, CS25, FCS25, CR

TBLOW - blowdown period (s)

TOPER - reactor operating time at beginning of blowdown period (s)

CS25 - absorption cross section of U^{235} (barn)

FCS25 - fission cross section of U^{235} (barn)

CR - conversion ratio

(See Section E.1.2.1.)

IF IGEOM = 0, SKIP CARD #13

CARD(S) #13 - Format (8F10.0) - Gap Heat Transfer Coefficients

Variables: HGAP(I), I = 1,KGAP

HGAP(I) - gap heat transfer coefficient at node I. (Btu/ft^2 s °F)

CARD #14 - Format (8F10.0) - Geometrical Parameters

Variables: FR, GT, CT, DH

FR - fuel radius (ft)

GT - gap thickness (ft)

CT - cladding thickness (if IGEOM = 1) or tube wall thickness (if IGEOM = 0) (ft)

DH - hydraulic diameter (ft)

CARD #15 - Format (16I5) - Nodalization

Variables: NF, NC, NA, NCPFN2, NCPFN1, NCPFN

NF - number of radial nodes in the fuel (if IGEOM = 1), or number of radial nodes in the tube wall (if IGEOM = 0). If NF = 2 and IGEOM = 0 transient conduction is carried out by the lumped-parameter subroutine CONDL.

NC - number of radial nodes in the cladding; set NC = 0 if IGEOM = 0; maximum allowable (NF + NC) is 15.

NA - number of axial fuel nodes; maximum allowable is 120.

NCPFN2 - minimum number of fluid elements per fuel node in control volume 1.

NCPFN1 - number of coolant nodes per fuel axial node in control volume 2.

NCPFN - number of coolant nodes per fuel node in control volume 3.

(See Sections E.1.1.1, E.1.1.5, E.1.1.10.)

CARD #16 - Format (8F10.0) - Fuel Rod Geometry

Variables: FLENGT, XN(I), I = 1,NR, where NR = NF + NC

FLENGT - fuel rod length (ft)

XN(I) - radial node positions (ft)

CARD #17 - Format (8F10.0) - Adjustable Parameters

Variables: WE, WED, COD, WEMISS, VEMISS, COA, COB, VGJA, VGJB

WE - Weber number at onset of carryover

WED - droplet Weber number

COD - minimum drag coefficient

WEMISS - wall emissivity

VEMISS - vapor emissivity

COB - drift-flux-model distribution parameter for the inverted-annular film-boiling (IAFB) flow regime

COA - distribution parameter for the annular flow regime

VGJB - gas drift velocity for the IAFB flow regime (ft/s)

VGJA - gas drift velocity for the annular flow regime (ft/s)

If COA is inputed as zero, COA and VGJA are calculated internally.

CARD(S) #18 - Format (I5,2F15.0,I5) - Table of Inlet Reflooding Velocities

Variables: K, TIME1(K), ULIN(K), KFLAG

TIME1(K) - time (s)

ULIN(K) - reflooding velocity (ft/s)

CARD(S) #19 - Format (I5,2F15.0,I5) - Table of Inlet Coolant Temperatures

Variables: K, TIME2(K), TLIN(K), KFLAG

TIME2(K) - time (s)

TLIN(K) - inlet coolant temperature (°F)

IF JOPT ≠ 0 SKIP CARD #20

CARD(S) #20 - Format (8F10.0) - Initial Temperature Distribution

Variables: TF(I,J), I = 1,NR, J = 1,NA

TF(I,J) - initial fuel rod temperature at the various nodes.

If INTF = 1, TF(1,1) only need to be inputed.

If INTF = 2, TF(1,J), J = 1,NA need to be inputed.

If INTF = 3, TF(I,J), I = 1,NR, J = 1,NA need to be inputed.

(See Section E.1.2.3.)

IF JOPT = 0 SKIP CARD #21

CARD #21 - Format (8F10.0) - Parameters for Calculated Initial Temperature Distribution

Variables: TW6FT, TWOFT

TW6FT - initial midplane-elevation wall temperature (°F)

TWOFT - initial zero-elevation wall temperature (°F)

CARD #22 - Format (8F10.0) - Problem Parameters

Variables: PL, TON, RPP, DT, TMAX

PL - peak linear power input, or reactor operating linear power if LOPT = 1 (kW/ft)

TON - time of reflooding initiation after beginning of power decay (s)

RPP - bundle radial power peaking, if IOPT ≠ 2 or 3 or IGEOM = 0 set RPP = 1.1

DT - code time step (s)

TMAX - code running time (s)

CARD #23 - Format (8F10.0) - Pressure and Temperatures

Variables: PSAT, TSAT, TQUENC, TAMB

PSAT - system pressure (psia)

TSAT - saturation temperature (°F)

TQUENC - quench temperature (°F)

TAMB - ambient temperature; needs specification only if IGEOM = 0

If subroutine QFRCY is being used, this is the last input card.

E.2.2 Input Data Read in at the First Call of Subroutine QFRONT

From here on all the input variables are for the quench front model and they do not have any relation to variables inputed previously having the same name.

IF IQFRQ = 0 SKIP CARDS #24 TO 30

CARD #24 - Format (16I5) - Nodalization

Variables: NF, NC, NA

NF - number of radial nodes in the fuel; if IGEOM = 0 set NF = 0

NC - number of radial nodes in the cladding (if IGEOM = 1) or in tube wall (if IGEOM = 0). Maximum allowable value for NR = NF + NC is 10

NA - initial number of axial nodes; maximum allowable is 199

(See Section E.1.3.3.)

CARD #25 - Format (8F10.0) - Nodalization, etc.

Variables: DZ, DZM, DZL, GRAM, DT, TMAX

DZ - size of the small axial nodes (ft)

DZM - size of the large axial nodes (ft)

DZL - increments in the quench front length (ft)

GRAM - limiting axial temperature gradient (°F/ft)

DT - time step (s)

TMAX - maximum running time (s) for subroutine QFRONT calls

CARD #26 - Format (8F10.0) - Radial Nodalization

Variables: R(I), I = 1,NR

R(I) - radial node positions (ft)

IF IGEOM = 0 SKIP CARDS #27 AND 28

CARD #27 - Format (4E15.0) - Fuel Pin Thermal Conductivities

Variables: TKFR1, TKFR2, TKFA1, TKFA2, TKCR1, TKCR2, TKCA1, TKCA2

Coefficients for the linear fits representing the fuel and cladding thermal conductivities as a function of temperature (Btu/ft s °F)

TKFR1, TKFR2 - for the fuel in the radial direction

TKFA1, TKFA2 - for the fuel in the axial direction

TKCR1, TKCR2 - for the cladding in the radial direction

TKCA1, TKCA2 - for the cladding in the axial direction

CARD #28 - Format (4E15.0) - Fuel Pin Heat Capacities

Variables: NCF1, HCF2, HCC1, HCC2

Coefficients for the linear fits representing the fuel and cladding heat capacities as a function of temperature (Btu/ft^3°F)

HCF1, HCF2 - for the fuel

HCC1, HCC2 - for the cladding

IF IGEOM = 1 SKIP CARDS #29 AND 30

CARD #29 - Format (4E15.0) - Tube Thermal Conductivities

Variables: TKTB(I), I = 1,4

Coefficients for the linear fits representing the tube wall thermal conductivity as a function of temperature (Btu/ft s °F)

TKTB(I), I = 1,2 - in the radial direction

TKTB(I), I = 3,4 - in the axial direction

CARD #30 - Format (4E15.0) - Tube Heat Capacities

Variables: GPTB(I), I = 1,2

Coefficients for the linear fits representing the tube wall heat capacity as a function of temperature ($Btu/ft^3 °F$)

IF IQFRQ ≠ 0 SKIP CARD #31

CARD #31 - Format (I5,2F15.0,I5) - Table of Quench Front Positions

Variables: I, TIMQ(I), ZQP(I), IFLAG

TIMQ(I) - time (s)

ZQP(I) - quench front position (ft)

(See Section E.1.3.1.)

E.2.3 Data Input for UC-B Runs 114, 120, and 188

The data input cards for these runs are listed in pages E-52 to E-54.

REFERENCES

1. American Nuclear Society Standard (draft), "Decay Energy Release Rates Following Shutdown of Uranium-Fueled Thermal Reactors", ANS-5 (October 1971).

2. C. J. Hocevar and T. W. Wineinger, "THETA1-B, A Computer Code for Nuclear Reactor Core Thermal Analysis", TID-4500 (February 1971).

3. L. E. Hochreiter, Letter communication (March 1976).

```
  0  **** UCFLOOD CODE VERSION 2 --- PREDICTION OF UCB RUN NO. 114 ****
  1     0     0     2     0     0     0     1     1     0     1     2     3   20     1
525.0
  1     70.0         0.106
  2    200.0         0.111
  3    400.0         0.116
  4    600.0         0.121
  5    800.0         0.126
  6   1000.0         0.132
  7   1200.0         0.140
  8   1400.0         0.145
  9   1600.0         0.149                1
  1                                        1
  1     70.0         0.002384167
  2    200.0         0.002730556
  3    400.0         0.0028000917
  4    600.0         0.003078694
  5    800.0         0.003356472
  6   1000.0         0.0036575
  7   1200.0         0.003980556
  8   1400.0         0.004305556
  9   1600.0         0.004629722          1
  1                                        1
3.3028389E-04  1.2999781E-06 -9.1905528E-10  1.0241969E-12
  1    0.0           1.0                  1
  1    0.0           1.0                  1
0.0      0.0         0.0025     0.047083
  2     0    40     4     2     1
12.0     0.023541670.02604167
10.0     2.0         0.44       0.7        0.1        1.1        1.0        1.0
1.0
  1    0.0           0.41667              1
  1    0.0           149.0                1
1000.0
0.28     0.0         1.1        1.0        150.0
14.7     212.0       356.0      70.0
```

```
  0  **** UCFLOOD CODE VERSION 2 --- PREDICTION OF UCB RUN NO. 120 ****
  0    0    2    0    0    0    1    1    0    1    2    1   20    1
525.0
  1    70.0        0.106
  2   200.0        0.111
  3   400.0        0.116
  4   600.0        0.121
  5   800.0        0.126
  6  1000.0        0.132
  7  1200.0        0.140
  8  1400.0        0.145
  9  1600.0        0.149               1
  1                                     1
  1    70.0        0.002384167
  2   200.0        0.002730556
  3   400.0        0.002800917
  4   600.0        0.003078694
  5   800.0        0.003356472
  6  1000.0        0.0036575
  7  1200.0        0.003980556
  8  1400.0        0.004305556
  9  1600.0        0.004629722         1
  1                                     1
3.3028389E-04  1.2999781E-06 -9.1905E28E-10  1.0201969E-12
  1   0.0          1.0                 1
  1   0.0          1.0                 1
0.0     0.0        0.0025    0.047083
  2    0   40    4    2    1
12.0    0.023541670.02604167
10.0    2.0        0.44      0.7       0.1       1.1       1.0       1.0
1.0
  1   0.0          0.416667            1
  1   0.0          73.0                1
1000.0
0.28    0.0        1.1       1.0       80.0
14.7    212.0      356.0     70.0
```

```
  0  **** UCFLOOD CODE VERSION 2 --- PREDICTION OF UCB RUN NO. 188 ****
  0    0    2    0    0    0    1    1    0    1    2    2   20    1
525.0
  1    70.0        0.106
  2   200.0        0.111
  3   400.0        0.116
  4   600.0        0.121
  5   800.0        0.126
  6  1000.0        0.132
  7  1200.0        0.140
  8  1400.0        0.145
  9  1600.0        0.149                1
  1                                     1
  1    70.0        0.002384167
  2   200.0        0.002730556
  3   400.0        0.002800917
  4   600.0        0.003078694
  5   600.0        0.003356472
  6  1000.0        0.0036575
  7  1200.0        0.003980556
  8  1400.0        0.004305556
  9  1600.0        0.004629722          1
  1                                     1
3.3028389E-04  1.2999781E-06 -9.1905528E-10  1.0201969E-12
  1   0.0          1.0                  1
  1   0.0          1.0                  1
0.0     0.0        0.0025     0.047083
  2    0   40    4    2    1
12.0    0.023541670.02604167
10.0    2.0        0.44       0.7        0.1        1.1        1.0        1.0
1.0
  1   0.0          0.24667              1
  1   0.0          78.0                 1
994.2
0.31    0.0        1.1        1.0        150.
14.7    212.0      356.0      70.0
```